

# POLITENICO DI TORINO

Dipartimento di Ingegneria Strutturale, Edile e Geotecnica (DISEG)

**Corso di Laurea Magistrale in Ingegneria Civile**



Tesi di Laurea Magistrale

## **Finite Element Model Calibration of a Reinforcement Concrete Building from Laboratory Tests for Seismic Retrofitting Interventions**

Relatore:

Prof. Marco Domaneschi

Correlatore:

Prof. Luca Martinelli

Candidato:

Daniel Camilo Ballesteros Puerto

Luglio 2021



# Acknowledgment

I am grateful to all the people who stand by me during *La Laurea Magistrale in Ingegneria Civile al Politecnico di Torino*. It has been three years far away from home, facing the world and undertaking the most difficult challenges. I want to thank my family, my principal life support, especially my parents, *papito y mamita*, and my siblings, *hermanito y hermanita*; without the love provided by them, I would not be able to overcome this stage of my fortune. Additionally, I want to thank my second family: my friends in Italy, the people I came with in 2018, as well as those who met in the path. We came here to look for a better future, better opportunities, to explore the world, and to confirm that we are ready for big things in life. *En especial, quiero mencionar a mis más grandes amigos y soportes esenciales de mi vida en Turín: Serna, Carlitos, Luis, Pipe y Carolina. Vi voglio bene a tutti!*

Last but not the least, I would like to express my genuine gratitude to my advisors Prof. Marco Domaneschi and Prof. Luca Martinelli, for the patience, the trust, and the guidance during the thesis.

Gracias, Javeriana Cali por ofrecerme la oportunidad de vivir esta experiencia.

Grazie Politecnico di Torino per tutta la conoscenza, gli amici e le esperienze.

*Daniel Camilo Ballesteros Puerto*



# Contents

1	Introduction .....	1
2	Seismic Protection Systems.....	4
2.1	Dissipating Devices .....	6
2.1.1	Device's typology:.....	6
2.2	Fluid Viscous Dampers (FV Dampers) .....	9
2.2.1	Mounting Arrangements and Damper Configuration.....	12
2.3	Metallic-Yielding Dampers .....	13
2.3.1	Mounting Arrangements and Damper Configuration.....	15
3	Seismic Demand.....	16
3.1	Response Spectrum.....	17
3.2	Natural Accelerograms and Spectrum .....	17
4	Four-Story Full-Scale R/C Frame – Study Case .....	20
4.1	Numerical Model .....	20
4.1.1	Structural Scheme- Floor Plan View and Elevation.....	20
4.1.2	Structural Elements .....	21
4.1.3	Masses and Loads.....	34
4.1.4	Schiavo's Model Verification.....	35
4.2	Optimization of the Model.....	36
5	Structural Analysis of Pre-Retrofit Structure .....	41
5.1	Modal Analysis .....	41
5.2	Static Pushover Analysis .....	42
5.2.1	Profile of Forces: .....	42
5.2.2	Modal And Uniform Approach: .....	42
5.2.3	Equivalent Mass and Participation Factor: .....	43
5.2.4	Capacity Curves.....	44
5.2.5	SDOF-Bilinear Equivalent Curve.....	47
5.2.6	Seismic Demand Linked to The Effective Period: .....	48

5.2.7	Safety Checks .....	49
5.3	Nonlinear Time-history Analysis.....	52
6	Retrofitting of the Structure.....	58
6.1	Fluid Viscous Damper .....	58
6.1.1	Mounting Arrangement and Damper Configuration: .....	59
6.1.2	Strain Energy-Based Method.....	60
6.1.3	Selection of Damper .....	63
6.1.4	FEM Simulation on SAP2000 .....	64
6.2	Metallic-Yielding Damper - TADAS .....	65
6.2.1	Mounting arrangement and damper configuration: .....	66
6.2.2	Design Seismic Demand: .....	67
6.2.3	Bilinear capacity curves of the pre-retrofit building: .....	68
6.2.4	Influence of the bracing system on the pre-retrofit building (SLD):.....	69
6.2.5	Estimate the required added damping ratio (SLV):.....	70
6.2.6	TADAS dampers geometry: .....	71
6.2.7	Strain Energy-Based Method: .....	72
6.2.8	FEM simulation on SAP2000.....	78
7	Structural Analysis of Retrofitted Structure with Fluid Viscous Dampers .....	81
7.1	Modal Analysis .....	81
7.2	Static Pushover Analysis .....	82
7.3	Nonlinear Time-history Analysis.....	84
8	Structural Analysis of Retrofit Structure with Metallic-Yielding Dampers.....	89
8.1	Modal Analysis .....	89
8.2	Static Pushover Analysis .....	90
8.2.1	Idealized pushover curves in SDOF: .....	90
8.2.2	Static pushover curve in SAP2000: .....	95
8.2.3	SDOF-Bilinear Equivalent Curve.....	99
8.2.4	Seismic Demand Linked to The Effective Period: .....	101
8.2.5	Safety Checks .....	101
8.3	Nonlinear Time-history Analysis.....	105
9	Analysis of the results .....	111

9.1	Vulnerability index .....	111
9.2	Internal forces .....	113
9.2.1	Retrofitted structure with fluid viscous dampers.....	116
9.2.2	Retrofitted structure with metallic-yielding dampers.....	119
9.3	Interstory Drift .....	125
9.4	Summary of the results .....	126
Conclusions .....		128
Bibliography .....		131

# List of Tables

Table 1. Passive Energy Dissipation Systems [6] .....	5
Table 2. Structures with installed Tuned Liquid Dampers [10] .....	8
Table 3. Results of seismic test, Negro (1994).....	16
Table 4. Input parameters of the seismic design demand.....	17
Table 5. Beams.....	22
Table 6. Columns.....	25
Table 7. Average cubic compressive strength of concrete (from. Negro P. et al, 1994) and material models.....	26
Table 8. Average tensile properties of steel (from. Negro P. et al, 1994) and material models.....	26
Table 9. Structural elements and materials.....	27
Table 10. Hinge distribution and properties .....	30
Table 11 Mass Arrangement for 2D-Analysis .....	35
Table 12. Mass Arrangement for 3D-Analysis.....	35
Table 13. Distributed loads on beams.....	35
Table 14. Descriptive Statistics .....	38
Table 15. Descriptive statistical for displacement from the numerical and experimental displacement-time relationship.....	39
Table 16. Descriptive statistical for the absolute percentage error.....	39
Table 17. Periods and frequencies from bare frame.....	41
Table 18. Mass participation from bare frame.....	41
Table 19. Total mass by floor.....	41
Table 20. Normalized modal shape.....	42
Table 21. Pushover profiles: Modal and Uniform.....	43
Table 22. Modal participation factor and effective mass.....	44
Table 23. Bilinear curve (MDOF).....	46
Table 24. Output - Bilinear capacity curve (MDOF) .....	46
Table 25. MDOF capacity curve to SDOF capacity curve for the pre-retrofit structure .....	47
Table 26. Effective stiffness from bare frame.....	48
Table 27. Effective period, elastic base shear and displacement demand from response spectrum. [26]..	49
Table 28. Response spectrum demand for the pre-retrofit structure.....	49
Table 29. Relation between the reduction factor, ductility, and period ( $q - \mu - T$ ). [26].....	50
Table 30. Reduction factor, ductility demand and ductility capacity.....	50
Table 31. Response spectrum equations (ADRS) .....	50
Table 32. Pre-Retrofit- Time-history maximum displacement and maximum base shear.....	55
Table 33. Required damping.....	59
Table 34. Damper distribution on story, eigenvector, mass, and inclination of devices.....	62
Table 35. Linear damper-Simplified equation.....	63
Table 36. Linear damper-Complete equation.....	63
Table 37. Nonlinear damper-Complete equation .....	63
Table 38. Damper design force.....	64



Table 39. Commercial dampers from Taylor Devices Inc.[11]	64
Table 40. Limit states used to design seismic demand for retrofitting intervention with metallic dampers	67
Table 41. Pseudo-accelerations and displacements from response spectrum.	67
Table 42. Main features of the capacity curve from pre-retrofit building in SDOF	68
Table 43. Estimation of the 1 <sup>st</sup> natural period of the retrofit building and initial required stiffness of the Brace-Damper system.	69
Table 44. Required added damping ratio.	70
Table 45. Geometry of the metallic dampers placed on each floor.	71
Table 46. Configuration on the dampers: Frame, Elevation, Eigenvector and Mass.	73
Table 47. Shear interstory force, post-yielding coefficient, Yielding Displacement of the Device, Interstory Displacement when all devices yields and Interstory Displacement.	74
Table 48. Design damping force and Yielding Damping Force.	75
Table 49. Energy dissipated by the metallic damper, Strain energy of the main structure, Strain energy of added metallic dampers in the retrofitted structure.	76
Table 50. Equivalent hysteretic damping ratio.	76
Table 51. Suggested Damper Limitations	76
Table 52. Design safety verifications.	77
Table 53. Number of plates and displacement ductility of the dampers.	78
Table 54. Equivalent geometry for the TADAS devices	79
Table 55. Chevron bracing system configuration	80
Table 56. Periods and frequencies from bare frame.	81
Table 57. Normalized modal shape.	81
Table 58. MDOF capacity curve to SDOF capacity curve	82
Table 59. Reduction factor, ductility demand and ductility capacity.	83
Table 60. Retrofit building FVD- Time-history maximum displacement and maximum base shear.	86
Table 61. Natural periods of the pre-retrofit structure.	89
Table 62. Natural of the retrofit structure with metallic dampers.	89
Table 63. Geometrical and mechanical properties of triangular plates of the metallic dampers.	92
Table 64. Mechanical properties of the metallic dampers.	92
Table 65. Pushover Curve in SDOF of the pre-retrofit building.	92
Table 66. Expected features of the retrofit building with metallic dampers.	92
Table 67. Interstory displacements and roof displacement.	92
Table 68. Base shear strength of the combined system.	93
Table 69. Base shear strength in SDOF of the building with metallic dampers	93
Table 70. Displacement intersection between Trilinear and Bilinear pushover curves in SDOF	94
Table 71. Effective period and yielding displacement of the equivalent bilinear capacity curve in SDOF of the building with metallic dampers.	95
Table 72. Idealized trilinear and bilinear equivalent capacity curve in SDOF of the retrofit building with metallic dampers according with the Technical Report MCEER-00-0010	95
Table 73. Pushover profiles: Modal and Uniform.	96
Table 74. Modal participation factor and effective mass.	96
Table 75. Bilinear curve (MDOF).	97
Table 76. Output - Bilinear capacity curve (MDOF)	97
Table 77. MDOF capacity curve to SDOF capacity curve for the retrofit building with metallic dampers.	99
Table 78. MDOF capacity curve to SDOF capacity curve for the retrofit building with metallic dampers.	100
Table 79. Effective stiffness of for retrofit building with metallic dampers.	100

Table 80. Effective period, elastic base shear and displacement demand from response spectrum. [26]	101
Table 81. Response spectrum demand.....	101
Table 82. Relations between the reduction factor, ductility, and period ( $q - \mu - T$ ). [26].....	102
Table 83. Reduction factor, ductility demand and ductility capacity. ....	102
Table 84. Response spectrum equations (ADRS) .....	103
Table 85. Retrofit Building with metallic dampers - Time-history maximum displacement and maximum base shear.....	108
Table 86. Vulnerability indexes by Pushover Method - Force criterium.....	112
Table 87. Maximum displacement and pseudo-acceleration from nonlinear time-history analysis of the structure with and without dampers .....	113
Table 88. Maximum displacement and shear base from nonlinear time-history analysis of the structure with and without dampers. ....	114
Table 89. Change in percentage of the displacement and base shear - Structure with fluid viscous dampers respect to the pre-retrofit structure.....	115
Table 90. Change in percentage of the displacement and base shear - Structure with metallic yielding dampers respect to the pre-retrofit structure.....	115
Table 91. Change in percentage of the displacement and base shear - Structure with metallic yielding dampers respect to the structure with fluid viscous dampers. ....	116
Table 92. Maximum and minimum change of the average normal force in beams and columns regards percentage-FVD.....	116
Table 93. Maximum and minimum change of the average normal force in beams and columns regards absolute values-FVD. ....	117
Table 94. Maximum and minimum change of average shear forces in beams and columns regards percentage-FVD.....	117
Table 95. Maximum and minimum change of average shear forces in beams and columns regards absolute values-FVD. ....	117
Table 96. Maximum and minimum change of the average flexural moment in beams and columns regards percentage-FVD.....	118
Table 97. Maximum and minimum change of the average flexural moment in beams and columns regards absolute values-FVD. ....	118
Table 98. Maximum and minimum change of the average normal force in beams and columns regards percentage-HYD.....	120
Table 99. Maximum and minimum change of the average normal force in beams and columns regards absolute values-HYD. ....	120
Table 100. Histogram-Increment of the average normal force on Columns.....	120
Table 101. Maximum and minimum change of the average shear in beams and columns regards percentage -HYD.....	121
Table 102. Maximum and minimum change of the average shear in beams and columns regards absolute values-HYD. ....	121
Table 103. Maximum and minimum change of the average flexural moment in beams and columns regards percentage -FVD.....	122
Table 104. Maximum and minimum change of the average flexural moment in beams and columns regards absolute values-HYD.....	122
Table 105. Summary of the effects of the dampers on the structure. ....	127

# List of Figures

Figure 1. Passive and Active Control Solutions Workflow Diagram[4] .....	4
Figure 2. Semi-Active Control Solution Work Flow Diagram.[4] .....	4
Figure 3. Summary of seismic protection systems[5] .....	5
Figure 4. Summary of construction, hysteretic behavior, physical models, advantages, and disadvantages of passive energy dissipation devices for seismic protection applications (modified from Symans et al. 2008) [8] .....	6
Figure 5. Summary of construction, hysteretic behavior, physical models, advantages, and disadvantages of passive energy dissipation devices for seismic protection applications (modified from Symans et al. 2008) [8] .....	7
Figure 6. Response of SDOF to El Centro excitation with and without TMD [9] .....	7
Figure 7. Effect of energy dissipation systems on Force-Deformation Curves of a Structure.[6] .....	8
Figure 8. Spectral capacity and demand curves for rehabilitated one-story building[11] .....	9
Figure 9. Standard Fluid Damper and Components[11] .....	9
Figure 10. Hysteresis loops of dampers with pure viscous and viscoelastic behavior[8].....	10
Figure 11. Force-Velocity Relationship of Viscous Damper[11].....	11
Figure 12. Comparison of Energy Absorbed with Varying Damping Exponents with Sinusoidal Input[11] .....	11
Figure 13. Damper-Brace configuration: Diagonal Brace, Chevron Brace and Toggle Brace [11, 13] ..	12
Figure 14. Magnification factor for dampers in Chevron Brace, Diagonal Brace and Toggle Brace [13] .....	13
Figure 15. Details of Steel Welded TADAS device (units in mm) [14].....	13
Figure 16. Triangular-plate Added Damping and Stiffness (TADAS) and typical configuration[14] .....	13
Figure 17. Mechanical properties of the TADAS devices. ....	14
Figure 18.TADAS device hysteresis loops [Tsai and Hong, 1992][19] .....	14
Figure 19. Ideal elasto-plastic model.....	14
Figure 20. Metallic damper with chevron brace. [20] .....	15
Figure 21. Static and cyclic behavior of the analytical model in the plastic field [20, 21].....	15
Figure 22. Response Spectrum EC8 for Nonlinear analysis[2] .....	17
Figure 23. Accelerograms1 and 2 at equal 0.01 sec time intervals. ....	17
Figure 24. Accelerograms3 and 4 at equal 0.01 sec time intervals. ....	18
Figure 25. Accelerogram 5 and 6 at equal 0.01 sec time intervals. ....	18
Figure 26. Accelerogram 7 at equal 0.01 sec time intervals. ....	18
Figure 27. Horizontal spectra-Ux compatible with EC8[2].....	19
Figure 28. Layout of the building (From Negro P.et al,1994) .....	21
Figure 29. 2D SAP2000 model (Schiavo,2016)[2].....	21
Figure 30. 3D SAP2000 model (Schiavo,2016)[2].....	21
Figure 31. Beam cross section (From. Negro P.et al ,1994).....	22
Figure 32. Cross section type 1 and type 2. 45x30 cm with 15x50 collaborating slab by side. ....	22
Figure 33. Plans view detailing beams of floors one and two.....	23

Figure 34. Plans view detailing beams of floors three and four. ....	23
Figure 35. Columns cross section (from. Negro P. et al, 1994) .....	24
Figure 36. Column cross-section with confinement and without confinement .....	24
Figure 37. Columns distribution Y-Z plane grid A and B .....	25
Figure 38. Columns distribution Y-Z plane grid C and 3D view.....	25
Figure 39. Mander confined and unconfined curves.[22] .....	27
Figure 40. Steel rebars constitutive law [23] .....	28
Figure 41. Force-Deformation relationship, Takeda Hysteresis Model under Increasing Cyclic Load [23] .....	29
Figure 42. Kinematic Hysteresis Model under Increasing Cyclic Load [23] .....	29
Figure 43. Hinge distribution on structural elements. ....	31
Figure 44. Base nodes fixed .....	31
Figure 45. XY plane and XZ plane with the diaphragm constraint selected. ....	32
Figure 46. Constraint characteristics and 3D View with the diaphragm constraint selected .....	32
Figure 47. Constraint characteristics and 3D View with the body constraint selected. ....	33
Figure 48. XY plane and XZ plane zoom to visualize the gap before the columns. ....	33
Figure 49. Generic column's cross section-Fiber discretization .....	34
Figure 50. Generic internal frame beam's cross section-Fiber discretization.....	34
Figure 51. Generic external frame beam's cross section-Fiber discretization .....	34
Figure 52. Bare frame top story displacement: numerical vs experimental (Schiavo,2016) [2] .....	36
Figure 53. Cross section of the main beam, column, and transversal beam. ....	37
Figure 54. Displacement of the 4 <sup>th</sup> Story for the Nonlinear Time-history Analysis Thx1.5 in FE models: Exp, Schiavo, RBC, RBC+S and RBC+S+T. ....	37
Figure 55. Evolution of absolute percentage error in the calculation of displacement of the numerical models.....	39
Figure 56. Modal And Uniform distribution of forces.[26].....	43
Figure 57. Configuration of the Pushover Analysis on SAP2000. ....	44
Figure 58. The Plane Frame setup on SAP2000. ....	45
Figure 59. Modal applied loads-Uniform applied loads.....	45
Figure 60. Pushover Curves obtained from SAP2000 in MDOF. ....	46
Figure 61. Definition of the equivalent bilinear curve[26] .....	46
Figure 62. MDOF Pushover Curve vs Bilinear Pushover Curve. ....	47
Figure 63. Bilinear capacity curve (MDOF-SDOF) .....	48
Figure 64. Verification procedure with ADRS: a) $T < T_c$ ; b) $T > T_c$ . [26]. ....	51
Figure 65. ADRS-Ductility Verification: Modal Case - Pre-retrofit structure.....	51
Figure 66. ADRS-Ductility Verification: Uniform Case – Pre-retrofit structure. ....	52
Figure 67. Configuration of the time-history analysis on SAP2000– Pre-retrofit Building.....	53
Figure 68. Base shear-4th Story Displacement for TH1 and TH2– Pre-retrofit Building .....	54
Figure 69. Base shear-4th Story Displacement for TH3 and TH4– Pre-retrofit Building .....	54
Figure 70. Base shear-4th Story Displacement for TH5 and TH6– Pre-retrofit Building .....	54
Figure 71. Base shear-4th Story Displacement for TH7– Pre-retrofit Building .....	55
Figure 72. Bilinear Capacity Curve and TH results – Pre-retrofit Building .....	55
Figure 73. ADRS with 5% of damping, equivalent bilinear capacity curves and response of the time- history analyses. ....	56
Figure 74. Maximum interstory displacement of time-history analysis - Positive direction, pre-retrofit structure. ....	56
Figure 75. Maximum interstory displacement of time-history analysis - Negative direction, pre-retrofit structure .....	57

Figure 76. Bilinear capacity curve in SDOF.....	58
Figure 77. Mounting arrangement of fluid viscous dampers. ....	60
Figure 78. Scheme of the model[6] .....	61
Figure 79. Link Configuration: Fluid Viscous Dampers.....	65
Figure 80. Mounting arrangement of brace system and TADAS devices. ....	67
Figure 81. Elastic Response spectrum for ULS and SLS.....	68
Figure 82. Elastic acceleration response spectrum for ULS and SLS.....	68
Figure 83. Expected metallic device performance. Force-Displacement relationship.....	77
Figure 84. Metallic Damper Hinge Configuration on SAP2000.....	78
Figure 85. Braces release on SAP2000.....	78
Figure 86. Cross-section of the bracing system on SAP2000.....	80
Figure 87. Bilinear capacity curve (MDOF-SDOF) .....	83
Figure 88. ADRS-Ductility Verification: Modal Case.....	83
Figure 89. ADRS-Ductility Verification: Uniform Case. ....	83
Figure 90. Configuration of the time-history analysis on SAP2000.....	84
Figure 91. Base shear-4th Story Displacement for TH1 and TH2. ....	85
Figure 92. Base shear-4th Story Displacement for TH3 and TH4. ....	85
Figure 93. Base shear-4th Story Displacement for TH5 and TH6. ....	85
Figure 94. Base shear-4th Story Displacement for TH7. ....	86
Figure 95. Bilinear Capacity Curve and TH results – FVD-retrofit Building.....	86
Figure 96. Checking damper effects using the ADRS with Damping 20% - Retrofit structure with fluid viscous dampers. ....	87
Figure 97. Maximum interstory displacement of time-history analysis - Positive direction, retrofit structure with FVD.....	88
Figure 98. Maximum interstory displacement of time-history analysis - Negative direction, retrofit structure with FVD.....	88
Figure 99. 3D model of the pre-retrofit building and the retrofit building with metallic dampers. ....	90
Figure 100. Trilinear representation of pushover curve of building with yielding dampers[28].....	91
Figure 101. Trilinear and equivalent elastoplastic representation of pushover curve of building with yielding dampers[28] .....	91
Figure 102. Trilinear curve and equivalent bilinear curve of the retrofit building with metallic dampers according with the Technical Report MCEER-00-0010.....	95
Figure 103. Pushover curve obtained from SAP2000 in MDOF for structure with metallic dampers. ....	97
Figure 104. Definition of the equivalent bilinear curve[13] .....	98
Figure 105. MDOF Pushover Curve vs Bilinear Pushover Curve. ....	98
Figure 106. Idealized pushover curves and pushover curves from SAP2000 – Uniform case. ....	98
Figure 107. Idealized pushover curves and pushover curves from SAP2000 – Modal case. ....	99
Figure 108. Bilinear capacity curve (MDOF-SDOF) for retrofit building with metallic dampers. ....	100
Figure 109. Verification procedure with ADRS: a) $T < T_c$ ; b) $T > T_c$ . [26]. ....	103
Figure 110. ADRS-Ductility Verification: Modal Case - Retrofit structure with metallic dampers.....	104
Figure 111. ADRS-Ductility Verification: Uniform Case – Retrofit structure with metallic dampers.....	104
Figure 112. Configuration of the time-history analysis on SAP2000– Retrofit Building with metallic dampers.....	106
Figure 113. Base shear-4th Story Displacement for TH1 and TH2– Retrofit Building with metallic dampers.....	106
Figure 114. Base shear-4th Story Displacement for TH3 and TH4– Retrofit Building with metallic dampers.....	107

Figure 115. Base shear-4th Story Displacement for TH5 and TH6– Retrofit Building with metallic dampers. ....	107
Figure 116. Base shear-4th Story Displacement for TH7– Retrofit Building with metallic dampers. ....	107
Figure 117. Bilinear Capacity Curve and TH results – Retrofit Building with metallic dampers. ....	108
Figure 118. Checking damper effects using the ADRS with Damping 20% - Retrofit structure with metallic dampers. ....	109
Figure 119. Maximum interstory displacement of time-history analysis - Positive direction, retrofit structure with MYD. ....	110
Figure 120. Maximum interstory displacement of time-history analysis - Negative direction, retrofit structure with MYD. ....	110
Figure 121. Acceleration-displacement response spectrum for 5% and 20% of damping, maximum average demand and equivalent bilinear curves for structure with and without dampers. ....	113
Figure 122. Bilinear equivalent curves and average maximum demand from time-history analysis. ....	114
Figure 123. Verification of columns by interaction diagram in structure with FVD. ....	118
Figure 124. TH3-Verification of columns by interaction diagram in structure with FVD. ....	119
Figure 125. Histogram-Increment of normal force on Column ....	121
Figure 126. Verification of columns by interaction diagram in structure with MYD. ....	123
Figure 127. TH3- Verification of columns by interaction diagram in structure with MYD. ....	123
Figure 128. Verification of columns by interaction diagram in structure with MYD for all the TH analyses. ....	124
Figure 129. Average of the maximum interstory drift from nonlinear time-history analysis on positive direction (+) of the structure with and without dampers. ....	125
Figure 130. Average of the maximum interstory drift from nonlinear time-history analysis on positive negative (-) of the structure with and without dampers. ....	126
Figure 131. Interaction diagram verification for pre-retrofit building and building with FVD and MYD. ....	127



# Abstract

The passive control systems are the protection techniques most used in the construction and retrofit of buildings worldwide due to the construction simplicity, economic advantages, and the extensive literature review produced through different researchers since the '70s of the 20th century. These strategies have been compared recently in many papers based on finite element methods (FEM); however, many do not replicate the authentic and unique building behavior under dynamic and static demand, letting uncertainties about the benefits and the disadvantages in the implementation.

Therefore, the present study evaluates the effects of the dissipation devices as the seismic protection system for retrofitting interventions on a four-story reinforcement concrete building subjected in 1994 to an experimental campaign in the European Laboratory for Structural Assessment (ELSA) to study the dynamic behavior of the structure under different seismic actions [1]. The starting point is the reproduction of the experimental results on a finite element model through the geometrical configurations, the definition of strain-stress material models, localization and type of hinges on the structure, and setting of loads and masses. In addition, the FE model employed is an optimization of a previous model from a master's thesis of Politecnico di Milano[2]. Finally, the calibration validates the retrofit interventions' performance and the design methodologies applied, minimizing the uncertainties, and defining the real benefits and drawbacks in applying the control systems.

The fluid viscous dampers and the metallic yielding dampers are the strategies selected to be utilized in this paper. They have been designed to improve the seismic performance of the building under a specific seismic demand according to the Eurocode and the current Italian Standard for Constructions. The process includes the modal analysis and nonlinear static analyses to extract all the information required by the methodologies employed. Additionally, the nonlinear time-history analyses are applied using different accelerograms carefully selected by previous researchers to validate the results.

Finally, the interstory drifts, the internal forces of the structural elements, and the vulnerability indexes are computed for the reinforcement concrete building with and without retrofit intervention to evaluate the seismic behavior improvement of the structure thanks to the passive control systems. Besides, the structural features mentioned before lets to compare the protection techniques to define the best performance between retrofitting interventions with dissipative devices.



# Chapter 1

## 1 Introduction

In current times, old buildings are the most vulnerable structures and represent more risk to human lives in a possible earthquake scenario. Due to the lack of knowledge, the outdated construction codes worldwide proposed inefficient and unsafe procedures that do not entirely fit the current requirements to warranty safety structural performance. Thus, to comply with the current standards, retrofitting interventions are done in the existing buildings when the economic and technical conditions allow it. The strategies to carry through the interventions classifies into adding new structural elements, strengthening existing elements, increasing deformation capacity, and implementing seismic protection systems [2].

Nowadays, the structural damage in buildings produced by earthquakes must be quantified to identify the structures' current state. For this purpose, the researchers developed different methodologies to perform the seismic vulnerability assessment to quantify damage in the entire structural systems defining two main procedures: the empirical methods and analytical approaches [1]. These concepts help to accomplish intervention decisions, meaning the choice of no intervention, total or partial demolition, local damage reparation, retrofitting, maintenance, or survey and monitoring. The advantage of using these strategies is the representation of the state of the building through a category or index, reducing the variables that must be considered and allowing the selection of the most economical and proper solution to each specific case.

The empirical assessment approach focuses on the building's typology and observations of damages without considering the mechanical properties and limits states of the elements [1]. However, the materials and structural system must be detailed to start the classification process and determine building parameters. This approach works like qualifiers to establish the statistical procedure's base to calculate the vulnerability index. According to codes and government authorities, the index, with expert judgment, determines the vulnerability of the structure and the intervention required. It is worth highlighting that different methodologies and rules depend on the countries.

On the other hand, the analytical approach focuses on the performance of the building. In other words, it uses the simulation of powerful ground motions on software to evaluate the limit states of the structural system. To precise, the seismic design demand usually used is related to the ultimate limit state and the analysis methods employed are the Nonlinear Time-history Analysis (NLTHA) and the Pushover Analysis (POA) [1]. Once executed the structural analysis, the required output data is obtained from the software to determine the building's capacity. Thenceforth, the capacity is compared with the demand in terms of acceleration, force, or displacement, computing the vulnerability indexes to describe the overall seismic performance in the most straightforward possible representation, concluding the investigation by establishing the structural vulnerability and the intervention strategy required.

It is crucial to clear that the empirical assessment is not considered in this paper because it works to classify the structures in a range of least or most vulnerable buildings without evaluating the calibrated structure in a Finite Element Model.

The main goal of the paper is to identify the advantages and drawbacks of the effects of the fluid viscous dampers and yielding metallic dampers used like passive control system for seismic protection technique based on the internal forces of the structural elements, interstory drifts, and the vulnerability indexes to evaluate the performance between retrofitting interventions with dissipative devices. For this purpose, the master thesis investigates a four-story reinforced concrete framed building modeled on the commercial finite element software SAP2000. The model can predict the real dynamic response concerning the experimental campaign executed by Negro in 1994 and carried out in the European Laboratory for Structural Assessment (ELSA) of the Joint Research Center of the European Commission in Ispra (VA), in compliance with the European and Italian Standards.

In addition, the thesis is based on the work of the student Emilio Schiavo and professor Luca Martinelli for the thesis degree "Influence of Masonry Infills on Dynamic Behavior of Reinforced Concrete Framed Structures" from Politecnico di Milano [1], where was obtained all the information and the SAP2000 model.

The thesis is organized as follows:

Chapter 2 introduces the seismic control systems, the passive control systems, and the dissipative devices regarding the typology and the seismic behavior's influence. Chapter 3 regards the seismic design demand. The ground characteristics, limit state of analysis, structure features, and the accelerograms used on the time-history analyses are defined. In addition, important results regarding the seismic demand from the experimental campaign are summarized. Chapter 4 describes the case study and the finite element model created on SAP2000, which includes the structural scheme regarding the floor plan view and the elevation of the building, all the features of the structural elements and the distribution of loads and masses. Furthermore, the optimization of the SAP2000 model is presented. Chapter 5 present the structural analysis of the pre-retrofit structure. The nonlinear static pushover analysis and

the nonlinear time-history analyses are evaluated according to the Eurocode and the current Italian Standard for Constructions. Chapter 6 explains the retrofit interventions' design methodologies with fluid viscous dampers and the metallic-yielding dampers and the corresponding FEM simulation on SAP2000. Chapter 7 and 8 present the structural analysis of the retrofit structures with fluid viscous dampers and metallic-yielding dampers. The nonlinear static pushover analysis and the nonlinear time-history analyses are evaluated according to the Eurocode and the current Italian Standard for Constructions. In Chapter 9, the internal forces of the structural elements and the interstory drifts are obtained from the time-history analyses to evaluate the structural performance once the dissipative devices are introduced in the building. In addition, the vulnerability indexes are calculated to evaluate the seismic performance improvement due to the intervention with passive control systems designed in Chapter 6. Finally, Chapter 10 reports the conclusions and recommendations.

## Chapter 2

### 2 Seismic Protection Systems

The strategy focuses on reducing structural damage provoked by external natural or/and artificial actions on the constructions employing response control systems. These divide into passive control systems, active control systems, semi-active control systems, and hybrid control systems. The main difference between them is the null, partially, or totally implementation of an external power source of energy, electronic devices, and computer control algorithms to generate active forces able to stand against the motion in real-time to mitigate the movement in the structure [3]. Figure 1 and Figure 2 summarizes the flow chart of the passive, active and semi-active seismic protection systems mainly by the following concepts: Input excitation, Structure, Response, Energy Dissipation or Actuators, or both. [4]

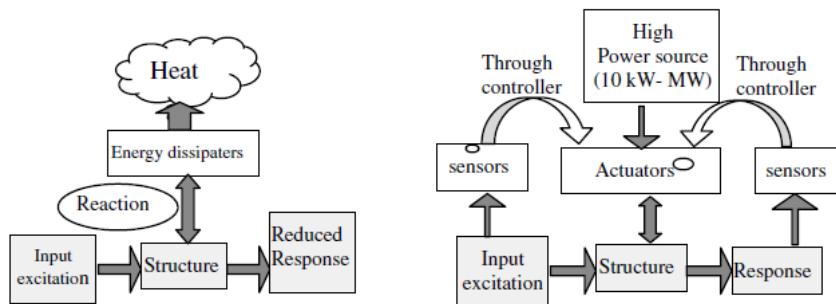


Figure 1. Passive and Active Control Solutions Workflow Diagram[4]

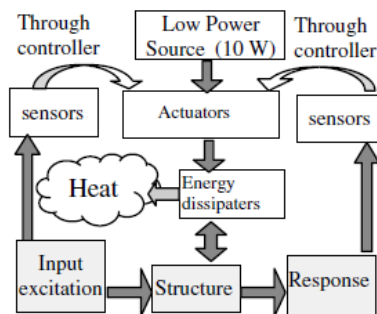


Figure 2. Semi-Active Control Solution Work Flow Diagram.[4]

The passive control systems use the devices to transform the mechanical energy into heat employing viscoelasticity, yielding, or friction principles. They can even transfer energy among vibrating modes and modify the free vibration characteristics transmitted from the foundation[4]. All this, without an external source of energy and computer control algorithm. On the other hand, active and semi-active control systems use sensors, controllers, external power sources of energy, and computer control algorithms to measure and monitor the structural response in real-time, changing mechanical properties like stiffness, damping, or

both, to adapt the solicitation and optimize the structural performance [4]. However, the active methods are not recommended due to the possible energy breakdowns during an unexpected event, making the system partially unoperated or useless. In distinction, the semi-active methods can work at low energy, changing the reaction characteristics of the device and making the system work even during energy breakdowns thanks to electric batteries[3]. Thus, and due to the economic evaluation, the passive and semi-active methodologies are preferable to buildings worldwide instead of the option mentioned. Figure 3 summarizes the different categories of the passive control systems.

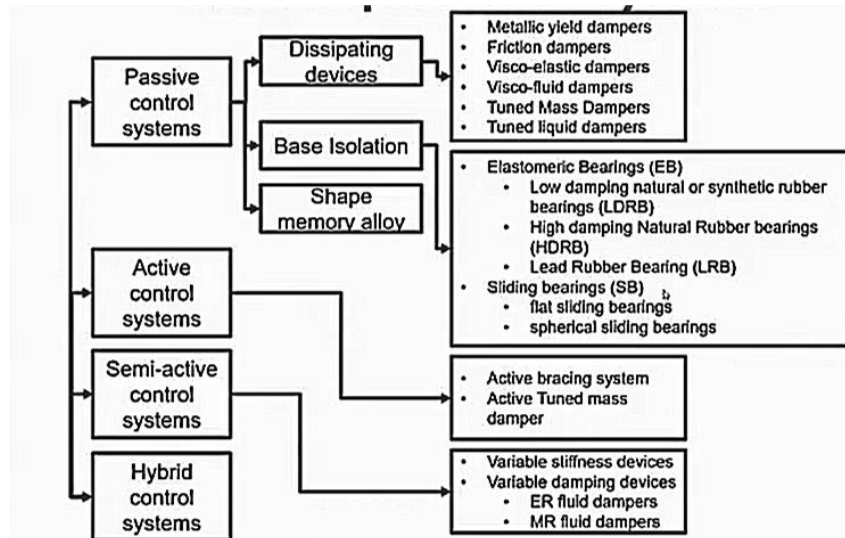


Figure 3. Summary of seismic protection systems[5]

The dissipative devices are cataloged into dissipation devices, dynamic vibration absorbers, and re-centering devices, which use different materials and designs to improve the structure's damping, strength, and stiffness. Table 1 lists the principles of operation, the material and technologies commonly used, and the performance objectives of each one:

	Principles of operation	Materials and technologies	Performance objectives
<b>Hysteretic Devices</b>	Yielding of materials	Steel or lead	Energy dissipation and strength enhancement
	Friction	Metal-to-metal or non-metal contact	
<b>Viscoelastic Devices</b>	Deformation of viscoelastic solids	Viscoelastic polymers	Energy dissipation and stiffness enhancement
	Deformation of viscoelastic fluids	Highly viscous fluids	
	Fluid orificing	Fluid; advanced orifice design and fluid sealing	
<b>Re-centering Devices</b>	Fluid pressurization and orificing	Compressible fluids, high pressure sealing	Energy dissipation and stiffness enhancement, re-centering capability
	Friction-spring action	Metal-to-metal or non-metal contact	
	Phase transformation in metals	Shape memory alloys, super-elastic behavior	
<b>Dynamic vibration absorbers</b>	Tuned mass oscillators	Mass-spring fluid damper	Damping enhancement
	Tuned liquid oscillators	Water tanks, U-shaped liquid containers	

Table 1. Passive Energy Dissipation Systems [6]

## 2.1 Dissipating Devices

The intervention strategy works to increase the structure's dissipation energy capacity to reduce displacements and accelerations, directly influencing the shear force acting on the structural members during the seismic event. The objective is to capture the structure nonlinearity produced by the nature of the earthquake, or wind, on the devices to reduce the vulnerability of the buildings and warranty safety performance during the service life. Consequently, the main structural elements remain in the elastic phase, avoiding the strength deterioration and decreasing the long- and short-term damage.

### 2.1.1 Device's typology:

The classification of dissipation devices depends on the hysteretic behavior, the idealized physical model, or both. They classify as rate-dependent devices (velocity-dependent), rate-independent devices (displacement-dependent), and harmonic absorber systems.

In velocity-dependent devices, the cyclic response depends on the relative velocity between the device's two extremes [7]. The advantage is the decoupling from the structural deflection stress; it means that the opposite force to the movement maximizes when the displacement is zero, and vice versa, for pure viscous behavior. It is usual on fluid viscous dampers, viscoelastic fluid dampers, and solid viscoelastic dampers. However, the last one does not achieve the maximum force at minimum displacement due to the stiffness's influence[8]. Figure 4 show the basis scheme, the idealized hysteretic behavior, and the idealized physical model of the viscous and viscoelastic damper:

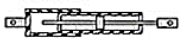
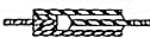
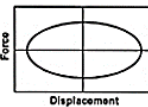
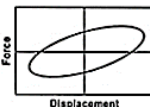
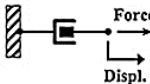
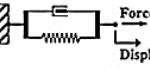
	Viscous damper	Viscoelastic damper
<i>Basic Construction</i>		
<i>Idealized Hysteretic Behavior</i>		
<i>Idealized Physical Model</i>		

Figure 4. Summary of construction, hysteretic behavior, physical models, advantages, and disadvantages of passive energy dissipation devices for seismic protection applications (modified from Symans et al. 2008) [8]

In the displacement-dependent devices, the cyclic response depends on the relative displacement between the device's two extremes and independent from the frequency [7]. It means that the opposite force, to the movement, is directly proportional to the displacement. Thus, the force maximizes when the displacement is maximum. In this case, there is not decoupling from the structural deflection stress. It is usual on metallic yielding dampers and

friction dampers. The behavior is described by nonlinear hysteretic models (bilinear or trilinear), elastoplastic models, or rigid-plastic models [8]. Figure 5 show the basis scheme, the idealized hysteretic behavior, and the idealized physical model of the metallic-yielding damper and friction damper:

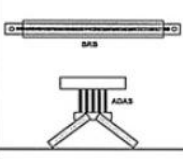
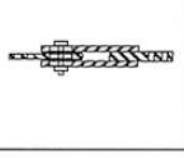
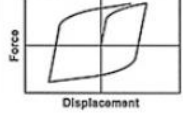
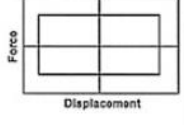
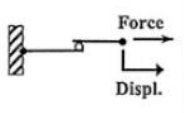
	Metallic damper	Friction damper
<i>Basic Construction</i>		
<i>Idealized Hysteretic Behavior</i>		
<i>Idealized Physical Model</i>	Idealized Model Not Available	

Figure 5. Summary of construction, hysteretic behavior, physical models, advantages, and disadvantages of passive energy dissipation devices for seismic protection applications (modified from Symans et al. 2008) [8]

The harmonic absorber, known as a tuned mass damper (TMD) or tuned liquid damper (TLD), consists of a mass (solid or liquid) attached to a specific location in a structure, which uses the resonance out of phase from the structural motion to dissipate energy and reduce the dynamic response provoked by earthquake or high winds hit [9]. Figure 6 shows the effect of this devices in the structural performance comparing the response of a system with and without TMD for El Centro excitation:

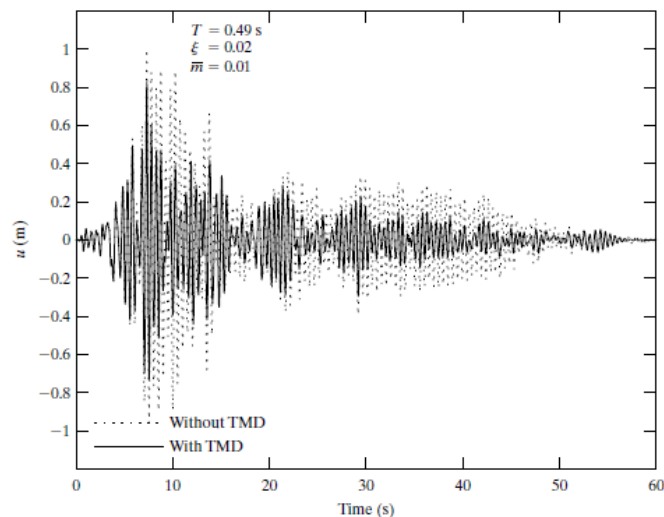


Figure 6. Response of SDOF to El Centro excitation with and without TMD [9]

The TMD is used in skyscrapers like in Emirate Towers Spires and Taipei101. The next table shows some applications of the TLD:

Name and Type of Host Structure	City/ Country	Type and number of dampers	Year of installation	Frequency, Wt., Damping
Nagasaki Airport Tower(42 m)	Nagasaki, Japan	25 tuned liquid dampers (circular sloshing type)	1987	1.07 Hz 1 t (approx.)
Yokohama Marine Tower (105 m)	Yokohama, Japan	39 tuned liquid damper (circular sloshing type)	1987	0.55 Hz 1.6 t
Gold Tower (136 m)	Udatsu, Japan	16 tuned liquid dampers (rectangular unidirectional type)	1988	0.42 Hz 9.6 t
Shin-Yokohama Prince Hotel (149m)	Yokohama, Japan	30 tuned liquid dampers (circular sloshing type)	1991	0.31 Hz 83.5 t
Mount Wellington Broadcasting Tower (lattice tower, 104 m)	Hobart, Australia	80 tuned liquid dampers (circular sloshing type)	1992	0.7 Hz 0.6 t
TYG Building (159 m)	Atsugi, Japan	720 tuned liquid dampers (double donut type)	1992	0.53 Hz 18.2 t
Narita Airport Tower (87 m)	Narita, Japan	tuned liquid dampers (circular sloshing type)	1993	1.3 Hz 16.5 t
Haneda Airport Tower (178 m)	Tokyo, Japan	Tuned liquid dampers (circular sloshing type)	1993	0.77 Hz 21 t

Table 2. Structures with installed Tuned Liquid Dampers [10]

The addition of energy dissipation systems improves the structure's capacity curve. In general, it results in a drift reduction due to energy dissipation and in the variation of the total base shear strength exerted in the structure due to the device yielding or friction. [6]. The effect mentioned before is showed in the Figure 7 for each energy dissipation system (EDS) and Figure 8 depicts the damping increment effects regards the demand from the acceleration-displacement response spectrum and capacity curve.

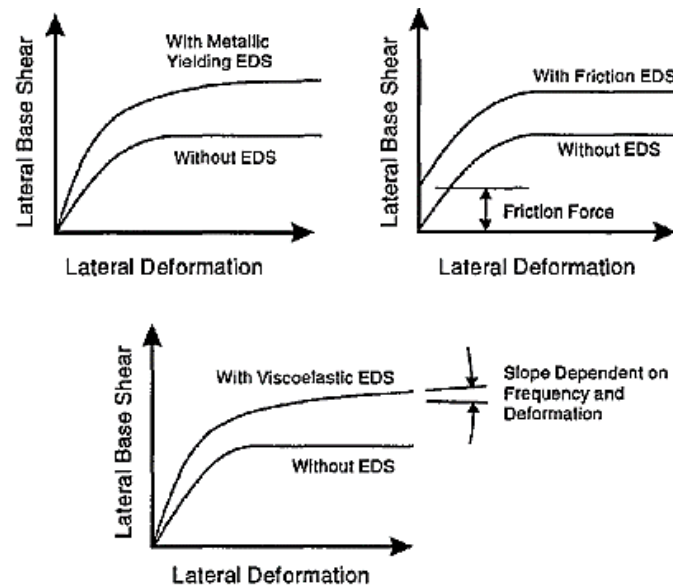


Figure 7. Effect of energy dissipation systems on Force-Deformation Curves of a Structure.[6]



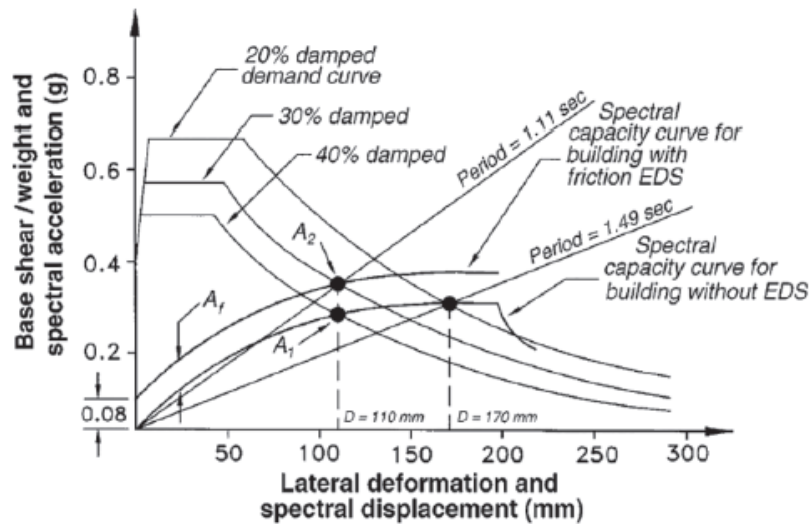


Figure 8. Spectral capacity and demand curves for rehabilitated one-story building[11]

After the brief description and introduction to the subject, it is essential to mention that the harmonic absorber systems are not evaluated in this paper.

## 2.2 Fluid Viscous Dampers (FV Dampers)

The device consists of a piston within a damper housing filled with silicone compound or a similar oil type. The piston contains tiny orifices through which the fluid passes from one side to another. As the damper piston rod and piston head strokes, fluid flows through orifices. The resulting differential in pressure across the piston head produces forces that resist the damper's relative motion. The fluid flows at high velocities creating friction between fluid particles and the piston head. The friction forces give rise to energy dissipation in the form of heat. Thus, fluid viscous dampers dissipate energy through a piston's movement into a highly viscous fluid, based on the fluid orifice concept [8, 11, 12]. Figure 9 illustrates the standard fluid damper and components:

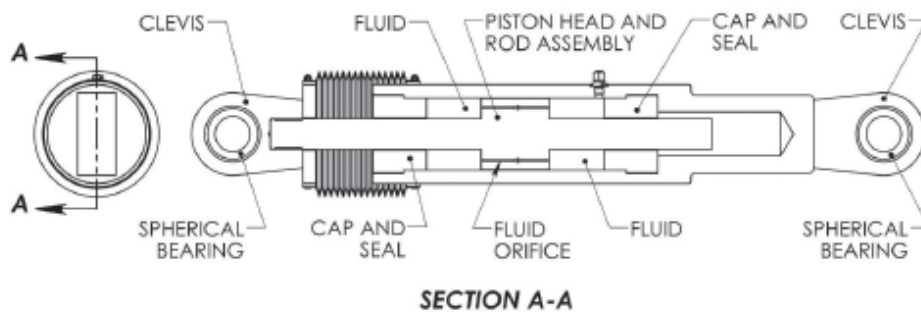


Figure 9. Standard Fluid Damper and Components[11]

The devices' behavior is equal to the ideal linear or nonlinear viscous dashpot, where the resistance force is directly related to the velocity. Figure 10 shows the cyclic or hysteretic behavior, one refers to the absence of storage stiffness (a); therefore, it does not develop the

restoring forces. In the second (b), there is the storage of stiffness, exposing a viscoelastic behavior, and developing restoring forces. [8].

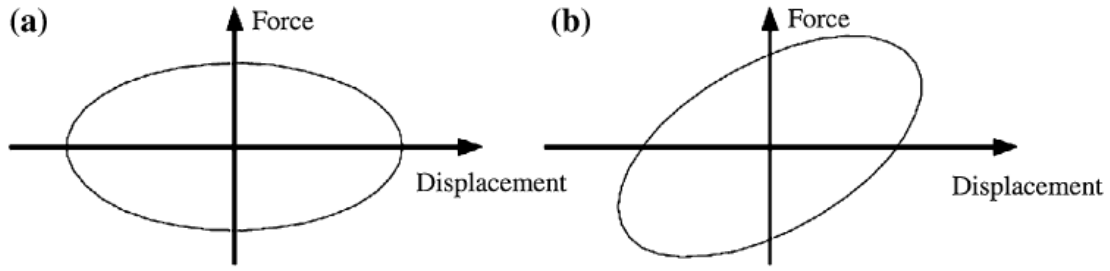


Figure 10. Hysteresis loops of dampers with pure viscous and viscoelastic behavior[8]

According to the Damper Design Manual [11], the forces created in the devices are typically characterized by the following equation:

$$F_d = C * \dot{u}(t)^\alpha \quad (1)$$

Where:

- $F_d$ : Damping force
- $C$ : Damping coefficient.
- $u$ : Displacement across the damper
- $\dot{u}$ : Velocity across the damper
- $\alpha$ : Damping exponent (determined by the piston head orifice design)

The physical model comes from a nonlinear viscous dashpot, where the damping exponent determines the linear or nonlinear relation between the force and the velocity. For values of  $\alpha$  equal to one, the force is linear-proportional to the relative velocity. For values of  $\alpha$  lower than 1, the force is nonlinear proportional to the relative velocity. This characteristic is important because it allows the dissipation of energy with lower damping forces, reducing the  $\alpha$  value and changing  $C$ . The values exponent can vary from 0.2 to 2.0; however, according to Taylor's Damper manual, the standard values are from 0.3 to 1.0 [11]. Figure 11 shows the force-velocity relationship of viscous damper for  $\alpha$  equal to 1 and to 0.3.

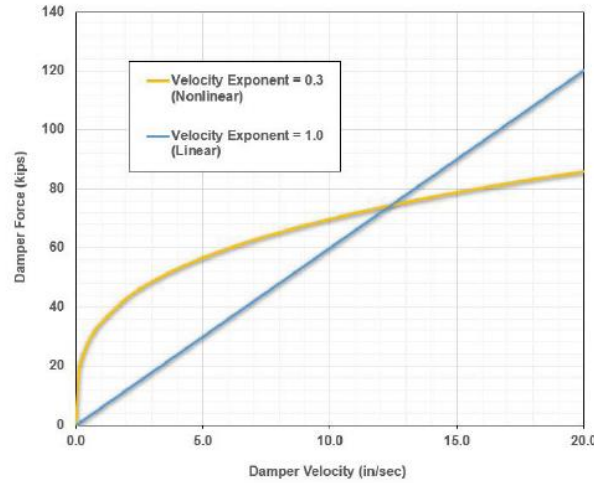


Figure 11. Force-Velocity Relationship of Viscous Damper[11]

Figure 12 shows the damping exponent's influence on the energy absorption and hysteresis of the device and the difference between a linear and nonlinear damping where it highlights the out-of-phase response between the force and deflection. [11].

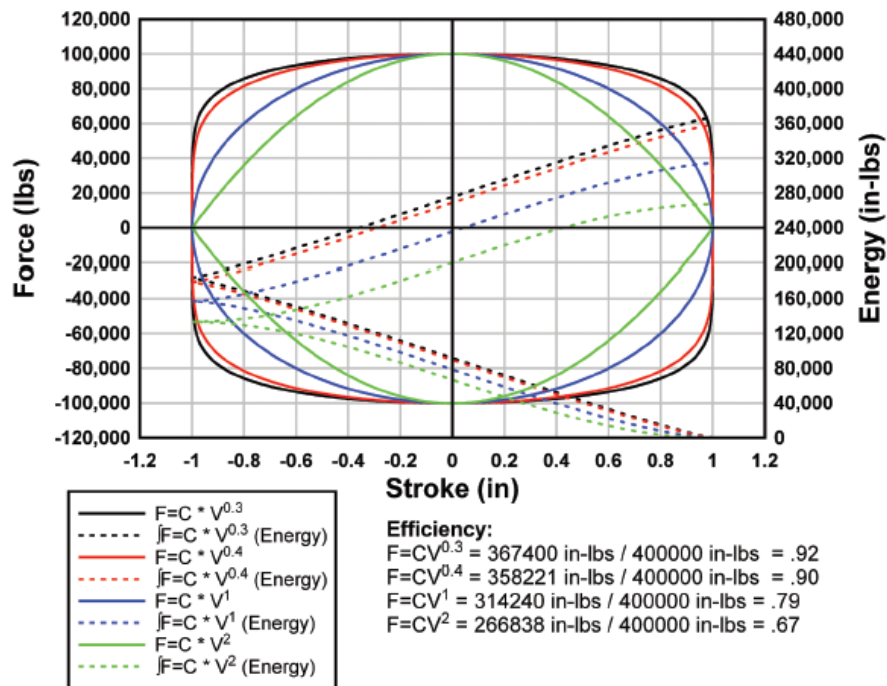


Figure 12. Comparison of Energy Absorbed with Varying Damping Exponents with Sinusoidal Input[11]

In the case when the damping coefficient ( $C$ ) is exceptionally high, the surrounding structure's stiffness becomes a limiting factor since the relative motion at the damper ends becomes very small if the surrounding stiffness is too low to transmit the motion into the damper. In the other hand, when the damping coefficient ( $C$ ) is minimal, the amount of energy absorbed by the damper is also small, and therefore the benefit provided by the damper is limited[11]. The fluid viscous dampers included in structural systems improve their response to lateral loads by

increasing the damping ratio ( $\zeta$ ) from 2–5 % in typical of constructions to 20–30 %; this dramatically reduces the accelerations and displacements of the structure[8].

### 2.2.1 Mounting Arrangements and Damper Configuration

The dampers are linked to a bracing system that connects the floors (moving masses) between them. Therefore, there must be continuity of the connections from the upper floor to the ground level. Figure 13 illustrates the standard damper-bracing distribution on frames:

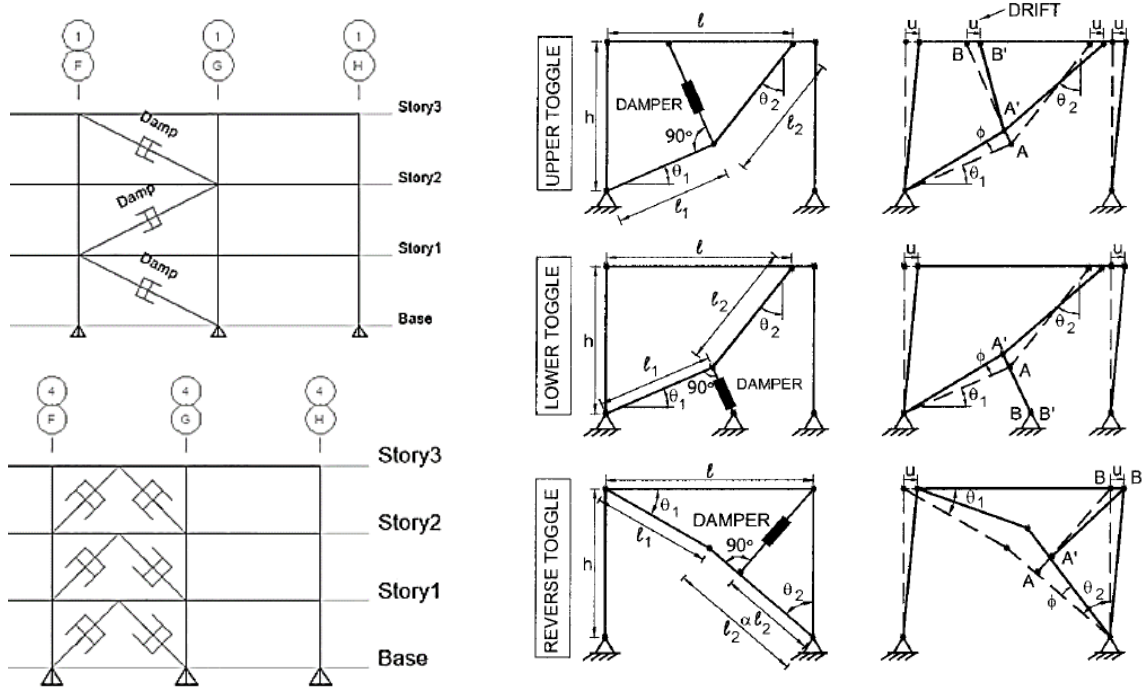


Figure 13. Damper-Brace configuration: Diagonal Brace, Chevron Brace and Toggle Brace [11, 13]

It is suitable for moment frame buildings to use chevron braces, diagonal bracing schemes, or toggle braces; each has its mechanism, connections, and interaction with the dampers. The magnification factor ( $f$ ) represents the effect of the bracing configuration; high values signify great dissipation of energy. In the chevron brace configuration, the dampers are placed horizontally. Thus, the plane flexibility injects the complete movement directly into the damper's horizontal orientation, and the  $f$  is equal to one. On the other hand, the diagonal bracing scheme is the most basic method; the horizontal movement produces an angular component of the full deflection, which goes to the damper. Thence, the brace takes the motion directly to the next floor, and the  $f$  is a function of the diagonal angle. Finally, the toggle brace is a mechanism to amplify the movement of the damper, obtaining magnification factors higher than the unity, characterizing a more efficient damping system than chevron or diagonal configuration [11, 13]. Figure 14 illustrates the configuration of the damper-bracing system in the frame with their corresponding magnification factor.

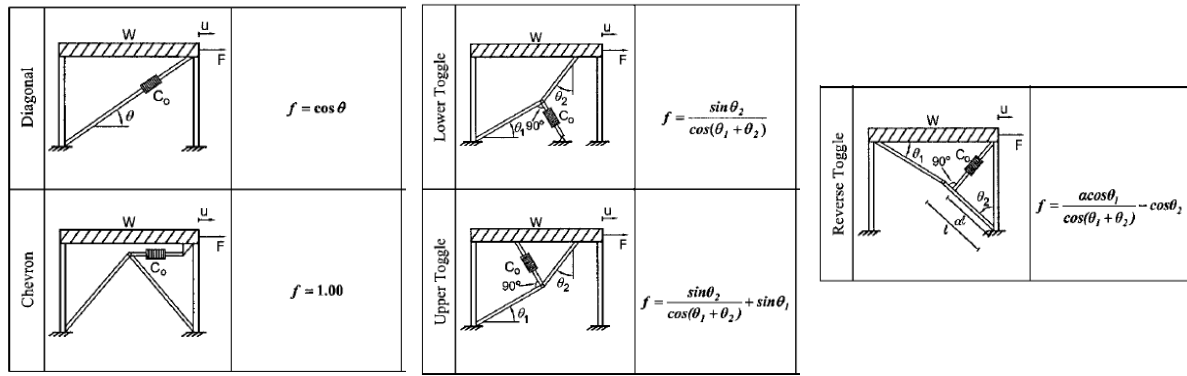


Figure 14. Magnification factor for dampers in Chevron Brace, Diagonal Brace and Toggle Brace [13]

## 2.3 Metallic-Yielding Dampers

The damper consists of a series of steel plates joined by a metallic mechanism. All the set is known as ADAS (adding damping and stiffness). The energy dissipation is achieved through the inelastic deformation of metallic bodies, using the device's hysteretic behavior to keep the primary structural system in an elastic state. It has different shapes, but multiple investigations demonstrate better performance with the triangular plate (TADAS)[14]. The triangular device has some essential characteristics: no carry the gravity loads, no rotational restrain at the top of the brace connection assemblage, and no instability phenomena in the plate due to excessive axial load [15]. Figure 15 and Figure 16 illustrate the triangular devices' common shapes and the configuration of the bracing on the structure. The type of steel commonly used is mild steel because it can sustain many cycles of stable yielding behavior, avoiding precipitate failure [15].

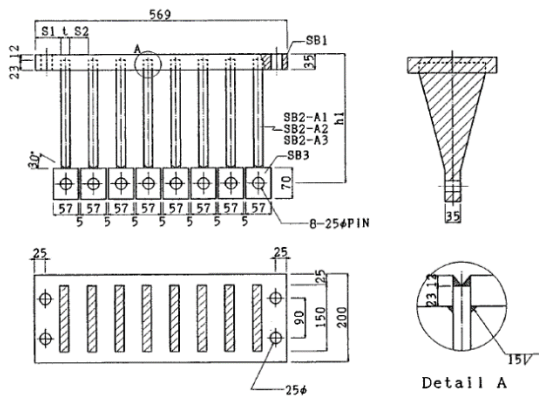


Figure 15. Details of Steel Welded TADAS device (units in mm) [14]

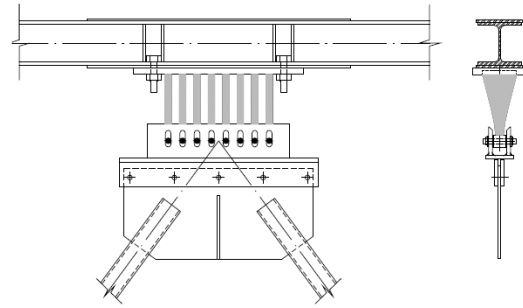


Figure 16. Triangular-plate Added Damping and Stiffness (TADAS) and typical configuration[14]

According to Tsai, the basic mechanical properties of the triangular metallic dampers can be obtained assuming a bending curvature distributed uniformly, the base of the plate fixed, and neglecting the deformation due to the shear. Consequently, the theoretical elastic stiffness, yield and plastic strength, and yield displacement and rotation for a TADAS device can be expressed as[14]:

The elastic Lateral Stiffness ( $K_d$ ): $K_d = \frac{NEbt^3}{6h^3} \quad (2)$	
The yield strength ( $P_y$ ): $P_y = \frac{F_y Nbt^2}{6h} \quad (3)$	The plastic strength ( $P_p$ ): $P_p = \frac{F_y Nbt^2}{4h} \quad (4)$
Yield displacement ( $\Delta_y$ ): $\Delta_y = \frac{F_y h^2}{Et} \quad (5)$	The yield rotation angle ( $\gamma_y$ ): $\gamma_y = \frac{F_y h}{Et} \quad (6)$

Figure 17. Mechanical properties of the TADAS devices.

Where:

- E: The elastic modulus of the steel.
- b: The width of the plate.
- t: The thickness of the plate.
- h: The height of the plate.
- $F_y$ : The steel tensile yield strength.

The hysteretic devices are displacement dependent, which means that the cyclic response is independent of the relative velocity between the device's tip and the excitation frequency. Therefore, the relation between the force and the displacement depends on the relative displacement between the device extremes[7]. The mechanic model employed usually is the idealized elastoplastic, where the control parameters are the elastic stiffness (K), the post-yielding coefficient ( $\alpha$ ), and the ductility of the device ( $\mu$ ). Also, it can be described for multiple models which consider the kinematic hardening or the isotropic hardening in the hysteresis of the steel. For example, the Bouc-Wen model can consider the post-yield force increment with the increment of deformation and the increment of the yield force due to the inelastic deformation [16-18]. Figure 18 shows the representation of the force-deformation relationships of a regular TADAS device during a pseudo dynamic test[19] and Figure 19 illustrates the idealized elasto-plastic model:

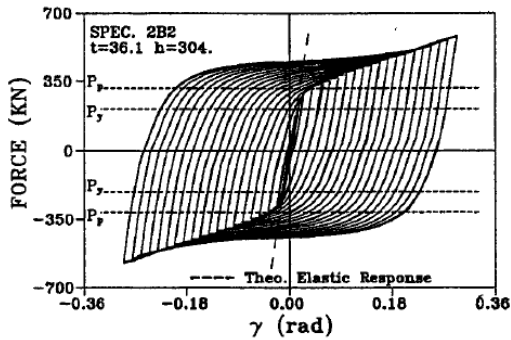


Figure 18. TADAS device hysteresis loops [Tsai and Hong, 1992][19]

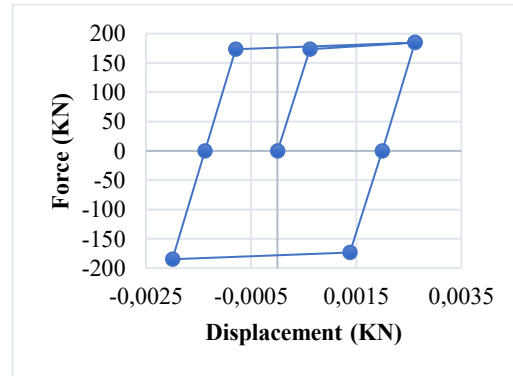


Figure 19. Ideal elasto-plastic model.

### 2.3.1 Mounting Arrangements and Damper Configuration

The damper is implemented into the structure by using the Chevron concentric bracing system. This configuration is commonly used in the seismic design of buildings thanks to their dissipative capacity and mechanical characteristics. However, the standard approach applies the whole movement of the floor directly into the damper's horizontal orientation and generates the dissipation of energy exclusively by the hysteretic damping of the mild steel. The conditions of the application of the Chevron brace in the simplified model are the pinned connections on the extremes of the bracing and the permanently elastic behavior to concentrate the displacements on the metallic dampers [19, 20]. Figure 20 illustrates the typical configuration of the damper-bracing system into the building.

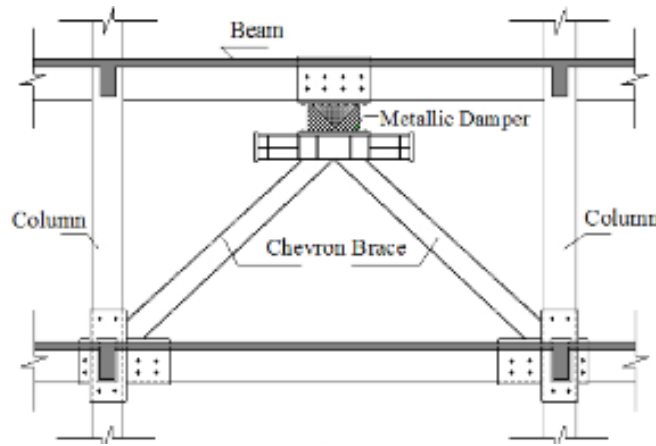


Figure 20. Metallic damper with chevron brace. [20]

The energy-based seismic design method is used to calculate the geometry of the TADAS devices used in this paper. According to Zhang and Mahmoudi [20, 21], the analytical model of the frame with the chevron-damper system can be considered as the independent contribution of the mainframe model and metallic damper-brace model; it is linked assuming a system of two springs in parallel. In the other hand, the combination of the damper and bracing system is called a device-brace assembly, and it can be modeled assuming a system of two springs in series [21]. Figure 21 shows the expected resistance behavior of a frame with damper-bracing system.

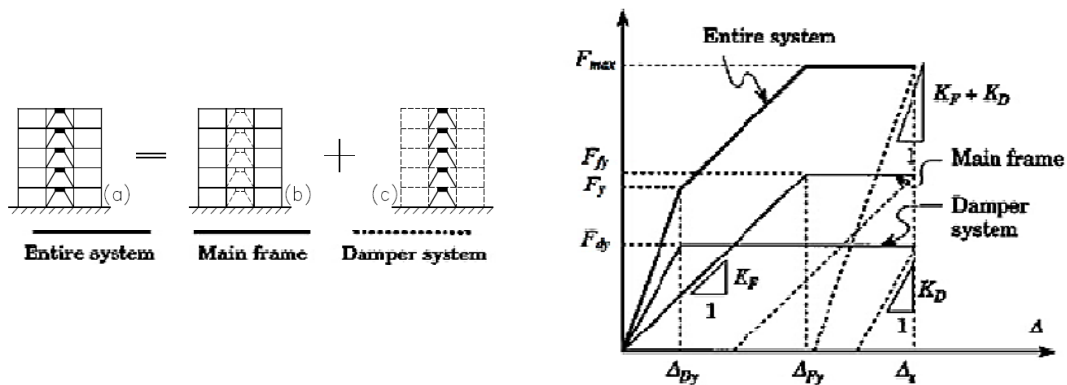


Figure 21. Static and cyclic behavior of the analytical model in the plastic field [20, 21]

## Chapter 3

### 3 Seismic Demand

According with Negro (1994), the preliminary design of the building was made with Eurocode 2 and 8 assuming high seismicity and the following characteristics[1]:

- Peak ground motion equal to 0.3 g.
- Soil type B.
- Damping 5%.
- Importance factor equal to 1
- Structure factor equal to 5 ( $q=5$ ).
- High ductility class.
- Frame of high regularity in the ductility class H.
- Design performed using two independent planar models for each orthogonal direction.
- Torsional effects considered by the simplified method (EC8).

In the campaign performed in the European Laboratory for Structural Assessment (ELSA) done by Negro in 1994, different seismic actions have been applied to study the performance of the structure. To define the experimental program, a set of artificial accelerograms were generated to fit the response spectrum given by EC8 previously mentioned with a  $q=1$ . The artificial accelerograms were created by using the wave shape derived from the 1976 Friuli Earthquake (TH). To evaluate the seismic performance, the structure was subjected to 2 seismic actions scaled by 0.4 and 1.5, in order respectively, subjecting the building to normal ground acceleration equal to 0.125 g and 0.45g. The most remarkable information provided by Negro in the technical report is the following:

THx1.5	THx0.4
g	g
0,562	0,150
It produces damage in the structure, reduces the stiffness, and changes the natural frequencies, but it does not change the modal shape functions.	It does not produce any damage in the structure (not cause significant yielding inside the structure).

Table 3. Results of seismic test, Negro (1994)



In this investigation, the time-history scaled by 1.5 is used to calibrate the FEM model with the experimental data. In the FEM model performed on SAP2000 the damage is evaluated through the reduction of the moment of inertia in main beams and columns. The reduction value is defined in the previous investigation [1], and a new reduction value is defined in this investigation to optimize the FEM model.

### 3.1 Response Spectrum

Figure 22 shows the elastic response spectrum[2] used in the design of the retrofit strategies applied on this paper, which corresponds to the SLV limit state specified by the EC8 and NTC18. In addition, Table 4 list the design characteristics of the design response spectrum.

	SLV
Ground Type	B
ag	0,30
S	1,20
Tb	0,15
Tc	0,50
Td	2,00
$\xi$	5,00
$\eta$	1,00
q	1
$\beta$	0,20

Table 4. Input parameters of the seismic design demand.

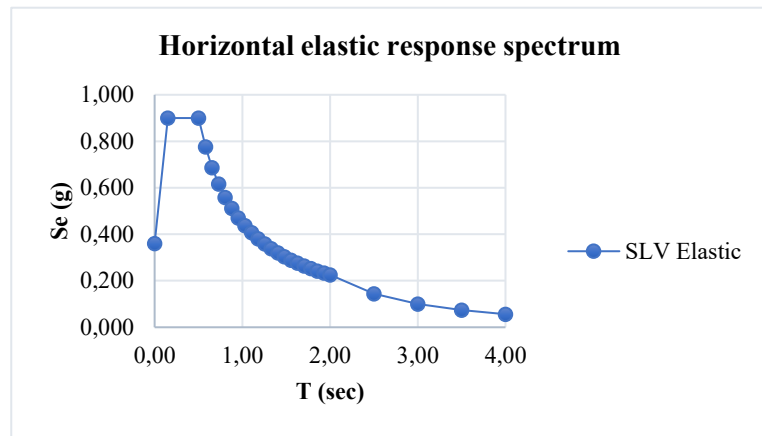


Figure 22. Response Spectrum EC8 for Nonlinear analysis[2]

### 3.2 Natural Accelerograms and Spectrum

The 2D analysis in X direction is performed with seven natural accelerograms selected by the European Strong Motion Data Base, with the axial REXEL SOFTWARE. These are compatible with the EC8 elastic response spectrum of Figure 22 [2]. Figure 23 to Figure 26 show the natural accelerograms mentioned before.

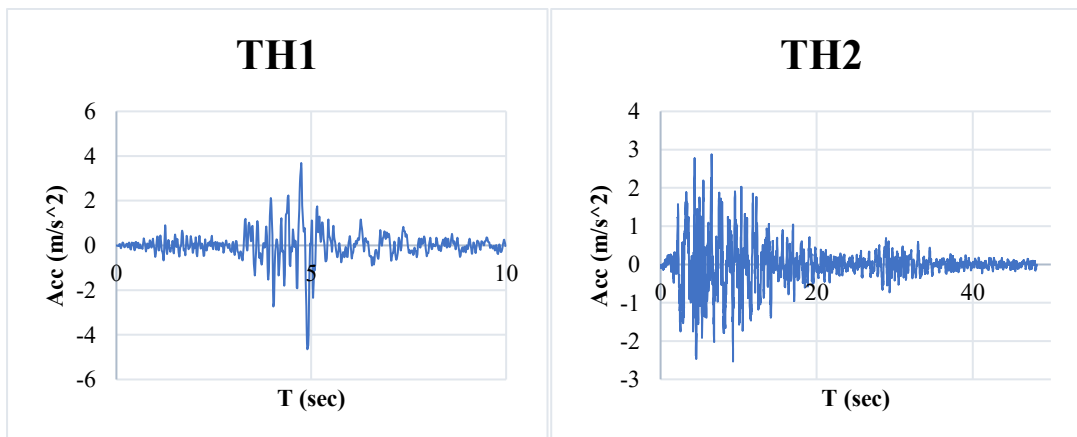


Figure 23. Accelerograms 1 and 2 at equal 0.01 sec time intervals.

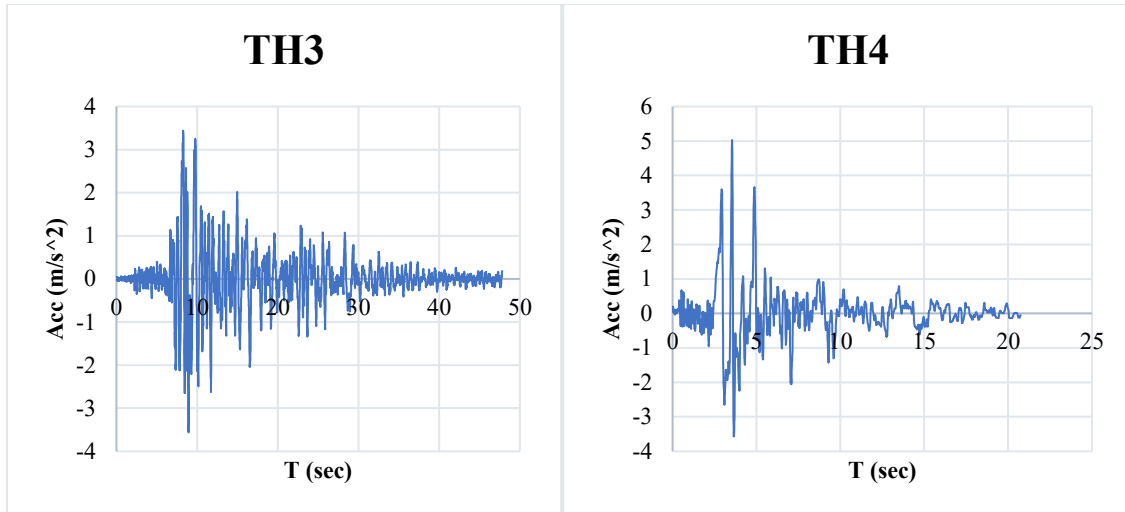


Figure 24. Accelerograms3 and 4 at equal 0.01 sec time intervals.

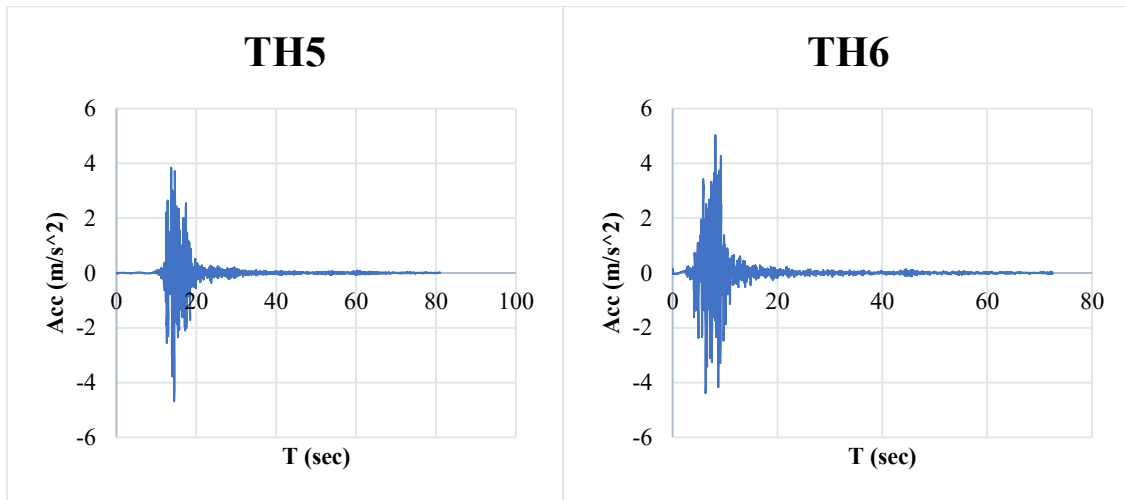


Figure 25. Accelerogram 5 and 6 at equal 0.01 sec time intervals.

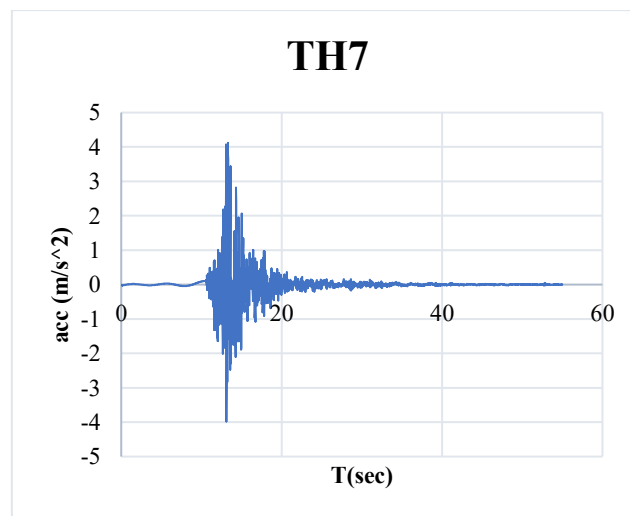


Figure 26. Accelerogram 7 at equal 0.01 sec time intervals.

Figure 27 shows the expected response spectrum due to each seismic action produced by the accelerograms. The red curve represents the average response. Thus, it verified the compatibility of the accelerograms with the design response spectrum mentioned before.

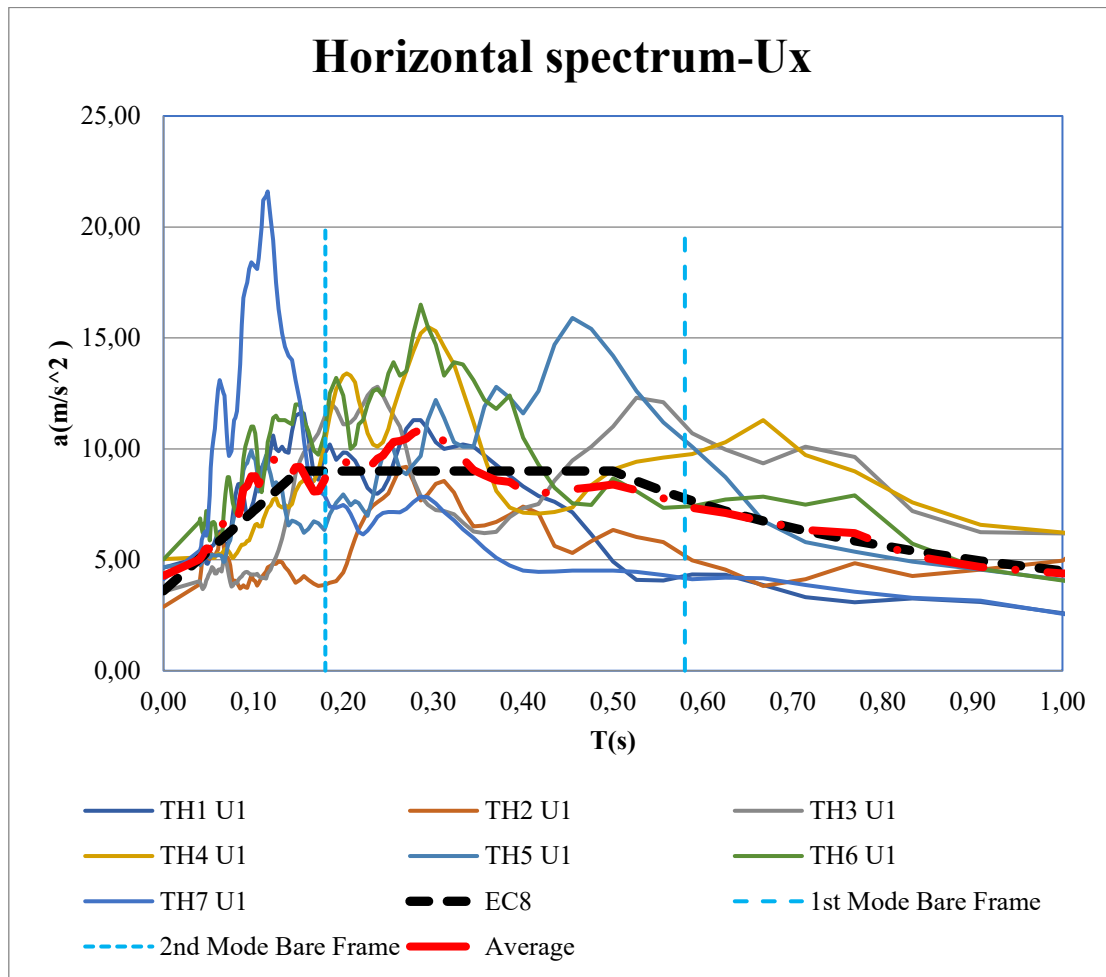


Figure 27. Horizontal spectra-Ux compatible with EC8[2]

In addition, the 3D analysis executed in the previous research used the seven natural earthquake records mentioned before (in the X direction) plus seven additional artificial accelerograms (in the Y direction), created with SIMQKE software, compatible with the EC8 elastic response spectrum. However, the 3D analysis is not used in this study. According to Schiavo, the 2D and 3D time-history analysis results regards the top displacements show shallow difference because of the high building's regularity both in plan and in elevation, with the absence of significant torsional effects confirming a decouple behavior between X and Y planes [2]. Therefore, it is used just the 2D nonlinear analysis to the study building with and without retrofitting interventions with dissipative devices.

## Chapter 4

### 4 Four-Story Full-Scale R/C Frame – Study Case

The structure to study is a four-story reinforcement concrete building designed by the European Association of Structural Mechanics Laboratories (EASML) using the Eurocodes 2 and 8 in 1991. The purpose was to study the building's assessment during an earthquake and the creation of damage indicators and failure criteriums for plastic hinges zones. For this goal, the experimental campaign has been applied in the European Laboratory for Structural Assessment (ELSA) of the Joint Research Center of the European Commission in 1993 [1]. The report published by Negro in 1994 is the basis of the thesis, as well as the master's degree thesis published by Schiavo from Politecnico di Milano in 2016 from where is obtained the finite element model which replicates the dynamic response obtained in the experimental campaign. The chapter describes the finite element model (FEM) done by Schiavo in SAP2000 and the model optimization executed in this investigation to improve the match with the experimental results.

#### 4.1 Numerical Model

The chapter focuses on describing the calibrated numerical model, which replicate the dynamic behavior of the four-story structure subjected to an experimental pseudo-dynamic test of the thesis degree "Influence of Masonry Infills on Dynamic Behavior of Reinforced Concrete Framed Structures" from Politecnico di Milano. [2].

##### 4.1.1 Structural Scheme- Floor Plan View and Elevation

The construction to study is a reinforcement concrete moment-frame structure composed of 4 floors. The plane distribution is a square of 10 by 10 meters (measured from the axis) with a total height of 12.5 meters, corresponding 3.5 meters to the ground story and 3 meters to a constant interstory height. To each side correspond three frames. In the X-direction, there is an equal span of 5 m, and in the Y-direction, there are different span lengths of 6 and 4 meters. A solid slab with a thickness of 150 mm is in all the stories. The next figures show the frame system described:

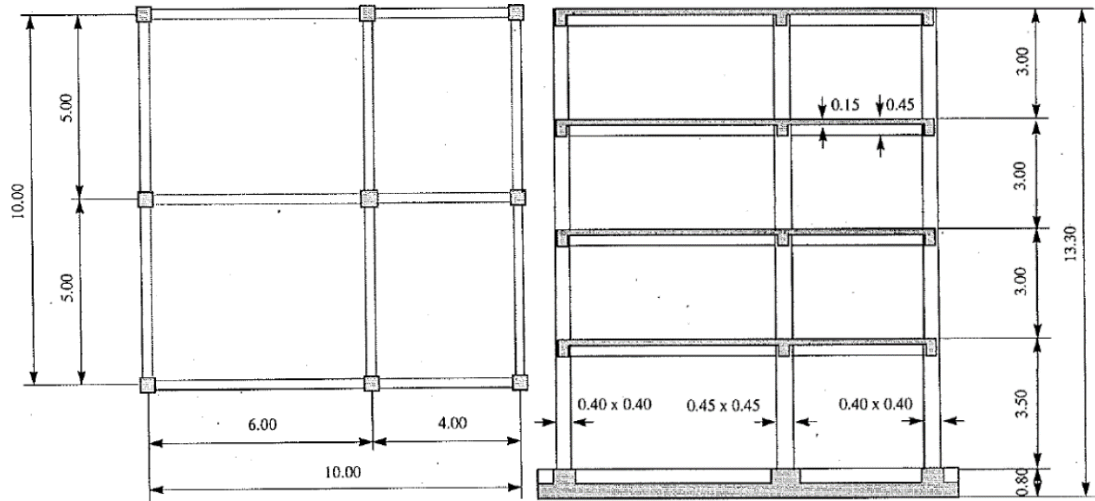


Figure 28. Layout of the building (From Negro P. et al, 1994)

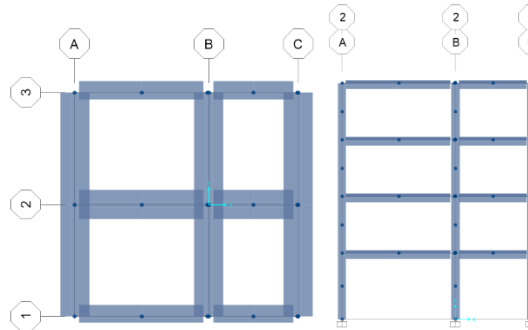


Figure 29. 2D SAP2000 model (Schiavo, 2016)[2]

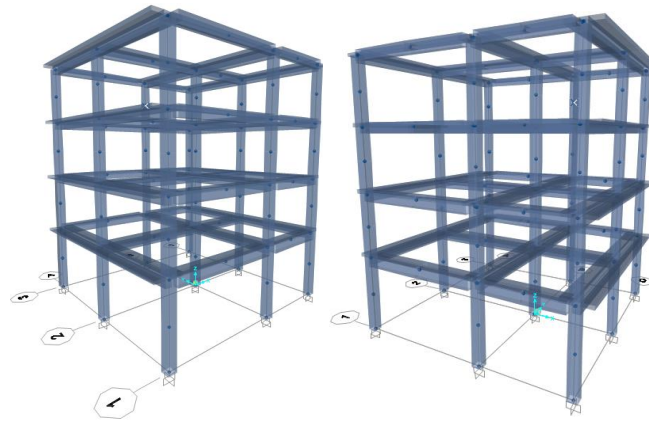


Figure 30. 3D SAP2000 model (Schiavo, 2016)[2]

#### 4.1.2 Structural Elements

The elements considered in the model are primary and secondary beams and columns. The collaborating slab is considered into the beam as a T-shape cross-section.

##### 4.1.2.1 Primary and Secondary Beams

These elements are T-shaped cross-section composed of a rectangular cross-section of 30 by 45 centimeters combined and an upper flange of 150 mm of thickness -see Figure 31.

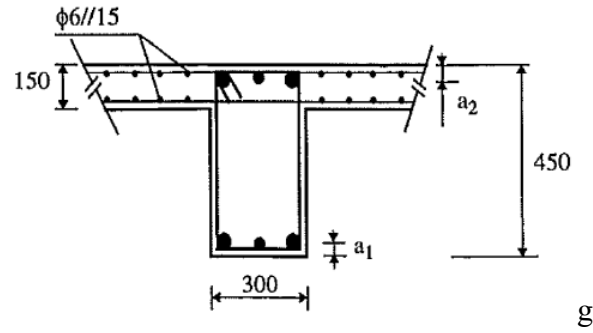


Figure 31. Beam cross section (From. Negro P. et al ,1994)

There are different typologies of Tee-beams in the model, one considering two flanges and the other one taking into consideration just one flange. In total, there are defined 11 sections to describe all the groups of beams of the structure[2]. Figure 32 shows the typologies:

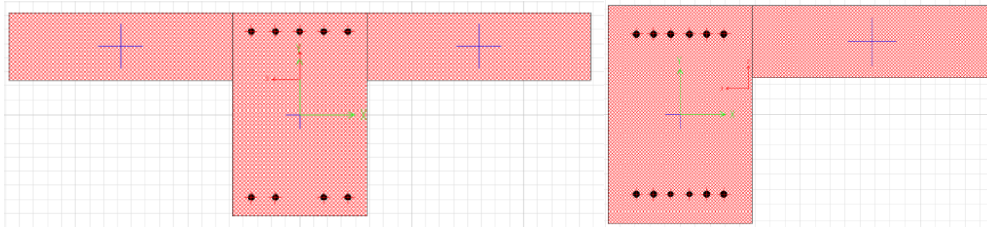


Figure 32. Cross section type 1 and type 2. 45x30 cm with 15x50 collaborating slab by side.

Table 5 summarizes the group of beams and their main characteristics, where:

- $h$ : Beam height.
- $b_w$ : Beam width.
- $e$ : Cover length.
- $b_{eff}$ : Effective width.
- $h_s$ : Height of the slab.
- $N_{long}$ : Longitudinal bars quantity.
- $\phi_L$ : Diameter of the longitudinal bars.

Type	Section name	h(m)	e(m)	bw(m)	beff(m)	hs(mm)	N.Long	ØL
1	BEAM T2 1	0,45	0,04	0,3	1,3	0,15	9	14d
1	BEAM T2 2	0,45	0,04	0,3	1,3	0,15	9	14d
1	BEAM T2 3	0,45	0,04	0,3	1,3	0,15	6	14d
1	BEAM T2 4	0,45	0,04	0,3	1,3	0,15	5	14d
2	BEAM Text 1 4.2	0,45	0,04	0,3	0,8	0,15	12	14d
2	BEAM Text 1 6e4.1	0,45	0,04	0,3	0,8	0,15	11	14d
2	BEAM Text 2 4.2	0,45	0,04	0,3	0,8	0,15	9	14d
2	BEAM Text 2 6.1	0,45	0,04	0,3	0,8	0,15	8	14d
2	BEAM Text 2 6.2e4.1	0,45	0,04	0,3	0,8	0,15	9	14d
2	BEAM Text 3	0,45	0,04	0,3	0,8	0,15	7	14d
2	BEAM Text 4	0,45	0,04	0,3	0,8	0,15	5	14d

Table 5. Beams.

Figure 33 and Figure 34 show the spatial distribution of the beams in each floor. The order is from the bottom to the top starting with the 3.5 meters height until 12.5 meters, each color and label represent the different cross sections[2]:

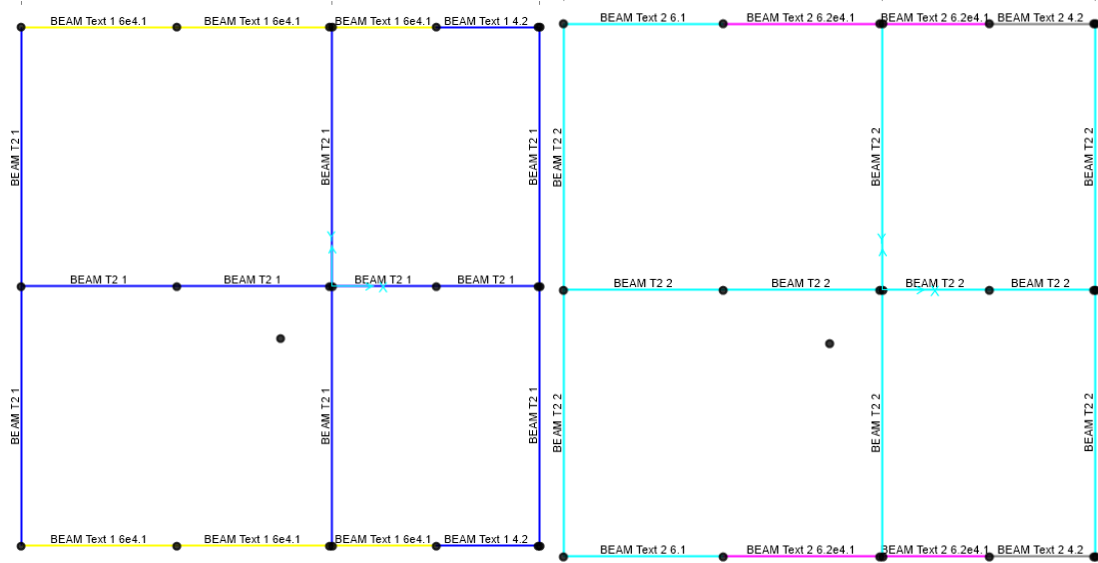


Figure 33. Plans view detailing beams of floors one and two.

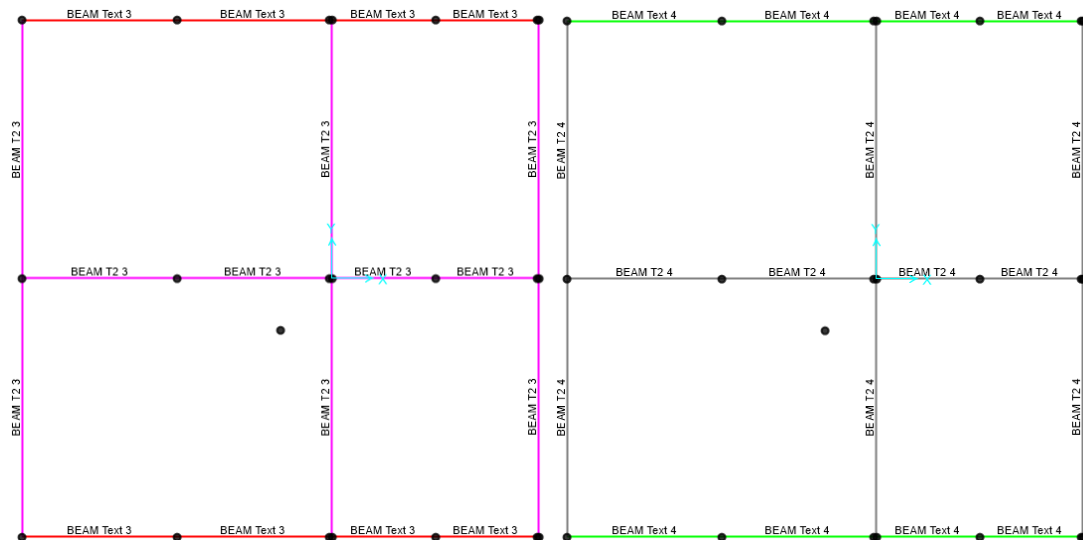


Figure 34. Plans view detailing beams of floors three and four.

#### 4.1.2.2 Central and lateral columns

These elements are a rectangular cross-section of 40x40 cm to the external frames and 45x45 cm to the internal frames- see Figure 35. There are 20 types of columns with variations in dimensions, longitudinal reinforcement, and material properties.

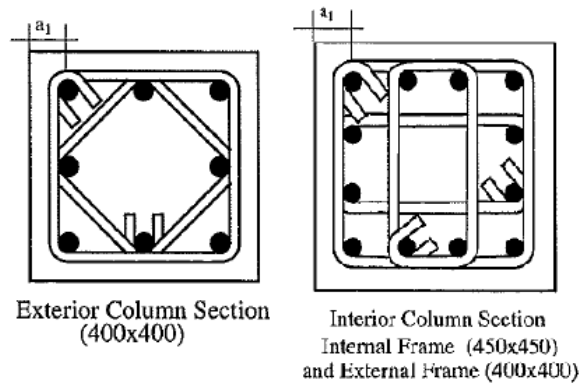


Figure 35. Columns cross section (from. Negro P. et a, 1994)

The next figure shows the two types of cross sections model used on SAP2000[2]:

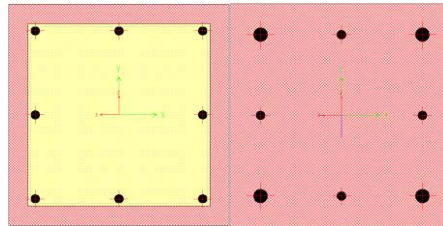


Figure 36. Column cross-section with confinement and without confinement

Table 6 summarizes the group of columns and their main characteristics. Where:

- $h$ : Column height.
- $b_w$ : Column width.
- $e$ : Cover length.
- $N_{long}$ : Longitudinal bars quantity.
- $\phi_L$ : Diameter of the longitudinal bars.

Note: highlighted sections are those with no confinement.

Section name	h(m)	e(m)	bw(m)	N.Long	ØL	Section name	h(m)	e(m)	bw(m)	N.Long	ØL
COL AeC 1.2	0,4	0,05	0,4	8	16d	COL T2 B 4	0,45	0,5	0,45	12	14d
COL AeC 2	0,4	0,05	0,4	8	16d	COL Text AeC 1.1	0,4	0,05	0,4	8	20d
COL AeC 3	0,4	0,05	0,4	8	16d	COL Text AeC 1.2	0,4	0,05	0,4	8	16d
COL AeC 4	0,4	0,05	0,4	8	16d	COL Text AeC 2.1	0,4	0,05	0,4	8	16d
COL T2 AeC 1.1	0,4	0,05	0,4	8	20d	COL Text B 1.1	0,4	0,05	0,4	12	20d
COL T2 B 1.1	0,45	0,5	0,45	12	20d	COL Text B 1.2	0,4	0,05	0,4	12	16d
COL T2 B 1.2	0,45	0,5	0,45	12	16d	COL Text B 2	0,4	0,05	0,4	12	16d
COL T2 B 2.1	0,45	0,5	0,45	12	16d	COL Text B 3	0,4	0,05	0,4	12	16d
COL T2 B 2.2	0,45	0,5	0,45	12	14d	COL Text B 4.1	0,4	0,05	0,4	12	16d
COL T2 B 3	0,45	0,5	0,45	12	14d	COL Text B 4.2	0,4	0,05	0,4	12	14d



Table 6. Columns

Figure 37 and Figure 38 show the spatial distribution of the columns in the building. The order is from grid A to grid C; each color and label represent a different column type. The columns with the “AeC” indication are those chosen to the grid A and C; the rest are implemented in grid B.



Figure 37. Columns distribution Y-Z plane grid A and B

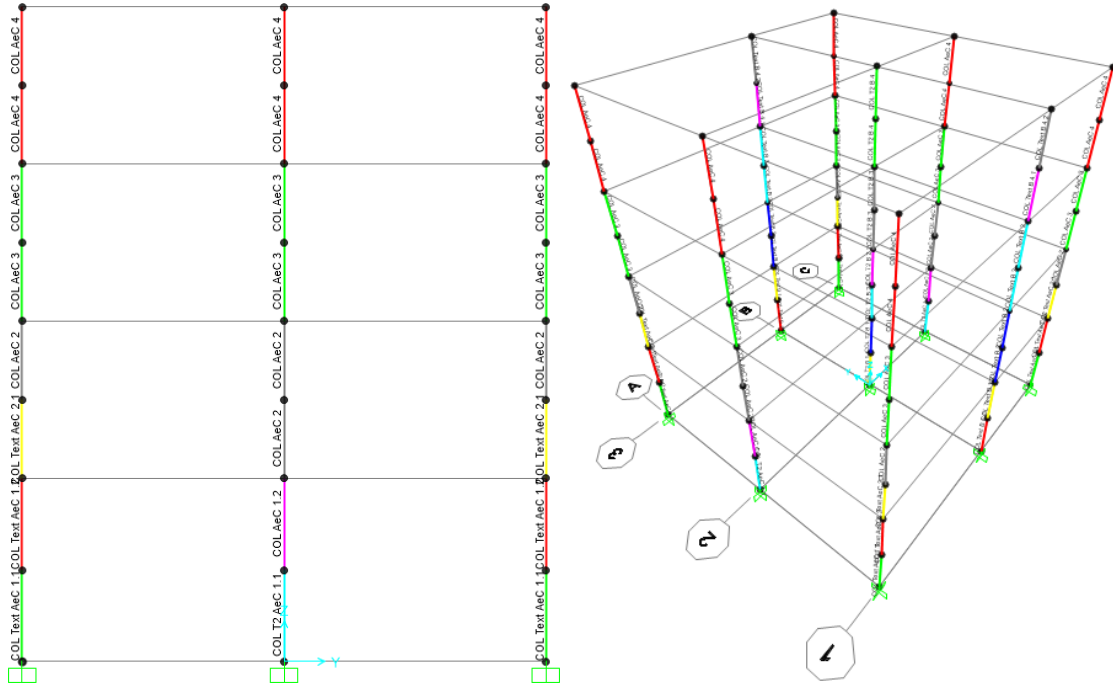


Figure 38. Columns distribution Y-Z plane grid C and 3D view.

#### 4.1.2.3 Material properties

The compressive strength of the concrete and tensile strength of the steel were obtained from laboratory test [1], the results are showing in the next tables:

Concrete Type	$f_c$ (KN/m <sup>2</sup> )	Strain-Stress Model	Hysteresis type	Symmetry type
C25/30	25000	Mander	Takeda	Isotropic
CLS BEAM 1 STORY	56400	Mander	Takeda	Isotropic
CLS BEAM 2 STORY	53200	Mander	Takeda	Isotropic
CLS BEAM 3 STORY	47200	Mander	Takeda	Isotropic
CLS BEAM 4 STORY	42100	Mander	Takeda	Isotropic
CLS COL 1 STORY	49800	Mander	Takeda	Isotropic
CLS COL 2 STORY	47600	Mander	Takeda	Isotropic
CLS COL 3 STORY	32000	Mander	Takeda	Isotropic
CLS COL 4 STORY	46300	Mander	Takeda	Isotropic

Table 7. Average cubic compressive strength of concrete (from. Negro P. et al, 1994) and material models.

Steel Type	$F_y$ (KN/m <sup>2</sup> )	$F_u$ (KN/m <sup>2</sup> )	Strain-Stress Model	Hysteresis type	symmetry type
B500 F10	545000	618000	Simple	Kinematic	Uniaxial
B500 F12	589000	689000	Simple	Kinematic	Uniaxial
B500 F14	583000	667000	Simple	Kinematic	Uniaxial
B500 F16	595000	681000	Simple	Kinematic	Uniaxial
B500 F20	553000	660000	Simple	Kinematic	Uniaxial
B500 F26	555000	657000	Simple	Kinematic	Uniaxial

Table 8. Average tensile properties of steel (from. Negro P. et al, 1994) and material models.

Table 9 lists the corresponding concrete and steel type to each structural element defined in the finite element model from SAP2000. The column “confinement” refers to the possibility of edge and corner reinforcing associated with the Solid Rectangle shape in the section designer from the cross-sections (software).

Section name	Concrete Type	Steel Type	Confinement
BEAM T2 1	CLS BEAM 1 STORY	B500 F14	No
BEAM T2 2	CLS BEAM 2 STORY	B500 F14	No
BEAM T2 3	CLS BEAM 3 STORY	B500 F12	No
BEAM T2 4	CLS BEAM 4 STORY	B500 F12	No
BEAM Text 1 4.2	CLS BEAM 1 STORY	B500 F12	No
BEAM Text 1 6e4.1	CLS BEAM 1 STORY	B500 F12	No
BEAM Text 2 4.2	CLS BEAM 2 STORY	B500 F14	No
BEAM Text 2 6.1	CLS BEAM 2 STORY	B500 F12	No
BEAM Text 2 6.2e4.1	CLS BEAM 2 STORY	B500 F14	No
BEAM Text 3	CLS BEAM 3 STORY	B500 F14	No
BEAM Text 4	CLS BEAM 4 STORY	B500 F12	No
COL AeC 1.2	CLS COL 1 STORY	B500 F16	Yes
COL AeC 2	CLS COL 2 STORY	B500 F16	Yes
COL AeC 3	CLS COL 3 STORY	B500 F16	Yes

COL AeC 4	CLS COL 4 STORY	B500 F16	Yes
COL T2 AeC 1.1	CLS COL 1 STORY	B500 F20	Yes
COL T2 B 1.1	CLS COL 1 STORY	B500 F20	Yes
COL T2 B 1.2	CLS COL 1 STORY	B500 F16	Yes
COL T2 B 2.1	CLS COL 2 STORY	B500 F16	Yes
COL T2 B 2.2	CLS COL 2 STORY	B500 F14	No
COL T2 B 3	CLS COL 3 STORY	B500 F14	No
COL T2 B 4	CLS COL 4 STORY	B500 F14	No
COL Text AeC 1.1	CLS COL 1 STORY	B500 F16	No
COL Text AeC 1.2	CLS COL 1 STORY	B500 F16	No
COL Text AeC 2.1	CLS COL 2 STORY	B500 F16	No
COL Text B 1.1	CLS COL 1 STORY	B500 F20	Yes
COL Text B 1.2	CLS COL 1 STORY	B500 F16	Yes
COL Text B 2	CLS COL 2 STORY	B500 F16	Yes
COL Text B 3	CLS COL 3 STORY	B500 F16	Yes
COL Text B 4.1	CLS COL 4 STORY	B500 F16	Yes
COL Text B 4.2	CLS COL 4 STORY	B500 F14	No

Table 9. Structural elements and materials

#### 4.1.2.4 Strain-stress model of materials

The materials considered in the model are concrete and reinforcement steel. Thus, this subsection explains the confinement model for the reinforcement concrete section and the constitutive model for the rebar steel for static loads and its corresponding hysteretic models due to the dynamic loads.

##### 4.1.2.4.1 Concrete model:

The Mander Model is used to predict concrete behavior describing the material's stress-strain relationships. The confined case is applied to model the internal core surrounded by the stirrups. In contrast, the unconfined case is for the Tee beam's flange[2]. Figure 39 shows the representation of the constitutive model for confined and unconfined concrete cross-section.

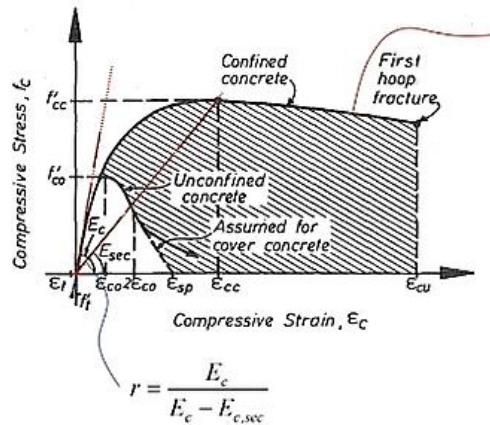


Figure 39. Mander confined and unconfined curves. [22]

The Mander unconfined concrete model is obtained with the following equations[22]:

$$f(\varepsilon) = \begin{cases} \frac{f'_c x r}{r - 1 + x^r} \rightarrow \varepsilon \leq 2\varepsilon'_c \\ \frac{2f'_c r}{r - 1 + 2^r} * \left( \frac{\varepsilon_u - \varepsilon}{\varepsilon_u - \varepsilon'_u} \right) \rightarrow 2\varepsilon'_c < \varepsilon \leq \varepsilon_u \end{cases} ; x = \frac{\varepsilon}{\varepsilon'_c} ; r = \frac{E}{E - \frac{f'_c}{\varepsilon'_c}} \quad (7)$$

The Mander confined concrete model is obtained with the following equations[22]:

$$f(\varepsilon_c) = f'_{cc} * x * \frac{r}{r - 1 + x^r} \quad (8)$$

$$\varepsilon_{cc} = \varepsilon_{co} \left[ 1 + 5 * \left( \frac{f'_{cc}}{f'_{co}} - 1 \right) \right] ; \varepsilon_{co} = 0.002 \quad (9)$$

$$r = \frac{E_c}{E_c - E_{E,sec}} \quad (10) \quad k = \frac{f'_{cc}}{f'_{co}} \quad (11)$$

$$x = \frac{\varepsilon_c}{\varepsilon_{cc}} = \frac{\text{long. compressive concrete strain}}{\text{Confined concrete strain}} \quad (12)$$

$$E_c = 5000 * \sqrt{f'_{co}} \text{ MPa} ; E_{sec} = \frac{f'_{cc}}{\varepsilon_{cc}} \quad (13)$$

Note: From a graphical approach using the equivalent lateral confinement pressure is calculated the  $f'_{cc}$  to execute the equation.

Where:

- $r$ : Variation coefficient of slope of concrete modulus.
- $f'_{cc}$ : compressive strength of confined concrete.
- $k$ : Confined strength ratio.
- $x$ : Ratio of deformations.

#### 4.1.2.4.2 Steel Rebars:

The constitutive model is used to predict steel behavior describing the material's stress-strain relationships[2]. Figure 40 illustrates the steel rebars constitutive law:

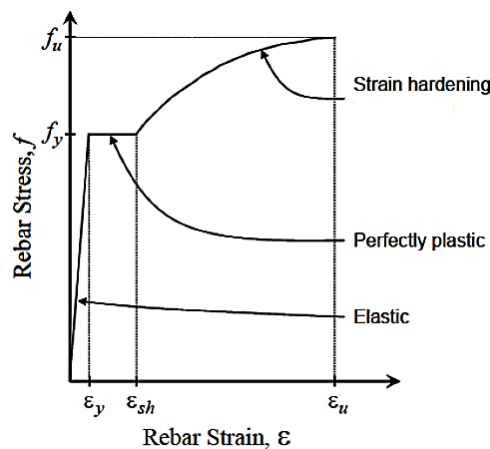


Figure 40. Steel rebars constitutive law [23]

#### 4.1.2.5 Hysteric model of materials

The hysteretic models can simulate the nonlinear mechanic behavior of the structural elements and the dissipative devices. In addition, it is only defined the model for the reinforcement concrete and the steel rebars. The model for the dissipative device was already well-defined in Chapter 2.

##### 4.1.2.5.1 Reinforced concrete model:

The Takeda hysteresis model is used to define the force-displacement relationship during cyclic loading to capture the nonlinearity for the structural members. In addition, the model defines the hysteresis rules holding the strain-stress specifications of the Mander Model. It means that the unloading-loading curves can describe the stiffness degradation considering the strains corresponding to the maximum concrete stress ( $\varepsilon_{cc}$ ) and the ultimate concrete strain ( $\varepsilon_{cu}$ ) from Mander model [2, 24, 25]. Figure 41 illustrates the model under cyclic loads:

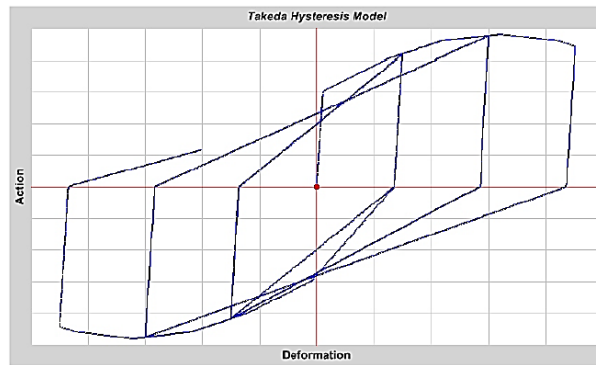


Figure 41. Force-Deformation relationship, Takeda Hysteresis Model under Increasing Cyclic Load [23]

##### 4.1.2.5.2 Steel Rebars:

The Kinematic hysteresis model is used to define the force-displacement relationship during cyclic loading to capture the material's nonlinearity. This model dissipates a significant amount of energy and is appropriate for ductile materials[2]. Figure 42 illustrates the model under cyclic loads:

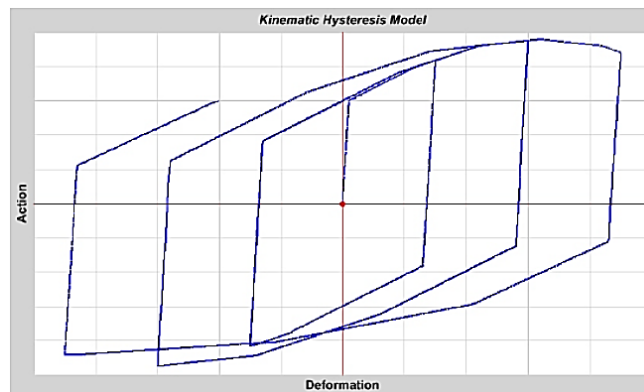


Figure 42. Kinematic Hysteresis Model under Increasing Cyclic Load [23]

#### 4.1.2.6 Hinges distribution and properties

The hinge objects are the elements that capture the nonlinear behavior of the materials and cross-sections on the finite element model. The distribution and length were obtained from the previous research. Table 10 lists the typology and the absolute length of each hinge of the model; in total, there are 64 over the entire structure. Figure 43 shows the hinge distribution on structural elements.

Hinge Name	DOF Type	Hinge Length	Hinge Name	DOF Type	Hinge Length
BEAM T2 1 4.1	Fiber P-M2-M3	0,58	COL T2 AeC 1.1	Fiber P-M2-M3	0,62
BEAM T2 1 4.2	Fiber P-M2-M3	0,58	COL T2 AeC 1.2	Fiber P-M2-M3	0,57
BEAM T2 1 6.1	Fiber P-M2-M3	0,7	COL T2 AeC 2.1	Fiber P-M2-M3	0,55
BEAM T2 1 6.2	Fiber P-M2-M3	0,7	COL T2 AeC 2.2	Fiber P-M2-M3	0,55
BEAM T2 2 4.1	Fiber P-M2-M3	0,58	COL T2 AeC 3.1	Fiber P-M2-M3	0,62
BEAM T2 2 4.2	Fiber P-M2-M3	0,58	COL T2 AeC 3.2	Fiber P-M2-M3	0,62
BEAM T2 2 6.1	Fiber P-M2-M3	0,7	COL T2 AeC 4.1	Fiber P-M2-M3	0,55
BEAM T2 2 6.2	Fiber P-M2-M3	0,7	COL T2 AeC 4.2	Fiber P-M2-M3	0,55
BEAM T2 3 4.1	Fiber P-M2-M3	0,62	COL T2 B 1.1	Fiber P-M2-M3	0,63
BEAM T2 3 4.2	Fiber P-M2-M3	0,62	COL T2 B 1.2	Fiber P-M2-M3	0,57
BEAM T2 3 6.1	Fiber P-M2-M3	0,74	COL T2 B 2.1	Fiber P-M2-M3	0,56
BEAM T2 3 6.2	Fiber P-M2-M3	0,74	COL T2 B 2.2	Fiber P-M2-M3	0,51
BEAM T2 4 4.1	Fiber P-M2-M3	0,62	COL T2 B 3.1	Fiber P-M2-M3	0,57
BEAM T2 4 4.2	Fiber P-M2-M3	0,62	COL T2 B 3.2	Fiber P-M2-M3	0,57
BEAM T2 4 6.1	Fiber P-M2-M3	0,72	COL T2 B 4.1	Fiber P-M2-M3	0,56
BEAM T2 4 6.2	Fiber P-M2-M3	0,72	COL T2 B 4.2	Fiber P-M2-M3	0,56
BEAM Text 1 4.1	Fiber P-M2-M3	0,58	COL Text AeC 1.1	Fiber P-M2-M3	0,62
BEAM Text 1 4.2	Fiber P-M2-M3	0,58	COL Text AeC 1.2	Fiber P-M2-M3	0,58
BEAM Text 1 6.1	Fiber P-M2-M3	0,7	COL Text AeC 2.1	Fiber P-M2-M3	0,56
BEAM Text 1 6.2	Fiber P-M2-M3	0,7	COL Text AeC 2.2	Fiber P-M2-M3	0,55
BEAM Text 2 4.1	Fiber P-M2-M3	0,58	COL Text AeC 3.1	Fiber P-M2-M3	0,62
BEAM Text 2 4.2	Fiber P-M2-M3	0,58	COL Text AeC 3.2	Fiber P-M2-M3	0,52
BEAM Text 2 6.1	Fiber P-M2-M3	0,7	COL Text AeC 4.1	Fiber P-M2-M3	0,55
BEAM Text 2 6.2	Fiber P-M2-M3	0,7	COL Text AeC 4.2	Fiber P-M2-M3	0,55
BEAM Text 3 4.1	Fiber P-M2-M3	0,6	COL Text B 1.1	Fiber P-M2-M3	0,62
BEAM Text 3 4.2	Fiber P-M2-M3	0,6	COL Text B 1.2	Fiber P-M2-M3	0,57
BEAM Text 3 6.1	Fiber P-M2-M3	0,72	COL Text B 2.1	Fiber P-M2-M3	0,55
BEAM Text 3 6.2	Fiber P-M2-M3	0,72	COL Text B 2.2	Fiber P-M2-M3	0,55
BEAM Text 4 4.1	Fiber P-M2-M3	0,62	COL Text B 3.1	Fiber P-M2-M3	0,62
BEAM Text 4 4.2	Fiber P-M2-M3	0,52	COL Text B 3.2	Fiber P-M2-M3	0,62
BEAM Text 4 6.1	Fiber P-M2-M3	0,74	COL Text B 4.1	Fiber P-M2-M3	0,55
BEAM Text 4 6.2	Fiber P-M2-M3	0,74	COL Text B 4.2	Fiber P-M2-M3	0,55

Table 10. Hinge distribution and properties

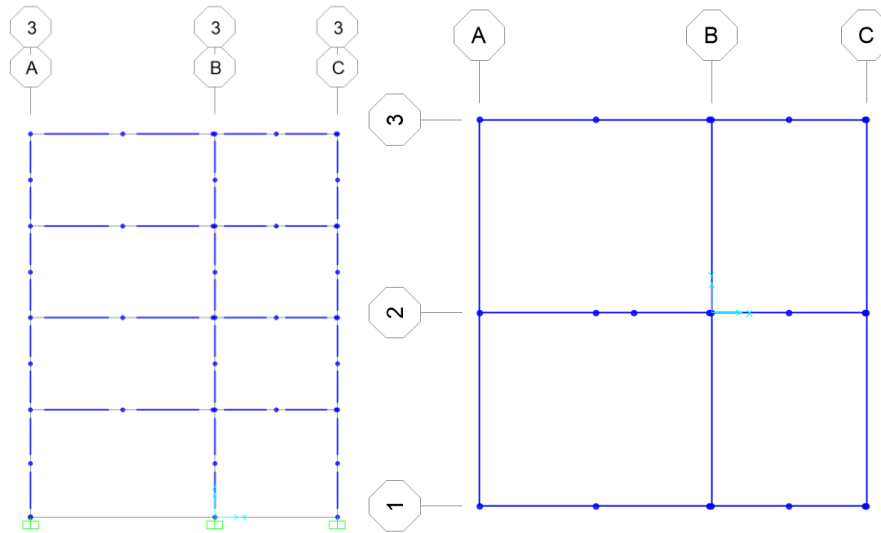


Figure 43. Hinge distribution on structural elements.

According to the SAP2000 Manual, the hinges must be assigned to the frame objects to capture the post-yield behavior on the nonlinear analysis's structural elements, and the best option for hysteretic dynamics is the fiber hinge element. In addition, The elastic behavior occurs over member length, while the non-elastic deformation occurs entirely within hinges, modeled in specific positions following the recommendations of the EC8 [23].

#### 4.1.2.7 Constraints and restraints

Constraints and restraints are assigned to the joints' structure to model the building's real behavior. The restraints concern only the individual joints' behavior; in this case, the base joints are fixed avoided the rotation and translation in all directions considering the basement as infinite rigid. Figure 44 shows the configuration in SAP2000.

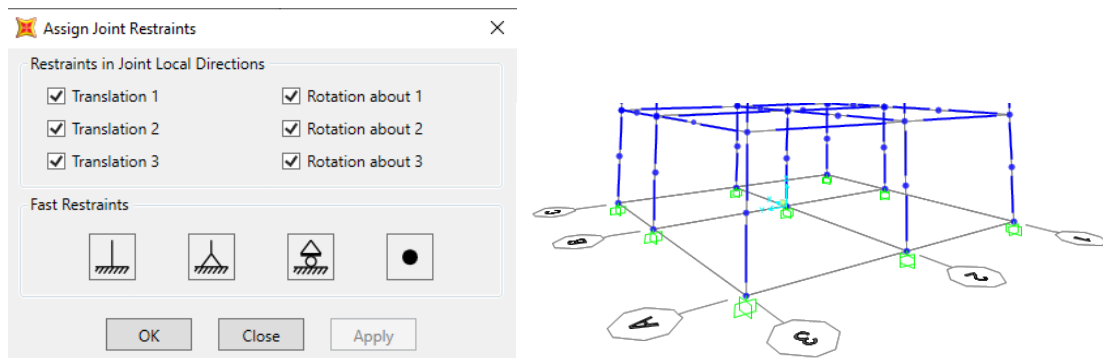


Figure 44. Base nodes fixed

On the other hand, the constraints are nodes where the displacements relate between them. In this case, each node is assigned a Diaphragm Constraint to control each floor's movement and simulate a rigid floor . They move together as a planar diaphragm, rigid against membrane deformation (in-plane) but susceptible to plate deformation (out-of-plane) and associated

effects [23]. Figure 45 and Figure 46 show the nodes with diagram constraints and the configuration in SAP2000.

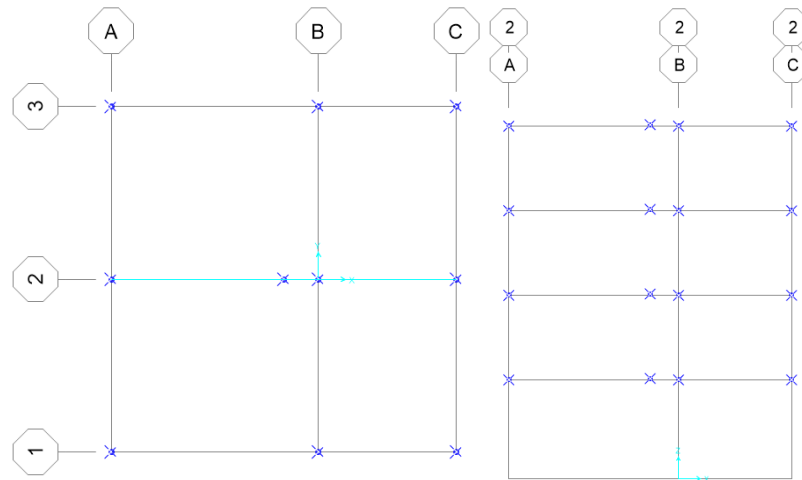


Figure 45. XY plane and XZ plane with the diaphragm constraint selected.

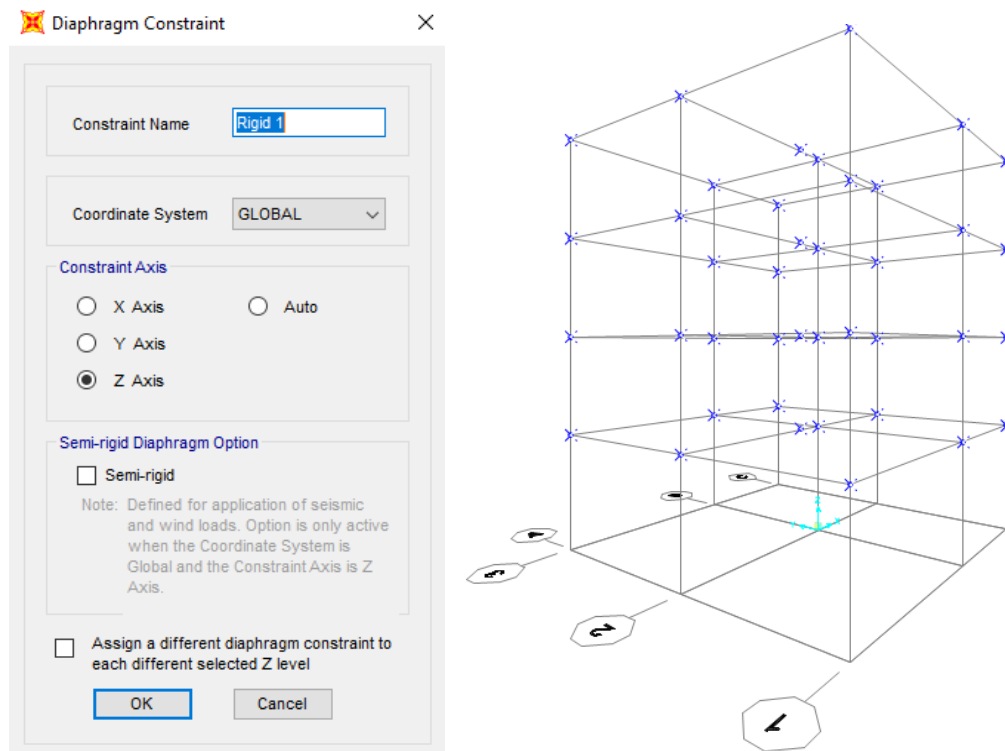


Figure 46. Constraint characteristics and 3D View with the diaphragm constraint selected

For the beams, void gaps are placed before the intersection with the columns. For the nodes inclosing the void gap is assigned the Body Constraint to translate and rotate together as a rigid body letting free just the translation in X direction [23]. Figure 47 and Figure 48 show the nodes with body constraints and the configuration on SAP2000.



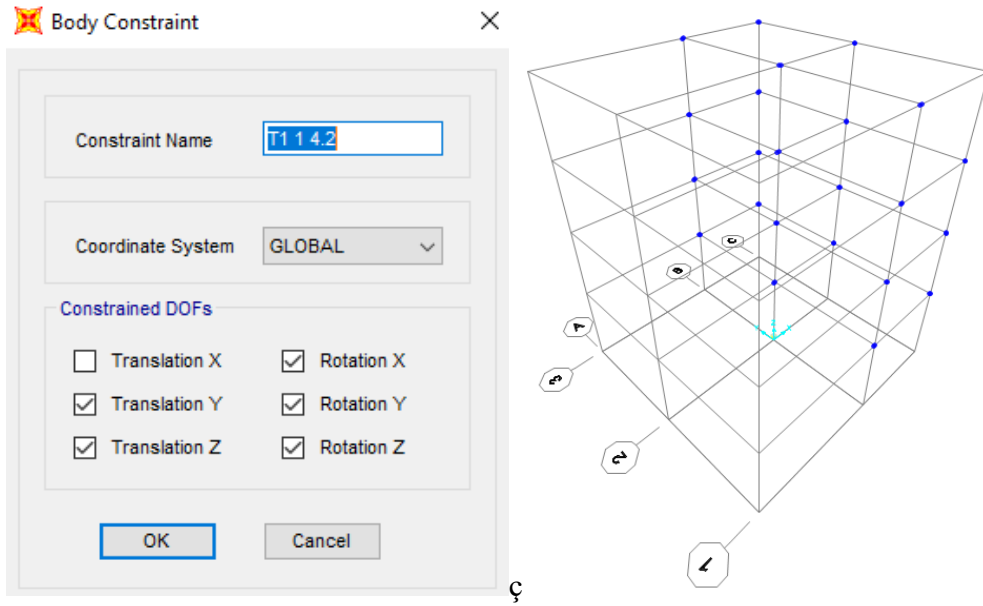


Figure 47. Constraint characteristics and 3D View with the body constraint selected.

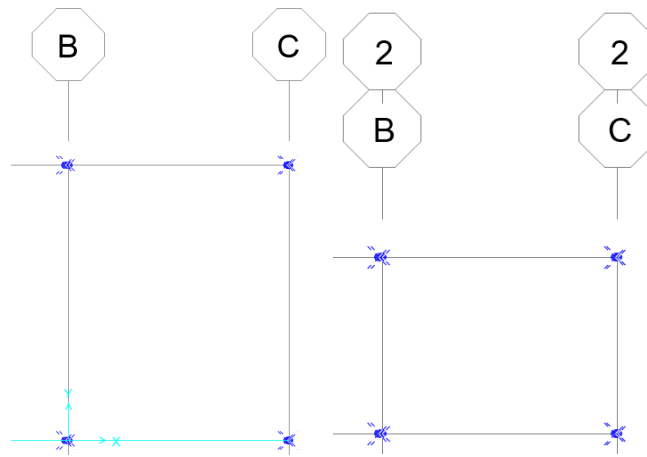


Figure 48. XY plane and XZ plane zoom to visualize the gap before the columns.

#### 4.1.2.8 Member Discretization

The columns' mesh is divided into 22 fibers in the X and Y direction to model the coupled bi-directional behavior. On the other hand, the beams' mesh is divided into 23 fibers in the X direction and three fibers in the Y direction to model the mono-directional behavior. Figure 49, Figure 50 and Figure 51 illustrate the mesh on the columns and T-beams.

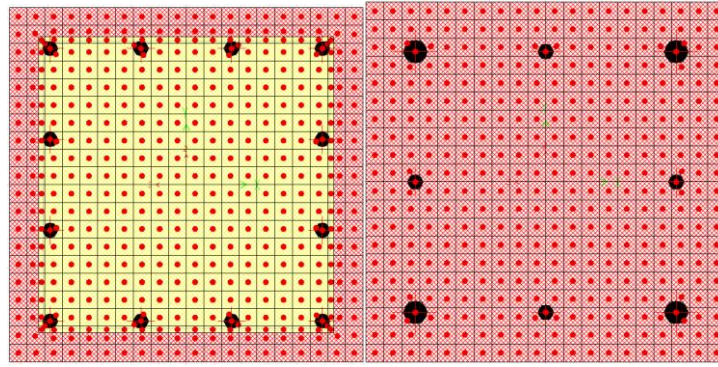


Figure 49. Generic column's cross section-Fiber discretization

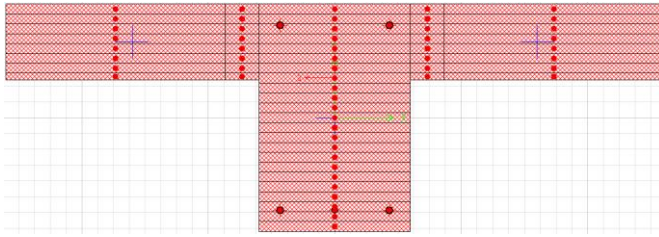


Figure 50. Generic internal frame beam's cross section-Fiber discretization

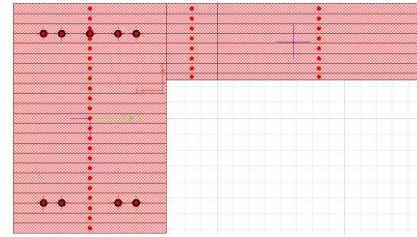


Figure 51. Generic external frame beam's cross section-Fiber discretization

#### 4.1.3 Masses and Loads

Regards the mass of the building, it has been lumped in each story's geometric centroid called the "Master node" point. To perform the dynamic structural analysis is assigned different mass arrangements for the 2D-analysis and 3D-analysis to consider the rigid story hypothesis. The next tables show the masses attached to the master node of each story[2].

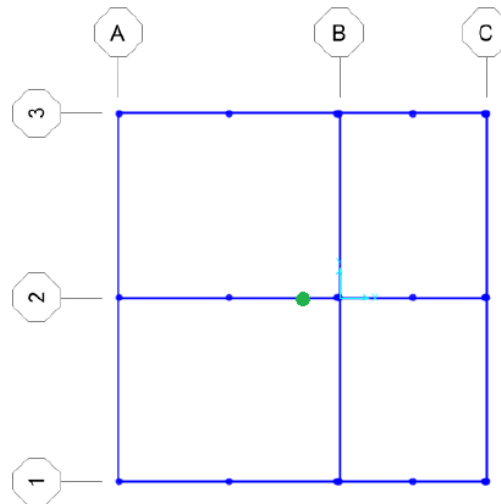


Illustration 1 Master Node.

Story	Joint	TMass_X(TON)
1	26	86,9
2	27	85,9
3	28	85,9
4	50	83

Table 11 Mass Arrangement for 2D-Analysis

Story	Joint	TMass_X(KN)	TMass_Y(KN)	RMass_Z(KN-m)
1	26	86,9	86,9	1448,33
2	27	85,9	85,9	1431,67
3	28	85,9	85,9	1431,67
4	50	83	83	1383,33

Table 12. Mass Arrangement for 3D-Analysis.

Where:

- TMass\_X: Translational mass assigned to the specified joint in the local 1 (or global X) direction.
- TMass\_Y: Translational mass assigned to the specified joint in the local 2 (or global Y) direction.
- RMass\_Z: Rotational mass moment of inertia assigned to the specified joint about the local 3 (global Z) axis.

Arrangement of loads:

The Seismic assessment is realized by the combination of load presented in the Eurocode 8, which is depicted in the following equation:

$$q_{seismic} = G_1 + G_2 + \sum \psi_{2,j} * Q_{2,j} \quad (14)$$

Where:

- $G_1$ : structural load (element self-mass is included in the analysis of SAP2000).
- $G_2$ : Non-structural load.
- $Q_{2,j}$ : j-th variable action that acts on the structure.
- $\psi_{2,j}$ : coefficient of permanency (0.3)

The distributed loads assigned to the frames are[2]:

	Internal frame	External frame
Story	q(KN/m)	q(KN/m)
1	28,85	14,48
2	28,85	14,48
3	28,85	14,48
4	29,75	14,93

Table 13. Distributed loads on beams

#### 4.1.4 Schiavo's Model Verification

Schiavo's investigation concludes that the following characteristics are the best to replicate on SAP2000 the experimental campaign performed in the European Laboratory for Structural Assessment (ELSA) done by Negro in 1994 for a Four-Story Full-Scale R/C Frame [2]:

- The plastic hinge length calculated according to EC8.
- The replication of the experimental campaign conditions and the previous damage of the sample building is obtained by reducing 70% and 50% of the total moment of inertia about 3-axis for beams and columns, respectively. It is denoted as T30 and P50.
- The collaborating slab has 50 cm of width on each flange to fit with the experimental survey(S50).

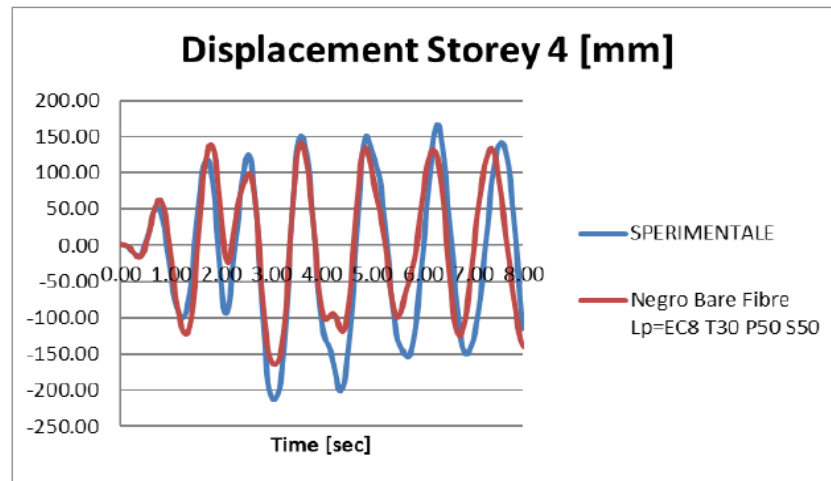


Figure 52. Bare frame top story displacement: numerical vs experimental (Schiavo,2016) [2]

Despite a reasonable approximation from the numerical results (red) to the experimental data (blue), the model is improved due to some inaccuracies in the input parameters on the finite element software (SAP2000).

Inaccuracies in the Schiavo Model to improving:

- It does not have a proper definition of the Mander Model for the structural elements.
- The transversal beams are no confined, and they are not correctly defined. It is used the same concrete for all the floors. The longitudinal and transversal reinforcement is arbitrary.
- The collaborating slab has not longitudinal reinforcement.

## 4.2 Optimization of the Model

The new model presents a better approximation than Schiavo's model to replicate the experimental results obtained from the campaign performed in the European Laboratory for Structural Assessment (ELSA) done by Negro in 1994 for a Four-Story Full-Scale R/C Frame. The next adjustments were applied:

- The replication of the experimental campaign conditions and the previous damage of the sample building is obtained by reducing the moment of inertia about 3-axis of the gross cross sections. The fraction of moment of inertia used for beams and columns is 20% and 50%, respectively (T20 and P50). It generates better results in the response of the structural model.

- All the structural elements have confinement and the correct Mander Model defined on the section designer tool on SAP2000.
- The transversal beams are correctly confined by the section designer tool on SAP2000. The longitudinal and transversal reinforcement is 4Ø14 and 2Ø6/8cm, respectively.
- The collaborating slab has longitudinal reinforcement. It is specified by the section designer tool on SAP2000.

Figure 53 shows the configuration of the typical cross section on SAP2000:

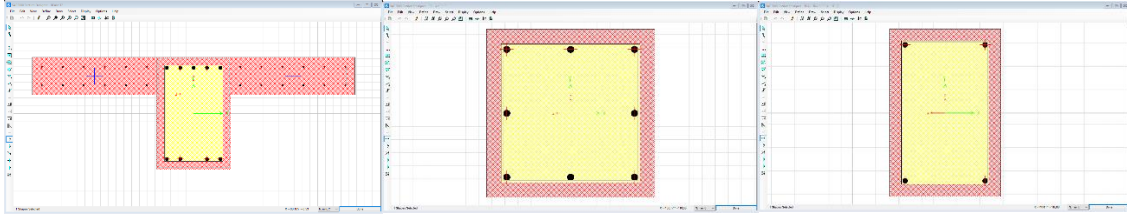


Figure 53. Cross section of the main beam, column, and transversal beam.

To select the best approach, it is considered 3 different models:

- RBC: Main beams and columns with the correct Mander Model and confinement.
- RBC+S: Main beams and columns with the correct Mander Model and confinement, with the addition of the longitudinal reinforcement in the collaborating slab.
- RBC+S+T: Main beams, transversal beams, and columns with the correct Mander Model and confinement, with the addition of the longitudinal reinforcement into the collaborating slab.

The election of the best model is done through descriptive statistics, which outlines the features from all numerical models to evaluate which one is the most accurate to the experimental results. Figure 54 shows the displacement on the 4th floor of the structure produced by the time-history analysis (THx1,5) to compare the different model results with the experimental results; the plot is displacement in function of the time.

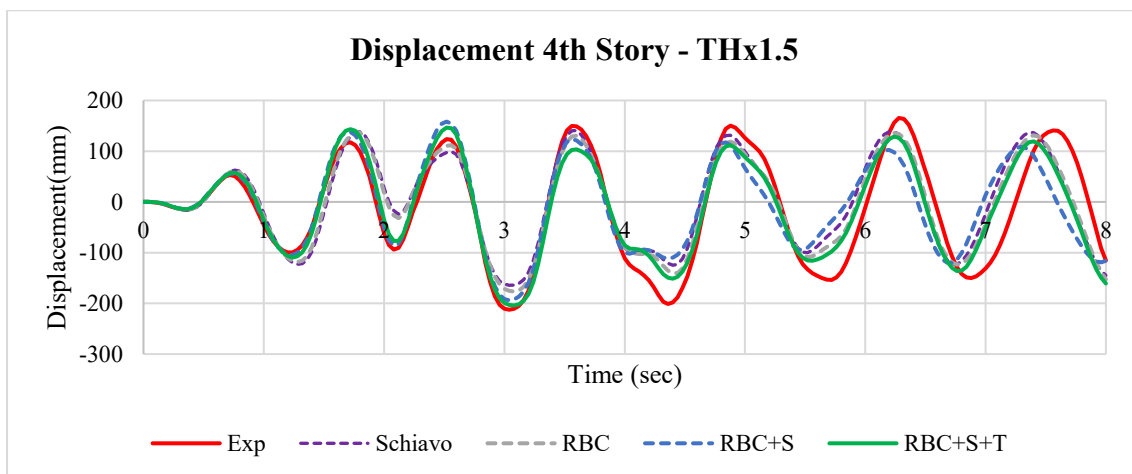


Figure 54. Displacement of the 4<sup>th</sup> Story for the Nonlinear Time-history Analysis Thx1.5 in FE models: Exp, Schiavo, RBC, RBC+S and RBC+S+T.

The plot “Exp” is the reference curve corresponding to the experimental results obtained from Negro (1994), for this case is only calculated the mean, variance, and standard deviation. The determination coefficient, Pearson coefficient, square error and percentage error are computed concerning the curve previously mentioned. To each numerical model (Schiavo, RBC, RBC+S, RBC+S+T) is calculated the following coefficients from descriptive statistics:

Mean of the sample: $Mean(\bar{d}) = \frac{\sum d_i}{n} \quad (15)$	Calculate Variance: $\sigma^2 = \frac{\sum (d - \bar{d})^2}{n} \quad (16)$	Calculate Standard Deviation: $\sigma = \sqrt{\frac{\sum (d - \bar{d})^2}{n}} \quad (17)$
Square error with respect to the experimental displacement: $S_{E,dexp} = (d_{exp} - d_{model})^2 \quad (18)$	Square error with respect to the mean experimental displacement: $S_{E,\bar{d}exp} = (\bar{d}_{exp} - d_{model})^2 \quad (19)$	
Percentage of variation not explained by the approximation (V): $V = \frac{S_{E,dexp}}{S_{E,\bar{d}exp}} \quad (20)$	Absolute percentage error (APE): $APE = 100 * \frac{ (d_{exp_i} - d_{model_i}) }{ d_{exp_i} } \quad (21)$	
Mean absolute percentage error (MAPE): $MAPE = \frac{100}{n} * \sum \frac{ (d_{exp_i} - d_{model_i}) }{ d_{exp_i} } \quad (22)$	Root mean squared error (RMSE): $RMSE = \sqrt{\frac{1}{n} \sum \frac{ (d_{exp_i} - d_{model_i}) }{ d_{exp_i} }} \quad (23)$	

Table 14. Descriptive Statistics

Coefficient of determination ( $R^2$ ): It is the percentage of variation explained by the approximation. In other words, it is how much accurate the approximation is. If the value tends to one means a good estimation.

$$R^2 = 1 - V \quad (24)$$

$\rho$  (Pearson correlation coefficient): it explains how strong the linear relation between 2 variables is. The value of 1 or -1 refers to the perfect linear correlation. Equal to  $R^2$  just in case of linear relationship.

$$\rho = \frac{covariance(d_{exp}, d_{model})}{\sqrt{\sigma^2(d_{exp}) * \sigma^2(d_{model})}} \quad (25)$$

Descriptive statistics results and analysis:

Starting from the displacement (d) in function of time, the model RBC+S+T has the best approximation concerning the experimental results in terms of mean, variance, and standard deviation. In addition, the R squared value is proximate to the Pearson coefficient compared with other cases, and both tend to the unity, showing the best linear correlation concerning the experimental results. Table 15 list the results for each numerical model.

	d Exp	d Schiavo	d RBC	d RBC+S	d RBC+S+T
Mean( $\mu$ )	-12,95	0,82	-3,55	-5,87	-11,03
Variance	10921,21	7726,33	7905,90	7370,01	8506,91
Standard deviation	104,50	87,90	88,92	85,85	92,23
$S_{E,dexp}$		535497	372177	762199	329516
$S_{E,\bar{d}exp}$		1591101	1606818	1491429	1710622
V		0,337	0,232	0,511	0,193
R squared		0,663	0,768	0,489	0,807
Covariance		8086	8532	7275	8896
$\rho$		0,88	0,92	0,81	0,92

Table 15. Descriptive statistical for displacement from the numerical and experimental displacement-time relationship.

On the other hand, the absolute percentage error in the displacement obtained from the numerical models concerning the experimental results shows that the RBC+S+T model has a lower error than the other numerical models. Table 16 list the results for each numerical model.

	d Schiavo	d RBC	d RBC+S	d RBC+S+T
Mean	0,49%	0,39%	0,44%	0,31%
Variance	0,012%	0,007%	0,008%	0,004%
Standard deviation	1,11%	0,84%	0,87%	0,62%
MAPE	98%	79%	88%	62%
RMSE	17%	13%	14%	10%

Table 16. Descriptive statistical for the absolute percentage error.

In addition, Figure 55 shows the evolution of absolute percentage error of displacement of the numerical models through time. The curve RBC+S+T the most part of the time is below the other curves, demonstrating the most precise results.

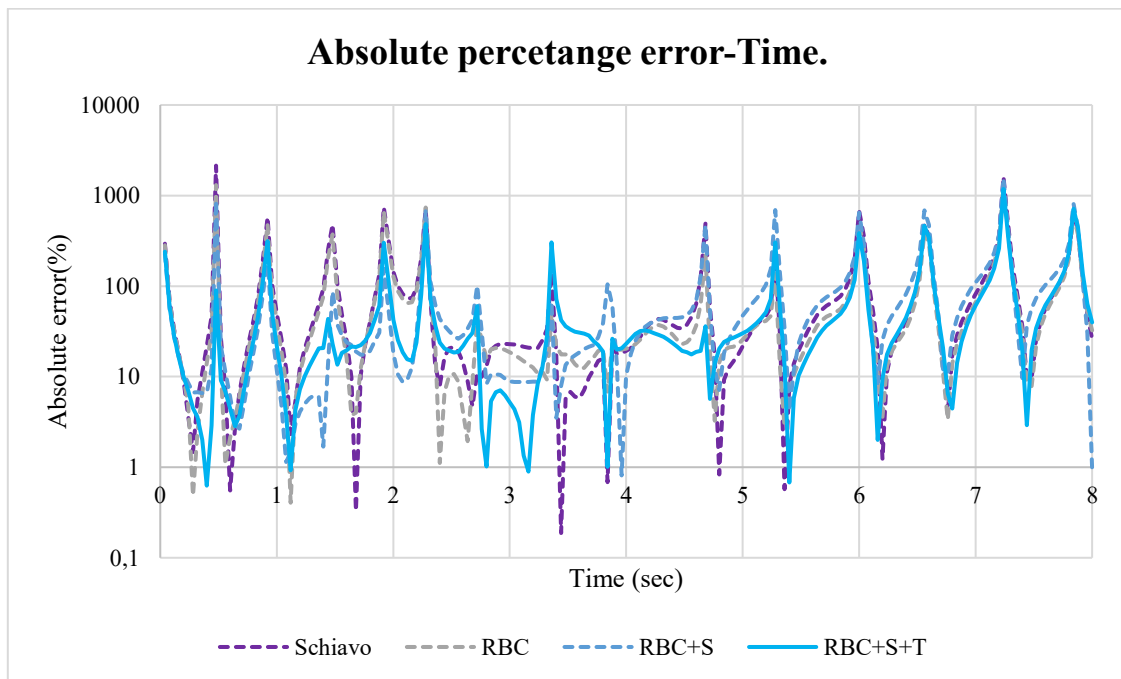


Figure 55. Evolution of absolute percentage error in the calculation of displacement of the numerical models.

In conclusion, the model RBC+S+T provides the best calibration regards the dynamic response obtained from the experimental campaign. Thus, this model is used to execute the structural analysis of the building without the dissipative devices and with fluid viscous dampers and metallic-yielding dampers.



## Chapter 5

### 5 Structural Analysis of Pre-Retrofit Structure

This chapter reports the structural analysis executed to the finite element model described in Chapter 4. The analytical methods considered are Modal Analysis, Static Nonlinear Analysis, Static Pushover Analysis, and Nonlinear Time-history Analysis. The goal is examines the static response, the dynamic response, and the nonlinear structural behavior to identify the current state of the building and obtain the parameters to design the dissipative devices.

#### 5.1 Modal Analysis

The modal analysis executed is the Eigenvector Analysis which determines the shapes and natural periods of the system in undamped free vibration[23]. The input parameters are zero initial conditions (unstressed state) and maximum number of modes equal to 12. Table 17 shows the periods and frequencies of the structure:

Mode	Period	Frequency	Angular Frequency
	(sec)	(Hertz)	(rad/sec)
1	0,58	1,73	10,84
2	0,19	5,37	33,72
3	0,10	9,89	62,15
4	0,07	14,12	88,70

Table 17. Periods and frequencies from bare frame.

From the software is extracted the mass participation percentage of each mode to identify the most important modes of vibration of the building. The results are listed in Table 18:

Mode	Period (sec)	Ux	Uy	RX	RY	RZ
1	0,58	87%	-	-	12%	-
2	0,19	10%	-	-	77%	-
3	0,10	2%	-	-	6%	-
4	0,07	1%	-	-	4%	-

Table 18. Mass participation from bare frame

Table 19 shows the total mass distributed on the floor, according with Schiavo's thesis degree [2]. This data is fundamental to execute the pushover analysis:

Z(m)	Joint	TMass_X(TON)
12,5	50	83
9,5	28	85,9
6,5	27	85,9
3,5	26	86,9
0	0	0

Table 19. Total mass by floor

In addition, to transform the pushover curve obtained in SAP2000 from the multi-degree freedom system (MDOF) to the single-degree freedom system (SDOF), the eigenvectors are normalized concerning the last floor. Table 20 shows the results:

<b>Z(m)</b>	<b><math>U_x(\text{m})</math></b>	<b><math>\phi_{xNi}</math></b>
12,5	0,0733	1,00
9,5	0,0629	0,86
6,5	0,0444	0,61
3,5	0,0228	0,31
0	0	0,00

Table 20. Normalized modal shape.

Where:

- $U_x$ : Eigenvector.
- $\phi_{xNi}$ : Normalized eigenvector with respect to the displacement of the last floor.

## 5.2 Static Pushover Analysis

The type of analysis done is Non-Adaptative (Static pushover analysis). Which comply the following assumptions[26]:

- Forces and displacement are one-monotonically increasing.
- Structure is dominated by 1<sup>st</sup> mode (Highest mass percentage).
- Shape of profile does not change during analysis.

### 5.2.1 Profile of Forces:

The loads are scaled to maintaining invariable the acting force between the floors. The analysis takes a control point of the structure as a reference while increasing horizontal displacement monotonically to evaluate the relationship between the base displacement and the control node. The force applied is the following[26]:

$$W_{IN} = W_i * \frac{\phi_{xNi}}{W_{max}} \quad (26)$$

Where:

- $W_i$ : Load of each floor.
- $W_{IN}$ : Load normalized with the first eigenvector distribution.
- $\phi_{xNi}$ : Normalized eigenvector with respect to the displacement of the last floor

### 5.2.2 Modal And Uniform Approach:

The modal and the uniform profile of forces on X direction are defined to apply the pushover analysis. The approach evaluates all the possible responses of the structure; therefore, the real

structural performance will be in the middle of both models mentioned before[26]. Table 21 indicates the force required to be applied on the center of masses of the floor and each column of the story and Figure 56 show the scheme the approach.

Z(m)	$\emptyset_{xNi}$	W(KN)	Wi(KN)	Modal		Uniform	
				WiN	WiN/c	WiNR	WiNR/c
12,5	1,00	814,23	814,23	1,00	0,11	1,0	0,11
9,5	0,86	842,68	723,12	0,89	0,10	1,0	0,11
6,5	0,61	842,68	510,44	0,63	0,07	1,0	0,11
3,5	0,31	852,49	265,17	0,33	0,04	1,0	0,11
0	0	0,00	0,00	0,00	0,00	0	0,00

Table 21. Pushover profiles: Modal and Uniform.

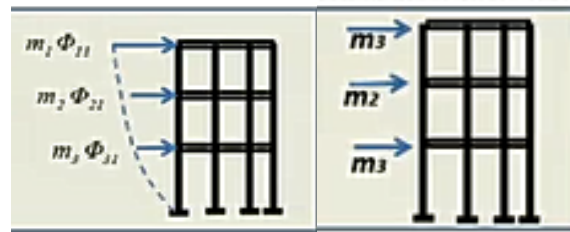


Figure 56. Modal And Uniform distribution of forces.[26]

### 5.2.3 Equivalent Mass and Participation Factor:

To obtain the simplified capacity curve and evaluate the ductility and the vulnerability indexes of the structure, the MDOF capacity curve will be transformed to SDOF capacity curve. It is done by dividing the shear force and the MDOF capacity curve's displacement from the linear pushover analysis by the modal participation factor associated with the equivalent mass matrix and the normalized eigenvector[26]. The modal parameters can be computed as:

$$\begin{aligned} \text{Equivalent mass[26]:} \\ m^* = \{\emptyset_{xN}\}^T * [M] * \{\tau\} \end{aligned} \quad (27)$$

$$\begin{aligned} \text{Modal participation factor[26]:} \\ \Gamma = \frac{\{\emptyset_{xN}\}^T * [M] * \{\tau\}}{\{\emptyset_{xN}\}^T * [M] * \{\emptyset_{xN}\}} \end{aligned} \quad (28)$$

Where:

- $\{\emptyset_{xN}\}$ : Normalized eigenvector with respect to the last floor.
- $[M]$ : Mass matrix
- $\{\tau\}$ : represent the contribution of each mode. In this case is a vector full of 1.

Table 22 shows the equivalent mass and the modal participation factor, obtained by the equations described previously.

Z(m)	U <sub>x</sub>	Total mass(TON)	ØXN	mi* ØXN (TON)	m <sub>x</sub> *(TON)
12,5	0,0733	83,0	1,00	83,00	235,77
9,5	0,0629	85,9	0,86	73,71	ØXN '*m* ØXN
6,5	0,0444	85,9	0,61	52,03	186,18
3,5	0,0228	86,9	0,31	27,03	Γ <sub>x</sub>
0	0	0	0,00	0,00	1,266

Table 22. Modal participation factor and effective mass.

#### 5.2.4 Capacity Curves

The analysis is executed on SAP2000, setting the kinematical constraints to move in the X-X coordinates solely; therefore, the rotational contribution of the main concentrated mass floor was neglected. The Plane Frame setup establishes the condition required by allowing the displacement in the X and the Z direction and the rotation in the Y direction [1]. Figure 57 and Figure 58 show the configuration into SAP2000.

The screenshot shows the 'Pushover X Modal' configuration in SAP2000. Key settings include:

- Load Case Name:** Pushover X Modal
- Initial Conditions:** Continue from State at End of Nonlinear Case (selected)
- Modal Load Case:** All Modal Loads Applied Use Modes from Case
- Loads Applied:**

Load Type	Load Name	Scale Factor
Load Pattern	Pushover X Modal	1,
- Analysis Type:** Nonlinear
- Geometric Nonlinearity Parameters:** None
- Mass Source:** MSSSRC1
- Other Parameters:** Load Application (Displ Control), Results Saved (Multiple States), Nonlinear Parameters (User Defined)

Figure 57. Configuration of the Pushover Analysis on SAP2000.

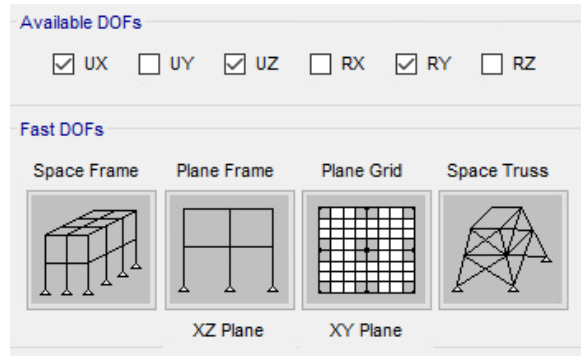


Figure 58. The Plane Frame setup on SAP2000.

The forces' profile was applied on the story columns instead of the center of masses of the floor. Figure 59 illustrates the applied loads used in the analysis for modal and uniform case (left and right, respectively):

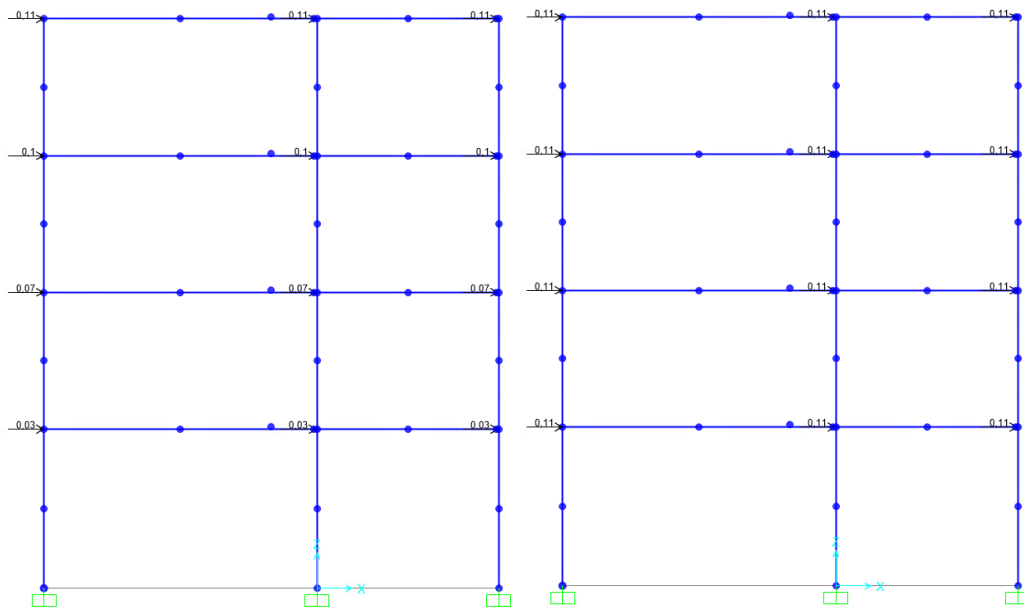


Figure 59. Modal applied loads-Uniform applied loads.

Characteristics of the load case:

- Load application control: Displacement control. The monitored node is joint 50 in UX direction, corresponding to the center of masses of the last story.
- Analysis type: Static Nonlinear.
- Initial conditions: Static nonlinear analysis which assess the effects of the dead loads on the structural elements.
- Load pattern: Pushover X modal and Pushover X uniform. (Horizontal concentrated loads). Analysis run separately.
- According to the EUROCODE, the analysis is run once the base shear reaches 80% of maximum force.

Finally, the capacity curve is obtained from SAP2000. Figure 60 illustrates the real performance of the structure in MDOF. In addition, it can be seen the excellent ductility performance of the structure; there is not any important brittle failure on beams and columns, and the displacement goes until the base shear is equal to  $0.85F_{max}$  to calculate the bilinear equivalent curve according to the EC8.

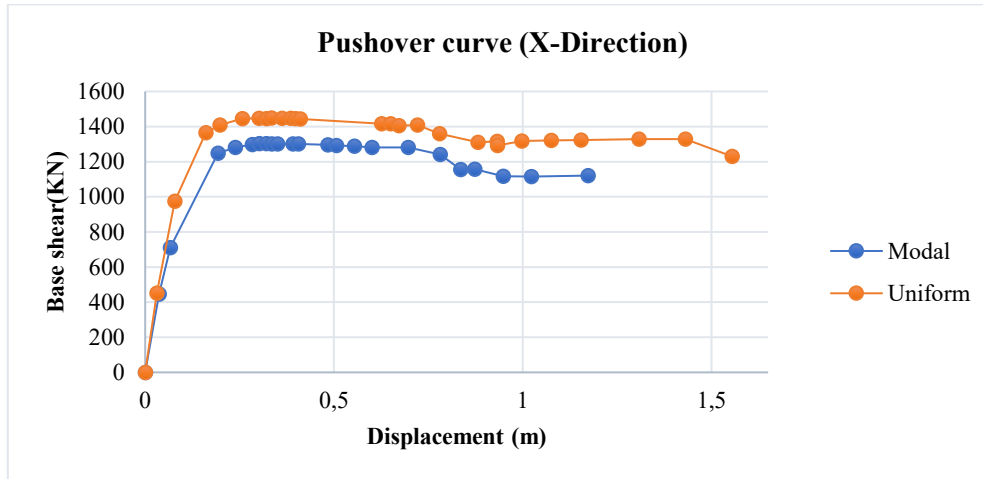


Figure 60. Pushover Curves obtained from SAP2000 in MDOF.

The equivalent bilinear curve is assessed following the NTC 18 and EC8 [6]. The approach is based on elastic energy equivalence; therefore, the arcs from Figure 60 and the bilinear shape must have the same area under the curve. For this purpose, a code in MATLAB has been created. Besides, the bilinear shape is used to describe in a simple shape the capacity curve obtained from SAP2000 and to the safety factors calculation. Figure 61 illustrates the definition of the equivalent bilinear curve, while Table 23 and Table 24 show the results regarding the stiffness, base shear strength, displacements, and energy.

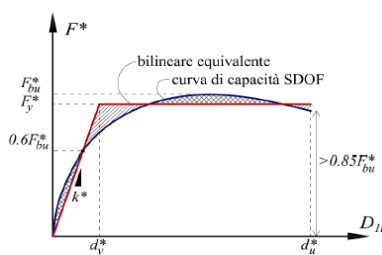


Figure 61. Definition of the equivalent bilinear curve[26]

Modal		Rectangular	
d	F	d	F
m	KN	m	KN
0,00	0,00	0,00	0,00
0,13	1214,75	0,11	1368,63
1,17	1214,75	1,55	1368,63

Table 23. Bilinear curve (MDOF).

	Modal	Uniform	
<b>0.6F_max</b>	782,392	868,943	KN
<b>d_y</b>	0,083	0,069	m
<b>K*</b>	9373,08	12625,71	KN/m
<b>dy*</b>	0,1296	0,1084	m
<b>Fy*</b>	1214,75	1368,63	KN
<b>du</b>	1,17	1,55	m
<b>E</b>	1,35E+03	2,05E+03	KN m

Table 24. Output - Bilinear capacity curve (MDOF)

Figure 62 compare the bilinear capacity curve and the capacity curve obtained from SAP2000.

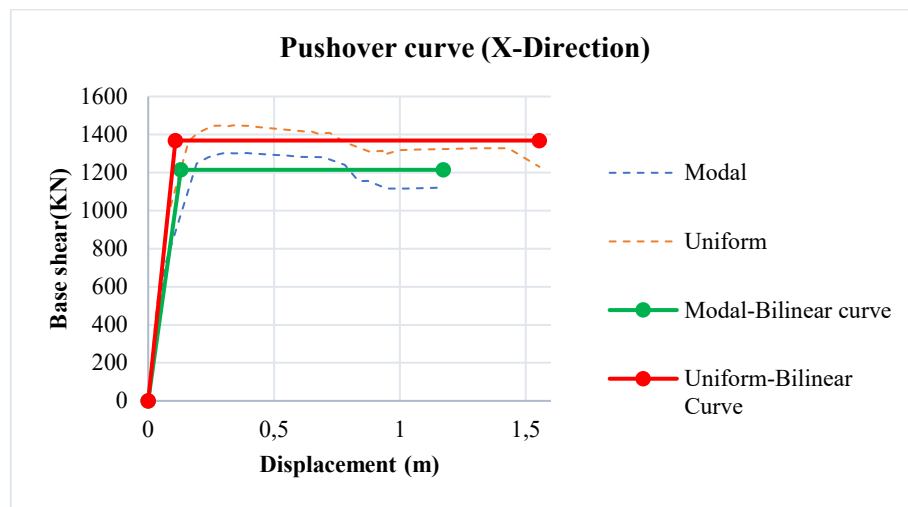


Figure 62. MDOF Pushover Curve vs Bilinear Pushover Curve.

### 5.2.5 SDOF-Bilinear Equivalent Curve

The bilinear equivalent curves in SDOF are required to execute the safety evaluation of the building. They are obtained from the MDOF system by dividing the displacement and base shear force by the participation factor ( $\Gamma$ ):

$$F^* = \frac{F}{\Gamma} ; d^* = \frac{d}{\Gamma} \quad (29)$$

Where:

- F and d: base shear force and displacement from the MDOF.
- F\* and d\*: base shear force and displacement from the SDOF.

Table 25 summarizes the calculations regarding the base shear strength and displacement in MDOF and SDOF.

Modal Pushover (MDOFS)		Modal Pushover (SDOFS)	
Top displacement	Base reaction	Top displacement	Base reaction
(m)	KN	(m)	KN
0,00	0,00	0	0
0,13	1214,75	0,102	959,23
0,21	1214,75	0,169	959,23
Uniform Pushover (MDOFS)		Uniform Pushover (SDOFS)	
Top displacement	Base reaction	Top displacement	Base reaction
(m)	KN	(m)	KN
0,00	0,00	0,000	0,00
0,11	1368,63	0,086	1080,73
0,18	1368,63	0,145	1080,73
$\Gamma x$	1,266		

Table 25. MDOF capacity curve to SDOF capacity curve for the pre-retrofit structure

Figure 63 illustrates the bilinear capacity curve transformation from the MDOFS to the SDOFS:

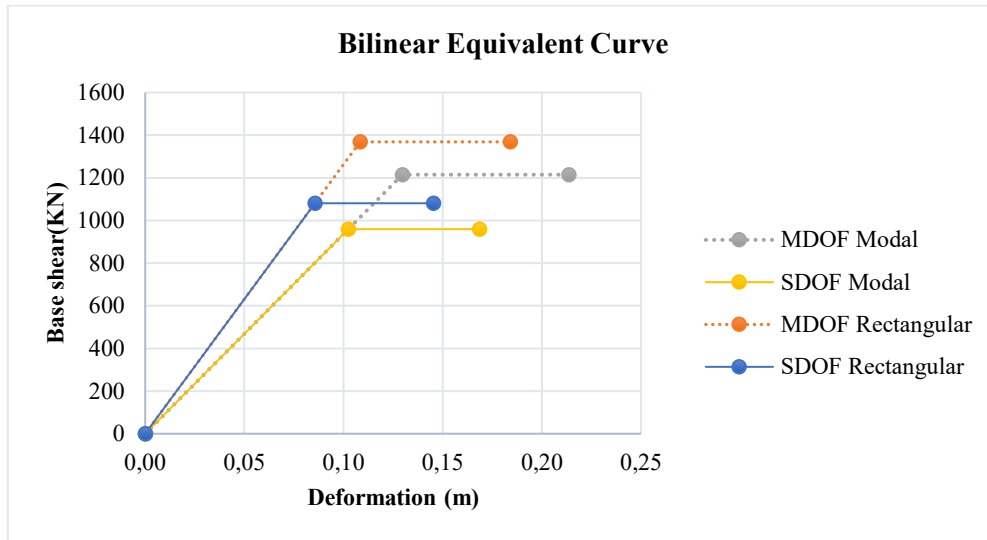


Figure 63. Bilinear capacity curve (MDOF-SDOF)

The effective stiffness ( $K^*$ ) obtained from the capacity curve as the ratio between the base shear and the last story displacement represents the structure's overall stiffness in a simple coefficient. In addition, the ultimate displacement ( $du'$ ) is 150% of the target displacement, following the Eurocode. Table 26 shows the ultimate and yielding displacement, yielding force and effective stiffness of the capacity curves for modal and uniform cases in SDOF:

Modal	$du'$ (m)	$F_y^*$ (KN)	$dy^*$ (m)	$K^*$ (KN/m)
X(+)	0,169	959,23	0,102	9373,08
Uniform	$du'$ (m)	$F_y^*$ (KN)	$dy^*$ (m)	$K^*$ (KN/m)
X(+)	0,145	1080,73	0,086	12625,71

Table 26. Effective stiffness from bare frame.

Where:

- $K^* = \frac{F_y^*}{d_y^*} \rightarrow$  Effective stiffness.
- $F_y^* \rightarrow$  Yielding base share from the SDOF.
- $d_y^* \rightarrow$  Yielding displacement from the SDOF.
- $du' \rightarrow$  Ultimate displacement equal to 1.5 times the displacement of the performance point from the ADRS (Figure 64 and 65).

#### 5.2.6 Seismic Demand Linked to The Effective Period:

The seismic demand associated with the elastic response spectrum at ultimate limit state is required to make the safety evaluation of the structural performance. Therefore, for each distribution of load (modal and uniform) is calculated the effective stiffness ( $K^*$ ) from the bilinear capacity curve (SDOF), to calculate the effective period associated with the elastic



stage ( $T^*$ ). In addition, it is calculated the elastic displacement related to the effective period ( $Sde(T^*)$ ) to compare it with the maximum displacement capacity of the system. Figure 27 list the equations of the  $K^*$ ,  $T^*$  and  $Sde(T^*)$ .

Effective period ( $T^*$ ):	Elastic Shear demand from the response spectrum ( $F_E^*$ ):
$T^* = 2 * \pi * \sqrt{\frac{m^*}{k^*}} \quad (30)$	$F_E^* = Sae(T^*) * 9.81 \frac{m}{s} * m^* \quad (31)$
Elastic displacement demand from the response spectrum $Sde(T^*)$ :	
$Sde(\omega^*) = Sae(T^*) * \frac{9.81 \frac{m}{s^2}}{\omega^{*2}} \quad (32)$	

Table 27. Effective period, elastic base shear and displacement demand from response spectrum. [26]

Where:

- $K^* = \frac{F_y^*}{d_y^*} \rightarrow$  Effective stiffness.
- $m^* \rightarrow$  Equivalent mass from Equation 27 and Table 22.
- $Sae(T^*)$ : Elastic acceleration associated with the effective period at ULS.
- $\omega^* \rightarrow$  Effective frequency (rad/s).

The results from the response spectrum demand are summarized in Table 28:

Modal	mx*(TON)	T*(s)	Tc*(s)	Sae(g)	SDe(m)	FE (KN)
X(+)	235,77	1,00	0,5	0,45	0,111	1043,51
Uniform	mx*(TON)	T*(s)	Tc*(s)	Sae(g)	SDe(m)	FE (KN)
X(+)	235,77	0,86	0,5	0,52	0,096	1211,10

Table 28. Response spectrum demand for the pre-retrofit structure.

### 5.2.7 Safety Checks

The safeness verification is executed by comparing the demand and the capacity in terms of displacement. If the capacity is greater than the demand, the structure can withstand the seismic design demand through the linear or nonlinear structural performance. In addition, the ductility is verified with the acceleration response spectrum (ADRS) using the elastic and inelastic response spectrum.

#### 5.2.7.1 Ductility Evaluation:

According to the NTC18 and EC8, to verify the structure's safety, the ductility capacity must be greater than the ductility demand ( $\mu_c \geq \mu_d$ ). To assess the ductility demand, the relations between the reduction factor ( $q$ ), ductility ( $\mu$ ), and period ( $T$ ) are evaluated to calculate the inelastic response spectrum with constant ductility following the N2-A Method from NTC18 [27]. Table 29 shows the sequence of calculations for the relationship  $q - \mu - T$ :

1. The reduction factor is defined as: $q^* = \frac{F_E^*}{F_y^*} \quad (33)$	2. The ductility capacity is defined as: $\mu_c = \frac{d_y^*}{d_u^*} \quad (34)$
3. The demand is calculated by means of the following relationship: $\mu_d = q^* ; (T^* \geq T_c) \quad (35)$ $\mu_d = (q^* - 1) * \frac{T_c}{T} + 1 ; (T^* < T_c) \quad (36)$	

Table 29. Relation between the reduction factor, ductility, and period ( $q - \mu - T$ ). [26].

Where:

- $\mu_c$ : Ductility capacity.
- $\mu_d$ : Ductility demand.
- $q^*$ : Reduction factor.
- $F_E^*$ : Base shear demand from the elastic response spectrum at ULS.
- $F_y^*$ : Yielding shear capacity from the SDOFs.
- $T^*$ : Equivalent fundamental period.
- $T_c$ : Period from response spectrum.
- $d_y^*$ : Yielding displacement of the bilinear model.
- $d_u^*$ : Ultimate displacement equal to 1.5 times the displacement of the performance point from the ADRS (Figure 64 and 65). The value is reported in Table 25 and 26.

Table 30 shows that the improvement of ductility is not required; the ductility demand ( $\mu_d$ ) is lower than the ductility capacity ( $\mu_c$ ) in both cases.

Modal	$q^*$	$\mu_d$	$\mu_c$
X(+)	1,09	1,09	1,65
Uniform	$q^*$	$\mu_d$	$\mu_c$
X(+)	1,12	1,12	1,70

Table 30. Reduction factor, ductility demand and ductility capacity.

#### 5.2.7.2 Acceleration-Displacement Response Spectrum (ADRS):

The method aims to verify the results from the ductility evaluation with a visual evaluation of the intersection between the inelastic spectrum and the bilinear equivalent curve. The intersection is known as performance point (PP), and the components must match with the demand  $S_{ai}$  and  $S_{Di}$ . Figure 64 illustrates the elastic spectrum, the inelastic spectrum with the required ductility demand, and the capacity curve (SDOF) obtained from the nonlinear pushover analysis. Table 31 lists the equations to obtain the elastic and inelastic ADRS[26]:

Elastic Displacement Response Spectrum	Inelastic ADRS
$Sd_e = Sa_e * \frac{1}{\omega^2} = \frac{T^2}{4\pi^2} Sa_e \quad (37)$	$Sa_i = Sa_e * \frac{1}{q^*(\mu_d, T)} ; Sd_i = Sd_e * \frac{\mu_d}{q^*(\mu_d, T)} \quad (38)$

Table 31. Response spectrum equations (ADRS)

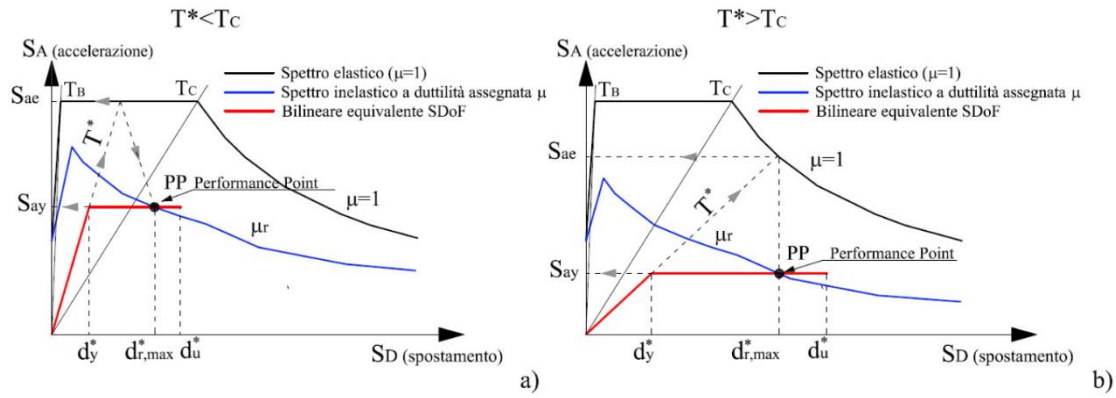


Figure 64. Verification procedure with ADRS: a)  $T^* < T_c$ ; b)  $T^* > T_c$ . [26].

Figure 65 and Figure 66 verify the results of the Table 28. The modal and uniform case exerts inelastic response for an effective period higher than  $T_c$ . In addition, the performance point for both cases is reported, the average value is used in the design of the fluid viscous damper and the yielding hysteretic dampers as the roof displacement in SDOF. It is done to have equal input parameters to compare later the strategies according to the results of each one.

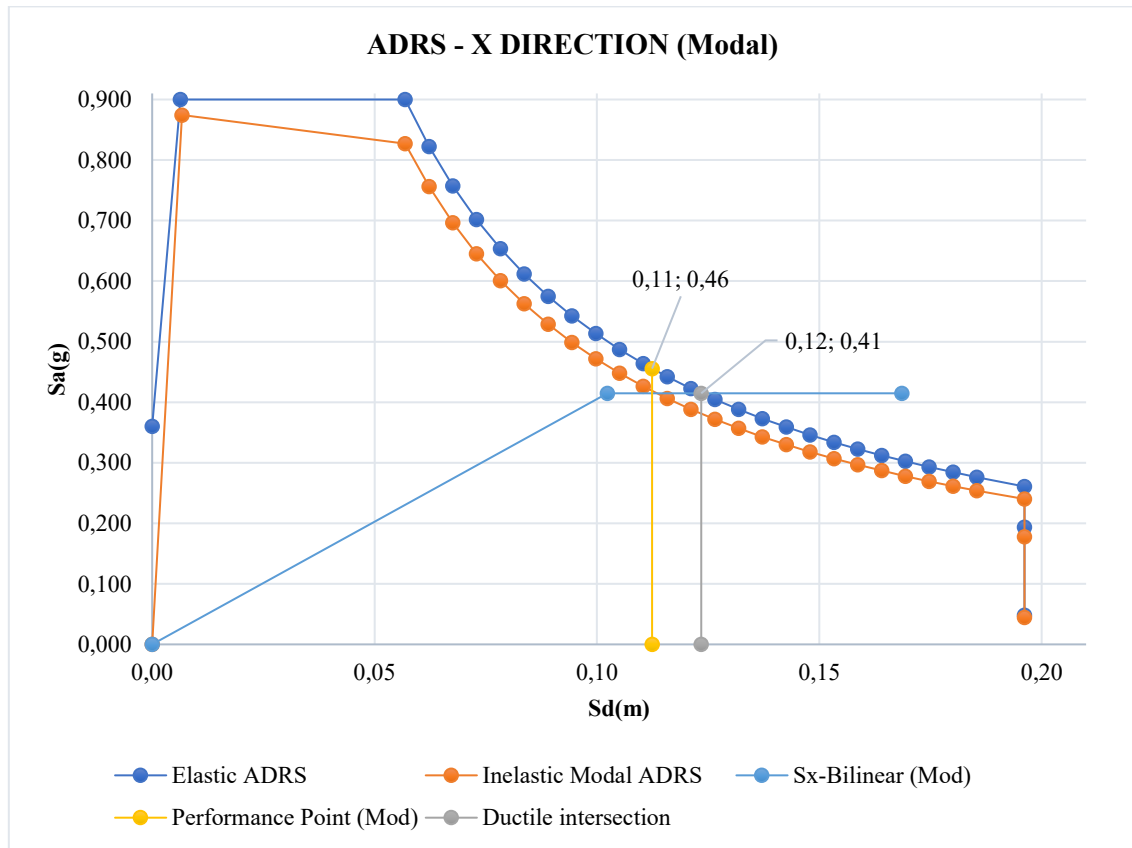


Figure 65. ADRS-Ductility Verification: Modal Case - Pre-retrofit structure.

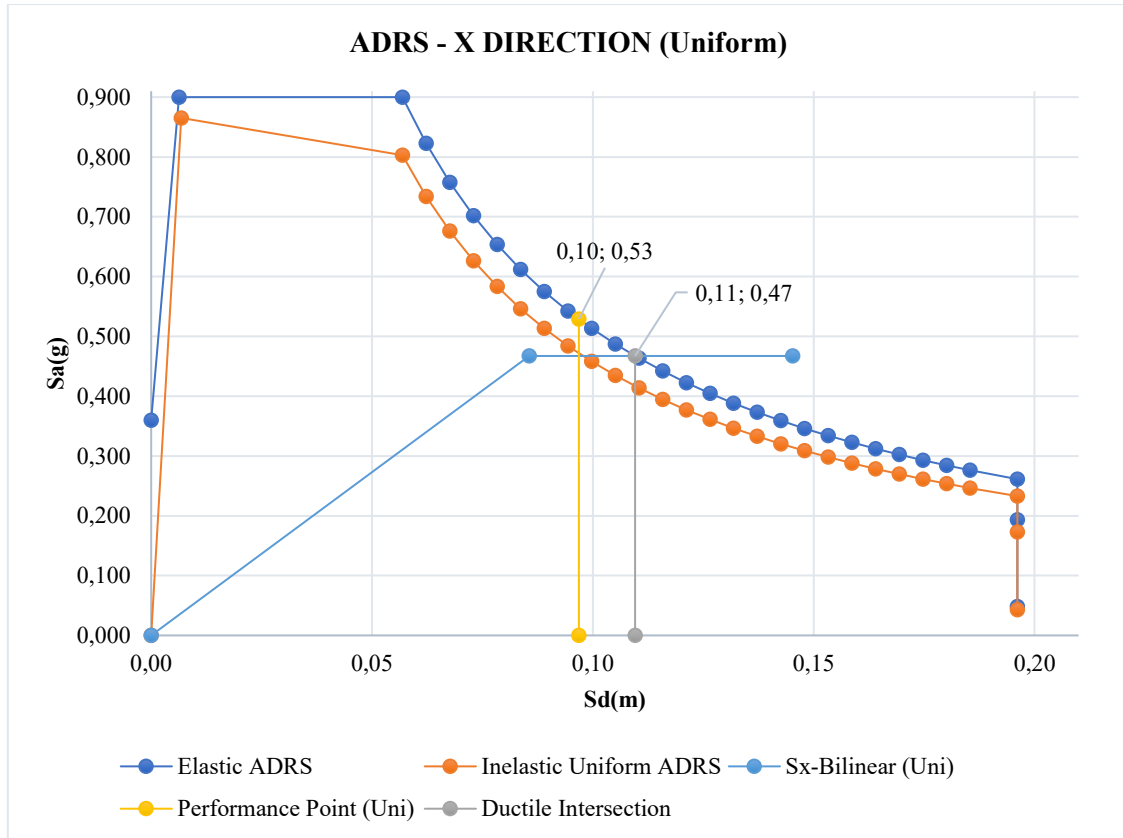


Figure 66. ADRS-Ductility Verification: Uniform Case – Pre-retrofit structure.

According to the safety verification, the following annotations can be done:

- The design and construction of the structure following the EC8 requirements provide excellent structural performance beyond the seismic design demand. According to Negro (1994), the structure was designed for a serviceability limit state with a behavior factor equal to 5. However, it is demonstrated that the structure can withstand seismic demand for a safe-life limit state with a constant ductility equal to 1,09 and 1,12.
- The performance point for the modal and uniform case in Figure 65 and Figure 66 complies with the seismic demand linked to the effective period reported in Table 28.
- The structure does not require a stiffening or weakening intervention due to a lack of seismic performance concerning the specific seismic demand.
- The structure has the ideal seismic performance to apply the dissipative devices due to its ductility capacity. As a result, the columns and beams can withstand without partial or total collapse for the specific seismic design demand.

### 5.3 Nonlinear Time-history Analysis

The analysis is executed on SAP2000, setting the kinematical constraints to move in the X-X coordinates solely. The Plane Frame setup establishes the condition required by allowing the displacement in the X and the Z direction and the rotation in the Y direction. In the other hand, the time functions used to execute the analysis are the seven accelerograms mentioned in Chapter 3. The Hilber-Hughes-Taylor algorithm (HHT) is the nonlinear direct integration

method applied to obtain structural response under dynamic loading. It is an implicit method from Newmark Algorithms Family that improves the rate of convergence without affecting the accuracy of results [23].

The load case is run with the following input data:

- Initial conditions: Continue analysis from state at end of static nonlinear analysis.
- Geometric parameters: None
- Stiffness-Proportional damping of stiff elements produced on nonlinear objects is considered in the analysis. The coefficients are computed automatically by the software in function of 2 different periods.
- Nonlinear behavior is capture by the strain-stress model of the materials and cross sections. As well as the nonlinear link properties.
- Time integration: Parameter alpha ( $\alpha$ ) set as -0.33.

Figure 67 shows the configuration of the time-history analysis using the accelerogram two. In addition, the number of Output Time Steps vary according to the duration of each input time function, while the Output Time Step Size is set as 0.04 for all cases.

The screenshot displays the 'Load Case' configuration window in SAP2000. The 'Load Case Name' is 'TH2'. Under 'Initial Conditions', the 'Continue from State at End of Nonlinear Case' option is selected. The 'Analysis Type' is 'Nonlinear' and the 'Solution Type' is 'Direct Integration'. The 'Geometric Nonlinearity Parameters' are set to 'None'. The 'History Type' is 'Transient'. The 'Mass Source' is 'MSSSRC1'. The 'Time Step Data' section shows 'Number of Output Time Steps' as 1206 and 'Output Time Step Size' as 0.04. The 'Other Parameters' section includes 'Damping' (Proportional), 'Time Integration' (Hilber-Hughes-Taylor), and 'Nonlinear Parameters' (User Defined). The 'Loads Applied' table shows a single load with 'Load Type' 'Accel', 'Load Name' 'U1', 'Function' 'TH 2', and 'Scale Factor' '1'.

Load Type	Load Name	Function	Scale Factor
Accel	U1	TH 2	1

Figure 67. Configuration of the time-history analysis on SAP2000– Pre-retrofit Building

Figure 68 to Figure 71 show the relation, in absolute value, between the base shear and the displacement of the 4-story taking as reference joint the center of the masses of the last floor. It is done to know the effects of the different seismic actions acting on the structure. In addition,

to verify the reliability of the results Figures 13-16 must match with the bilinear capacity curve in MDOF previously obtained.

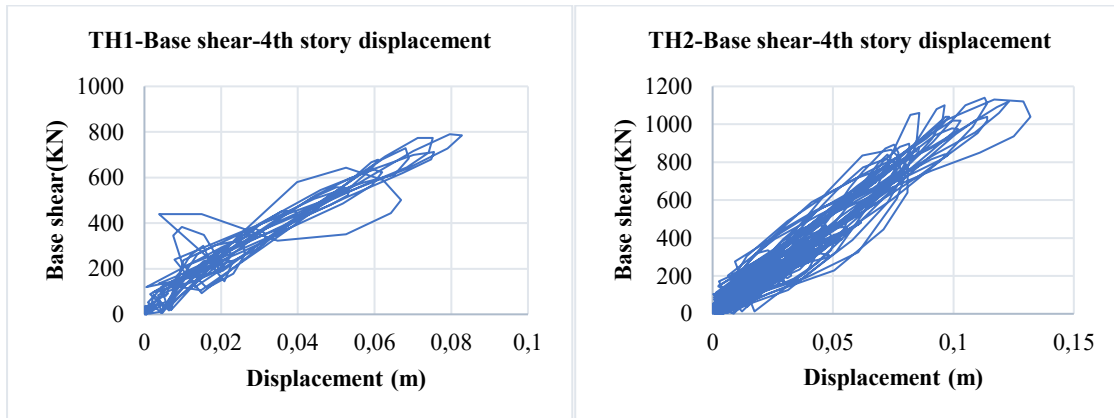


Figure 68. Base shear-4th Story Displacement for TH1 and TH2– Pre-retrofit Building

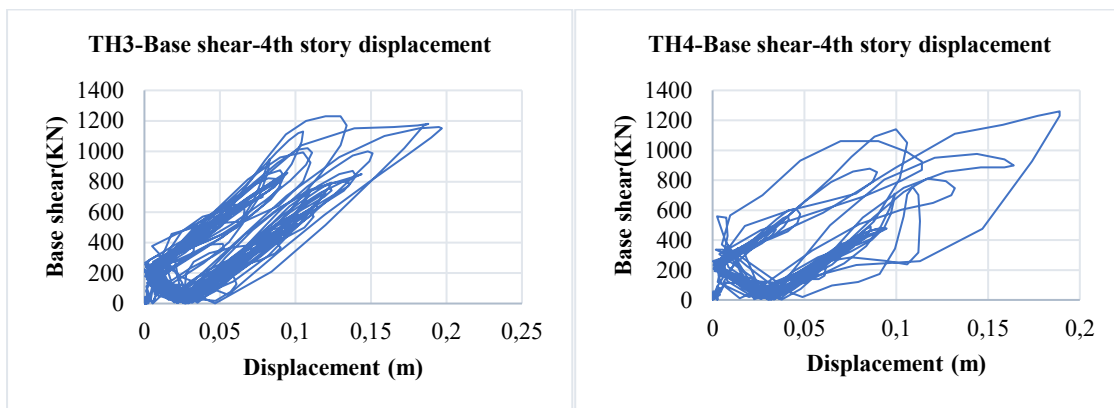


Figure 69. Base shear-4th Story Displacement for TH3 and TH4– Pre-retrofit Building

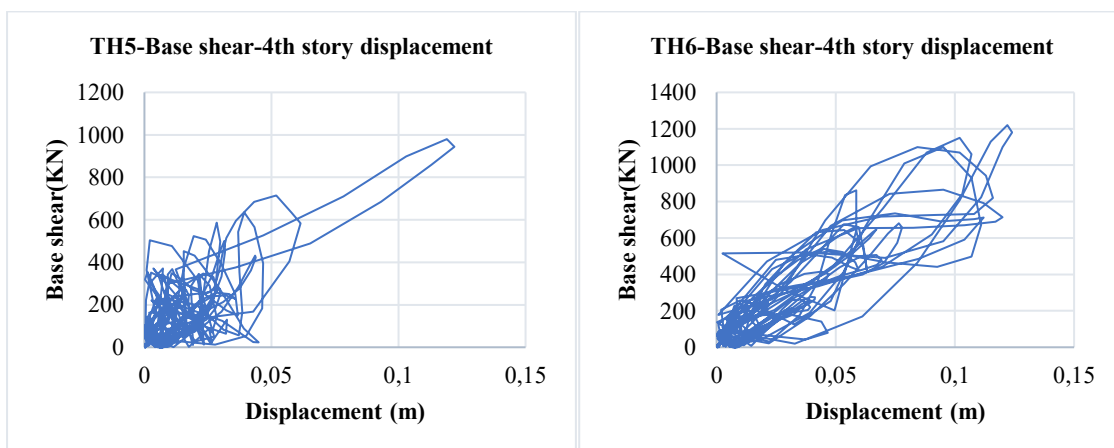


Figure 70. Base shear-4th Story Displacement for TH5 and TH6– Pre-retrofit Building

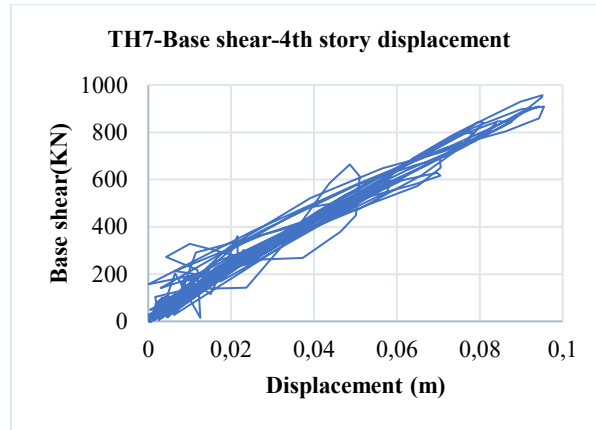


Figure 71. Base shear-4th Story Displacement for TH7– Pre-retrofit Building

Figure 72 plot the Figure 68 to Figure 71 in the same chart of the equivalent bilinear capacity curve from Figure 63 in MDOF. It is done to check the congruence between the dynamic response of the structure from time-history analysis and the simplified dynamic response of the structure obtained by the static pushover analysis. As expected, the curves are inside the domain of the equivalent bilinear capacity curve in MDOF. According to the figure, TH3 and TH4 are the most critical cases where the structure undergoes nonlinear behavior in some structural elements. In addition, Table 32 reports the average maximum demand, which considers only the maximum base shear and roof displacement of the time-history analyses.

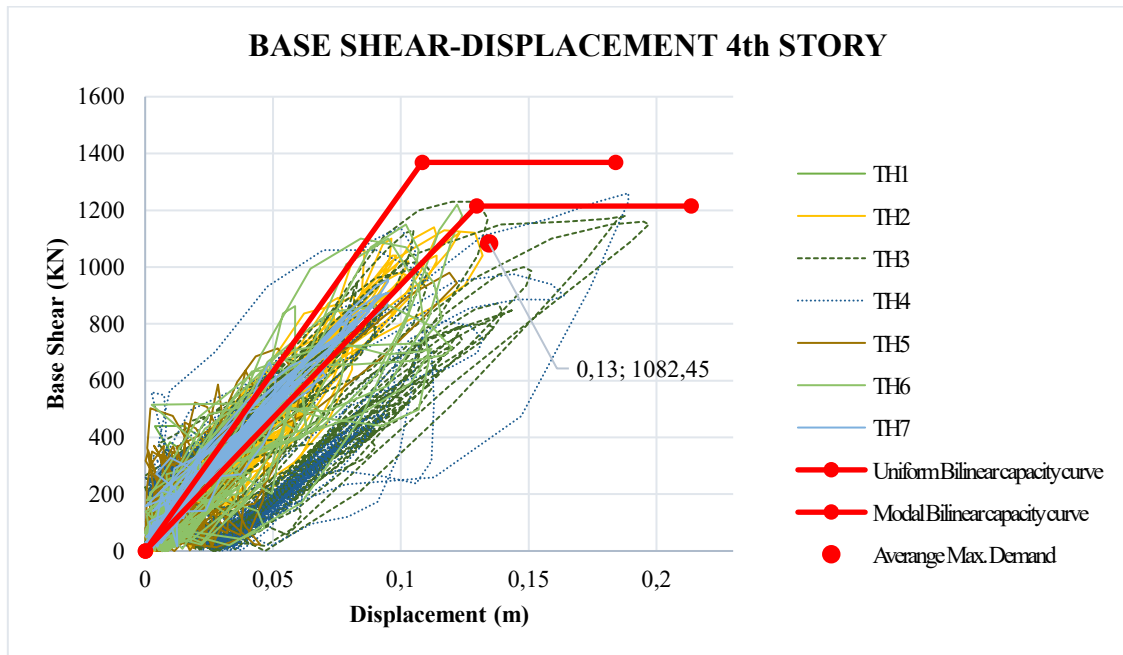


Figure 72. Bilinear Capacity Curve and TH results – Pre-retrofit Building

TH	1	2	3	4	5	6	7	Average
d(m)	0,083	0,132	0,197	0,189	0,122	0,124	0,096	0,135
F(KN)	790	1140	1230	1260	980	1220	957	1082,45

Table 32. Pre-Retrofit- Time-history maximum displacement and maximum base shear.

In addition, Figure 73 plot in the acceleration-displacement plane the Figure 72, with the addition of the ADRS with 5% of damping. As it can be seen, the TH3 and TH4 exerts a ductility demand larger than the evaluated in Figure 65 and Figure 66.

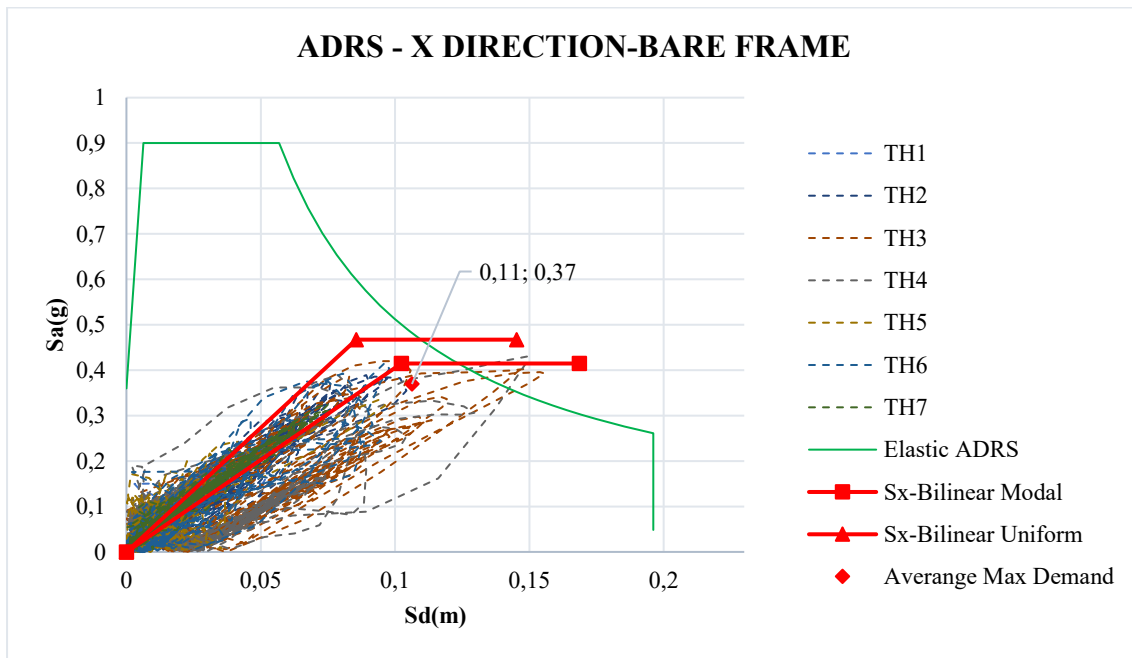


Figure 73. ADRS with 5% of damping, equivalent bilinear capacity curves and response of the time-history analyses.

Finally, Figure 75 and Figure 75 illustrate the structure's shape for the maximum interstory drift produced on the time-history analysis for the seventh accelerograms acting on the pre-retrofit structure; the time-history TH3 and TH4 are the most critical cases, where the maximum interstory drift is equal to 0.5% in the 1st floor and 0.49% in the 2nd floor, respectively. Additionally, there is no steady shape at the maximum interstory drift considering all the cases in the structure. Regarding the average shape, the maximum interstory drift is equal to 0.34% and is produced on the 2nd floor.

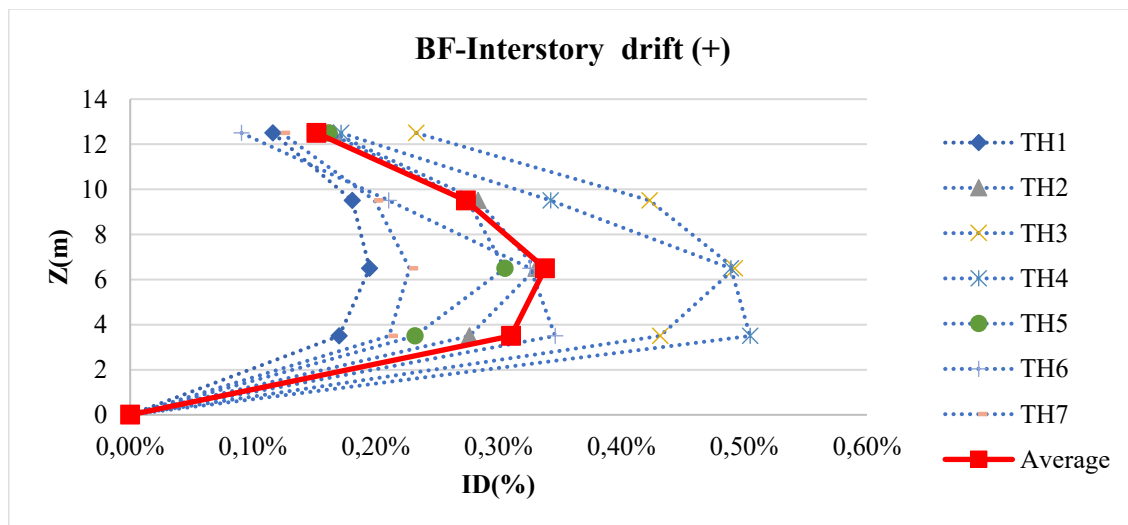


Figure 74. Maximum interstory displacement of time-history analysis - Positive direction, pre-retrofit structure.



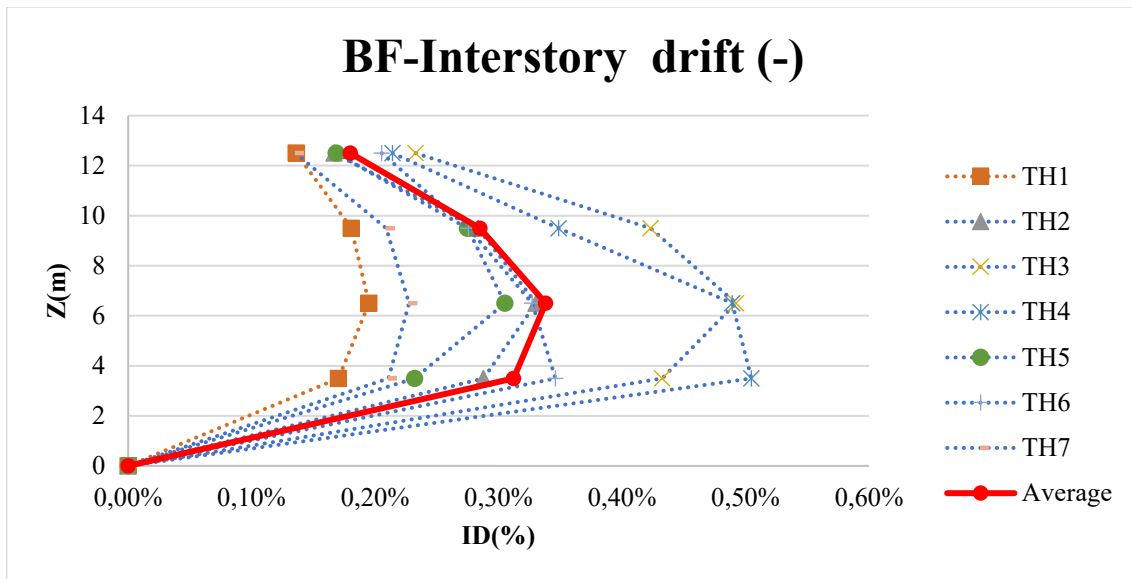


Figure 75. Maximum interstory displacement of time-history analysis - Negative direction, pre-retrofit structure

# Chapter 6

## 6 Retrofitting of the Structure

As discussed in Chapter 5, the bare frame does not require an intervention to comply with the seismic design demand at the ultimate limit state (SLV). However, the structure suffers damage represented by permanent deformation, as shown in Figure 65 and Figure 66. This phenomenon is verified once the seven nonlinear time-history analyses are executed individually, obtaining for the accelerogram 3 and 4, defined in Chapter 3, larger displacements than the yielding displacement of the capacity curves, as can be seen in Figure 73. For this reason, the goal of the retrofitting is reducing to elastic range the seismic response of the structure by the implementation of fluid viscous dampers and yielding metallic dampers (TADAS) to increase the serviceability life of the structure. In addition, the simplified design methodologies applied in this study require the elastic behavior of the structure during the seismic action once the devices are implemented.

To compare the performance of both control solutions by the vulnerability indexes is required to design them with the exact target damping ratio. For that reason, the seismic design demand is expected to decrease in equal proportion for both cases in the study, where the main difference would be the internal forces and displacements in the structural elements once the devices are placed.

### 6.1 Fluid Viscous Damper

The required damping is based on the equivalent capacity curve in SDOF obtained from nonlinear pushover analysis. The method N2-B from NTC 18 is applied, where the seismic demand is scaled in function of the equivalent hysteric damping, instead of the reduction factor ( $q$ ) or the ductility demand ( $\mu$ ). According to the NTC 18 and FEMA, the equivalent damping ratio provided exclusively by the frame is:

$$\xi_{eq} = \frac{2q(F_{by}^* d_{pp}^* - F_{pp}^* d_y^*)}{\pi * F_{pp}^* * d_{pp}^*} \quad (39)$$

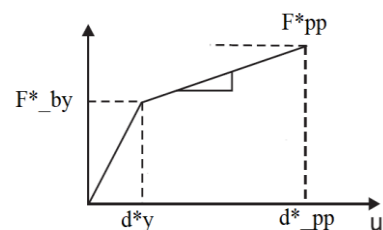


Figure 76. Bilinear capacity curve in SDOF.

Where:

- $F_{pp}^*$ : Performance point base shear.
- $d_{pp}^*$ : Performance point displacement.
- $F_y^*$ : Yielding shear capacity from the SDOFs.
- $d_y^*$ : Yielding displacement of the bilinear model.
- Efficiency factor ( $q$ ): Represent the dissipative capacity of the structure with respect to a perfect hysteresis loop [6].
  - High dissipative capacity:  $q=1.0$ .
  - Moderate dissipative capacity:  $q=0.66$ .
  - Low dissipative capacity:  $q=0.33$ .

The inelastic response spectrum curves from Chapter 5 are used to determine the performance point (PP) and verify the correct calculation of the hysteretic equivalent damping. The curves from Figure 65 and Figure 66 match for a efficiency factor equal to 0.33, checking the low dissipative capacity of the structure and the reliability of the results. However, the goal is to reduce the design seismic demand towards obtain an elastic performance of the structure, therefore, instead of considering the low dissipative capacity, the target damping is computed assuming the high dissipative capacity provided by the dissipative devices. Table 33 list the results, it has been defined a target damping ratio around 20%.

	<b>Modal</b>	<b>Uniform</b>	<b>Average</b>
$d_y^*$	0,102	0,086	0,094
$F_{by}^*$	959,23	1080,73	1019,979
$d_{pp}^*$	0,145	0,125	0,136
$F_{pp}^*$	959,225	1080,733	1019,979
K	1,00	1,00	1,00
$\xi_{eq}$	18,6%	20,0%	19,7%

Table 33. Required damping.

#### 6.1.1 Mounting Arrangement and Damper Configuration:

The damper distribution is defined following the recommendations from the Design Manual of Taylor Devices [11] and FEMA356 [7]:

- The devices are connected to a diagonal bracing system placed along the perimeter in X direction.
- The devices are placed in all the floors and satisfy the redundancy requirements.
- There must be continuity of the connections from the upper floor to the ground level.

Figure 77 shows the mounting arrangement of the bracing system where are placed the dissipative devices. In total, 16 fluid viscous dampers are placed in the building.

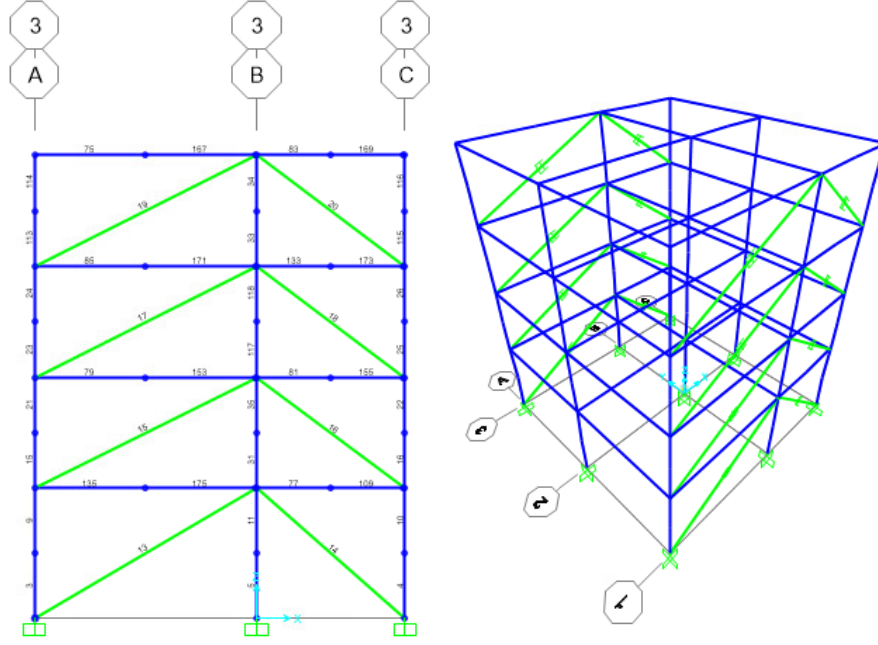


Figure 77. Mounting arrangement of fluid viscous dampers.

### 6.1.2 Strain Energy-Based Method

According to Constantinou and Symans (1992), using the natural periods and modal shapes of the pre-retrofit structure combined with the strain energy-based method provides an excellent evaluation of the equivalent damping ratio of the retrofitted structure with dissipative devices [28]. The assumptions are the unchangingness of the natural frequencies and mode shapes regarding the addition of damping [6].

The energy-based strain method relates the work done by all the linear viscous devices and the maximum strain energy in the building[28]. Therefore, the damping ratio is obtained by the damper contribution ( $W_D$ ) and the story shear effect on the building ( $W_S$ ). As well know, the stories have different masses, eigenvector components, and damper configurations. These conditions should be considered to determine a correct approach to solve the problem. In this case, four frames of four stories are introduced into the model, assessing a total of 16 components representing the overall dissipation system. According to the method, the damping ratio is expressed as (Chopra,1995):

$$\zeta_k = \frac{W_D}{4 * \pi * W_S} ; \zeta = \frac{\sum W_D}{4\pi \sum W_S} \quad (40)$$

Where:

- $\zeta$ : Viscous damping ratio in mode m.
- $W_D$ : Energy dissipated in each single cycle of motion or work done by viscous devices (1 complete cycle)
- $W_S$ : Maximum strain energy or the maximum kinetic energy at each floor level.

As discussed in Chapter 2, the energy dissipation of the fluid viscous dampers depends on the linear or nonlinear relation between the force and the velocity. This characteristic is important because it permits the calculation of lower damping force for a desirable dissipation of energy, representing an optimization criterion in the damper selection through the damping exponent ( $\alpha$ ). To sum up, the nonlinear damper represents the best decision in economic terms. The dissipation effect of a linear damper and a nonlinear damper designed for an equal target viscous damping must be the same, and the only difference would be the design damping force to select the commercial device placed into the bracing system. For this reason, the fluid viscous damper is modeled on SAP2000 using the nonlinear approach. Furthermore, the damping is calculated considering both cases to verify the reliability of the results.

According to Constantinou, assuming harmonic vibration in the structure following the undamped mode shape and overall elastic performance of the building, the maximum strain energy ( $W_s$ ) and the energy dissipated by the dampers ( $W_D$ ) can be expressed as [28]:

$$W_s = \frac{2\pi^2}{T_n^2} \sum_i \left( \frac{w_i}{g} \right) D_{roof}^2 \phi_{i1}^2 \quad (41)$$

$$W_D = \sum_j \left( \frac{2\pi}{T_n} \right)^\alpha C_{Nj} \lambda_j (D_{roof} f_j \phi_{rj})^{1+\alpha_j} \quad (42)$$

Obtaining a damping ratio ( $\zeta$ ) equal to:

$$\zeta = \frac{\sum W_D}{4\pi \sum W_s} = \frac{\sum_j (2\pi)^{\alpha_j} \cdot T_1^{2-\alpha} \cdot \lambda_j C_j f_j^{1+\alpha_j} D_{roof}^{\alpha_j-1} \phi_{rj}^{1+\alpha_j}}{8\pi^3 \sum_i \left( \frac{w_i}{g} \right) \phi_{i1}^2} \quad (43)$$

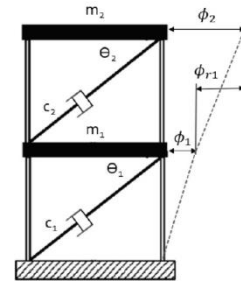


Figure 78. Scheme of the model[6]

Where:

- $\phi_{rj}$ : Device relative displacement (Interstory displacement).
- $\phi_i$ : Story displacement.
- $\theta_j$ : Inclination angle of jth device.
- $f_j$ : Amplification factor due to bracing system configuration.
- $T_1$ : 1<sup>st</sup> natural Building's period.
- $W_i$ : ith lumped weight of the structure
- $\alpha$ : Damping exponent. ( $\alpha = 1 \rightarrow$  Linear Damping.  $\alpha < 1 \rightarrow$  Nonlinear damping).
- $\lambda$ : Lambda parameter ( $\lambda = \pi$  for  $\alpha = 1$  ;  $\lambda = 3,496$  for  $\alpha = 0.5$ ) [28]

- $C_j$ : Damping coefficient of jth device ( $C_L \rightarrow$  Linear Damping,  $\alpha = 1 \rightarrow [F] \left[ \frac{s}{m} \right]$ .  $C_{NL} \rightarrow$  Nonlinear damping,  $\alpha = 0.5 \rightarrow [F] \left[ \frac{s}{m} \right]^{0.5}$ )
- $D_{roof}$ : Roof displacement.

In the linear damping case, the equation can be simplified as[6]:

$$\zeta = \frac{W_k}{4\pi * L_k} = \frac{\pi \omega_k \sum C_j' \cos^2 \theta_j * \phi_{rj}^2}{4\pi * \left( \frac{1}{2} * \{\Phi\}^T * [K] * \{\Phi\} \right)} = \frac{1}{2} * \frac{\omega_k \sum C_j \cos^2 \theta_j * \phi_{rj}^2}{\omega_k^2 * \sum (m_i * \phi_i^2)} \quad (44)$$

$$\zeta = \frac{1}{2} * \frac{\sum C_j \cos^2 \theta_j * \phi_{rj}^2}{\omega_k * \sum (m_i * \phi_i^2)} \quad (45)$$

Where:

- $\omega_k$ : angular frequency of k mode. (In this case is the 1<sup>st</sup> mode).
- $\cos \theta_j$ : Represent the amplification factor for the bracing configuration.

Table 34 lists all the information regarding the damper configuration based on Figure 77: the shape mode of the 1st mode, the mass supposed on each frame, and the inclination of the bracing system.

	Floor	Z(m)	Uxi(m)	UxiN(m)	UxNR(m)	Mass (Ton)	$\theta_j(^{\circ})$
Frame 1-A-B	4	12,5	0,158	1,00	0,142	21	26,565
	3	9,5	0,136	0,858	0,252	42	26,565
	2	6,5	0,096	0,606	0,295	64	26,565
	1	3,5	0,049	0,310	0,311	85	30,256
Frame 1-B-C	4	12,5	0,158	1,000	0,142	21	36,870
	3	9,5	0,136	0,858	0,252	42	36,870
	2	6,5	0,096	0,606	0,295	64	36,870
	1	3,5	0,049	0,311	0,311	85	41,186
Frame 3-A-B	4	12,5	0,158	1,000	0,142	21	36,870
	3	9,5	0,136	0,858	0,252	42	36,870
	2	6,5	0,096	0,606	0,295	64	36,870
	1	3,5	0,049	0,311	0,311	85	41,186
Frame 3-B-C	4	12,5	0,158	1,000	0,142	21	26,565
	3	9,5	0,136	0,858	0,252	42	26,565
	2	6,5	0,096	0,606	0,295	64	26,565
	1	3,5	0,049	0,311	0,311	85	30,256

Table 34. Damper distribution on story, eigenvector, mass, and inclination of devices.

As mentioned before, the damping ratio must be equal for all approaches because the same dissipation is expected. Therefore, the data from Table 33 is used for linear as well as nonlinear damping. Table 35 to Table 37 summarize the input to the Equations (41-45) and the theoretical damping ratio obtained from the effect of the fluid viscous dampers:

Linear damper Simplified equation	
CL (KN s/m)	308,0
$\sum C_j \cos^2 \theta_j \phi_{rj}^2$	229,61
$\sum (m_i \phi_i^2)$	52,76
T (sec)	0,58
$\omega$ (rad/s)	10,83
$\zeta$	20,1%

Table 35. Linear damper-Simplified equation.

Linear Damper Complete equation		
CL (KN s/m)	308	$\sum C_j (\cos \theta_j \phi_{rj})^{(1+\alpha)}$
$\alpha$	1	229,61
$\lambda$	3,14	$\sum (m_i \phi_i^2)$
T(sec)	0,58	52,76
$T^{(2-\alpha)}$	0,58	$\omega$ (rad/s)
$\eta$	1	10,83
$2\pi^{(3-\alpha)}$	39,48	$\zeta$
D_roof(m)	0,158	20,1%
$D_{\text{roof}}^{1-\alpha}$	1,00	

Table 36. Linear damper-Complete equation.

Nonlinear damper Complete equation		
CNL (KN (s/m) <sup>.5</sup> )	172,0	$\sum C_j (\cos \theta_j \phi_{rj})^{(1+\alpha)}$
$\alpha$	0,5	3,E+02
$\lambda$	3,50	$\sum (m_i \phi_i^2)$
T(sec)	0,58	52,76
$T^{(2-\alpha)}$	0,44	$\omega$ (rad/s)
$\eta$	1	10,83
$2\pi^{(3-\alpha)}$	98,96	$\zeta$
D_roof(m)	0,158	20,1%
$D_{\text{roof}}^{1-\alpha}$	0,40	

Table 37. Nonlinear damper-Complete equation

### 6.1.3 Selection of Damper

Once the target damping ratio from the N2-B method matches with the damping ratio calculated by the energy-based strain method, the design damping force is computed to define the commercial damping and obtain the information needed to run the FEM. The design damping force is calculated as:

$$F_d = C * \dot{u}^\alpha \quad (46)$$

Where:

- $F_d$ : Damping force.
- $C$ : Damping constant ( $C_L \rightarrow$  Linear damping,  $C_{NL} \rightarrow$  Non linear damping).

- $u$ : Displacement across the damper.
- $\dot{u}$ : Velocity across the damper.
- $\alpha$ : Damping exponent. ( $\alpha = 1 \rightarrow$  Linear Damping.  $\alpha < 1 \rightarrow$  Nonlinear damping).

According to the subsection 9.3.1.1 of FEMA 356, the velocity-dependent device shall be qualified to support the force associated with the velocity equal to 130% of the maximum calculated velocity for the device[7]. The velocity across the damper is supposed as pseudo-velocity and is calculated as:

$$V = 1.3 * \left( \frac{2\pi}{T} * d_{design} * \cos \theta \right) \quad (47)$$

Where:

- $d_{design}$ : Design roof displacement used in the energy-based strain method.
- $\cos \theta$ : Amplification factor due to the damper inclination.
- $T$ : Average effective period.

The dampers placed on the model are selected from the catalog of Taylor Devices Inc, where maxwell stiffness and the stroke tolerance are specified in function of the rated force. Table 38 summarizes the design forces for linear and nonlinear damping in International System and Imperial Units and Table 39 the damper catalog.

$\theta_j$	<b>d</b>	<b>T eff</b>	<b>V</b>	<b>CL</b>	<b>CNL</b>	<b>FL</b>	<b>FNL</b>	<b>FL</b>	<b>FNL</b>
°	<b>m</b>	<b>s</b>	<b>m/s</b>	<b>KN s/m</b>	<b>KN (s/m)<sup>0,5</sup></b>	<b>KN</b>	<b>KN</b>	<b>Kips</b>	<b>Kips</b>
26,56	0,141	0,93	1,24	308	172	383,3	191,9	86,2	43,1
30,26	0,136	0,93	1,20	308	172	370,2	188,6	83,2	42,4
36,87	0,126	0,93	1,11	308	172	342,8	181,5	77,1	40,8
41.19	0,119	0,93	1,05	308	172	322,5	176,0	72,5	39,6

Table 38. Damper design force.

<b>Taylor Devices Model Number</b>	<b>Rated Force (kip)</b>	<b>Stroke (in)</b>	<b>Maxwell Stiffness, Kd (kips/in)</b>
17120	55	±3	625
17130	110	±4	940

Table 39. Commercial dampers from Taylor Devices Inc.[11]

Finally, the product 17120 is selected to model the nonlinear damping on the retrofit intervention with fluid viscous dampers. The prototype provides a larger stroke than the damper's displacement and defines the maxwell stiffness required on the FEM model to execute the nonlinear time-history analysis.

#### 6.1.4 FEM Simulation on SAP2000

The fluid viscous dampers are simulated as Link Elements. According to the SAP2000 Manual, these objects are the most suitable for modeling nonlinear velocity-dependent devices. The



damper acts as a spring in series with a dashpot following the Maxwell model of viscoelasticity. The input parameters required are the stiffness, obtained from the catalog, and the damping coefficient and damping exponent, calculated previously[23].

The Damper Design Manual recommend set the nonlinear analysis to the translation on direction U1 (Globally X) , while the other DOFS remain free [11]. The input parameters are:

- Maxwell Stiffness ( $K_d$ ) equal to 109454.28 KN/m.
- Damping coefficient ( $C_{NL}$ ) equal to  $172 \text{ KN} \left(\frac{s}{m}\right)^{0.5}$
- Damping exponent ( $\alpha$ ) equal to 0.5.

Figure 79 shows the configuration on the software, and Figure 77 shows the 3D model:

Figure 79. Link Configuration: Fluid Viscous Dampers.

## 6.2 Metallic-Yielding Damper - TADAS

Mainly two methodologies have been used to design the metallic dampers. The first one is the methodology proposed by Ph. D. Chao Zhang from Guangzhou University, and the second one is the approach based on FEMA requirements of the Technical Report MCEER-00-0010 from the University of Buffalo.

According to Zhang, the metallic dampers are designed considering two seismic design demands: the ultimate limit state (SLV, NTC18) and the serviceability limit state (SLD, NTC18). These limits refer to the occurrence probability of the seismic event, where the lower probability of exceedance implies the most dangerous case. In addition, the approach is based on the following assumptions[20]:

- The analytical model is split into the pre-retrofit model and damper-braces system model.

- The metallic dampers add stiffness and damping. The first one during the serviceability limit state, while the second one during the ultimate limit state.
- The damper-brace system provides a significant increment in stiffness and damping.
- Seismic design of buildings assumes lumped mass matrix, rigid diaphragm, and classical damping theory.
- The unchangingness of the mode shapes despite the addition of damping and stiffness, while the natural frequencies are reduced.
- The damping force distributed according to the stiffness of the building.
- Harmonic vibration in the structure following the undamped mode shape and overall elastic performance of the building.
- The brace system remains in the elastic phase to let the concentration of displacements on metallic dampers.

The method uses the capacity curves from the pre-retrofit structure in SDOF obtained in Chapter 5 and the elastic response spectrum at SLD and ULS to calculate the required stiffness, the target damping ratio, and the damper's geometry. The overall procedure is described mainly in three parts:

1. The required initial stiffness of the metallic dampers can be estimated through displacement response spectrum at the serviceability limit state.
2. The required damping ratio provided by added metallic dampers can be estimated by the equivalent stiffness through acceleration response spectrum at the ultimate limit state.
3. Iterative procedure until the equivalent damping ratio from Strain-Energy Method approximates to the required damping ratio required by the seismic design demand.

#### 6.2.1 Mounting arrangement and damper configuration:

The damper distribution is defined following the recommendations from the Techno-Press Journals [20] and FEMA356 [7]:

- The devices are connected to a chevron bracing system placed along the perimeter in X direction.
- The devices are placed in all the floors and satisfy the redundancy requirements.
- There must be continuity of the connections from the upper floor to the ground level.

Figure 80 shows the mounting arrangement of the bracing system where are placed the dissipative devices. In total, 16 TADAS devices are placed in the building.

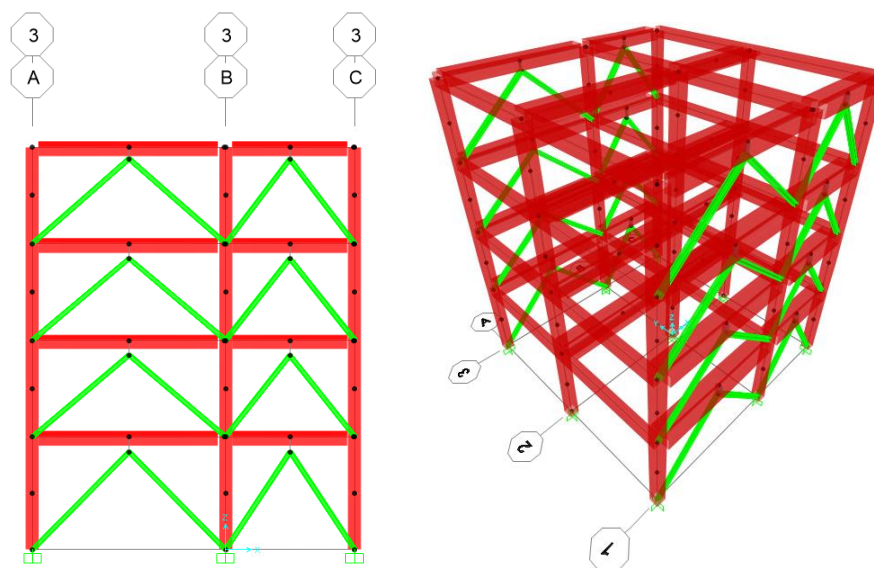


Figure 80. Mounting arrangement of brace system and TADAS devices.

### 6.2.2 Design Seismic Demand:

According to Negro (1994), the seismic design demand of the serviceability limit state can be assessed as the one produced by the THx0.4 with a ground acceleration equal to 0.125 g [1]. Table 40 shows the input parameters of the two horizontal elastic response spectra used in the design methodology: Ultimate Limit State (SLV, EC8) and Serviceability Limit State (SLD). On the other hand, Table 41 and Figure 81 and Figure 82 highlight the pairs' acceleration-time and the couples' accelerations-displacement from the natural and effective periods, the first one of the elastic response spectrums and the second one using the acceleration-displacement response spectrum (ADRS); both for the limit states mentioned before.

	SLV	SLD	
Ground Type	B	B	
ag	0,30	0,125	g
S	1,20	1,20	
Tb	0,15	0,15	sec
Tc	0,50	0,50	sec
Td	2,00	2,00	sec
$\xi$	5,00	5,00	%
$\eta$	1,00	1,00	

Table 40. Limit states used to design seismic demand for retrofitting intervention with metallic dampers

5%	Tn(sec)	Sd(m)	Sa(g)	
SLD	0,19	0,003	0,38	Tn2
SLV	0,19	0,008	0,90	Tn2
SLD	0,58	0,028	0,32	Tn1
SLV	0,58	0,066	0,78	Tn1
5%	Teff(sec)	Sd(m)	Sa(g)	
SLD	0,84	0,04	0,22	Uniform
SLV	0,84	0,10	0,53	Uniform
SLD	0,93	0,04	0,20	Modal
SLV	0,93	0,11	0,48	Modal

Table 41. Pseudo-accelerations and displacements from response spectrum.

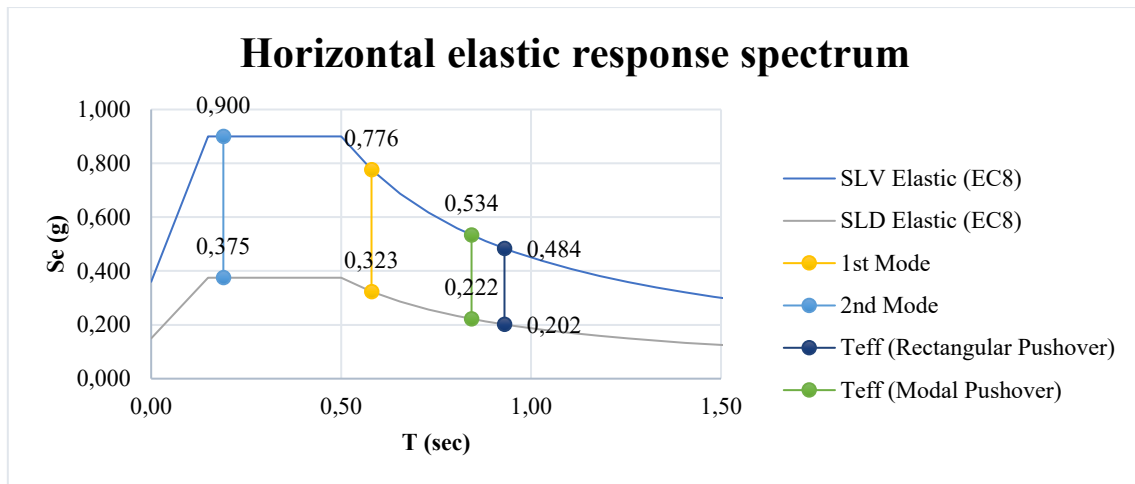


Figure 81. Elastic Response spectrum for ULS and SLS.

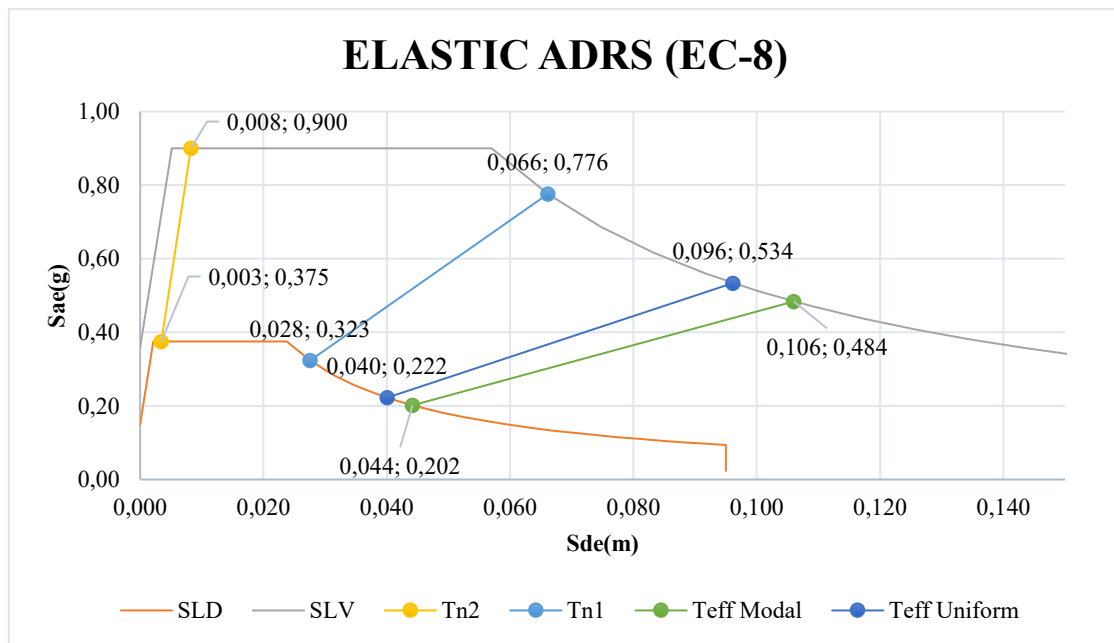


Figure 82. Elastic acceleration response spectrum for ULS and SLS.

### 6.2.3 Bilinear capacity curves of the pre-retrofit building:

The pushover curves (SDOF) obtained in Chapter 5 are used to estimate the required stiffness and the required damping ratio to comply with the design demand limit states. Table 42 list the main features of the curves required for the methodology:

	Modal	Uniform	
V <sub>y</sub>	1001,06	1131,78	KN
dy <sub>f</sub>	93,02	86,47	mm
T <sub>eff</sub>	0,93	0,84	sec
M <sub>eff</sub>	2312,95	2312,95	KN
Γ <sub>1f</sub>	1,27	1,27	
K <sub>eff</sub>	10761,68	13089,19	KN/m

Table 42. Main features of the capacity curve from pre-retrofit building in SDOF.

Where:

- $V_y$ : Yielding strength of the pre-retrofit building.
- $d_{yf}$ : Yielding displacement of the pre-retrofit building.
- $T_{eff}$ : Effective period of the pre-retrofit building.
- $M_{eff}$ : Equivalent mass of the pre-retrofit building.
- $\Gamma_{1f}$ : Transformation factor of the pre-retrofit building.
- $K_{eff}$ : Equivalent stiffness of the pre-retrofit building.

#### 6.2.4 Influence of the bracing system on the pre-retrofit building (SLD):

As mentioned before, the damper-brace system adds important stiffness producing the reduction of the natural period of the building. Therefore, the objectives are to evaluate the retrofit structure's natural period and the damper-brace system's initial stiffness by scaling the displacement response spectrum of the pre-retrofit structure. The Target Displacement Ratio ( $\lambda$ ) is the scale factor. It is obtained as the ratio between the yielding displacement of the pushover curves in SDOF and the elastic displacement in serviceability limit state (SLD) of the effective periods. Table 43 indicates the natural period of the building with metallic dampers, established by seeking the period that matches the assessment  $Sd_b$  in the response spectrum. According to the results, it must be around 0.38-0.372 seconds to comply with the required level of seismic design demand. Additionally, the initial stiffness ( $K_{do}$ ) refers to the brace-damper system, and it is used in selecting the chevron brace cross-section.

	Modal	Uniform	
$d_{yf}$	0,093	0,086	m
$u_t$	0,047	0,041	m
$\lambda$	0,509	0,472	
$T_{eff}$	0,93	0,84	sec
$Sd_f (T_o, \zeta_o)$	0,028	0,028	m
$Sd_b (T, \zeta_o)$ :	0,0133	0,0130	m
T	0,38	0,372	sec
$K_{do}$	53697	53651	KN/m

Table 43. Estimation of the 1<sup>st</sup> natural period of the retrofit building and initial required stiffness of the Brace-Damper system.

Where:

- $d_{yf}$ : Yielding displacement from pushover curve in SDOF of the pre-retrofit building. (Table 42).
- $u_t$ : Target displacement of braced structure. Intersection of the capacity curve with the seismic demand at SLD (Figure 82).
- $\lambda$ : Target displacement ratio.

$$\lambda = \frac{u_t}{d_{yf}} \quad (48)$$

- $T_{eff}$ : Effective period of the pre-retrofit building.
- $Sd_f(T_o, \zeta_o)$ : Displacement response spectrum of the pre-retrofit building at first natural period in SLD. (Figure 82).
- $Sd_b(T, \zeta_o)$ : Displacement response spectrum of the braced system at modified first natural period in SLD.

$$Sd_b(T, \zeta_o) = Sd_f(T_o, \zeta_o) * \lambda \quad (49)$$

- $T$ : First natural frequency of the retrofitted structure with metallic dampers.
- $K_{do}$ : Initial stiffness of the damper-brace system.

$$k_{do} = \left[ \left( \frac{T_{eff}}{T} \right)^2 - 1 \right] * K_{eff} \quad (50)$$

#### 6.2.5 Estimate the required added damping ratio (SLV):

As well known, the dampers dissipate energy once the demand overcomes the serviceability limit state. Thus, the objective is to evaluate the required damping ratio by scaling the acceleration response spectrum of the pre-retrofit structure at SLV. The Target Shear Force Ratio ( $\lambda_Q$ ) is the scale factor. It is obtained as the ratio between the pseudo-acceleration using the effective periods and the pseudo-acceleration of the retrofitted structure at the ultimate limit state. The required damping is obtained by varying the damping ratio in the response spectrum at SLV calculated in Chapter 3; this procedure is done until the elastic acceleration matches the assessment  $S_{ab}$ . Table 44 indicates the required hysteretic damping produced by the TADAS devices between 21% and 17%; therefore, the target damping ratio is set around 20%. This election is done to compare the retrofit structures and evaluate which one provides better results.

	Modal	Uniform	
$T_o$	0,58	0,58	sec
$T_1$	0,28	0,28	sec
$S_{af}(T_o, \zeta_o)$ :	0,78	0,78	g
$S_{ab}(T_1, \zeta_o)$ :	0,9	0,9	g
$\lambda_Q$	1,16	1,16	
$S_{af}(T_{eff}, \zeta_o)$	0,48	0,53	g
$S_{ab}(T_1, \zeta_o + \zeta_a)$	0,56	0,62	g
$\zeta_o + \zeta_a$	21%	17%	

Table 44. Required added damping ratio.

Where:

- $T_o$ : Natural period of the pre-retrofit structure in 1<sup>st</sup> mode.
- $T_1$ : Natural period of the pre-retrofit structure in 1<sup>st</sup> mode at SLV.

$$T_1 = \left( \frac{T_0}{\frac{k_{d0}}{K_{eff}} + 1} \right)^{1/2} \quad (51)$$

- $S_{af}(T_0, \zeta_0)$ : Elastic acceleration response spectrum of the pre-retrofit building at first natural period in SLV. (Figure 82).
- $S_{ab}(T_1, \zeta_0)$ : Elastic acceleration response spectrum of the retrofit building at first natural period in SLV. (Figure 82).
- $\lambda_Q$ : Target shear force ratio.

$$\lambda_Q = \frac{S_{ab}(T_1, \zeta_0)}{S_{af}(T_0, \zeta_0)} \quad (52)$$

- $S_{af}(T_{eff}, \zeta_0)$ : Elastic acceleration response spectrum of the pre-retrofit building in effective period at SLV. (Figure 82).
- $S_{ab}(T_1, \zeta_0 + \zeta_a)$ : Elastic acceleration response spectrum of the retrofit building in natural period at SLV. (Figure 82).
- $\zeta_0 + \zeta_a$ : Required equivalent damping ratio.

#### 6.2.6 TADAS dampers geometry:

The configuration of the TADAS devices is selected by an iterative procedure using the strain-energy method. As consequence, the width, height, and thickness are changed until the equivalent damping ratio is between the required damping ratios computed previously. The resultant geometries were compared with previous investigations to verify the standard outcomes[14]. Table 45 shows the results from the method and summarizes the plate's geometrical and mechanical properties of the single device of each story. The equations used to find the mechanical properties are specified in Chapter 2.

ASTM A36 Mild/Low Carbon Steel		4th	3rd	2nd	1st	
Steel Yield Strength	$f_y$	248	248	248	248	Mpa
Width	$b$	150	150	150	150	mm
Height	$h$	100	200	200	200	mm
Thickness	$t$	20	35	35	35	mm
Young Modulus	$E$	200	200	200	200	KN/mm <sup>2</sup>
Yield Strength	$V_{dy}$	24,80	37,98	37,98	37,98	KN
Plastic Strength	$V_{dp}$	37,20	56,96	56,96	56,96	KN
Stiffness	$K_{di}$	40,00	26,80	26,80	26,80	KN/mm
Yield Rotation	$\gamma_y$	0,0062	0,0071	0,0071	0,0071	
Yielding Displacement	$\Delta y_{di}$	0,62	1,42	1,42	1,42	mm

Table 45. Geometry of the metallic dampers placed on each floor.

### 6.2.7 Strain Energy-Based Method:

According to Zhang, for moment-resistant frames (MRF) equipped with TADAS devices, the equivalent damping ratio can be calculated by the Strain Energy-Based method [20]. According to Chopra (1995), the damping ratio is obtained by the damper contribution ( $W_D$ ) and the story shear effect on the building ( $W_S$ )[6]. As well know, the stories have different masses, eigenvector components, and damper configurations. These conditions should be considered to determine a correct approach to solve the problem. In this case, four frames of four stories are introduced into the model, assessing a total of 16 components representing the overall dissipation system. In order to adapt the method to the metallic dampers, Cough and Penzien (1993) propose the equations to evaluate the energy dissipated by the metallic damper in one cycle of motion ( $W_c$ ) and the total strain energy of the structure considering the damper contribution ( $W_s$ ) to replace in the equivalent hysteretic damping ratio ( $\zeta_a$ ) [20] as:

$$\zeta_a = \frac{W_c}{4\pi W_s} = \frac{W_c}{4\pi(W_{fs} + W_{ds})} \quad (53)$$

Where:

- $W_c$ : Energy dissipated by the metallic damper.

$$W_c = 4 \sum_{i=1}^N W_{ci} = 4 \sum_{i=1}^N \sum_{j=1}^{N_{di}} \left[ \frac{(1 - \alpha_{dij}) \left(1 - \frac{1}{\mu_{dij}}\right)}{1 + \alpha_{dij} * \mu_{ij} - \alpha_{dij}} * F_{dij} * \Delta_{dij} \right] \quad (54)$$

- $W_{fs}$ : Strain energy of the main structure.

$$W_{fs} = \frac{1}{2} \sum_{i=1}^N (Q_{1i} * \Delta_{1i}) \quad (55)$$

- $W_{ds}$ : Strain energy of added metallic dampers in the retrofitted structure.

$$W_{ds} = \frac{1}{2} \sum_{i=1}^N \sum_{j=1}^{N_{di}} [F_{dij} * \Delta_{dij}] \quad (56)$$

- $\alpha_{dji}$ : Device's post yielding stiffness ratio.
- $\mu_{dij}$ : Device's Displacement ductility
- $\Delta_{dij}$ : Maximum deformation of the  $j^{th}$  damper of the  $i^{th}$  floor.
- $Q_{1j}$ : Story shear force of the retrofitted structure under ultimate limit state (SLV).
- $\Delta_{1j}$ : Story drift on the  $j^{th}$  floor of retrofitted structure under ultimate limit state (SLV).
- $F_{dij}$ : Design damping force.

Table 46 lists all the information regarding the damper configuration based on Figure 80: the shape mode of the 1st mode and the mass supposed on each frame. In this case the roof



displacement is the design displacement specified in Chapter 5 by the performance point in the ADRS.

	Floor	Z(m)	U <sub>x</sub> (m)	U <sub>xN</sub>	U <sub>xNI</sub>	Mass (Ton)
Frame 1-A-B	4	12,5	0,130	1,00	0,142	21
	3	9,5	0,112	0,858	0,252	42
	2	6,5	0,079	0,606	0,295	64
	1	3,5	0,040	0,310	0,311	85
Frame 1-B-C	4	12,5	0,130	1,000	0,142	21
	3	9,5	0,112	0,858	0,252	42
	2	6,5	0,079	0,606	0,295	64
	1	3,5	0,040	0,311	0,311	85
Frame 3-A-B	4	12,5	0,130	1,000	0,142	21
	3	9,5	0,112	0,858	0,252	42
	2	6,5	0,079	0,606	0,295	64
	1	3,5	0,040	0,311	0,311	85
Frame 3-B-C	4	12,5	0,130	1,000	0,142	21
	3	9,5	0,112	0,858	0,252	42
	2	6,5	0,079	0,606	0,295	64
	1	3,5	0,040	0,311	0,311	85

Table 46. Configuration on the dampers: Frame, Elevation, Eigenvector and Mass.

Where:

- U<sub>x</sub>: Eigenvector.
- U<sub>xN</sub>: Normalized eigenvector with respect to the displacement of the last floor.
- U<sub>xNI</sub>: Normalized Interstory drift of the modal shape.

The story shear force is calculated as the mass placed on each story specified in Table 47 multiplied by the corresponding pseudo-acceleration in SLV. In addition, the interstory displacement when all dampers yield at the same time ( $\Delta y_{di}$ ) is calculated as the ratio between the device's yielding displacement (Table 45) and the interstory drift (U<sub>xNR</sub>) reported in Table 46, while the maximum damper deformation is assumed as the interstory drift multiplied by the maximum roof displacement.

	Floor	Z(m)	Q1(KN)	Qo(KN)	$\alpha_{di}$	$\Delta y_{di}(m)$	$dy_{di}(m)$	df(m)
Frame 1-A-B	4	12,5	183,20	108,62	0,02	6,20E-04	4,4E-03	0,018
	3	9,5	372,80	221,04	0,02	1,42E-03	5,6E-03	0,033
	2	6,5	562,41	333,46	0,02	1,42E-03	4,8E-03	0,038
	1	3,5	754,22	447,19	0,02	1,42E-03	4,6E-03	0,040
Frame 1-B-C	4	12,5	183,20	108,62	0,02	6,20E-04	4,4E-03	0,018
	3	9,5	372,80	221,04	0,02	1,42E-03	5,6E-03	0,033
	2	6,5	562,41	333,46	0,02	1,42E-03	4,8E-03	0,038

	1	3,5	754,22	447,19	0,02	1,42E-03	4,6E-03	0,040
Frame 3-A-B	4	12,5	183,20	108,62	0,02	6,20E-04	4,4E-03	0,018
	3	9,5	372,80	221,04	0,02	1,42E-03	5,6E-03	0,033
	2	6,5	562,41	333,46	0,02	1,42E-03	4,8E-03	0,038
	1	3,5	754,22	447,19	0,02	1,42E-03	4,6E-03	0,040
Frame 3-B-C	4	12,5	183,20	108,62	0,02	6,20E-04	4,4E-03	0,018
	3	9,5	372,80	221,04	0,02	1,42E-03	5,6E-03	0,033
	2	6,5	562,41	333,46	0,02	1,42E-03	4,8E-03	0,038
	1	3,5	754,22	447,19	0,02	1,42E-03	4,6E-03	0,040

Table 47. Shear interstory force, post-yielding coefficient, Yielding Displacement of the Device, Interstory Displacement when all devices yields and Interstory Displacement.

Where:

- $Q_{1j}$ : Story shear force of the retrofit structure under ultimate limit state on the  $i^{th}$  floor (SLV).
- $Q_0$ : Story shear force of the pre-retrofit structure under ultimate limit state on the  $i^{th}$  floor (SLV).
- $\alpha_{dji}$ : Device's post yielding stiffness ratio.
- $\Delta y_{di}$ : Device's yielding displacement.
- $\Delta_{dyi}$ : Metallic damper yield deformation
- $d_f$ : Metallic damper maximum deformation.

According to the Japanese code (JSSI Manual and JGJ 297-2013) [20], the damping force is calculated imposing the dampers stiffness proportional to the structural stiffness along the vertical story and the damping force proportional to the structural yield shear force. Based on this, the damping force ( $F_{di}$ ) and the yield damping force ( $F_{dyi}$ ) can be writing as:

$$F_{di} = \zeta_r \beta Q_{oi} \quad (57)$$

$$F_{dyi} = \frac{F_{di}}{(1 + \mu_{di} \alpha_{di} - \alpha_{di})} \quad (58)$$

Where:

- $\zeta_r$ : Required damping.
- $\beta$ : Scale coefficient.
- $Q_0$ : Story shear force of the pre-retrofit structure under ultimate limit state on the  $i^{th}$  floor (SLV).
- $\alpha_{dji}$ : Device's post yielding stiffness ratio.

The scale coefficient ( $\beta$ ) describes the ratio between the device's damping force and the building's shear force. If the dampers are mounted on all floors and the structure has well-proportioned story stiffness, it can be written as[20]:

$$\beta = \frac{\phi \pi \lambda_Q}{2 \left(1 - \frac{1}{\mu_d}\right) - \phi \pi \zeta_r} \quad (59)$$

Where:

- $\phi = \frac{\zeta_a}{\zeta_r} \rightarrow$  Damping safety factor.
- $\lambda_{Qj} = \frac{Q_{1j}}{Q_{0j}} \rightarrow$  Target shear force ratio.
- $\mu_d$ : Device's Displacement ductility
- $\zeta_r$ : Required damping.

Table 48 list the ductility, damping force, and yielding damping force of the devices. The number of triangular plates of each device is calculated in function of the yielding damping force, and the plastic limit of the devices is checked; in all cases, the damping force is lower than the plastic strength.

	Floor	Z(m)	$\mu_{di}$	$\beta$	$F_{di}$ (KN)	$F_{dy}$ (KN)
Frame 1-A-B	4	12,5	4,22	7,54	175,38	164,77
	3	9,5	5,84	6,16	290,00	264,39
	2	6,5	7,97	5,44	384,27	337,29
	1	3,5	8,88	5,14	482,50	416,84
Frame 1-B-C	4	12,5	4,22	7,54	175,38	164,77
	3	9,5	5,84	6,16	290,00	264,39
	2	6,5	7,97	5,44	384,27	337,29
	1	3,5	8,88	5,14	482,50	416,84
Frame 3-A-B	4	12,5	4,22	7,54	175,38	164,77
	3	9,5	5,84	6,16	290,00	264,39
	2	6,5	7,97	5,44	384,27	337,29
	1	3,5	8,88	5,14	482,50	416,84
Frame 3-B-C	4	12,5	4,22	7,54	175,38	164,77
	3	9,5	5,84	6,16	290,00	264,39
	2	6,5	7,97	5,44	384,27	337,29
	1	3,5	8,88	5,14	482,50	416,84

Table 48. Design damping force and Yielding Damping Force.

In conclusion of the strain-energy method, Table 50 shows the sum of the energies on each floor and the hysteretic damping ratio equal to 19.5%. The result is between the required damping ratio indicated in Table 44, which is approximate to target one (20%). Table 49 lists the energy dissipated by the metallic damper, the strain energy of the story, and the strain energy of added metallic dampers on each floor.

		$[F_{dij} * \Delta_{dij}] / 2$	$(Q_{1i} * \Delta_{1i}) / 2$	$4(1 - \alpha_{di})(1 - 1/\mu_{di}) * F_{dyi} * \Delta_{di}$
	Story	$W_{ds}$	$W_{fs}$	$W_c$
Frame 1-A-B	4	1,62	1,69	9,09
	3	4,76	6,12	28,19
	2	7,36	10,77	44,29
	1	9,76	15,25	58,63
Frame 1-B-C	4	1,62	1,69	9,09
	3	4,76	6,12	28,19
	2	7,36	10,77	44,29
	1	9,76	15,25	58,63
Frame 3-A-B	4	1,62	1,69	9,09
	3	4,76	6,12	28,19
	2	7,36	10,77	44,29
	1	9,76	15,25	58,63
Frame 3-B-C	4	1,62	1,69	9,09
	3	4,76	6,12	28,19
	2	7,36	10,77	44,29
	1	9,76	15,25	58,63

Table 49. Energy dissipated by the metallic damper, Strain energy of the main structure, Strain energy of added metallic dampers in the retrofitted structure.

$4\pi * W_{ds}$	$4\pi * W_{fs}$	$W_c$	$\zeta_a$
1180,77	1700,33	560,79	19,5%

Table 50. Equivalent hysteretic damping ratio.

In addition, the damping force and the device's yielding displacement are limited to control the design procedure. The recommendations provide by Weng and Lu (2004), the Chinese code (GB 50011-2010), and the Japanese code (JGJ 297-2013) relate the features mentioned before with the interstory yielding strength and the interstory yielding displacement of the pre-retrofit structure. Both values of the building are obtained from the pushover curve in SDOF. Table 51 shows the recommendations, and Table 52 list the verification in all the dampers.

Damper force limitation	Damper displacement limitation
$R = \frac{F_{py}}{F_{sy}} \leq 0.6 \quad (60)$ <p>Where:</p> <ul style="list-style-type: none"> <li>- <math>F_{py}</math>: Yield strength of energy dissipation.</li> <li>- <math>F_{sy}</math>: Interstory yield strength of the main structure</li> </ul>	$D = \frac{\Delta_{ydi}}{\Delta_{sy}} \leq \frac{2}{3} \quad (61)$ <p>Where:</p> <ul style="list-style-type: none"> <li>- <math>\Delta_{ydi}</math>: Device's yielding displacement.</li> <li>- <math>\Delta_{sy}</math>: Inter-tory yield displacement of the main structure.</li> </ul>

Table 51. Suggested Damper Limitations

Z	$F_{py}$	$F_{sy}$	R	R<0.6	$\Delta_{py}$	$\Delta_{sy}$	D	D<2/3
m	KN	KN	$F_{py}/F_{sy}$		m	m	$\Delta_{py}/\Delta_{sy}$	
12,5	175,38	1316,86	0,13	CHECK	0,004	0,12	0,04	CHECK
9,5	290,00	1314,08	0,20	CHECK	0,006	0,10	0,05	CHECK
6,5	384,27	1314,44	0,26	CHECK	0,005	0,07	0,07	CHECK
3,5	482,50	1315,86	0,32	CHECK	0,005	0,04	0,13	CHECK
12,5	175,38	1316,86	0,13	CHECK	0,004	0,12	0,04	CHECK
9,5	290,00	1314,08	0,20	CHECK	0,006	0,10	0,05	CHECK
6,5	384,27	1314,44	0,26	CHECK	0,005	0,07	0,07	CHECK
3,5	482,50	1315,86	0,32	CHECK	0,005	0,04	0,13	CHECK
12,5	175,38	1316,86	0,13	CHECK	0,004	0,12	0,04	CHECK
9,5	290,00	1314,08	0,20	CHECK	0,006	0,10	0,05	CHECK
6,5	384,27	1314,44	0,26	CHECK	0,005	0,07	0,07	CHECK
3,5	482,50	1315,86	0,32	CHECK	0,005	0,04	0,13	CHECK
12,5	175,38	1316,86	0,13	CHECK	0,004	0,12	0,04	CHECK
9,5	290,00	1314,08	0,20	CHECK	0,006	0,10	0,05	CHECK
6,5	384,27	1314,44	0,26	CHECK	0,005	0,07	0,07	CHECK
3,5	482,50	1315,86	0,32	CHECK	0,005	0,04	0,13	CHECK

Table 52. Design safety verifications.

Finally, the complete TADAS damper geometry is defined once each triangular device's plates are obtained. The results show 11 plates for the devices of the 1<sup>st</sup> story, 9 for those of the 2<sup>nd</sup> story, and seven plates for the ones on the 3<sup>rd</sup> and 4<sup>th</sup> floor. Figure 83 shows the device's force-displacement relationship expected under seismic action. As projected, due to the stiffness-proportional criterium mentioned in the calculation of the damping force, the required mechanical features of the devices are reduced with the elevation; what represents an advantage of the design methodology compared to more conservative approaches where a unique device is applied to all the stories. Table 53 confirms the before mentioned due to the reduction of the number of plates and the ductility in the devices with the stories.

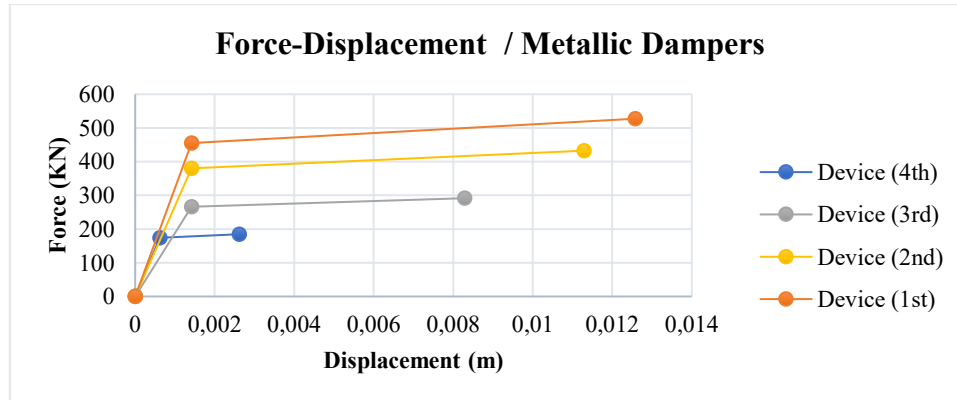


Figure 83. Expected metallic device performance. Force-Displacement relationship.

ASTM A36 Mild/Low Carbon Steel		4th	3rd	2nd	1st
Displacement ductility	$\mu_{di}$	4,22	5,84	7,97	8,88
Number Triangular Plates per device	N	7,0	7,0	9,0	11,0

Table 53. Number of plates and displacement ductility of the dampers.

### 6.2.8 FEM simulation on SAP2000

The Frame Object is used to model the damper's nonlinear behavior instead of the Link Object. According to the SAP2000 manual, the hysteretic behavior from links, like Multilinear Plastic or Plastic Wen, cannot be captured in the nonlinear time-history direct integration analyses for limitations in the software[23]. Therefore, the device's hysteretic behavior is modeled by the Fiber Hinge P-M2-M3, setting the relative hinge length equal to 0.1. Figure 84 shows the metallic damper hinge configuration on SAP2000.

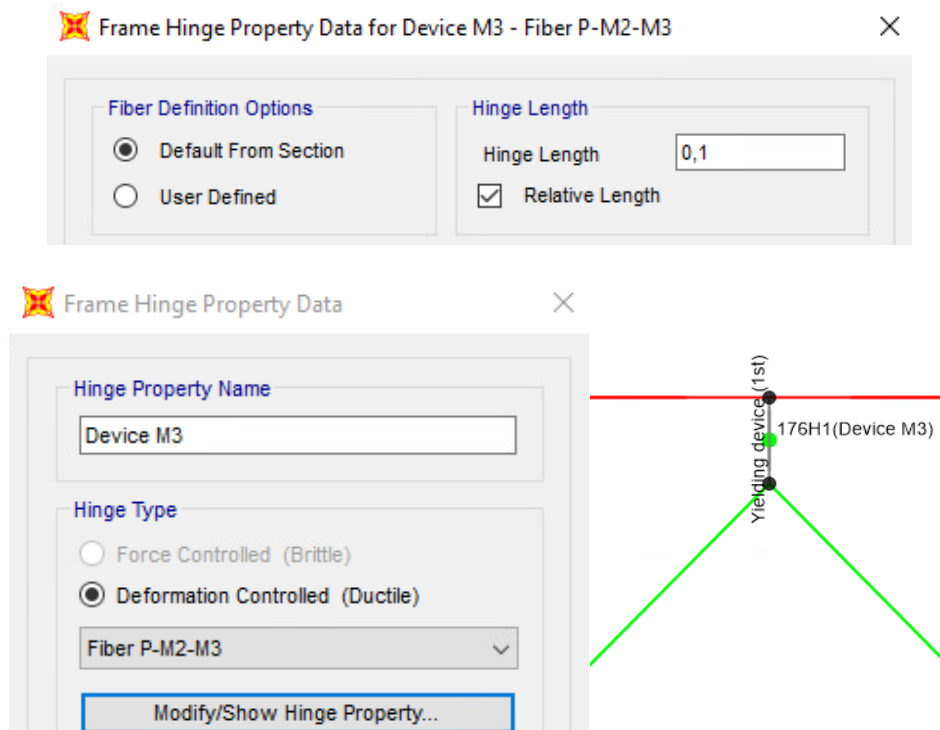


Figure 84. Metallic Damper Hinge Configuration on SAP2000.

The braced system is Chevron typology and remain elastic; therefore, it is not assigned any hinge. The pinned connection is modeled with end-releases for M2 and M3 at the extremes of the element. Thus, it only works in compression and tension. Figure 85 shows the release configuration of the Chevron bracing systems.

Section Property	HEA140 133x5.5x140x...
Property Modifiers	None
Material Overwrite	None
Releases End-I	T, M2, M3
Releases End-J	M2, M3

Figure 85. Braces release on SAP2000.

The triangular plates (TP) of the TADAS devices are modeled like an equivalent rectangular prismatic (RP) element due to software requirements. Thus, the equivalent width needed to obtain the same mechanical properties is computed by equivalent stiffnesses. Meanwhile, the thickness cannot be changed because it defines the device's yield displacement and yield rotation angle. Table 54 shows the equivalent geometry used on SAP2000 to model the TADAS device. In addition, the device has a release in the top for the normal force, as well known, the damper-bracing system does not carry dead loads.

TP - Height	h	100	200	200	200	mm
TP - Stiffness	$K_p$	40	27	27	27	N
TP - Thickness	t	20,0	35,0	35,0	35,0	mm
TP - Quantity	N	7	7	9	11	0
RP - Width	$b_{eq}$	25,0	25,0	25,0	25,0	mm
RP - Yielding rotation	$\gamma_y$	0,00620	0,00709	0,00709	0,00709	
RP - stiffness	$K_{eq}$	40,0	26,8	26,8	26,8	KN/mm
RP - Yielding strength	$V_{dy}$	24,8	38,0	38,0	38,0	KN
RP - Total width	$B_{eq}$	175	175	225	275	mm

Table 54. Equivalent geometry for the TADAS devices

Chevron bracing system:

The inverted-V concentric bracing configuration is based on the required initial stiffness at the serviceability limit state. According to Mahmoudi, the model of the damper-bracing system can be considered as two springs linked in parallel. Thus, to comply with the requirements, the cross-section selected is a European Standard Wide Flange H profile (HEA), following Zhang's research work. The stiffness of the metallic dampers ( $K_d$ ) are obtained from Tables 43 and the stiffness of the bracing system ( $K_b$ ) can be calculated as [6]:

$$K_b = A * E * \frac{\cos^2 \theta}{L} \quad (62)$$

Where:

- A: Cross-section area of the diagonal.
- E: Elasticity modulus of the material.
- $\theta$ : Inclination angle.
- L: Length of the diagonal.

Finally, the stiffness of the damper-bracing system can be computed as:

$$\frac{1}{K_{bd}} = \frac{1}{K_b} + \frac{1}{K_d} \quad (63)$$

Table 55 shows the chevron bracing system configuration, and Figure 86 shows the input parameters on SAP2000. The bracing system on SAP2000 is considered elastic during all the

analyses. In addition, the average value of  $K_{bd}$  equal to 58184 KN/m is really close to the defined in Table 43 around 53674 KN/m.

Chevron brace							
	1st Floor		2nd-3rd Floor		4th Floor		
	1	2	1	2	1	2	
	HEA140	HEA140	HEA140	HEA140	HEA140	HEA140	
<b>b</b>	14,00	14,00	14,00	14,00	14,00	14,00	cm
<b>h</b>	13,30	13,30	13,30	13,30	13,30	13,30	cm
<b>tw</b>	0,55	0,55	0,55	0,55	0,55	0,55	cm
<b>tf</b>	0,85	0,85	0,85	0,85	0,85	0,85	cm
<b>A</b>	31,40	31,40	31,40	31,40	31,40	31,40	cm <sup>2</sup>
<b>E</b>	2E+05	2E+05	2E+05	2E+05	2E+05	2E+05	MPa
<b>B</b>	5,58	3,58	5,58	3,58	5,58	3,58	MPa
<b>h_d</b>	200	200	200	200	100	100	mm
<b>H</b>	3,04	3,04	2,35	2,35	2,45	2,45	m
<b>L</b>	4,12	3,53	3,65	2,95	3,71	3,03	m
<b>θ</b>	0,83	1,04	0,70	0,92	0,72	0,94	°
<b>θ</b>	47,48	59,54	40,13	52,74	41,31	53,89	rad
<b>Kb</b>	69545	45750	100687	77956	95469	71934	N/mm
<b>Kd</b>	294766	294766	187578	187578	280000	280000	N/mm
<b>Kbd</b>	56269	39603	65518	55070	71195	57231	N/mm

Table 55. Chevron bracing system configuration.

Section Name
HEA140 133x5.5x140x8.5
Display Color

Section Notes
Modify/Show Notes...

Dimensions

Outside height ( t3 )
0,133
Top flange width ( t2 )
0,14
Top flange thickness ( tf )
8,500E-03
Web thickness ( tw )
5,500E-03
Bottom flange width ( t2b )
0,14
Bottom flange thickness ( tfb )
8,500E-03

Material
+ S275
Property Modifiers
Set Modifiers...

Section

Properties
Section Properties...
Time Dependent Properties...

Figure 86. Cross-section of the bracing system on SAP2000.



## Chapter 7

# 7 Structural Analysis of Retrofitted Structure with Fluid Viscous Dampers

This chapter reports the structural analysis executed to the finite element model described in Chapter 4 with addition of the fluid viscous dampers designed in Chapter 6. The analytical methods considered are Modal Analysis, Static Nonlinear Analysis, Static Pushover Analysis, and Nonlinear Time-history Analysis. The goal is examines the static response, the dynamic response, and the nonlinear structural behavior to identify the dissipative action and the effects on internal forces and displacements produced by the implementation of the fluid viscous dampers.

### 7.1 Modal Analysis

The fluid viscous damper does not increase the stiffness or the mass in the structure. As consequence, the mass matrix and stiffness matrix of the system remain unchanged. The modal analysis is executed by Eigenvector analysis, which determines the shapes and natural periods of the system in undamped free vibration[23] by solving the eigenvalue problem using both matrix mentioned before. Therefore, it is obtained the same results as in the pre-retrofit building. Table 56 shows the four natural frequencies of the first modal shapes and Table 57 shows the modal shape of the first natural frequency which has the higher mass participation factor on X direction, thus is the one required in the next pushover analysis.

Mode	Period	Frequency	Angular Frequency
	(sec)	(Hertz)	(rad/sec)
1	0,58	1,73	10,84
2	0,19	5,37	33,72
3	0,10	9,89	62,15
4	0,07	14,12	88,70

Table 56. Periods and frequencies from bare frame.

Z(m)	U_x(m)	$\emptyset_{XNi}$
12,5	0,073	1,00
9,5	0,063	0,86
6,5	0,044	0,61
3,5	0,023	0,31
0	0,000	0,00

Table 57. Normalized modal shape.

Where:

- $U_x$ : eigenvector
- $\emptyset_{XNi}$ : Normalized eigenvector with respect to the displacement of the last floor

## 7.2 Static Pushover Analysis

The type of analysis done is Non-Adaptative (Static pushover analysis). Which comply the following assumptions[26]:

- Forces and displacement are one-monotonically increasing.
- Structure is dominated by 1<sup>st</sup> mode (Highest mass percentage).
- Shape of profile does not change during analysis.

The characteristics of the load case are listed below:

- Load application control: Displacement control. The monitored node is joint 50 in UX direction, corresponding to the center of masses of the last story.
- Initial conditions: Static nonlinear analysis which assess the effects of the dead loads on the structural elements.
- Load pattern: Pushover X modal and Pushover X uniform. (Horizontal concentrated loads). Analysis ran separately.
- According to the EUROCODE, the analysis is run once the base shear reaches 80% of maximum force.
- Setting the kinematical constraints to move in the X-X coordinates solely; therefore, the rotational contribution of the main concentrated mass floor was neglected [1]. The Plane Frame setup establishes the condition required by allowing the displacement in the X and the Z direction and the rotation in the Y direction.
- The forces' profile was applied on the story columns instead of the center of masses of the floor.

As mentioned in the modal analysis, the modal shapes and the mass on the floors remain unchanged. Therefore, the pushover analysis is the same as in the pre-retrofit building. The procedure is detailed in the Chapter 5. The main characteristics are listed in the following figures and tables:

<b>Modal Pushover (MDOFS)</b>		<b>Modal Pushover (SDOFS)</b>	
Top displacement	Base reaction	Top displacement	Base reaction
<b>(m)</b>	<b>KN</b>	<b>(m)</b>	<b>KN</b>
0,00	0,00	0	0
0,13	1214,75	0,102	959,23
0,21	1214,75	0,169	959,23
<b>Uniform Pushover (MDOFS)</b>		<b>Uniform Pushover (SDOFS)</b>	
Top displacement	Base reaction	Top displacement	Base reaction
<b>(m)</b>	<b>KN</b>	<b>(m)</b>	<b>KN</b>
0,00	0,00	0,000	0,00
0,11	1368,63	0,086	1080,73
0,18	1368,63	0,145	1080,73

Table 58. MDOF capacity curve to SDOF capacity curve

Modal	$q^*$	$\mu d$	$\mu c$
X(+)	1,09	1,09	1,65
Uniform	$q^*$	$\mu d$	$\mu c$
X(+)	1,12	1,12	1,70

Table 59. Reduction factor, ductility demand and ductility capacity.

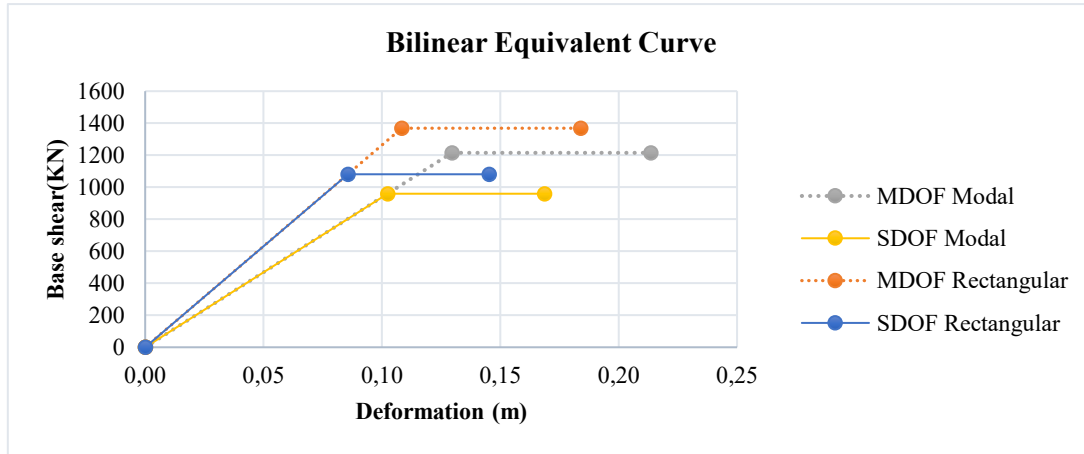


Figure 87. Bilinear capacity curve (MDOF-SDOF)

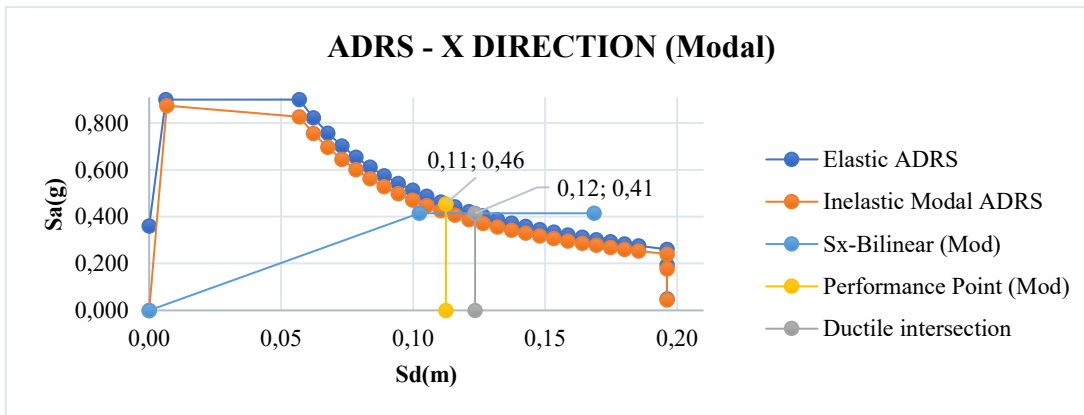


Figure 88. ADRS-Ductility Verification: Modal Case.

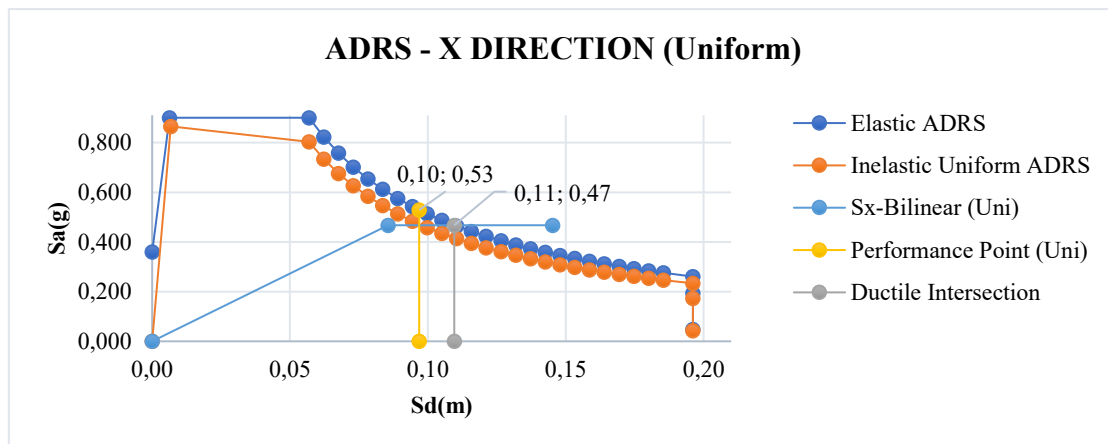


Figure 89. ADRS-Ductility Verification: Uniform Case.

### 7.3 Nonlinear Time-history Analysis

The analysis is executed on SAP2000, setting the kinematical constraints to move in the X-X coordinates solely. The Plane Frame setup establishes the condition required by allowing the displacement in the X and the Z direction and the rotation in the Y direction. In the other hand, the time functions used to execute the analysis are the seven accelerograms mentioned in Chapter 3. The Hilber-Hughes-Taylor algorithm (HHT) is the nonlinear direct integration method applied to obtain structural response under dynamic loading. It is an implicit method from Newmark Algorithms Family that improves the rate of convergence without affecting the accuracy of results.

The load case is run with the following input data:

- Initial conditions: Continue analysis from state at end of static nonlinear analysis.
- Geometric parameters: None
- Stiffness-Proportional damping of stiff elements produced on nonlinear objects is considered in the analysis. The coefficients are computed automatically by the software in function of 2 different periods.
- Nonlinear behavior is capture by the strain-stress model of the materials and cross sections. As well as the nonlinear link properties.
- Time integration: Parameter alpha ( $\alpha$ ) set as -0.33.

Figure 90 shows the configuration of the time-history analysis using the accelerogram two. In addition, the number of Output Time Steps vary according to the duration of each input time function, while the Output Time Step Size is set as 0.04 for all cases.

The screenshot shows the 'Time History' configuration window in SAP2000. The 'Load Case Name' is 'TH2'. Under 'Initial Conditions', 'Continue from State at End of Nonlinear Case' is selected. The 'Modal Load Case' is 'Modal analysis'. The 'Loads Applied' table has one entry: 'Accel' (Load Type), 'U1' (Load Name), 'TH 2' (Function), and '1' (Scale Factor). The 'Time Step Data' section shows 'Number of Output Time Steps' as 1206 and 'Output Time Step Size' as 0.04. Under 'Other Parameters', 'Damping' is 'Proportional', 'Time Integration' is 'Hilber-Hughes-Taylor', and 'Nonlinear Parameters' is 'User Defined'. The 'Analysis Type' is 'Nonlinear' and the 'Solution Type' is 'Direct Integration'. The 'History Type' is 'Transient' and the 'Mass Source' is 'MSSSRC1'.

Load Type	Load Name	Function	Scale Factor
Accel	U1	TH 2	1

Figure 90. Configuration of the time-history analysis on SAP2000.

The Figure 91 to Figure 94 show the relation, in absolute value, between the base shear and the displacement of the 4-story taking as reference joint the center of the masses of the last floor. It is done to know the effects of the different seismic actions acting on the structure. To verify the reliability of the results, Figures 91-94 must match with the bilinear capacity curve in MDOF previously obtained.

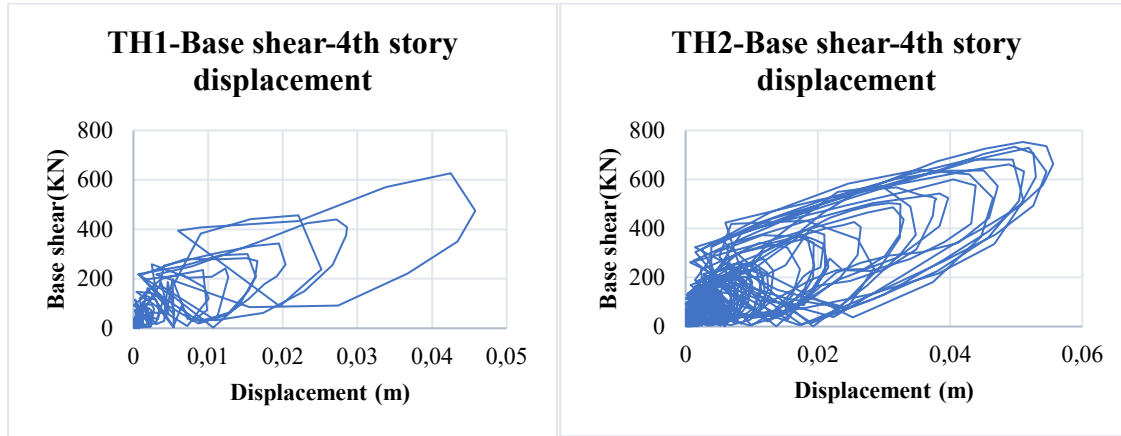


Figure 91. Base shear-4th Story Displacement for TH1 and TH2.

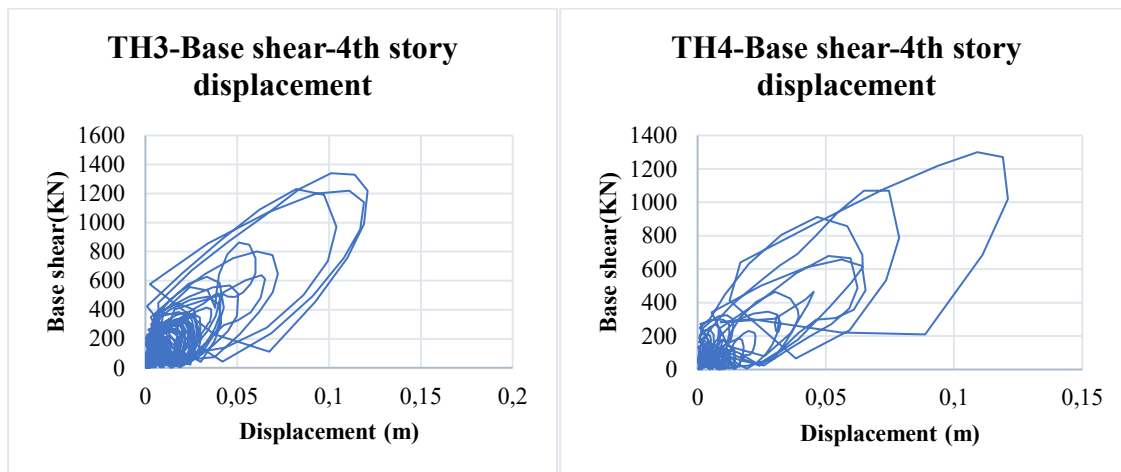


Figure 92. Base shear-4th Story Displacement for TH3 and TH4.

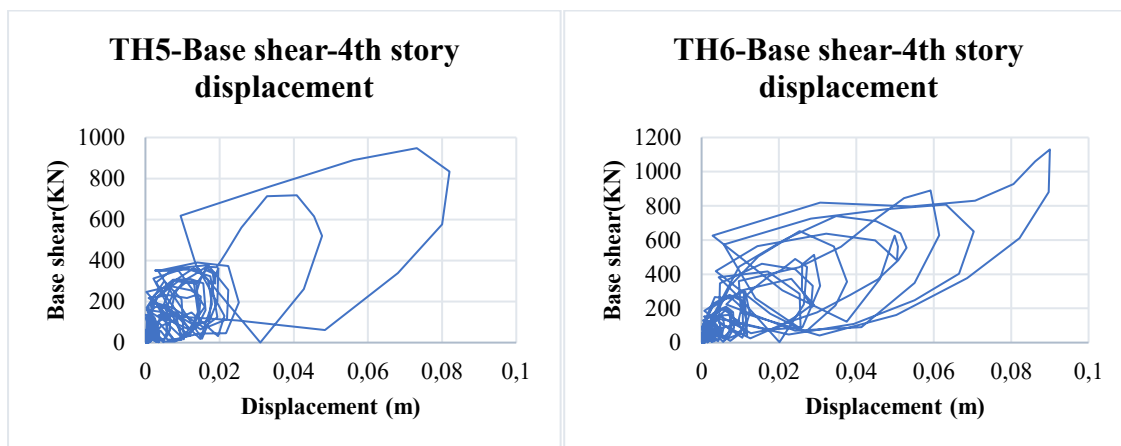


Figure 93. Base shear-4th Story Displacement for TH5 and TH6.

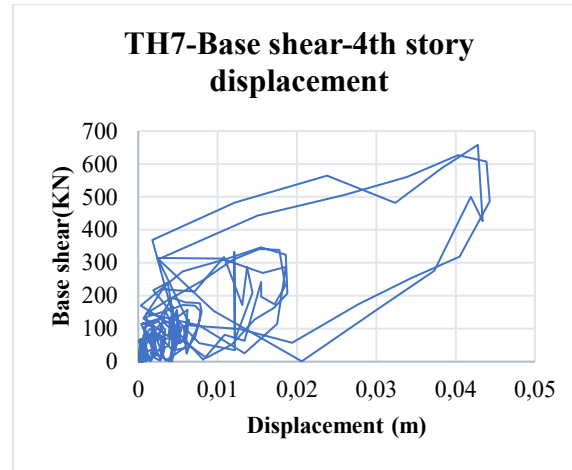


Figure 94. Base shear-4th Story Displacement for TH7.

Figure 95 illustrates the dynamic response of the structure for the seven different accelerograms plotted below the equivalent bilinear pushover curve in MDOF for modal and uniform case; the effect of the fluid viscous dampers is evident in comparison with the results from Chapter 5. The average maximum demand is located between both capacity curves in the elastic region. In addition, it checks the congruence between the dynamic response of the structure under seismic action and the simplified dynamic response of the structure obtained by the static pushover analysis. Lastly, Table 60 reports the maximum base shear and displacement of each time-history analysis, as well as the average maximum base shear and displacement. The analysis of the results and the comparison between the models is discussed in Chapter 9.

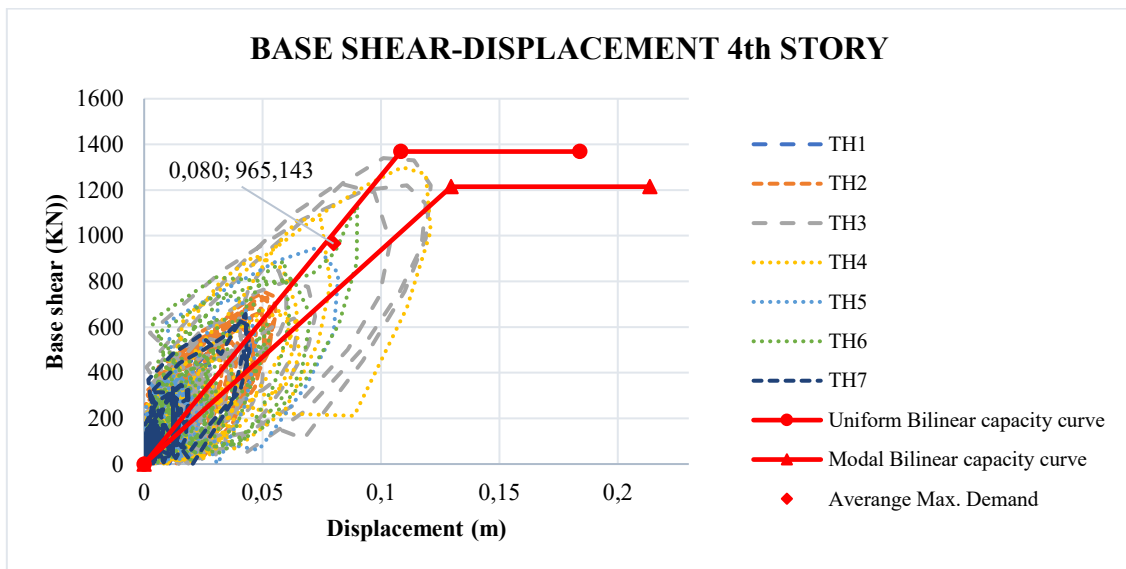


Figure 95. Bilinear Capacity Curve and TH results – FVD-retrofit Building.

TH	1	2	3	4	5	6	7	Average
d(m)	0,046	0,056	0,121	0,121	0,082	0,09	0,044	0,080
F(KN)	627	753	1340	1300	948	1130	658	965,143

Table 60. Retrofit building FVD- Time-history maximum displacement and maximum base shear.

Based on the results from nonlinear dynamic and static analyses, the fluid viscous dampers through the hysteretic loop dissipate energy on the structure, reducing the displacements and base shear on the building. Figure 96 verifies the dampers' exact effect through the acceleration-displacement response spectrum with a 20% damping ratio. In addition, the average maximum demand from Table 44 is nearly accurate to the ADRS with the target damping ratio defined in Chapter 6. These results check the reliability of the design method applied and the configuration of the FE model on SAP2000. Thenceforth, the comparison of both control solutions is made for the same seismic design demand.

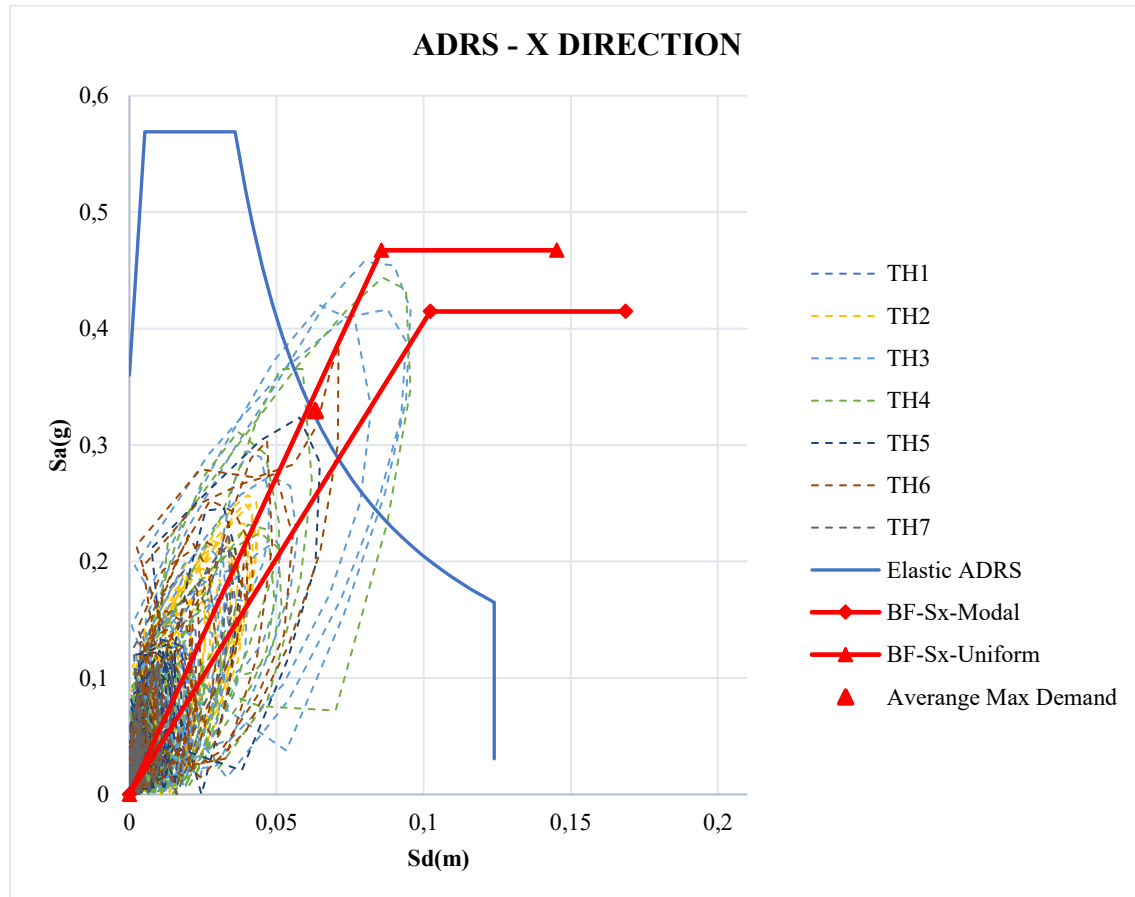


Figure 96. Checking damper effects using the ADRS with Damping 20% - Retrofit structure with fluid viscous dampers.

Finally, Figure 97 and Figure 98 plot the structure's shape for the maximum interstory drift produced on the time-history analysis for the seventh accelerograms acting on the retrofit structure with fluid viscous dampers. The time-history TH3 and TH4 are the most critical cases like in the pre-retrofit structure; however, in this case, both cases behave similarly, achieving the same interstory drift and the shape, with a slight difference in the 1st story; the maximum interstory displacement is 0.31% on the 1st floor and 0.3% on the 2nd floor, respectively. Additionally, there is an almost steady shape at the maximum interstory drift considering all the cases in the structure. Regarding the average shape, the maximum drift is equal to 0.20%, and it is produced on the 2nd floor.

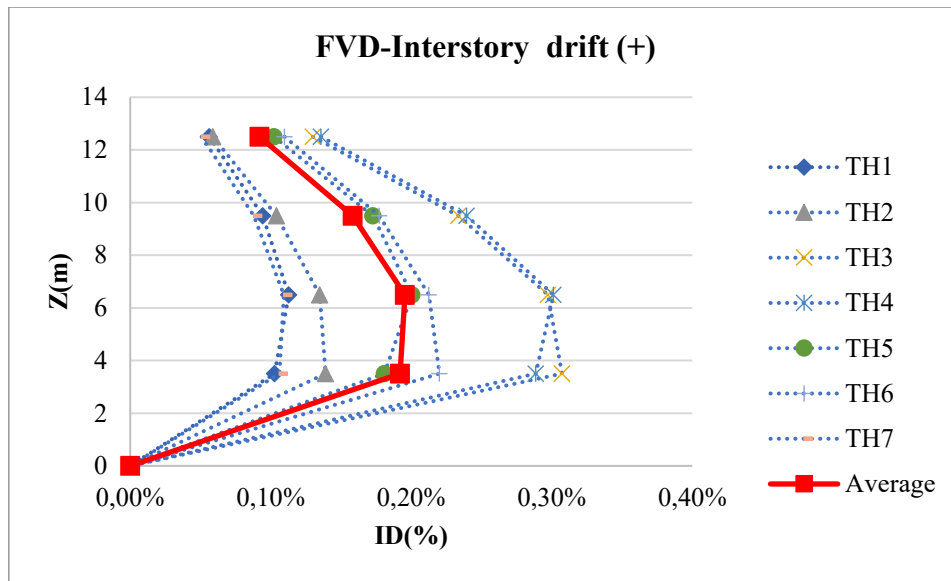


Figure 97. Maximum interstory displacement of time-history analysis - Positive direction, retrofit structure with FVD.

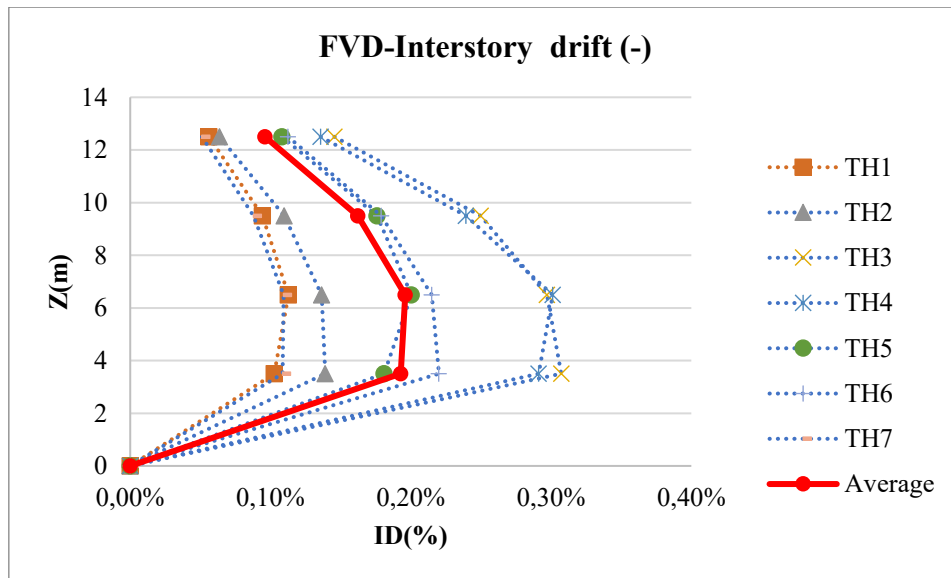


Figure 98. Maximum interstory displacement of time-history analysis - Negative direction, retrofit structure with FVD.



## Chapter 8

# 8 Structural Analysis of Retrofit Structure with Metallic-Yielding Dampers

This chapter reports the structural analysis executed to the finite element model described in Chapter 4 with addition of the Yielding Hysteretic Dampers (TADAS) designed in Chapter 6. The analytical methods considered are Modal Analysis, Static Nonlinear Analysis, Static Pushover Analysis, and Nonlinear Time-history Analysis. The goal is examine the static response, the dynamic response, and the nonlinear structural behavior to identify the dissipative action and the effects on internal forces and displacements produced by the implementation of the TADAS dampers.

### 8.1 Modal Analysis

The metallic dampers and the chevron bracing system increase the stiffness in the structure. Consequently, the stiffness matrix of the system changes, while the mass matrix does not, producing a decrement of the natural periods of the structure and the change in the modal shapes; however, the change is insignificant. The modal analysis is executed by Eigenvector analysis, which determines the shapes and natural periods of the system in undamped free vibration [23] by solving the eigenvalue problem using both matrices mentioned before. Table 61 shows the first three natural periods of the pre-retrofit structure. In contrast, Table 62 shows the natural periods of the building with metallic dampers and bracing system, obtaining the target period computed in Chapter 6. Figure 99 shows both buildings, the bare one and the retrofitted.

Mode	Period	Frequency	Angular Frequency
	(sec)	(Hertz)	(rad/sec)
1	0,58	1,73	10,84
2	0,19	5,37	33,72
3	0,10	9,89	62,15

Table 61. Natural periods of the pre-retrofit structure.

Mode	Period	Frequency	Angular Frequency
	(sec)	(Hertz)	(rad/sec)
1	0,38	2,62	16,46
2	0,13	7,64	47,98
3	0,08	13,09	82,23

Table 62. Natural of the retrofit structure with metallic dampers.

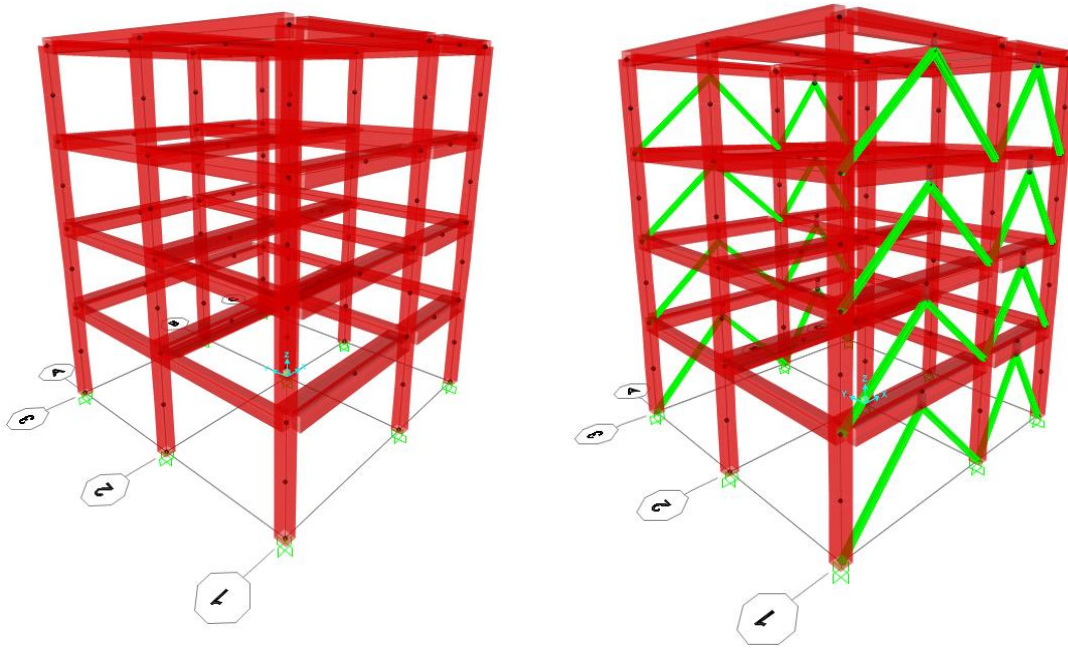


Figure 99. 3D model of the pre-retrofit building and the retrofit building with metallic dampers.

## 8.2 Static Pushover Analysis

The damper-bracing system add stiffness to the structure; therefore, it is expected the increment of the shear base strength and reduction of the displacement capacity represented by the pushover curve. Regards to the assessment, the type of analysis done is Non-Adaptative (Static pushover analysis). Which comply the following assumptions[26]:

- Forces and displacement are one-monotonically increasing.
- Structure is dominated by 1<sup>st</sup> mode (Highest mass percentage).
- Shape of profile does not change during analysis.

Despite reducing the natural frequencies, the modal shapes for the first mode do not change; consequently, the profile of forces for modal and uniform case, the participation factor ( $\Gamma$ ) and the effective mass ( $m^*$ ) do not change. Therefore, the procedure followed is the same than Chapter 5 but applied in the structure illustrated in Figure 99.

Previously to execute the analysis in SAP200, to verify the FE model, the idealized pushover curves in SDOF are calculated following the recommendations of The Technical Report MCEER-00-0010 from the University of Buffalo [28]. The results are plotted in Figure 100 and Figure 101, based on the Modal and the Uniform capacity curves from Chapter 5 and the modal properties: fundamental mode shape (1<sup>st</sup> mode) and participation factor ( $\Gamma$ ).

### 8.2.1 Idealized pushover curves in SDOF:

The method to calculate the idealized pushover curve in SDOF assumes the yield of metallic dampers while the frame system remains elastic, Chevron configuration of the bracing system, rigid floors diaphragms, and a trilinear and bilinear equivalent pushover curve SDOF to describe the performance of the system. In addition, it suppose horizontal loads proportional to

the first mode, the yield of all the dampers located at the same floor for the same interstory drift, and modal properties under elastic conditions to calculate the effective period ( $T_1$ ) and the base shear strength ( $V_d + K_f D_{yd}$ ) for the combined system, the displacement intersection between curves ( $D_0$ ) and the yield displacement of the equivalent bilinear curve ( $D_y$ ) .

Figure 100 illustrates the trilinear representation; the behavior of the combined system before the yielding of the dampers is displayed in the segment OA and the system's behavior after yielding dampers in segment AB. In addition, the segment BC goes until the maximum deformation of the capacity curve in SDOF of the pre-retrofit structure. Figure 101 represents the bilinear equivalent elastoplastic representation of the trilinear curve and the corresponding relationship regarding the intersection between the curves at  $0.6V$  and the maximum yielding strength.

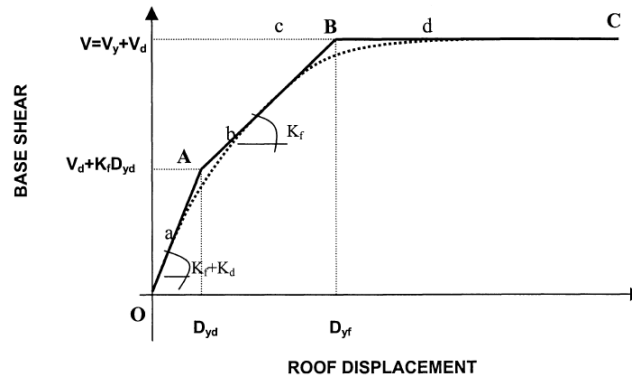


Figure 100. Trilinear representation of pushover curve of building with yielding dampers[28]

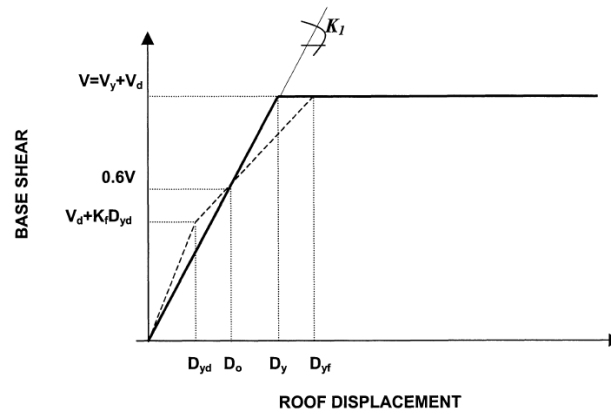


Figure 101. Trilinear and equivalent elastoplastic representation of pushover curve of building with yielding dampers[28]

The procedure starts with the definition of the geometry of the dampers placed on the building. Then, Table 63 and Table 64 lists the geometry and mechanical properties of the triangular plates and metallic dampers from the 1st to the 4th story; these features are obtained from Chapter 6. In addition, Table 65 shows the features of the pushover curves in SDOF obtained from Chapter 5, and Table 66 reports the expected features of the braced building specified in Chapter 6.

		1st	2nd	3rd	4th	
<b>Steel yield strength</b>	<b>f<sub>y</sub></b>	248	248	248	248	Mpa
<b>width</b>	<b>b</b>	150	150	150	150	mm
<b>height</b>	<b>h</b>	200	200	200	100	mm
<b>thickness</b>	<b>t</b>	35	35	35	20	mm
<b>Young modulus</b>	<b>E</b>	200	200	200	200	KN/mm <sup>2</sup>
<b>Yield strength</b>	<b>V<sub>di</sub></b>	37,98	37,98	37,98	24,80	KN
<b>Stiffness</b>	<b>K<sub>di</sub></b>	26,80	26,80	26,80	40,00	KN/mm
<b>Yielding displacement</b>	<b>Δ<sub>ydi</sub></b>	1,42	1,42	1,42	0,62	mm

Table 63. Geometrical and mechanical properties of triangular plates of the metallic dampers.

	Quantity of plates	Damper Yield strength	Damper Stiffness	Damper Yielding Displacement	Damper Ductility	Damper maximum Displacement
<b>Story</b>	<b>N<sub>i</sub></b>	<b>V<sub>di</sub> (KN)</b>	<b>K<sub>di</sub> (KN/mm)</b>	<b>D<sub>yd</sub>(mm)</b>	<b>μ</b>	<b>d<sub>u</sub>(mm)</b>
4	7	173,60	187,58	4,37	4,22	18,44
3	7	265,83	187,58	5,61	5,84	23,70
2	9	341,78	241,17	4,81	7,97	9,88
1	11	417,73	294,77	4,56	8,88	19,23

Table 64. Mechanical properties of the metallic dampers.

Input Bare Frame			
	Modal	Uniform	
<b>V<sub>y</sub></b>	1001,06	1131,78	KN
<b>d<sub>yf</sub></b>	93,02	86,47	mm
<b>T<sub>eff</sub></b>	0,93	0,84	sec
<b>m*f</b>	2312,95	2312,95	KN
<b>Γ<sub>1f</sub></b>	1,27	1,27	

Table 65. Pushover Curve in SDOF of the pre-retrofit building

Input Braced Frame			
	Modal	Uniform	
<b>T</b>	0,38	0,37	sec
<b>m*</b>	2312,95	2312,95	KN
<b>Γ<sub>1</sub></b>	1,27	1,27	

Table 66. Expected features of the retrofit building with metallic dampers.

Secondly, it must be computed the roof displacement. When the dampers at  $i_{th}$  story yield simultaneously, the interstory displacement can be expressed as  $D_{ydi} = \frac{\Delta_{dyi}}{\phi_i}$ , where  $\Delta_{dyi}$  is the damper's yield displacement and  $\phi_i$  is interstory eigenvector normalized to unity at the roof level. Consequently, when all dampers of the building yield, the displacement of the roof is the maximum between the interstory displacements. Table 67 shows the design roof displacement  $D_{ydMAX}$  equal to 5.6 mm used in the approach.

$\phi_1$	$\phi_i$	<b>D<sub>yd</sub>(mm)</b>
1,00	0,142	4,4
0,86	0,252	5,6
0,61	0,295	4,8
0,31	0,311	4,6
		<b>D<sub>ydMAX</sub>(mm)</b>
		5,6

Table 67. Interstory displacements and roof displacement.

The base shear strength of the combined system when all the dampers of the first story yields ( $V_d + K_f D_{yd}$ ) is calculated according to the modal properties, hence, considers the fundamental mode of the structure with dampers. Table 68 shows the results for the modal and uniform cases, and the equation can be written as [28]:

$$V_d + K_f D_{yd} = \left( \frac{4\pi^2}{g * T^2} \right) * \left( \frac{D_{yd}}{\Gamma} \right) * m^* \quad (64)$$

Where:

- $g$ : Gravity acceleration.
- $T$ : Natural period of the retrofit structure with metallic dampers from Chapter 6.
- $D_{yd}$ : Roof displacement when all the dampers yield from Table 67.
- $\Gamma$ : Participation factor from Chapter 5.
- $m^*$ : Effective mass from Chapter 5.

<b>V_d+K_f D_yd</b>			
	Modal	Uniform	
<b>Dyd</b>	5,6	5,6	mm
<b><math>\Gamma</math></b>	1,27	1,27	
<b><math>m^*</math></b>	2312,95	2312,95	KN
<b>T</b>	0,38	0,37	sec
<b>V_d+K_f D_yd</b>	285,80	298,23	KN

Table 68. Base shear strength of the combined system.

The base shear strength of the retrofit building with metallic dampers can be computed as the sum of the base shear strength from the capacity curve in SDOF of the pre-retrofit structure and the yield strength of one metallic damper placed on the first floor. This condition is only true if there is a symmetrical distribution of one unique type of damper in the first story. Table 69 list the results for modal and uniform cases:

$$V = V_y + V_{d1} \quad (65)$$

Where:

- $V_y$ : Base shear strength from Table 65.
- $V_{d1}$ : Yield strength of one metallic damper from Table 64.

	Modal	Uniform	
<b>Vy</b>	1001,06	1131,78	KN
<b>Vd1</b>	417,73	417,73	KN
<b>V</b>	1418,78	1549,50	KN

Table 69. Base shear strength in SDOF of the building with metallic dampers.

The displacement where the trilinear and the bilinear curve intersects ( $D_0$ ) can be obtained using the modal properties and the base shear strength of the retrofit building and the yield

strength of one metallic damper placed on the first floor. Table 70 shows the results for modal and uniform cases, and the equation can be written as:

$$D_0 = \left( \frac{g}{4\pi^2} \right) * \Gamma * \left( \frac{0.6 * V - V_{d1}}{m_f^*} \right) * T^2 \quad (66)$$

Where:

- $g$ : Gravity acceleration.
- $\Gamma$ : Participation factor from Chapter 5.
- $V_y$ : Base shear strength from Table 65.
- $V_{d1}$ : Yield strength of one metallic damper from Table 64.
- $m^*$ : Effective mass from Chapter 5.
- $T$ : Natural period of the retrofit structure with metallic dampers from Chapter 6.

	Modal	Uniform	
V	1418,78	1549,50	KN
Vd1	417,73	417,73	KN
m*f	2312,95	2312,95	KN
Teff	0,93	0,84	sec
$F_{1f}$	1,27	1,27	
$D_0$	51,02	49,15	mm

Table 70. Displacement intersection between Trilinear and Bilinear pushover curves in SDOF.

Later, to find the effective period ( $T_1$ ) and the yielding displacement of the equivalent bilinear capacity curve in SDOF ( $D_y$ ) are used the modal properties, the displacement ( $D_0$ ), the effective mass ( $m^*$ ) and the yield strength of the retrofit building from Table 69. Table 71 shows the results for modal and uniform cases and the equations can be written as:

$$T_1 = 2\pi \sqrt{\frac{\left(\frac{D_0}{\Gamma}\right)}{\left(\frac{0.6V}{m^*}\right) * g}} \quad (67)$$

$$D_y = \left( \frac{g}{4\pi^2} \right) * \Gamma * \left( \frac{V}{m_f^*} \right) * T_1^2 \quad (68)$$

Where:

- $D_0$ : Displacement from Table 70.
- $\Gamma$ : Participation factor from Chapter 5.
- $V$ : Base shear strength from Table 69.
- $m^*$ : Effective mass from Chapter 5.

	Modal	Uniform	
$D_0$	51,02	49,15	mm
$\Gamma_1$	1,27	1,27	
$V$	1418,78	1549,50	KN
$m^*$	2312,95	2312,95	KN
$T_1$	0,66	0,62	sec
$D_y$	85,03	81,92	mm

Table 71. Effective period and yielding displacement of the equivalent bilinear capacity curve in SDOF of the building with metallic dampers.

Finally, Table 72 list base shear strength and the displacement of the idealized trilinear and bilinear capacity curves in SDOF, while Figure 102 plot the curves. These results are congruent with the pushover analysis from SAP2000 reported later, verifying the finite element model and the design procedure.

TRILINEAR					BILINEAR EQUIVALENT				
	MODAL		UNIFORM			MODAL		UNIFORM	
	D(mm)	V	D(mm)	V		D(mm)	V	D(mm)	V
	0,00	0,00	0,00	0,00		0,00	0,00	0,00	0,00
<b>Dyd</b>	5,61	285,80	5,61	298,23	<b>Do</b>	51,02	851,27	49,15	929,70
<b>dyf</b>	93,02	1418,78	86,47	1549,50	<b>dy</b>	85,03	1418,78	81,92	1549,50
<b>du</b>	129,59	1418,78	140,31	1549,50	<b>du</b>	129,59	1418,78	140,31	1549,50

Table 72. Idealized trilinear and bilinear equivalent capacity curve in SDOF of the retrofit building with metallic dampers according with the Technical Report MCEER-00-0010

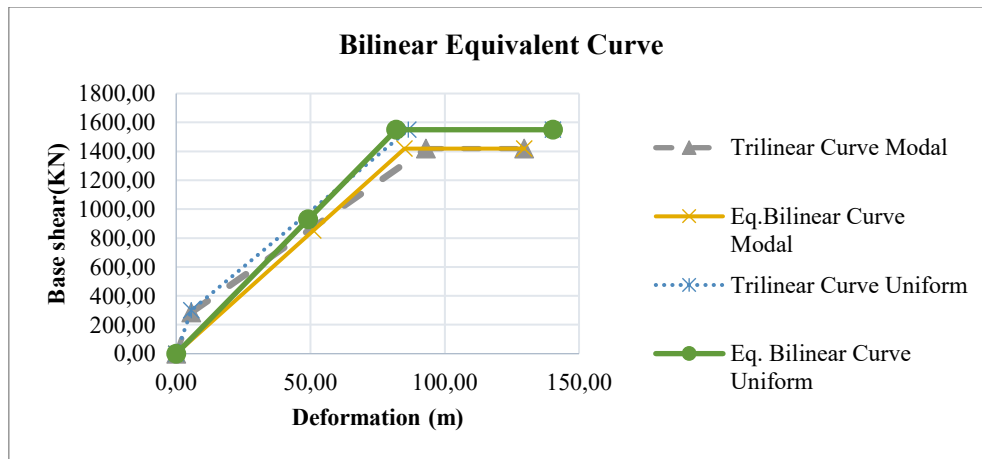


Figure 102. Trilinear curve and equivalent bilinear curve of the retrofit building with metallic dampers according with the Technical Report MCEER-00-0010.

### 8.2.2 Static pushover curve in SAP2000:

Table 73 and Table 74 report the profile of forces for modal and uniform case, the effective mass, and the participation factor calculated in Chapter 5; as well known, these parameters do not change with the implementation of the metallic dampers.

<b>Z(m)</b>	<b><math>\emptyset_{xNi}</math></b>	<b>W(KN)</b>	<b>Wi(KN)</b>	<b>Modal</b>		<b>Uniform</b>	
				<b>WiN</b>	<b>WiN/c</b>	<b>WiNR</b>	<b>WiNR/c</b>
12,5	1,00	814,23	814,23	1,00	0,11	1,0	0,11
9,5	0,86	842,68	723,12	0,89	0,10	1,0	0,11
6,5	0,61	842,68	510,44	0,63	0,07	1,0	0,11
3,5	0,31	852,49	265,17	0,33	0,04	1,0	0,11
0	0	0,00	0,00	0,00	0,00	0	0,00

Table 73. Pushover profiles: Modal and Uniform.

<b>Z(m)</b>	<b>U<sub>x</sub></b>	<b>Total mass(TON)</b>	<b><math>\emptyset_{xN}</math></b>	<b><math>m_i^* \emptyset_{xN}</math> (TON)</b>	<b><math>m_x^*(TON)</math></b>
12,5	0,0733	83,0	1,00	83,00	235,77
9,5	0,0629	85,9	0,86	73,71	<b><math>\emptyset_{xN}^* m^* \emptyset_{xN}</math></b>
6,5	0,0444	85,9	0,61	52,03	186,18
3,5	0,0228	86,9	0,31	27,03	<b><math>\Gamma_x</math></b>
0	0	0	0,00	0,00	1,266

Table 74. Modal participation factor and effective mass.

The characteristics of the load case are listed below:

- Load application control: Displacement control. The monitored node is joint 50 in UX direction, corresponding to the center of masses of the last story.
- Analysis type: Static Nonlinear.
- Initial conditions: Static nonlinear analysis which assess the effects of the dead loads on the structural elements.
- Load pattern: Pushover X modal and Pushover X uniform. (Horizontal concentrated loads). Analysis ran separately.
- According to the EUROCODE, the analysis is run once the base shear reaches 80% of maximum force.
- Setting the kinematical constraints to move in the X-X coordinates solely; therefore, the rotational contribution of the main concentrated mass floor was neglected [1]. The Plane Frame setup establishes the condition required by allowing the displacement in the X and the Z direction and the rotation in the Y direction.
- The forces' profile (Table 28) was applied on the story columns instead of the center of masses of the floor.

Finally, the capacity curve is obtained from SAP2000. Figure 103 illustrates the real performance of the structure in MDOF. In addition, it can be seen the excellent ductility performance of the structure; there is not any important brittle failure on beams and columns. However, there is a lower ductility capacity in the pushover curve than the previously computed in Chapter 5 due to software limitations. Once the curves arrive at the larger displacement, the system's stiffening is a secondary effect of the metallic dampers. In the analysis, the software changes the local reference system of the damper, and instead of been subjected to lateral force, the structure starts to stretch the equivalent plates as if they were in a uniaxial tension



solicitation. Nonetheless, the effect does not affect the results because it is far away from the seismic ductility demand of the building. Thus, the maximum displacement is the displacement where starts the phenomenon described previously.

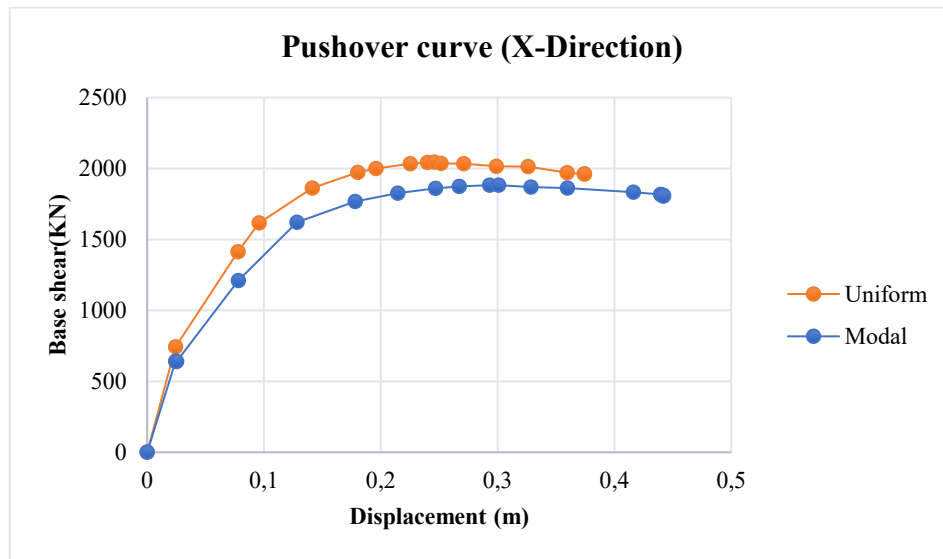


Figure 103. Pushover curve obtained from SAP2000 in MDOF for structure with metallic dampers.

The equivalent bilinear curve is assessed following the NTC 18 and EC8 [6]. The approach is based on elastic energy equivalence; therefore, the arcs from Figure 103 and the bilinear shape must have the same area under the curve. For this purpose, a code in MATLAB has been created. Besides, the bilinear shape is used to describe in a simple shape the capacity curve obtained from SAP2000 and to the safety factors calculation. Figure 104 illustrates the definition of the equivalent bilinear curve, while Table 75 and Table 76 show the results regarding the stiffness, base shear strength, displacements, and energy.

Modal		Rectangular	
d	F	d	F
m	KN	m	KN
0.00	0.00	0.00	0.00
0.12	1831.10	0.09	1942.80
0.44	1831.10	0.37	1942.80

Table 75. Bilinear curve (MDOF).

	Modal	Uniform	
<b>0.6F<sub>max</sub></b>	1129.776	1227.259	KN
<b>d<sub>y</sub></b>	0.071	0.055	m
<b>K*</b>	15990	22245	KN/m
<b>dy*</b>	0.1154	0.0873	m
<b>Fy*</b>	1831.10	1942.80	KN
<b>du</b>	0.442	0.374	m
<b>E</b>	7.25E+02	6.62E+02	KN m

Table 76. Output - Bilinear capacity curve (MDOF)

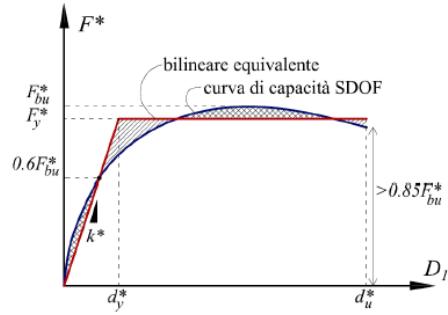


Figure 104. Definition of the equivalent bilinear curve[13]

Figure 105 contrasts the equivalent bilinear capacity curve and the capacity curve obtained from SAP2000 in MDOF. In addition, Figure 106 and Figure 107 confronts the capacity curves calculated previously following the Technical Report MCEER-00-0010 with the equivalent bilinear curve calculated from the pushover curve obtained from SAP2000 following the recommendations of the EC8 and the NTC18.

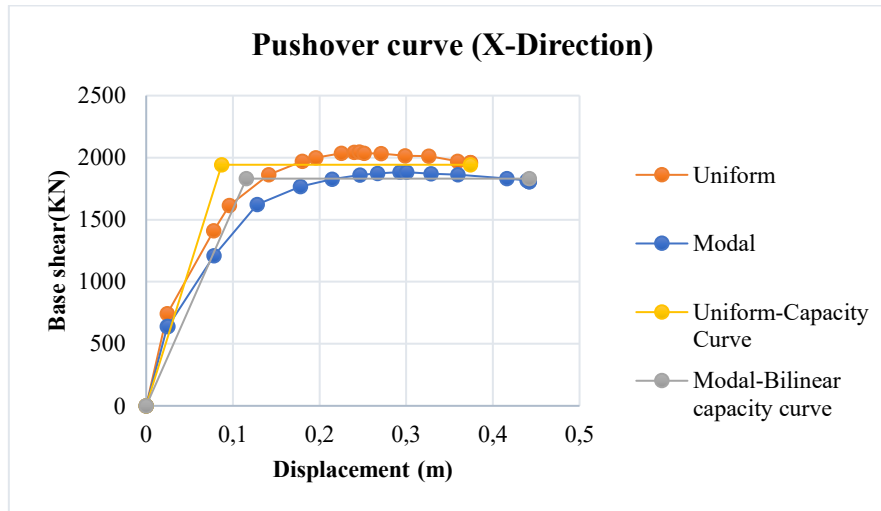


Figure 105. MDOF Pushover Curve vs Bilinear Pushover Curve.

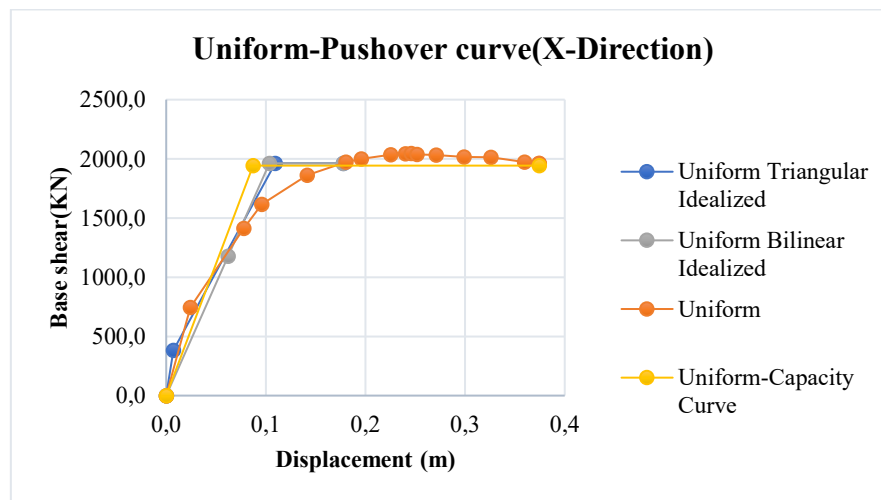


Figure 106. Idealized pushover curves and pushover curves from SAP2000 – Uniform case.

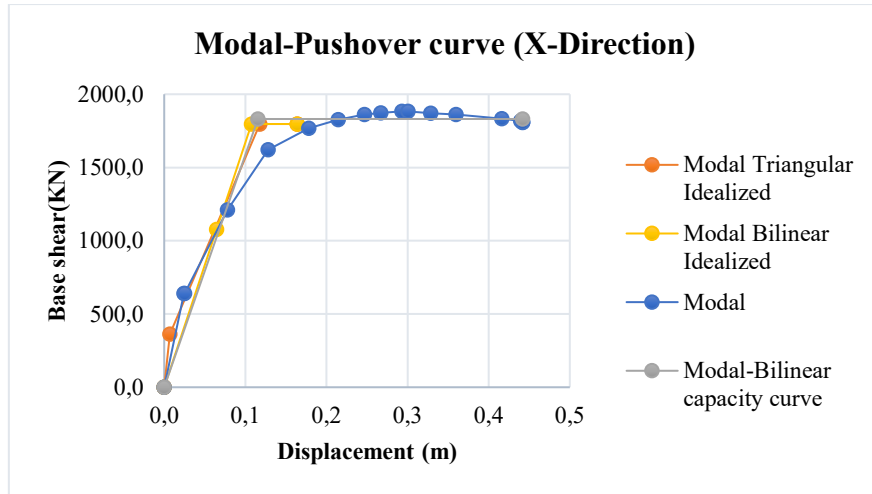


Figure 107. Idealized pushover curves and pushover curves from SAP2000 – Modal case.

The uniform and modal cases provide an excellent approximation between the curves. However, the uniform case presents an offset in the displacement. This imprecision is produced because the Technical Report MCEER-00-0010 assumes the horizontal loads proportional to the first mode [28] and the uniform case is proportional to the higher mass of the stories. In conclusion, the equivalent geometry of the dampers, the chevron bracing configuration, and the load case definition on the program are done correctly.

### 8.2.3 SDOF-Bilinear Equivalent Curve

The bilinear equivalent curves in SDOF are required to execute the safety evaluation of the building. They are obtained from the MDOF system by dividing the displacement and base shear force by the participation factor ( $\Gamma$ ):

$$F^* = \frac{F}{\Gamma} ; d^* = \frac{d}{\Gamma} \quad (69)$$

Where:

- $F$  and  $d$ : base shear force and displacement from the MDOF.
- $F^*$  and  $d^*$ : base shear force and displacement from the SDOF.

Table 78 summarizes the calculations regarding the base shear strength and displacement in MDOF and SDOF. The reduction factor is 1.266, according to Chapter 5.

Modal Pushover (MDOFS)		Modal Pushover (SDOFS)	
Top displacement	Base reaction	Top displacement	Base reaction
(m)	KN	(m)	KN
0,00	0,00	0,00	0,00
0,12	1831,10	0,09	1445,92
0,16	1831,10	0,13	1445,92

Table 77. MDOF capacity curve to SDOF capacity curve for the retrofit building with metallic dampers.

Uniform Pushover (MDOFS)		Uniform Pushover (SDOFS)	
Top displacement	Base reaction	Top displacement	Base reaction
(m)	KN	(m)	KN
0,00	0,00	0,00	0,00
0,09	1942,80	0,07	1534,13
0,18	1942,80	0,14	1534,13

Table 78. MDOF capacity curve to SDOF capacity curve for the retrofit building with metallic dampers.

Figure 108 illustrates the bilinear capacity curve transformation from the MDOFS to the SDOFS:

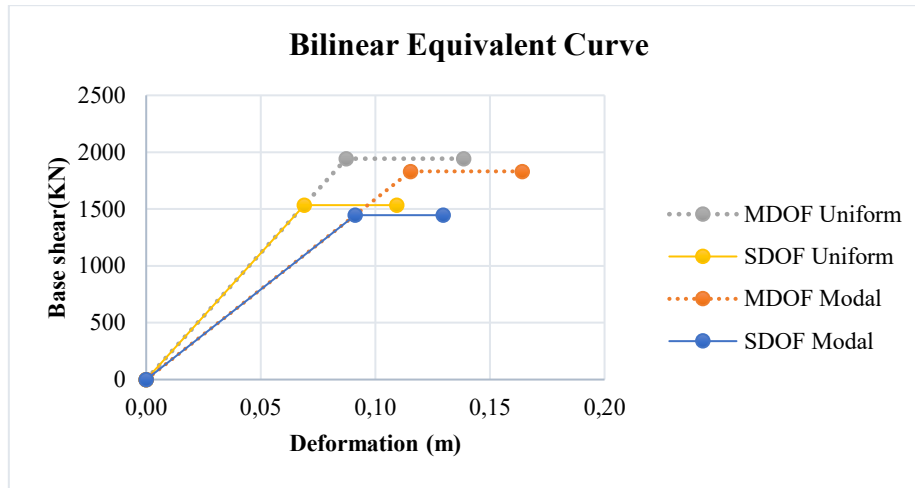


Figure 108. Bilinear capacity curve (MDOF-SDOF) for retrofit building with metallic dampers.

The effective stiffness ( $K^*$ ) obtained from the capacity curve as the ratio between the base shear and the last story displacement represents the structure's overall stiffness in a simple coefficient. In addition, the ultimate displacement ( $du'$ ) is 150% of the target displacement, following the Eurocode. Table 79 shows the ultimate and yielding displacement, yielding force and effective stiffness of the capacity curves for modal and uniform cases in SDOF:

Modal	$du'$ (m)	$F_y^*$ (KN)	$dy^*$ (m)	$K^*$ (KN/m)
X(+)	0,130	1445,92	0,091	15867,42
Uniform	$du'$ 0.85(m)	$F_y^*$ (KN)	$dy^*$ (m)	$K^*$ (KN/m)
X(+)	0,140	1534,13	0,069	22254,30

Table 79. Effective stiffness of for retrofit building with metallic dampers.

Where:

- $K^* = \frac{F_y^*}{d_y^*} \rightarrow$  Effective stiffness.
- $F_y^*$ : Yielding base share from the SDOF.
- $d_y^*$ : Yielding displacement from the SDOF.
- $du' \rightarrow$  Ultimate displacement equal to 1.5 times the displacement of the performance point from the ADRS (Figure 110 and 111).

#### 8.2.4 Seismic Demand Linked to The Effective Period:

The seismic demand associated with the response spectrum is required to make the safety evaluation of the structural performance. Therefore, for each distribution of load (modal and uniform) is calculated the effective stiffness ( $K^*$ ) from the bilinear capacity curve (SDOF), to calculate the effective period associated with the elastic stage ( $T^*$ ). In addition, it is calculated the elastic displacement related to the effective period ( $Sde(T^*)$ ) to compare it with the maximum displacement capacity of the system:

Effective period ( $T^*$ ):	Elastic base shear demand from the response spectrum ( $F_E^*$ ):
$T^* = 2 * \pi * \sqrt{\frac{m^*}{k^*}} \quad (70)$	$F_E^* = Sae(T^*) * 9.81 \frac{m}{s} * m^* \quad (71)$
Elastic displacement demand from the response spectrum $Sde(\omega)$ :	
$Sde(\omega) = Sae(T^*) * \frac{9.81 \frac{m}{s^2}}{\omega^2} \quad (72)$	

Table 80. Effective period, elastic base shear and displacement demand from response spectrum. [26]

Where:

- $K^* = \frac{F_y^*}{d_y^*} \rightarrow$  Effective stiffness.
- $m^* \rightarrow$  Equivalent mass from Equation 26 and Table 22.
- $Sae(T^*)$ : Elastic acceleration associated with the effective period.
- $\omega \rightarrow$  Effective frequency (rad/s).

The results are summarized in the next table for the modal and the uniform case.

Modal	$m x^*(TON)$	$T^*(s)$	$T_c^*(s)$	$Sae(g)$	$SDe(m)$	FE (KN)
X(+)	235,77	0,77	0,5	0,59	0,086	1357,71
Uniform	$m x^*(TON)$	$T^*(s)$	$T_c^*(s)$	$Sae(g)$	$SDe(m)$	FE (KN)
X(+)	235,77	0,65	0,5	0,70	0,072	1607,91

Table 81. Response spectrum demand.

In comparison to the results from Chapter 5, as expected, it is obtained lower effective period, smaller elastic displacement demand, higher elastic shear base demand and larger effective stiffness.

#### 8.2.5 Safety Checks

The safeness verification is executed by comparing the demand and the capacity in terms of displacement. If the capacity is greater than the demand, the structure can withstand the seismic design demand through the linear or nonlinear structural performance. In addition, the ductility is verified with the acceleration response spectrum (ADRS) using the elastic and inelastic response spectrum.

### 8.2.5.1 Ductility Evaluation:

According to the NTC18 and EC8, to verify the structure's safety, the ductility capacity must be greater than the ductility demand ( $\mu_c \geq \mu_d$ ). To assess the ductility demand, the relations between the reduction factor ( $q$ ), ductility ( $\mu$ ), and period ( $T$ ) are evaluated to calculate the inelastic response spectrum with constant ductility following the N2-A Method from NTC18 [27]. Table 29 shows the sequence of calculations for the relationship  $q - \mu - T$ :

1. The reduction factor is defined as: $q^* = \frac{F_E^*}{F_y^*} \quad (73)$	2. The ductility capacity is defined as: $\mu_c = \frac{d_y^*}{d_u^*} \quad (74)$
3. The demand is calculated by means of the following relationship: $\mu_d = q^* ; (T^* \geq T_c) \quad (75)$ $\mu_d = (q^* - 1) * \frac{T_c}{T} + 1 ; (T^* < T_c) \quad (76)$	

Table 82. Relations between the reduction factor, ductility, and period ( $q - \mu - T$ ). [26]

Where:

- $\mu_c$ : Ductility capacity.
- $\mu_d$ : Ductility demand.
- $q^*$ : Reduction factor.
- $F_E^*$ : Base shear demand.
- $F_y^*$ : Yielding shear capacity from the SDOFs.
- $T^*$ : Equivalent fundamental period.
- $T_c$ : Period from response spectrum.
- $d_y^*$ : Yielding displacement of the bilinear model.
- $d_u^*$ : Ultimate displacement equal to 1.5 times the displacement of the performance point from the ADRS (Figure 64 and 65). The value is reported in Table 25 and 26.

Table 83 shows that the improvement of ductility is not required; the ductility ( $\mu_d$ ) is lower than the ductility capacity ( $\mu_c$ ) in both cases. The damper-bracing system implementation produce an overall change in the seismic response; the modal case does not exert inelastic response, while the uniform case generates a demand lower than in the pre-retrofit structure. In addition, the ductility capacity of the system for modal and uniform case also decreases in comparison with Chapter 5 because the addition of stiffness.

<b>Modal</b>	<b>q*</b>	<b>μ d</b>	<b>μ c</b>
X(+)	0,94	0,94	1,42
<b>Uniform</b>	<b>q*</b>	<b>μ d</b>	<b>μ c</b>
X(+)	1,05	1,05	1,59

Table 83. Reduction factor, ductility demand and ductility capacity.

### 8.2.5.2 Acceleration-Displacement Response Spectrum (ADRS):

The method aims to verify the results from the ductility evaluation with a visual estimation of the intersection between the inelastic spectrum and the bilinear equivalent curve. The intersection is known as performance point (PP), and the components must match with the demand  $S_{ai}$  and  $S_{Di}$ . Figure 109 illustrates the elastic spectrum, the inelastic spectrum with the required ductility demand, and the capacity curve (SDOF) obtained from the nonlinear pushover analysis. The following equations obtain the ADRS[26]:

Elastic Displacement Spectrum	Inelastic ADRS
$Sd_e = Sa_e * \frac{1}{\omega^2} = \frac{T^2}{4\pi^2} Sa_e \quad (77)$	$Sa_i = Sa_e * \frac{1}{q^*(\mu_d, T)} ; Sd_i = Sd_e * \frac{\mu_d}{q^*(\mu_d, T)} \quad (78)$

Table 84. Response spectrum equations (ADRS)

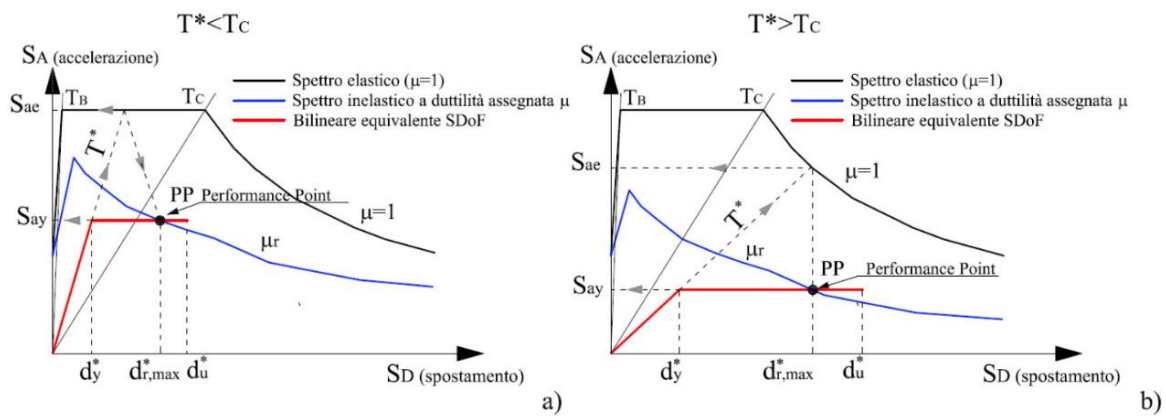


Figure 109. Verification procedure with ADRS: a)  $T^* < T_c$  ; b)  $T^* > T_c$ . [26].

Figure 110 and Figure 111 illustrate the results of Table 81 and evidence that the effective period is higher than  $T_c$ . In addition, the modal case does not have an inelastic response, producing a performance point related to the elastic displacement. On the other hand, the uniform case has a low inelastic solicitation, almost insignificant; the performance point is related to the inelastic displacement. Henceforth, the performance points related to this structure are not considered to the device's design, only is used to confront the intervention strategies later.

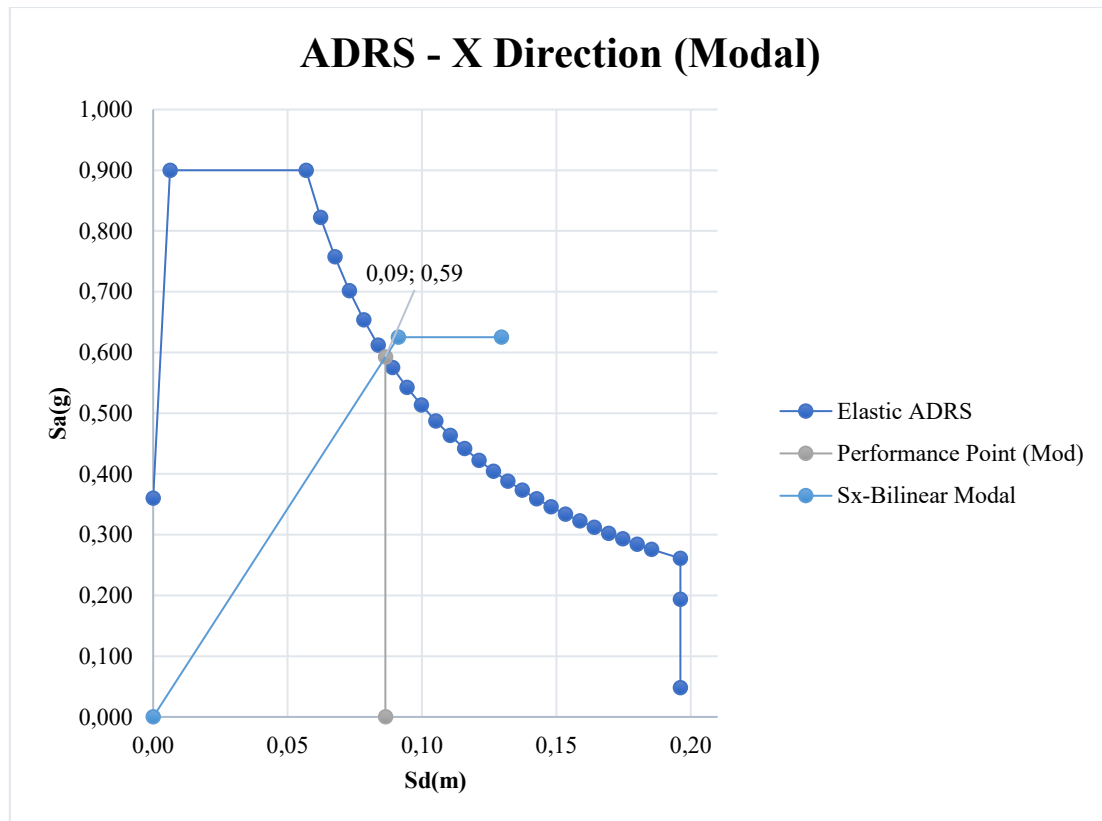


Figure 110. ADRS-Ductility Verification: Modal Case - Retrofit structure with metallic dampers.

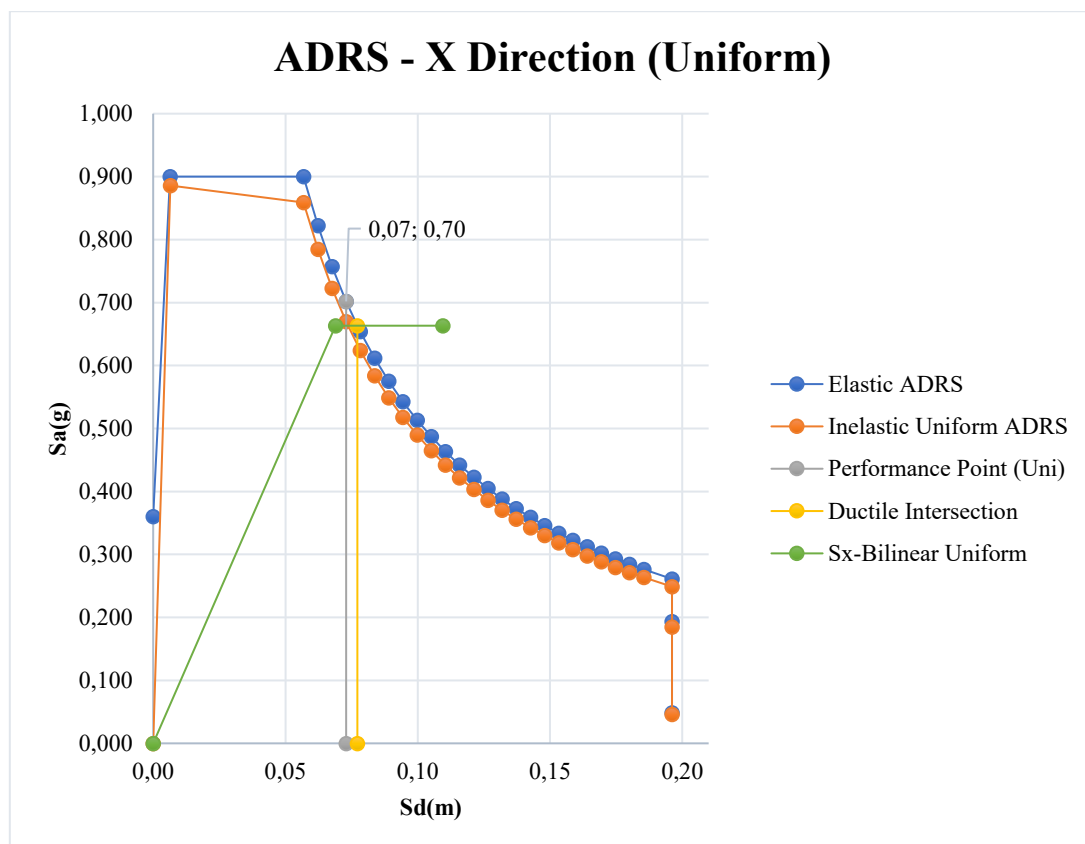


Figure 111. ADRS-Ductility Verification: Uniform Case – Retrofit structure with metallic dampers.



According to the safety verification, the following annotations can be done:

- The retrofit with metallic dampers and bracing system reduces the ductility demand and ductility capacity due to the increment of stiffness in the structure.
- The damper-bracing system produce increment in the base shear strength, what represents an increment of internal forces in the structural elements connected with the system. The increment of internal forces is evaluated in Chapter 9.
- The performance point for the modal and uniform case in Figure 110 and Figure 111 complies with the seismic demand linked to the effective period reported in Table 81.

### **8.3 Nonlinear Time-history Analysis**

The analysis is executed on SAP2000, setting the kinematical constraints to move in the X-X coordinates solely. The Plane Frame setup establishes the condition required by allowing the displacement in the X and the Z direction and the rotation in the Y direction. In the other hand, the time functions used to execute the analysis are the seven accelerograms mentioned in Chapter 3. The Hilber-Hughes-Taylor algorithm (HHT) is the nonlinear direct integration method applied to obtain structural response under dynamic loading. It is an implicit method from Newmark Algorithms Family that improves the rate of convergence without affecting the accuracy of results.

The load case is run with the following input data:

- Initial conditions: Continue analysis from state at end of static nonlinear analysis.
- Geometric parameters: None
- Stiffness-Proportional damping of stiff elements produced on nonlinear objects is considered in the analysis. The coefficients are computed automatically by the software in function of 2 different periods.
- Nonlinear behavior is capture by the strain-stress model of the materials and cross sections. As well as the nonlinear link properties.
- Time integration: Parameter alpha ( $\alpha$ ) set as -0.33.

Figure 12 shows the configuration of the time-history analysis using the accelerogram two. In addition, the number of Output Time Steps vary according to the duration of each input time function, while the Output Time Step Size is set as 0.04 for all cases.

**Load Case Name**  
TH2 Set Def Name Modify/Show...

**Initial Conditions**  
☐ Zero Initial Conditions - Start from Unstressed State  
☒ Continue from State at End of Nonlinear Case STATIC LOADS  
 Important Note: Loads from this previous case are included in the current case

**Modal Load Case**  
 Use Modes from Case Modal analysis

**Loads Applied**

Load Type	Load Name	Function	Scale Factor
Accel	U1	TH 2	1
Accel	U1	TH 2	1

Add Modify Delete

☐ Show Advanced Load Parameters

**Time Step Data**  
 Number of Output Time Steps: 1206  
 Output Time Step Size: 0,04

**Other Parameters**  
 Damping: Proportional Modify/Show...  
 Time Integration: Hilber-Hughes-Taylor Modify/Show...  
 Nonlinear Parameters: User Defined Modify/Show...

**Load Case Type**  
Time History Design...

**Analysis Type**  
☐ Linear ☐ Modal  
☒ Nonlinear ☒ Direct Integration

**Solution Type**  
☒ None  
☐ P-Delta  
☐ P-Delta plus Large Displacements

**Geometric Nonlinearity Parameters**

**History Type**  
☒ Transient ☐ Consider Collapse  
☐ Periodic

**Mass Source**  
MSSSRC1

OK Cancel

Figure 112. Configuration of the time-history analysis on SAP2000– Retrofit Building with metallic dampers.

Figure 113 to Figure 116 show the relation, in absolute value, between the base shear and the displacement of the 4-story taking as reference joint the center of the masses of the last floor. It is done to know the effects of the different seismic actions acting on the structure. To verify the reliability of the results, Figure 113 to Figure 116 must match with the bilinear capacity curve in MDOF previously obtained.

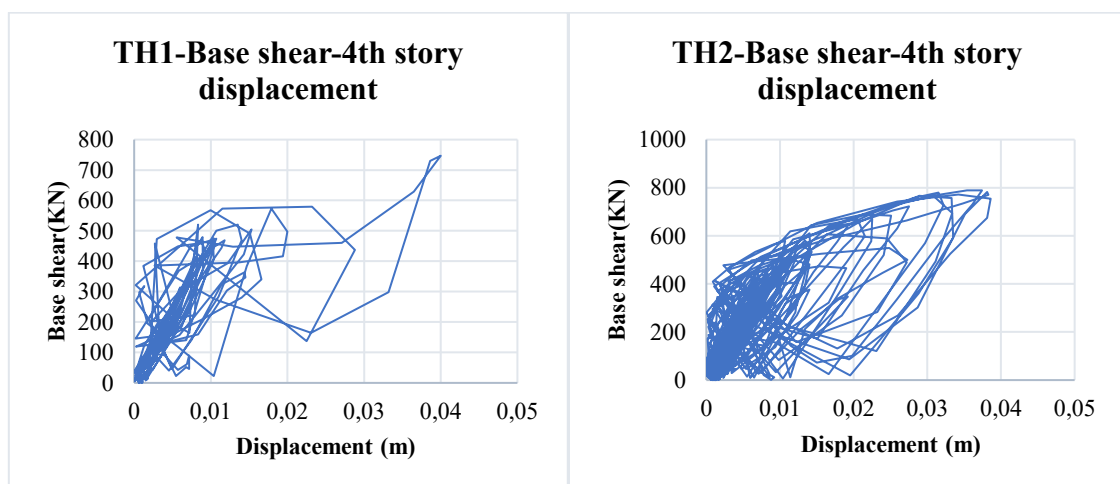


Figure 113. Base shear-4th Story Displacement for TH1 and TH2– Retrofit Building with metallic dampers.

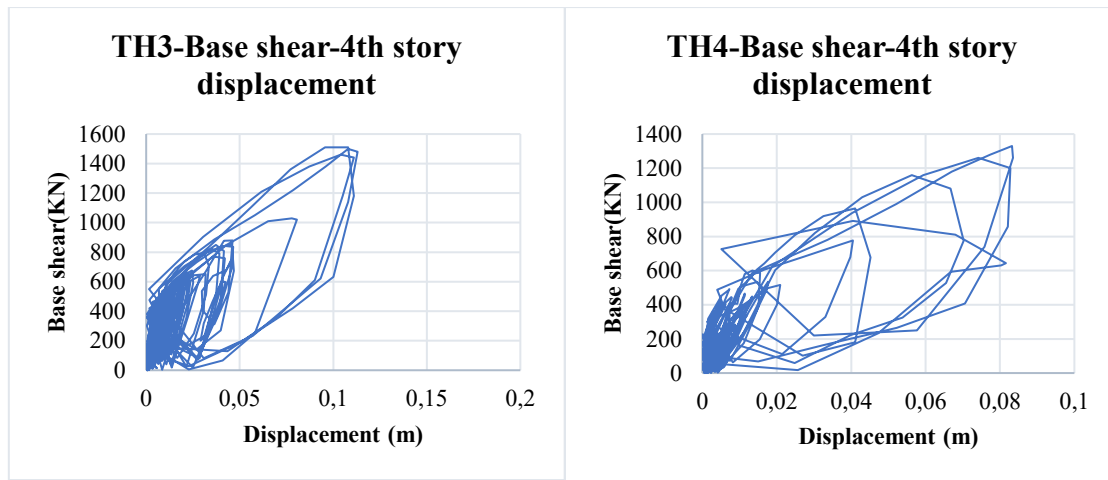


Figure 114. Base shear-4th Story Displacement for TH3 and TH4– Retrofit Building with metallic dampers.

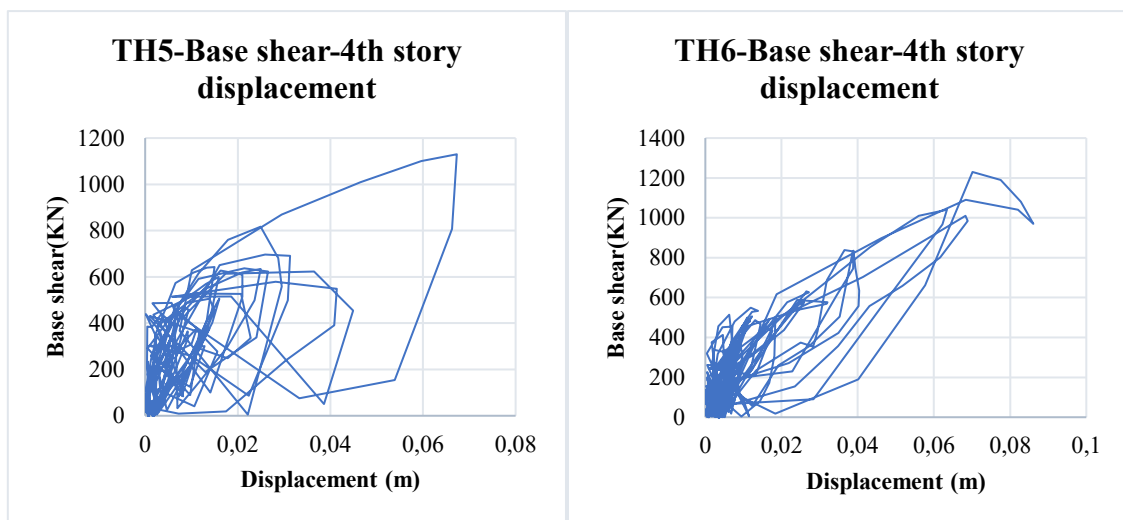


Figure 115. Base shear-4th Story Displacement for TH5 and TH6– Retrofit Building with metallic dampers.

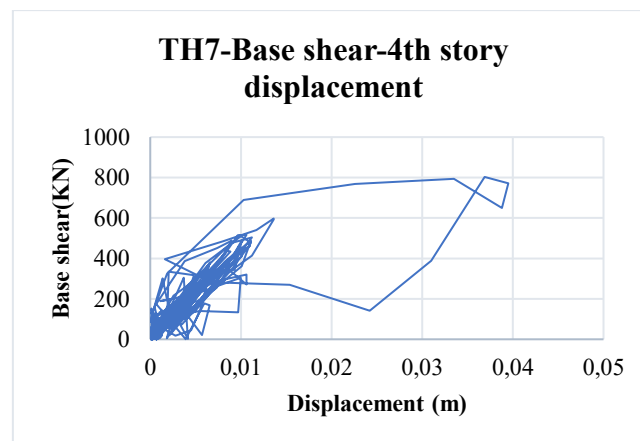


Figure 116. Base shear-4th Story Displacement for TH7– Retrofit Building with metallic dampers.

Figure 117 illustrates the dynamic response of the structure for the seven different accelerograms plotted below the equivalent bilinear pushover curve in MDOF for modal and uniform case; the effect of the metallic dampers is evident in comparison with the results from

Chapter 5, the average maximum demand is located on between both capacity curves in the elastic region, In addition, it checks the congruence between the dynamic response of the structure under seismic action and the simplified dynamic response of the structure obtained by the static pushover analysis. Lastly, Table 85 reports the maximum base shear and displacement of each time-history analysis, as well as the average maximum base shear and displacement. The analysis of the results and the comparison between the models is discussed in Chapter 9.

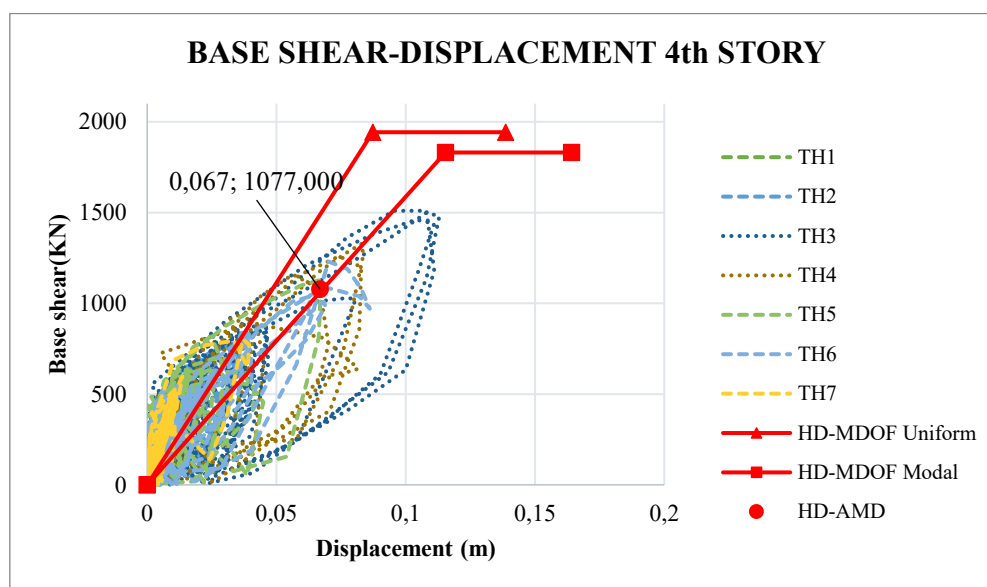


Figure 117. Bilinear Capacity Curve and TH results – Retrofit Building with metallic dampers.

TH	1	2	3	4	5	6	7	Average
d(m)	0,040	0,039	0,113	0,084	0,067	0,086	0,040	0,067
Fy(KN)	747	789	1510	1330	1130	1230	803	1077

Table 85. Retrofit Building with metallic dampers - Time-history maximum displacement and maximum base shear.

Based on the results from nonlinear dynamic and static analyses, the metallic dampers through the hysteretic cycle dissipate energy on the structure, reducing the displacements on the building. Figure 118 verifies the dampers' exact effect through the acceleration-displacement response spectrum with a 20% damping ratio. In addition, the average maximum demand from Table 44 is nearly accurate to the ADRS with the target damping ratio defined in Chapter 6. These results check the reliability of the design method applied and the configuration of the FE

model on SAP2000. Thenceforth, the comparison of both control solutions is made for the same seismic design demand.

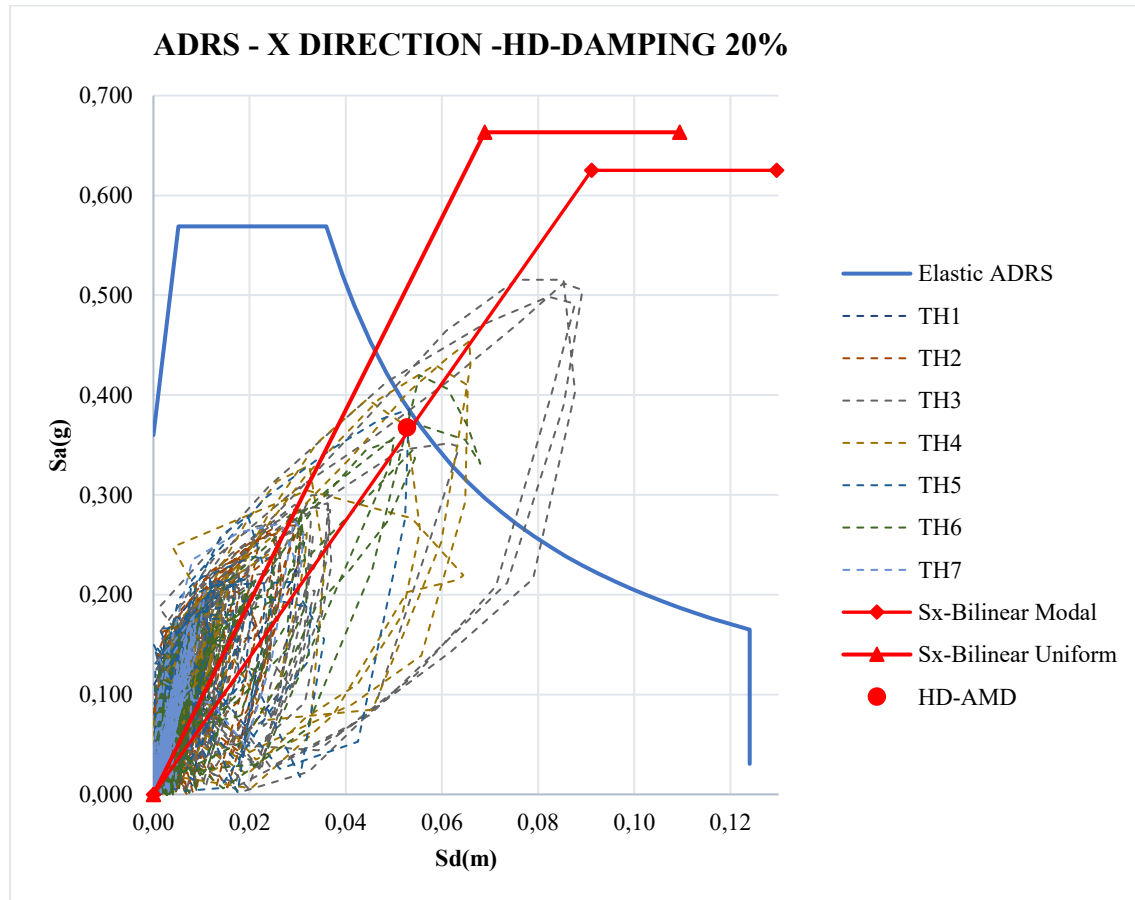


Figure 118. Checking damper effects using the ADRS with Damping 20% - Retrofit structure with metallic dampers.

Finally, Figure 119 and Figure 120 plot the structure's shape for the maximum interstory drift produced on the time-history analysis for the seventh accelerograms acting on the retrofit structure with fluid viscous dampers. The time-history TH3 and TH4 are the most critical cases like in the pre-retrofit structure; however, in this case, both cases behave similarly, achieving the same interstory drift and the shape, with a small difference in the 1st story; the maximum interstory displacement is 0.30% on the 2<sup>nd</sup> floor and 0.21% on the 3<sup>rd</sup> floor, respectively. Additionally, there is not steady shape at the maximum interstory drift considering all the cases in the structure. Regarding the average shape, the maximum drift is equal to 0.16% and it is produced on the 2nd floor.

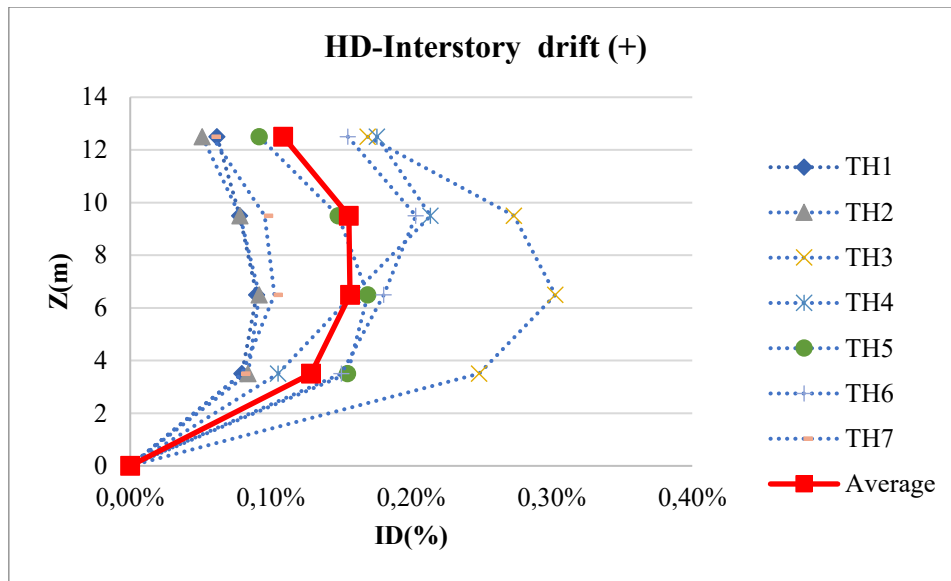


Figure 119. Maximum interstory displacement of time-history analysis - Positive direction, retrofit structure with MYD.

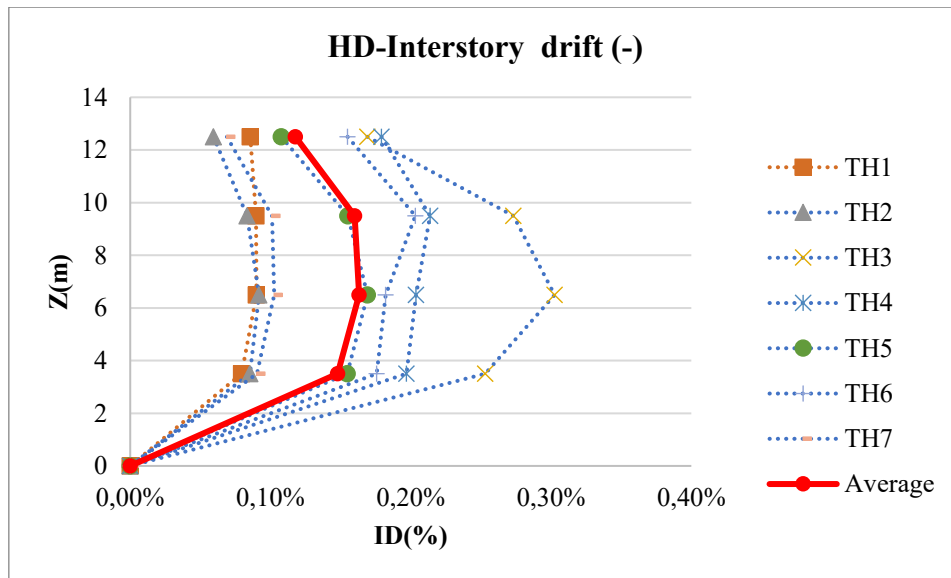


Figure 120. Maximum interstory displacement of time-history analysis - Negative direction, retrofit structure with MYD.

## Chapter 9

### 9 Analysis of the results

This chapter discusses the results from the structural analyses reported in Chapters 5, 7, and 8 to determine the effects of the implementation of the dissipative devices as a control strategy for seismic action based on the vulnerability index, the internal forces, and the interstory drifts. The main goal is to identify the advantages and drawbacks of the control solutions applied in this paper.

#### 9.1 Vulnerability index

The vulnerability index is used to describe the overall seismic performance in the most straightforward possible representation. The method utilized is based on the capacity curve in SDOF from pushover analysis and the design response spectrum. According to the current Italian Standards, the index can be written as:

$$\xi = \frac{F_{Collapse}^*}{F_{max}^*} \quad (79)$$

Where:

- $F_{Collapse}^*$ : Maximum bearable base shear strength from the capacity curve in SDOF of the existing building.
- $F_{max}^*$ : Maximum base shear force required to design the same structure accordingly to the NTC18.

In this case, the evaluation of the performance between the control strategies applied is based on the increment of the vulnerability index, which represents the reduction of the level of damage faced for the building once the seismic event happens. For this goal, the base shear of collapse refers to the yielding base shear strength from capacity curves in SDOF obtained in Chapters 5, 7, and 8. On the other hand, the maximum base shear force required is obtained from the response spectrum from Chapter 3 for the damping ratio of 5% and 20%, standard damping ratio and target damping ratio of the retrofit intervention, respectively. Table 86 reports the results from the equation. The bare frame refers to the pre-retrofit building, and the braced to the building with the dissipative devices; FVD indicates fluid viscous dampers and MYD means metallic yielding dampers.

<b>Frame</b>	<b>F Collapse</b>	<b>F* Collapse</b>	<b>F*max</b>	<b><math>\zeta</math></b>	<b><math>\xi</math></b>
	<b>KN</b>	<b>KN</b>	<b>KN</b>	<b>Damping ratio</b>	
Bare	1376.11	1086.64	1127.31	5%	0.96
Braced FVD	1376.11	1086.64	712.69	20%	1.52
Braced MYD	1886.95	1490.48	937.81	20%	1.59

Table 86. Vulnerability indexes by Pushover Method - Force criterium.

According to the results, both dissipative devices increase the vulnerability indexes of the building by 58% and 66%, allowing the bare frame to behave in the elastic stage during the seismic action while the devices dissipate energy, as shown in Figure 121. However, the internal forces and interstory drifts must be calculated to check the reduction of the vulnerability. The increment of the internal forces has an essential role in the retrofit interventions and the meaning of the index; if these increments too much, the vulnerability will not decrease. Furthermore, the internal forces increment may create partial or total damage on columns or beams despite the reduction of the interstory drift, which produces that the index does not represent the improvement of the overall performance of the building.

Figure 121 shows the acceleration-displacement response spectrum (ADRS) for 5% and 20% of damping, the capacity curves in SDOF for the building, and the average maximum demand (AMD), which describe the average of the maximum displacement and base shear force regards the time-history analysis with the seven accelerograms. In addition, The  $S_x$  indicates the bilinear equivalent capacity curve in the X direction, the BF refers to the pre-retrofit building, the FVD signifies fluid viscous dampers, and the MYD means metallic yielding dampers. Consequently, it can be seen the different effects for each intervention. Regarding the fluid viscous damper, the capacity curve is the same as in the case BF because there is no stiffness addition, while the dissipation achieves the desirable one of 20%. On the other hand, the metallic-yielding damper, despite change the capacity curve due to the stiffness addition, can accomplish the same desirable damping ratio of 20%. Both average maximum demands for FVD and MYD are placed on the ADRS for 20%, and the calculation can be seen in Table 87. Maximum displacement and pseudo-acceleration from nonlinear time-history analysis of the structure with and without dampers. It can be concluded the reduction of the seismic design demand of the building through the dissipative devices of the two different approaches. The simplified methodologies using a strain-energy method can be used to obtain very accurate results.



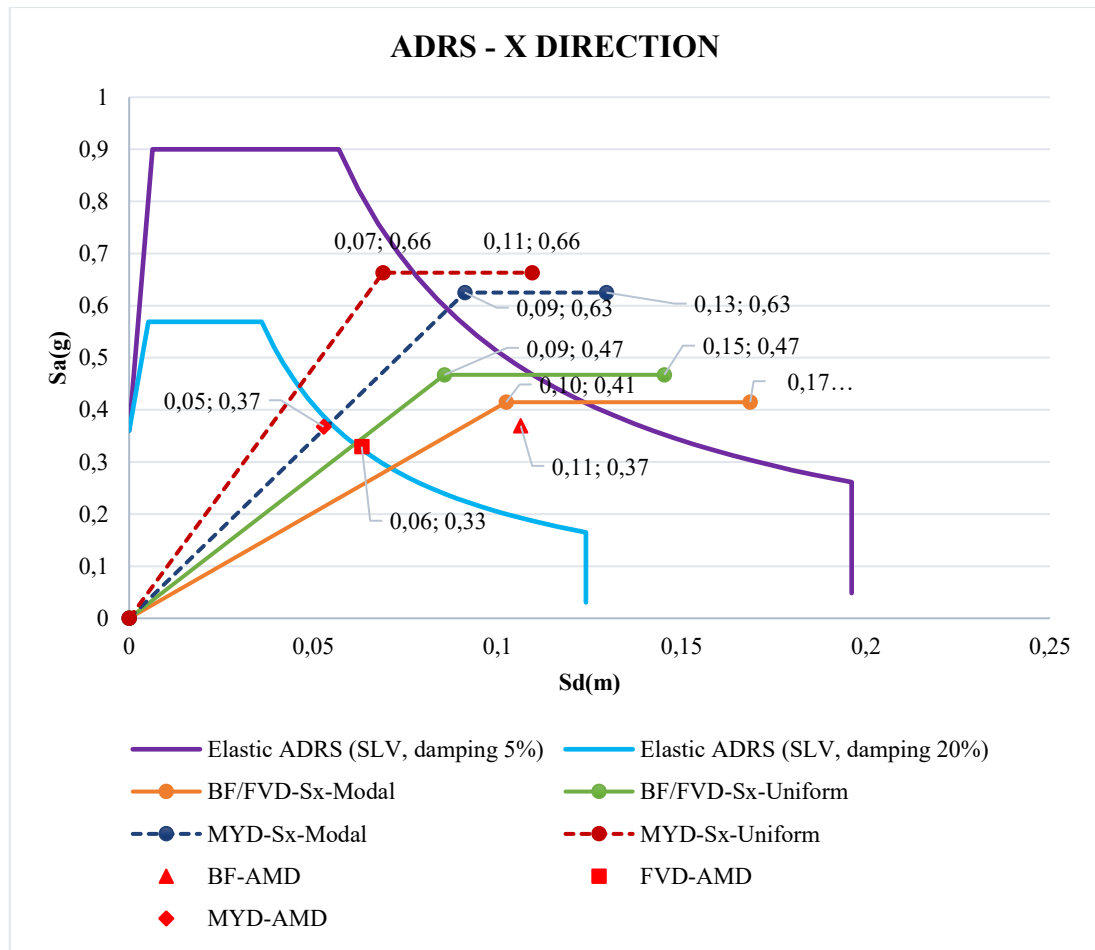


Figure 121. Acceleration-displacement response spectrum for 5% and 20% of damping, maximum average demand and equivalent bilinear curves for structure with and without dampers.

BARE FRAME- TIME-HISTORY ANALYSIS								
TH	1	2	3	4	5	6	7	Average
d(m)	0.07	0.10	0.16	0.15	0.10	0.10	0.08	0.11
S(g)	0.27	0.39	0.42	0.43	0.33	0.42	0.33	0.37
FVD-BRACED FRAME - TIME-HISTORY ANALYSIS								
TH	1	2	3	4	5	6	7	Average
d(m)	0.04	0.04	0.10	0.10	0.06	0.07	0.03	0.06
S(g)	0.21	0.26	0.46	0.44	0.32	0.39	0.22	0.33
MYD-BRACED FRAME - TIME-HISTORY ANALYSIS								
TH	1	2	3	4	5	6	7	Average
d(m)	0.03	0.03	0.09	0.07	0.05	0.07	0.03	0.05
S(g)	0.26	0.27	0.52	0.45	0.39	0.42	0.27	0.37

Table 87. Maximum displacement and pseudo-acceleration from nonlinear time-history analysis of the structure with and without dampers

## 9.2 Internal forces

Figure 122 represent the effect of the dissipative devices on the structure, as well than Figure 121. However, in this case the effects are reported in terms of base shear force and roof deformations at MDOF, instead the accelerations and roof displacements at SDOF. Regards to

the capacity curves, the yielding base shear strength is increased 42% and 51% and the yield displacement is reduced 19% and 11%, both for the uniform and modal case, respectively. What represent an increment of the internal forces acting on the columns and beams connected to the bracing system. Additionally, according to the average maximum demand (AMD), the MYD reduce the displacement while the base shear force remains almost equal than the one obtained from the building without dampers, while the FVD reduces the displacement and the base shear. Table 88 list the maximum roof displacements and base shear force for the time-history analyses of the building with and without dissipative devices.

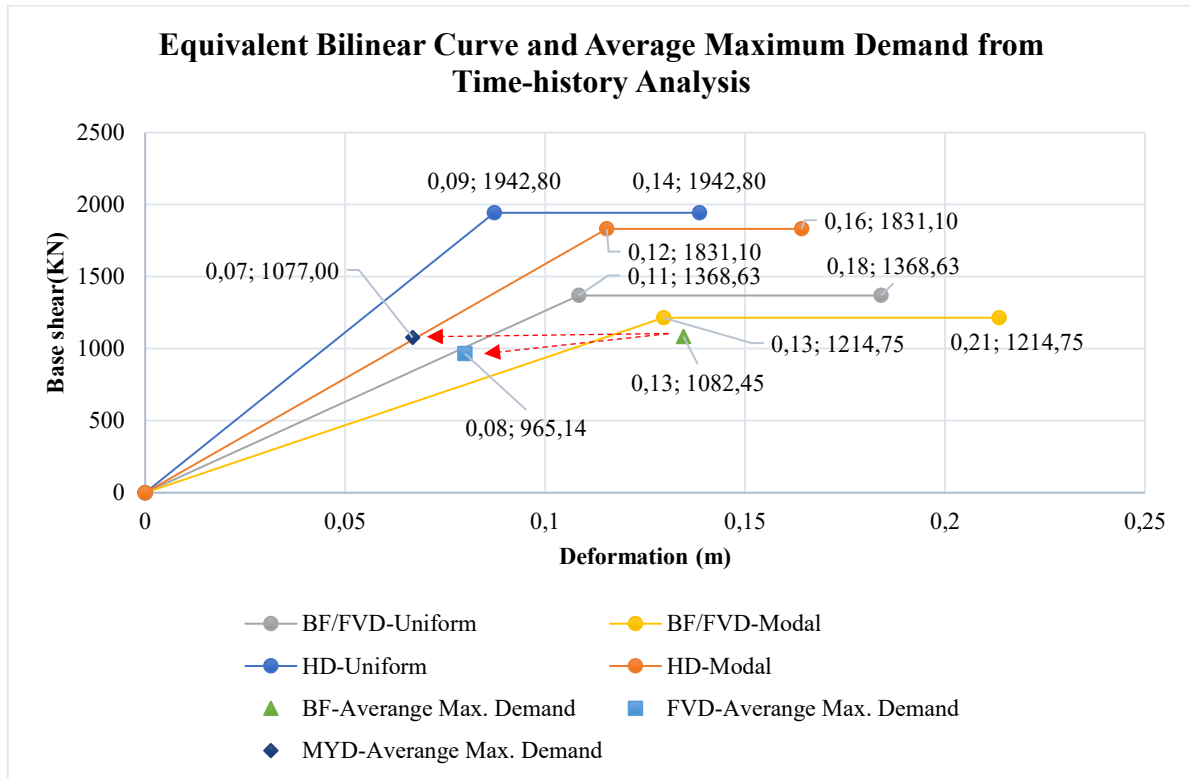


Figure 122. Bilinear equivalent curves and average maximum demand from time-history analysis

BARE FRAME- TIME-HISTORY ANALYSIS								
TH	1	2	3	4	5	6	7	Average
d(m)	0.08	0.13	0.20	0.19	0.12	0.12	0.10	0.13
F(KN)	790	1140	1230	1260	980	1220	957	1082
FVD-BRACED FRAME - TIME-HISTORY ANALYSIS								
TH	1	2	3	4	5	6	7	Average
d(m)	0.05	0.06	0.12	0.12	0.08	0.09	0.04	0.08
F(KN)	627	753	1340	1300	948	1130	658	965
MYD-BRACED FRAME - TIME-HISTORY ANALYSIS								
TH	1	2	3	4	5	6	7	Average
d(m)	0.04	0.04	0.11	0.08	0.07	0.09	0.04	0.07
F(KN)	747	789	1510	1330	1130	1230	803	1077

Table 88. Maximum displacement and shear base from nonlinear time-history analysis of the structure with and without dampers.

Table 89 and Table 90 show the change in percentage of the base shear force and roof displacements of structure with fluid viscous dampers and metallic-yielding damper concerning the pre-retrofit structure. Also, Table 91 reports the variation of maximum response of the building with metallic-yielding dampers respect to the intervention with fluid viscous damper.

Table 89 reveals a reduction in displacement and forces, except for TH3 and TH4, due to the fluid viscous dampers. The increment is evidenced in the normal force acting on the ground level columns; the maximum normal force rises around 9% for TH3 and 3% for TH4, while the shear forces and flexural moment decrease (Table 94 to Table 97). Thus, the increment of the normal forces is insignificant, and the average of the structure's performance may be an excellent qualifier to summarize the behavior of the structure. In addition, the fluid viscous damper produces an average reduction of 41% in the roof displacement and 11% in the base shear of the building.

	TH1	TH2	TH3	TH4	TH5	TH6	TH7	TH av
dmax	-45%	-58%	-39%	-36%	-33%	-27%	-54%	-41%
Fmax	-21%	-34%	9%	3%	-3%	-7%	-31%	-11%

Table 89. Change in percentage of the displacement and base shear - Structure with fluid viscous dampers respect to the pre-retrofit structure.

Table 90 reports a reduction in displacement on all cases and the base shear force increment in 4 of the 7 cases due to the metallic dampers. The increase of base shear is evidenced in the internal forces on the elements interacting directly with the bracing system. On the one hand, the maximum normal force rises at a maximum of 23% and decreases at a minimum of 31%. In this case, the internal forces changing is important; the column must be verified by interaction diagram, as well as all the beams must be evaluated to verify the ultimate resistance in compression and tension. Additionally, the metallic-yielding damper produces an average reduction of 50% in the roof displacement and 1% in the base shear of the building.

	TH1	TH2	TH3	TH4	TH5	TH6	TH7	TH av
dmax	-52%	-71%	-43%	-56%	-45%	-31%	-59%	-50%
Fmax	-5%	-31%	23%	6%	15%	1%	-16%	-1%

Table 90. Change in percentage of the displacement and base shear - Structure with metallic yielding dampers respect to the pre-retrofit structure.

Table 91 indicates the variations in roof displacement and base shear force between the structure with metallic dampers and fluid viscous dampers. Regarding the displacement, the metallic damper generates a more significant reduction in all the cases, from 4% to 31%. On the other hand, concerning the base shear, the structure exerts higher base shear force in all cases, obtaining a minimum of 2% and a maximum of 22%. This behavior is due to the stiffness addition of the MYD. Moreover, the metallic-yielding damper produces an average reduction of 16% in the roof displacement and an increment of 12% in the base shear concerning the fluid viscous damper.

	TH1	TH2	TH3	TH4	TH5	TH6	TH7	TH av
dmax	-13%	-31%	-7%	-31%	-18%	-4%	-11%	-16%
Fmax	19%	5%	13%	2%	19%	9%	22%	12%

Table 91. Change in percentage of the displacement and base shear - Structure with metallic yielding dampers respect to the structure with fluid viscous dampers.

The internal forces were evaluated in all the structural elements of the building. In total, there are 72 beams and 72 columns distributed in the FE model on SAP2000. Regards the subdivision of the element in the analyses, the columns are discretized into 6, and the beams into 10, 14 or 22. Additionally, the envelope is applied to each element to compute the maximum normal force, shear force, and flexural moment. For this purpose, an Excel sheet has been programmed; it is considered 1104 sections for beams and 432 for columns in total in each time-history analysis. The following tables report the maximum percentage variation and the maximum numerical value variation of the average internal forces of the beams and columns of the building with dampers concerning the pre-retrofit building.

### 9.2.1 Retrofitted structure with fluid viscous dampers.

In general, the average internal forces of the beams and columns are reduced. In the most critical case (TH3), there is a slight increment in the normal force of the columns; however, interaction curve checks the resistance of the elements.

#### 9.2.1.1 Normal forces:

According to Table 92 and Table 93, the dissipative action of the fluid viscous damper generates on the average normal forces the following features concerning the pre-retrofit building:

- The maximum reduction in the average normal forces acting on the beams about 74% and 54% represents an interval around 8 KN. Thus, there is no increment at any beams.
- The maximum reduction in the average normal forces acting on the columns is about 6% to 26%, representing an interval between 6 KN to 97 KN.

Type	P max Brace	P max Bare	P change	P change
	KN	KN	KN	%
Beams (Max)	0,00	0,00	0,00	0%
Beams (Min)	2,79	10,79	-7,99	-74%
Columns (Max)	95,44	101,66	-6,22	-6%
Columns (Min)	58,88	79,04	-20,16	-26%

Table 92. Maximum and minimum change of the average normal force in beams and columns regards percentage-FVD

Type	P max Brace	P max Bare	P change	P change
	KN	KN	KN	%
Beams (Max)	0,00	0,00	0,00	0%
Beams (Min)	7,28	15,67	-8,39	-54%
Columns (Max)	89,76	95,66	-5,90	-6%

Columns (Min)	537,36	634,37	-97,01	-15%
---------------	--------	--------	--------	------

Table 93. Maximum and minimum change of the average normal force in beams and columns regards absolute values-FVD.

#### 9.2.1.2 Shear force:

According to Table 94 and Table 95, the dissipative action of the fluid viscous damper generates on the average shear forces the following features concerning the pre-retrofit building:

- The maximum reduction in the average shear forces acting on the beams around 74% and 54% represents an interval around 33 KN. Additionally, the maximum increment is negligible, achieving a maximum increment of 4%, equivalent to 0.4 KN.
- The maximum reduction in the average shear forces acting on the columns is about 20% to 43%, representing an interval between 47 KN to 38 KN.

Type	V max BRACE	V max BARE	V change	V change
	KN	KN	KN	%
Beams (Max)	11,18	10,79	0,39	4%
Beams (Min)	61,39	92,65	-31,26	-34%
Columns (Max)	151,11	188,86	-37,76	-20%
Columns (Min)	28,60	50,24	-21,64	-43%

Table 94. Maximum and minimum change of average shear forces in beams and columns regards percentage-FVD

Type	V max BRACE	V max BARE	V change	V change
	KN	KN	KN	%
Beams (Max)	11,18	10,79	0,39	4%
Beams (Min)	112,49	146,90	-34,40	-23%
Columns (Max)	26,21	42,44	-16,24	-38%
Columns (Min)	138,48	185,46	-46,98	-25%

Table 95. Maximum and minimum change of average shear forces in beams and columns regards absolute values-FVD.

#### 9.2.1.3 Flexural moment:

According to Table 96 and Table 97, the dissipative action of the fluid viscous damper generates on the average flexural moment the following features concerning the pre-retrofit building:

- The maximum reduction in the average flexural moment acting on the beams around 32% and 45% represents an interval between 37 KN-m and 83 KN-m. Additionally, the maximum increment is insignificant, achieving a maximum increment of 8%, equivalent to 1 KN-m.
- The maximum reduction in the average flexural moment acting on the columns is about 15% to 45%, representing an interval between 16 KN-m to 91 KN-m.

Type	M max Brace	M max Bare	M change	M change
	KN-m	KN-m	KN-m	%
Beams (Max)	13,90	12,92	0,98	8%

Beams (Min)	45,41	82,13	-36,72	-45%
Columns (Max)	85,85	101,40	-15,55	-15%
Columns (Min)	40,95	74,96	-34,02	-45%

Table 96. Maximum and minimum change of the average flexural moment in beams and columns regards percentage-FVD

Type	M max Brace	M max Bare	M change	M change
	KN-m	KN-m	KN-m	%
Beams (Max)	13,90	12,92	0,98	8%
Beams (Min)	173,36	256,00	-82,64	-32%
Columns (Max)	85,85	101,40	-15,55	-15%
Columns (Min)	314,56	405,55	-91,00	-22%

Table 97. Maximum and minimum change of the average flexural moment in beams and columns regards absolute values-FVD.

#### 9.2.1.4 Verification of columns:

The interaction curves of the columns are obtained by SAP2000 to check the resistance of the columns. The cross-sections selected are 40cmx40cm and 45cmx45cm from the ground floor of the building. According to Figure 123, all the pairs of Average Normal Force-Average Flexural Moment for the bare building and the building with dampers are inside the design domain, which considers a safety factor  $\phi$ . In addition, the pairs move to a safer position in the domain for the damper effects; the movement is down left. In summary, the building without dissipative devices has columns close to the design limit resistance; the most critical case is the column with a moment around 389.60 KN-m and a normal force of 654.20 KN; however, this element has a cross-section equal to 45x45, hence, comply with the resistance criterium.

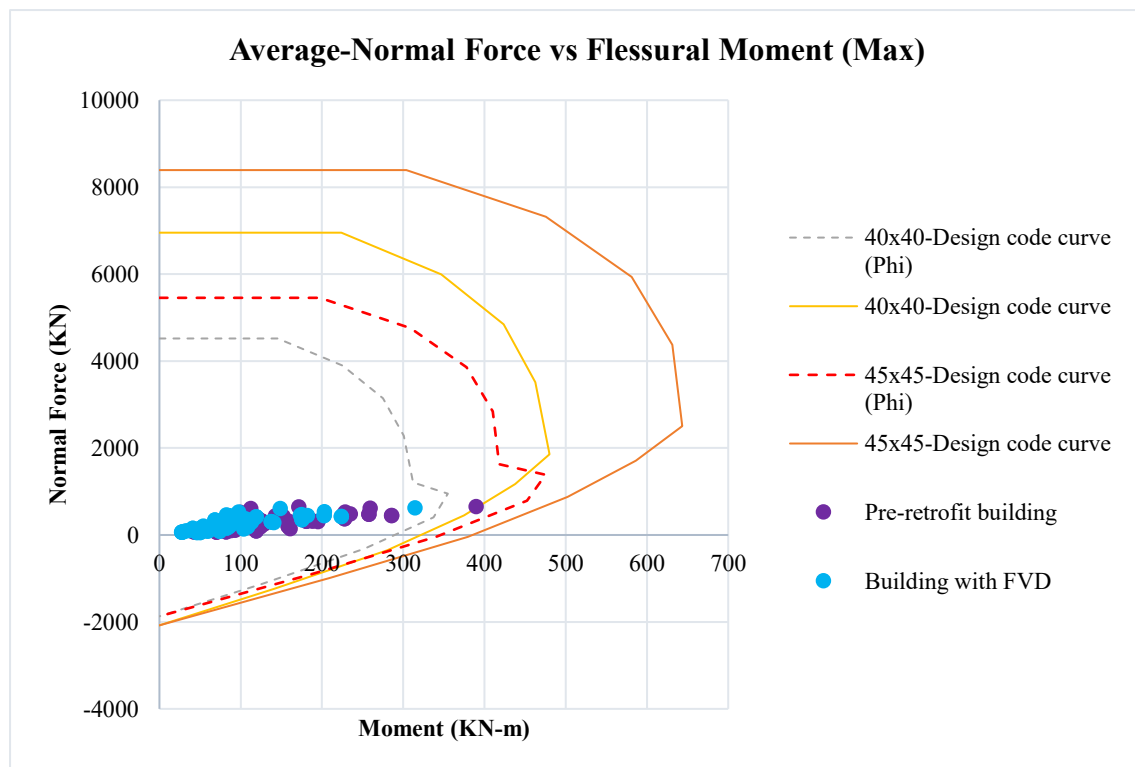


Figure 123. Verification of columns by interaction diagram in structure with FVD.

In the most critical time-history analysis (TH3), the maximum pairs of the moment-normal force of the columns are inside the interaction diagram for the building with and without dampers according to the Figure 124. The pairs outside the design domain of the cross-sections should worry about the safety; however, it does not represent a risk to the structure because the column associated has a cross section of 45cmx45, hence, it is inside the domain. In addition, the damper effects push the pairs into the design domain, improving the safety in the building. Next figure shows the interaction diagram verification for TH3:

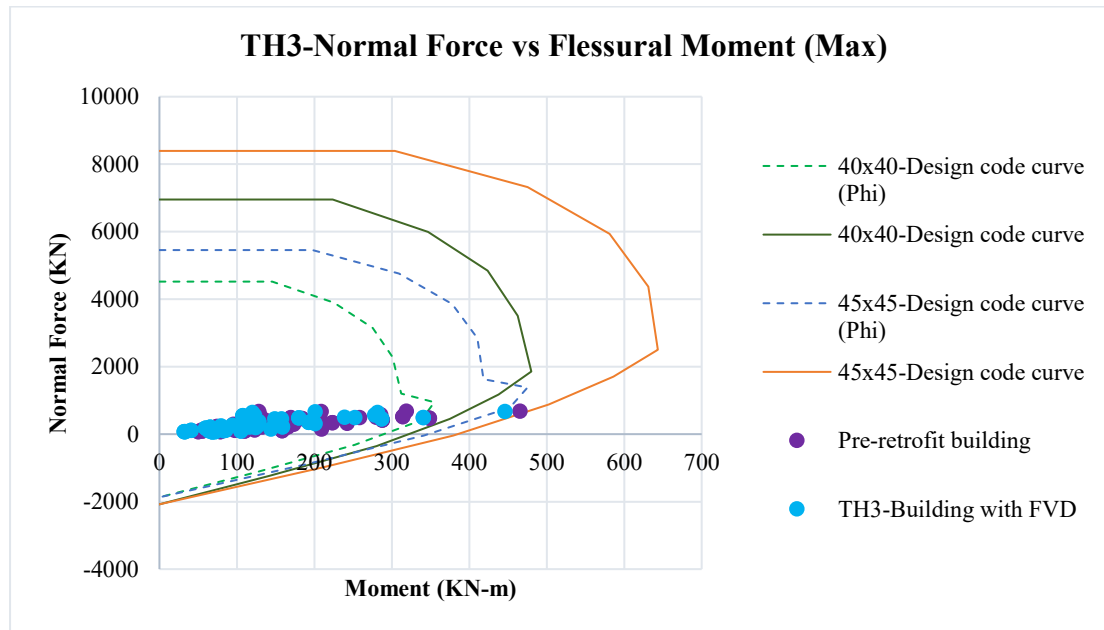


Figure 124. TH3-Verification of columns by interaction diagram in structure with FVD.

In conclusion, the effect of the fluid viscous damper reduces the vulnerability of the structure regards the internal forces.

### 9.2.2 Retrofitted structure with metallic-yielding dampers.

In general, the average internal forces of the structural elements are increased and reduced. Notwithstanding, the shear and moment reduction is predominant in the columns; in the opposite circumstance, the increment is insignificant. Concerning to the beams, the average flexural moment is reduced, and the average shear force does not have any relevant increment or reduction. Additionally, the most critical change is in the average normal forces of the columns and the beams connected to the bracing system. However, this does not represent a risk to the safety of the building. Finally, in the most critical case TH3, there is an increment in the columns' normal force, but the interaction curve checks the stability of the elements.

#### 9.2.2.1 Normal forces:

According to Table 98 and Table 99, the dissipative action of the metallic-yielding damper generates on the average normal forces the following features concerning the pre-retrofit building:

- The maximum increment in the average normal force acting on the beams connected to the bracing system is 817%, representing a value around 77 KN. Thus, the increment is in compression and tension. However, it does not overcome the ultimate resistance of the concrete. Also, the secondary beams have a maximum reduction in the average normal force about 40% and 59%, representing an interval between 6 KN to 8 KN.
- The maximum increment in the average normal force acting on the columns is about 32% to 38%, representing an interval between 55 KN to 209 KN. In addition, the maximum reduction is around 2% and equal to 13.72 KN.

Type	P max Brace	P max Bare	P change	P change
	KN	KN	KN	%
Beams (Max)	86,87	9,47	77,40	817%
Beams (Min)	4,49	10,85	-6,36	-59%
Columns (Max)	204,25	148,48	55,77	38%
Columns (Min)	606,02	619,74	-13,72	-2%

Table 98. Maximum and minimum change of the average normal force in beams and columns regards percentage-HYD

Type	P max Brace	P max Bare	P change	P change
	KN	KN	KN	%
Beams (Max)	86,87	9,47	77,40	817%
Beams (Min)	11,66	19,47	-7,81	-40%
Columns (Max)	854,68	645,23	209,46	32%
Columns (Min)	606,02	619,74	-13,72	-2%

Table 99. Maximum and minimum change of the average normal force in beams and columns regards absolute values-HYD.

The histogram has been made to represent in a graphic form the increment and the reduction of the average normal forces acting on the 72 columns concerning the pre-retrofit building. Table 100 shows the procedure and lists the intervals. The negative values represent the reduction and the positive the increment. The histogram is focused on the increment of normal force, and goes from 0 to 209.5 KN.

n		$F_{inf}$	$F_{sup}$	Quantity	Frequency
72	1		<0	6	8%
<b>K</b>	2	0,0	26,2	20,0	28%
7	3	26,2	52,4	14,0	19%
$\Delta_x$	4	52,4	78,5	14,0	19%
26,2	5	78,5	104,7	14,0	19%
<b>F<sub>max</sub></b>	6	104,7	130,9	6,0	8%
209,46	7	130,9	157,1	0,0	0%
	8	157,1	183,3	2,0	3%
	9	183,3	209,5	2,0	3%
	Sum			72	100%

Table 100. Histogram-Increment of the average normal force on Columns.

Figure 125 indicates that the increment of normal forces is between 0 KN and 104.7 KN for the 78% of the data and the distribution in the intervals is done symmetrically. Additionally,



the 10 elements with the higher increment (14% of data) are placed in the ground level. And lastly, there is a reduction in normal force only in 6 columns.

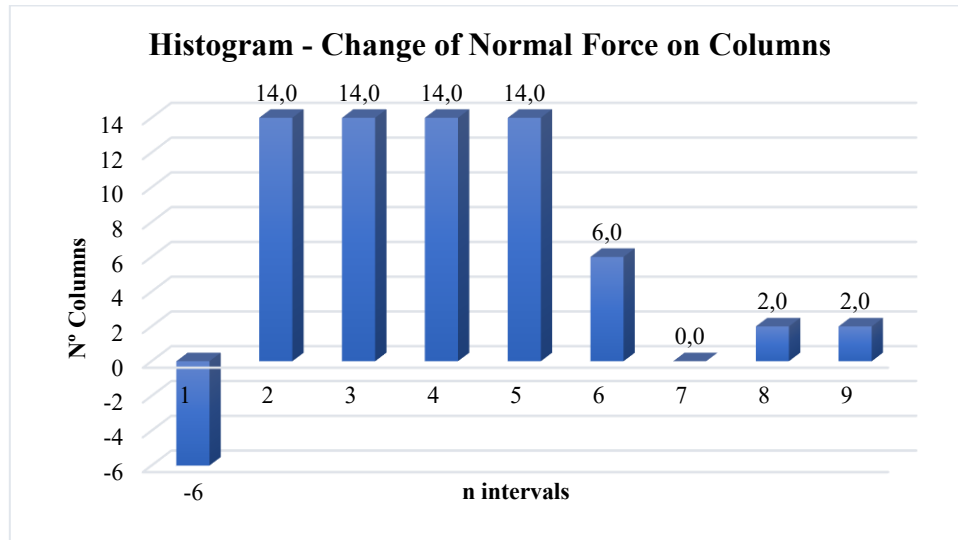


Figure 125. Histogram-Increment of normal force on Column

#### 9.2.2.2 Shear force:

According to Table 101 and Table 102, the dissipative action of the metallic-yielding damper generates on the average shear forces the following features concerning the pre-retrofit building:

- The maximum increment in the average shear forces acting on the beams around 36% equal to 28 KN. Additionally, the maximum reduction is about 13% equivalent to 15.5 KN. In these cases, both changes are irrelevant.
- The maximum reduction in the average shear forces acting on the columns is about 17% to 33%, representing an interval between 32.5 KN to 47.63 KN. Additionally, the maximum increment is about 11% equal to 5.62 KN.

Type	V max Brace	V max Bare	V change	V change
	KN	KN	KN	%
Beams (Max)	106,43	78,35	28,08	36%
Beams (Min)	108,29	123,85	-15,55	-13%
Columns (Max)	58,34	52,73	5,62	11%
Columns (Min)	67,06	99,59	-32,52	-33%

Table 101. Maximum and minimum change of the average shear in beams and columns regards percentage -HYD.

Type	V max Brace	V max Bare	V change	V change
	KN	KN	KN	%
Beams (Max)	106,43	78,35	28,08	36%
Beams (Min)	108,29	123,85	-15,55	-13%
Columns (Max)	58,34	52,73	5,62	11%
Columns (Min)	131,99	179,62	-47,63	-27%

Table 102. Maximum and minimum change of the average shear in beams and columns regards absolute values -HYD.

### 9.2.2.3 Flexural moment:

According to Table 103 and Table 104, the dissipative action of the metallic-yielding damper generates on the average flexural moment the following features concerning the pre-retrofit building:

- The maximum reduction in the average flexural moment acting on the beams around 32% and 30% represents an interval between 65 KN-m and 78 KN-m. Additionally, the maximum increment is insignificant, achieving a maximum increment of 30%, equivalent to 4 KN-m.
- The maximum reduction in the average flexural moment acting on the columns is about 27% to 36%, representing an interval between 45 KN-m to 104.76 KN-m. Additionally, the maximum increment is insignificant, achieving a maximum increment of 12%, equivalent to 6 KN-m.

Type	M max Brace	M max Bare	M change	M change
	KN-m	KN-m	KN-m	%
Beams (Max)	17,02	13,11	3,91	30%
Beams (Min)	139,51	204,46	-64,95	-32%
Columns (Max)	57,53	51,55	5,98	12%
Columns (Min)	79,07	124,17	-45,10	-36%

Table 103. Maximum and minimum change of the average flexural moment in beams and columns regards percentage -FVD.

Type	M max Brace	M max Bare	M change	M change
	KN-m	KN-m	KN-m	%
Beams (Max)	17,24	13,28	3,95	30%
Beams (Min)	184,81	262,79	-77,97	-30%
Columns (Max)	57,53	51,55	5,98	12%
Columns (Min)	284,84	389,60	-104,76	-27%

Table 104. Maximum and minimum change of the average flexural moment in beams and columns regards absolute values-HYD.

### 9.2.2.4 Verification of columns:

The interaction diagrams of the columns are obtained by SAP2000 to check the resistance of the columns. The cross-sections selected are 40cmx40cm and 45cmx45cm from the ground floor of the building. According to Figure 126, all the pairs of Average Normal Force-Average Flexural Moment for the bare building and the building with dampers are inside the design domain, which considers a safety factor  $\phi$ . In addition, the pairs move to a safer position in the interaction diagram for the damper effects; the movement is up left. In summary, the building without dissipative devices has columns close to the design limit resistance; the most critical case is the column with a moment around 389.60 KN-m and a normal force of 654.20 KN; however, this element has a cross-section equal to 45x45, hence, comply with the resistance criterium.

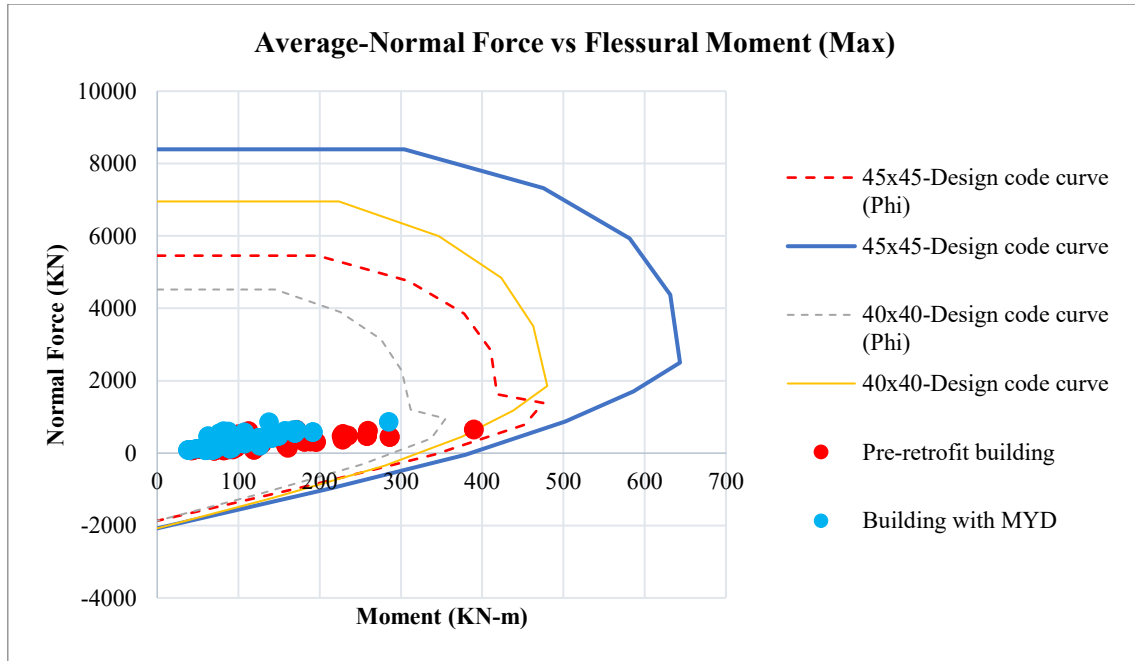


Figure 126. Verification of columns by interaction diagram in structure with MYD.

In the most critical time-history analysis (TH3), the maximum pairs of the moment-normal force of the columns are inside the interaction diagram for the building with and without dampers according to the Figure 127. The pairs outside the design domain of the cross-sections should worry about the safety; however, it does not represent a risk to the structure because the column associated has a cross section of 45cmx45, hence, it is inside the domain. In addition, the damper effects push the pairs into the design domain, improving the safety in the building.

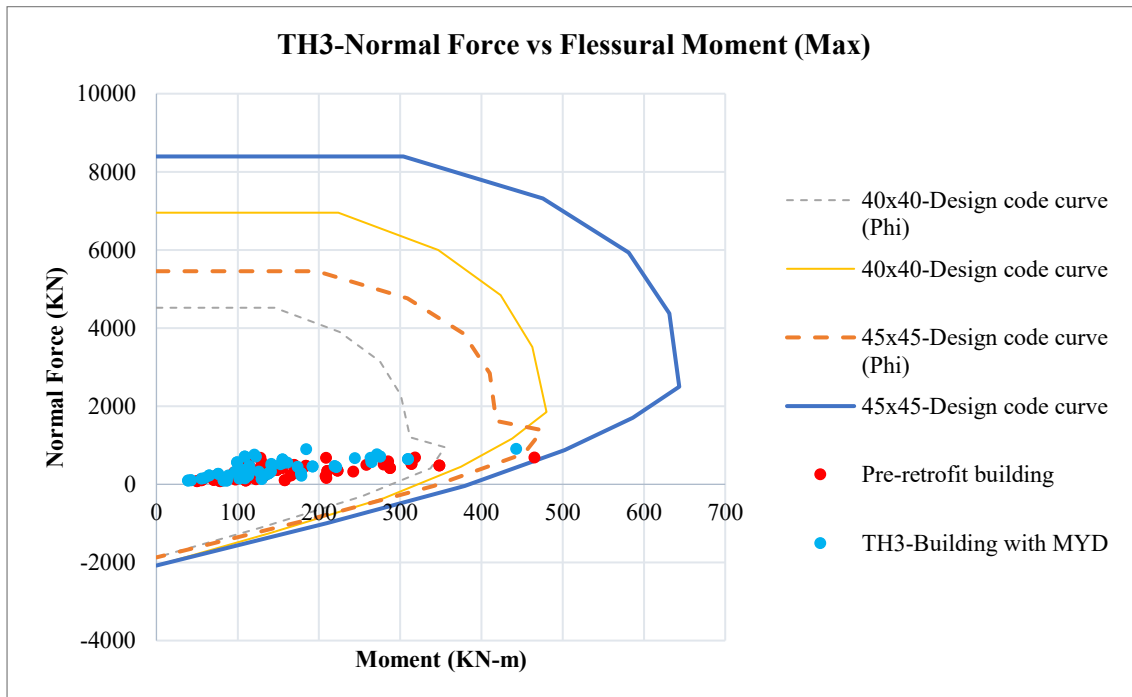


Figure 127. TH3- Verification of columns by interaction diagram in structure with MYD

Furthermore, Figure 128 shows the verification of resistance of the columns for all the time-history analyses. The pairs are obtained from each element at each analysis. Thus, there are 3024 pairs of normal force and flexural moment acting on the columns. The points outside the interaction diagram of the cross-section 40cmx40cm have a cross-section equal to 45cmx45cm, therefore comply with the resistance criterium.

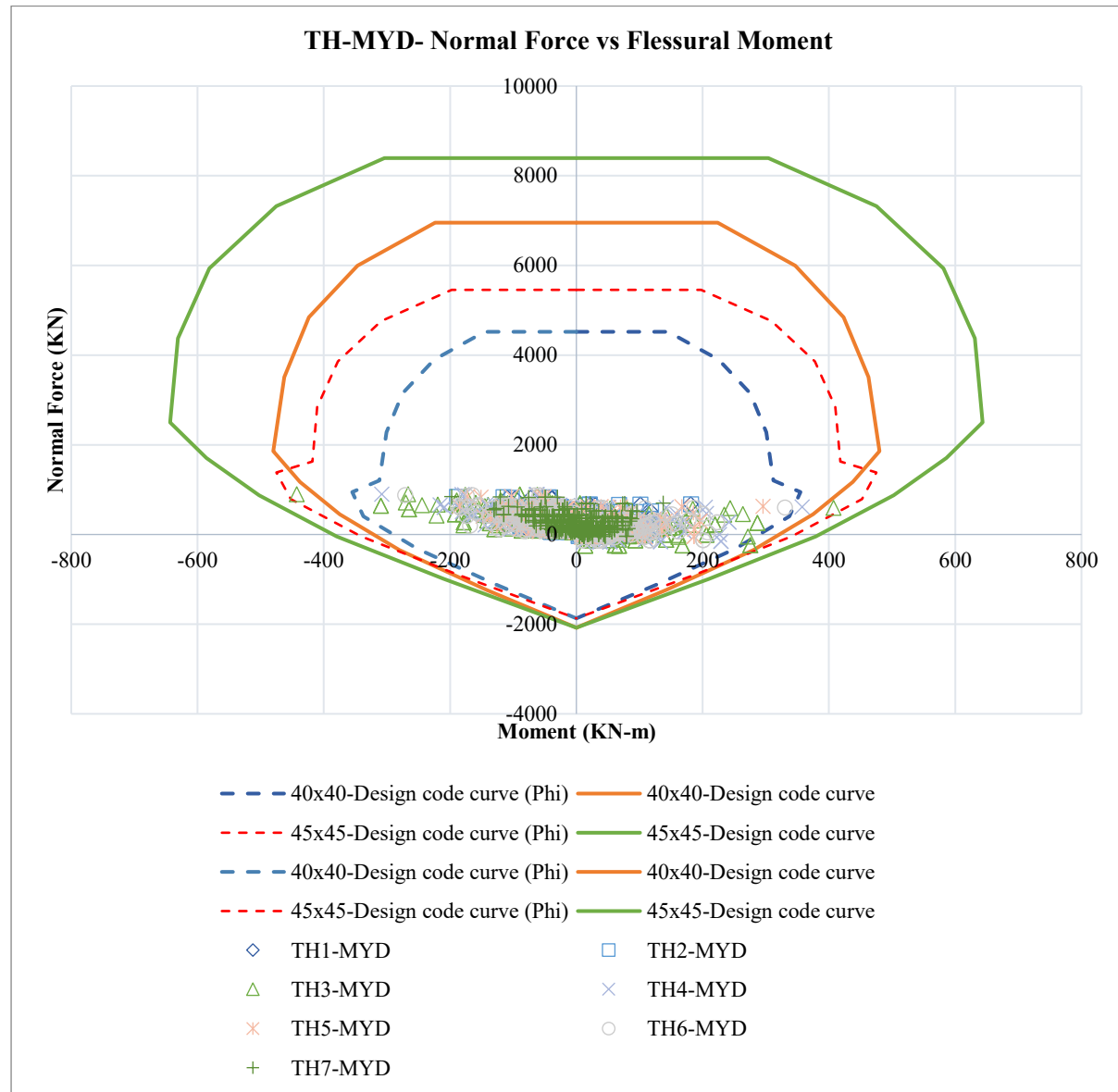


Figure 128. Verification of columns by interaction diagram in structure with MYD for all the TH analyses.

In conclusion, the effect of the metallic-yielding damper reduces the vulnerability of the structure regards the internal forces. However, for the beams must be verified that the normal force does overcome the ultimate resistance of the concrete for compression and tension.

### 9.3 Interstory Drift

The last analysis regards the effect of the dissipation devices on the interstory drift in the building due to the time-history analyses. This characteristic permits the evaluation of the building's safety according to the global ductility capacity following the indications on the Eurocode, either to achieve a precise performance displacement or to meet a minimum brittleness criterion. Figure 129 and Figure 130 illustrates the average interstory drift for the structure with metallic-yielding dampers (MYD), with fluid viscous dampers (FVD) and without any damper (BF). The shapes describe the average maximum interstory drift considering the seventh time-history analyses in each structure. As it can be seen, both control strategies reduce the interstory drift in the structure and produce a softer transition between stories.

According to Figure 129 and Figure 130, the metallic-yielding damper reduces the interstory drift on average 43% for the 4th and third story and 53% for the second and first story. On the other hand, the fluid viscous damper the 30%, 43%, 41%, and 39% for the 4th to the first story, respectively. This effect does not produce the increment of internal forces at the level of representing a risk to the building as confirmed previously. Indeed, both solutions can reduce the structure's vulnerability despite the increment of normal forces.

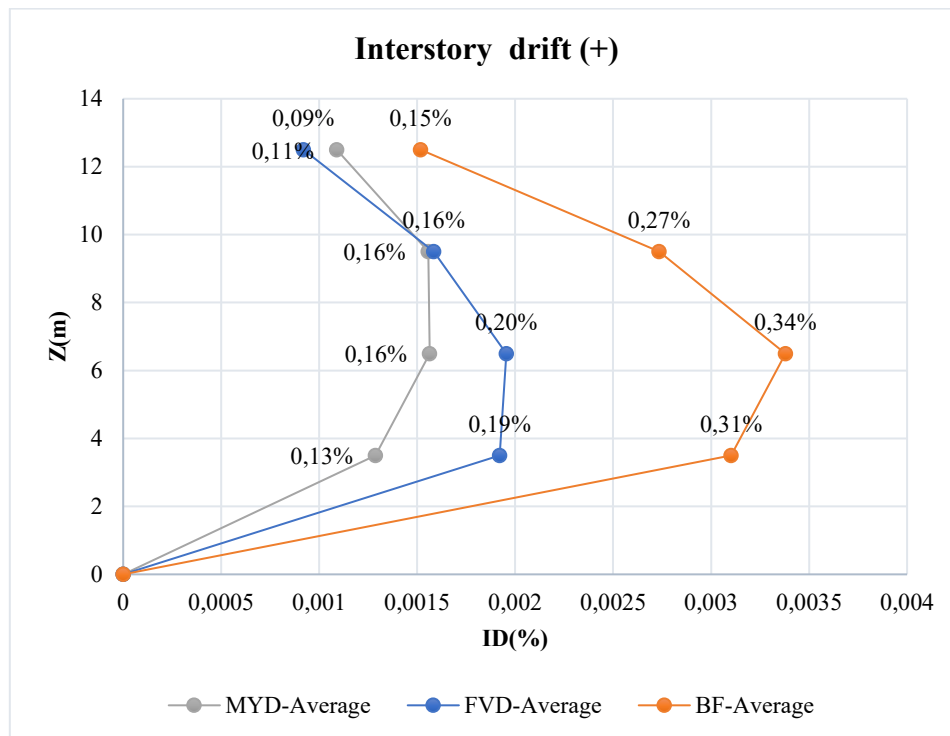


Figure 129. Average of the maximum interstory drift from nonlinear time-history analysis on positive direction (+) of the structure with and without dampers.

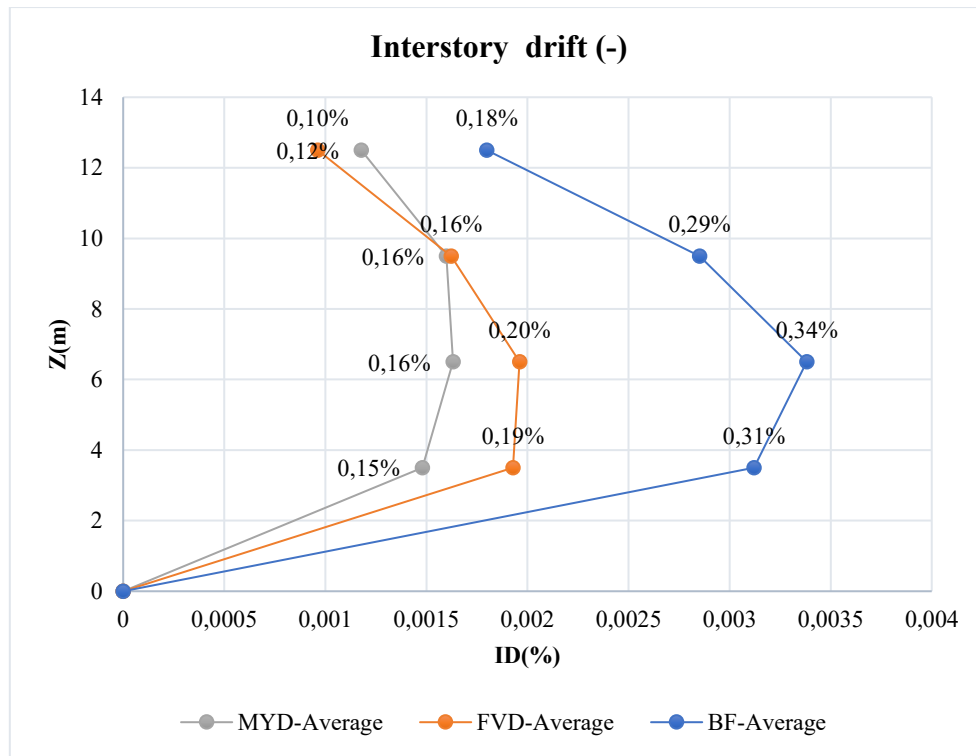


Figure 130. Average of the maximum interstory drift from nonlinear time-history analysis on positive negative (-) of the structure with and without dampers.

#### 9.4 Summary of the results

In conclusion, the improvement of the vulnerability index, the reduction of the interstory drift, and the verification of the internal forces on beams and columns confirms that the Metallic-Yielding Dampers and the Fluid Viscous Dampers reduces the level of the vulnerability of the structure and increases the seismic performance as was obtained through the safety evaluation with the Acceleration-Displacement Response Spectrum. Table 105 summarizes the results:

Retrofitted structure with fluid viscous dampers	Retrofitted structure with metallic-yielding dampers
<i>Internal forces of the structural elements.</i>	<i>Internal forces of the structural elements.</i>
<ul style="list-style-type: none"> <li>- Reduction of internal forces in all the beams, principally those elements connected with the damper.</li> <li>- Reduction of internal forces in all the columns.</li> <li>- The normal force is not incremented in beams.</li> </ul>	<ul style="list-style-type: none"> <li>- Reduction of flexural moments in all the beams, principally those elements connected with the damper. Regards shear forces, the changes are irrelevant.</li> <li>- Reduction of shear and moments in almost all the columns.</li> <li>- Increment of normal forces in beams and columns. Principally those elements connected with the damper</li> </ul>
<i>Verification of resistance on columns</i>	<i>Verification of resistance on columns</i>
The pairs normal force-flexural moment moves to a safer position into the interaction diagram of the columns.	The pairs normal force-flexural moment moves to a safer position into the interaction diagram of the columns.

<i>Interstory drift</i>	<i>Interstory drift</i>
Reduction of the interstory drift around 38%	Reduction of interstory drift around 48%
<i>Vulnerability Index</i>	<i>Vulnerability Index</i>
The index is equal to 1.52, indicating an improvement of the seismic performance and safety in comparison to the building without dampers.	The index is equal to 1.59, indicating an improvement of the seismic performance and safety in comparison to the building without dampers.

Table 105. Summary of the effects of the dampers on the structure.

Ultimately, Figure 131 shows the effect of the fluid viscous dampers (FVD) and metallic-yielding dampers (MYD) on the average maximum pairs of flexural moment-normal force acting on the columns. All pairs move to a safer position in comparison to the pre-retrofit building.

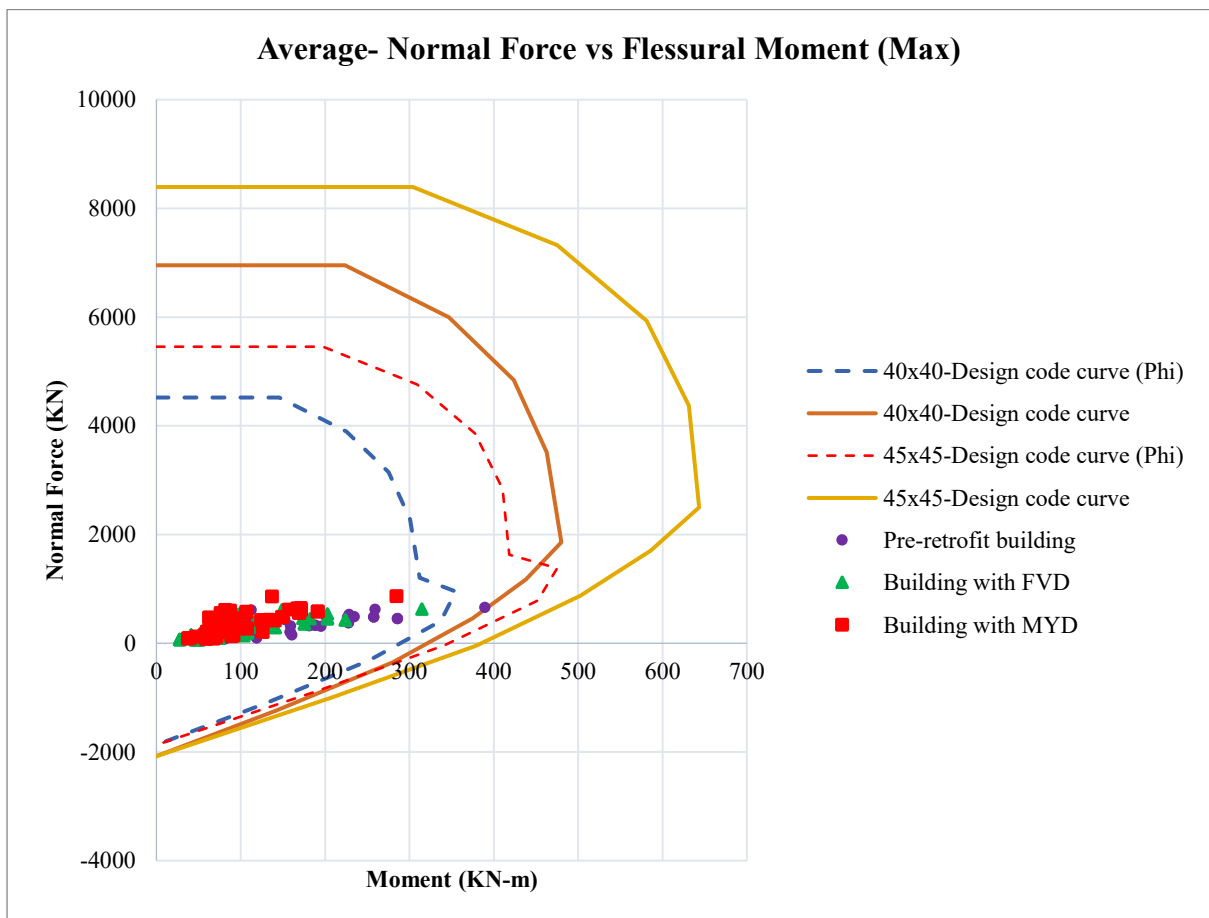


Figure 131. Interaction diagram verification for pre-retrofit building and building with FVD and MYD.

# Conclusions

The present study's objective was to evaluate the seismic performance improvement provided by implementing fluid viscous dampers and metallic-yielding dampers for seismic retrofitting intervention on a FE model of an RC building calibrated through the laboratory test to evaluate the benefits and drawbacks in applying these seismic control systems. Previous FE model from Schiavo was used, modifying strain-stress models of the cross-sections to improve the calibration concerning the dynamic response obtained from the experimental campaign. The study has found that both seismic control strategies reduce the level of vulnerability of the structure during the nonlinear time-history analyses, despite the increment of the normal force in some elements.

The design of the seismic retrofitting intervention with dissipative devices follows a simplified methodology that directly relates the actual seismic performance of the building with the seismic design demand defined by the previous research. The approaches consider the capacity curves from nonlinear pushover analysis and the design response spectrum to define the input parameters of the iterative procedure to calculate the geometry and mechanical properties of the devices positioned on the structure to obtain the required energy dissipation to reduce the seismic design response to the expected value. As a result of the randomness of the earthquake characteristics, seven different accelerograms have been used to check the retrofitting interventions, finding that the strain-energy method used on the design of both passive control systems can predict the dissipative action of the hysteretic loops on the structure without representing a risk to the structure. This conclusion is essential because the seismic control strategies are not commonly used in many countries with high seismic hazards due to the lack of knowledge and design difficulty. However, it has been confirmed that using the simplified method and finite element commercial software can provide accurate results. Therefore, this thesis aims to contribute to expanding the implementation of these devices in seismic-affected areas worldwide.

As demonstrated in Chapter 9 during the time-history analyses, both dissipative devices reduce the shear forces and the flexural moments acting on columns. In addition, the fluid viscous dampers reduce all internal forces in the beams, and the metallic-yielding dampers reduce the flexural moment while the shear force does not evidence significant variation concerning the bare building. The main difference between the passive control systems in the study is the effect on the normal forces in the beams and columns. The metallic-yielding dampers cause an increment in the normal forces of the elements connected with the chevron bracing system;



however, the increment does not cause a collapse in the structural elements. Chapter 9 confirms the safety in the columns thanks to the dissipative devices, the pair force-moment in the column's interaction diagram moves into a safer position on both cases. According to Figure 131, the movement is down-left for the fluid viscous damper into the column's interaction curve, while for the metallic-damper devices is up-left. In addition, the increment of the normal force in beams due to the chevron bracing system connection does not produce collapse by ultimate resistance of the element in compression or tension.

An important parameter evaluated in the paper is the maximum interstory drift in the structure. The retrofitting interventions applied can reduce the interstory displacement produced in the building during the seismic event, as discussed in Chapters 7, 8, and 9. Additionally, the metallic-yielding dampers cause a further reduction than the fluid viscous dampers. However, both have excellent performance, reducing the interstory drift on average 48% and 38% for MYD and FVD, respectively; this allows complying with the maximum displacement requirements of the codes if the case requires it.

Regards the vulnerability index, it can be verified that the index, based on the capacity curve in SDOF, represent in a simplified form the seismic performance of the building. As discussed in Chapter 9, the building without dampers has an index equal to 0.96, representing an unsafe condition and the requirement of seismic performance improvement for the seismic design demand at the ultimate limit state. In addition, the verification of collapse in the columns of this structure shows the formation of plastic hinges during the time-history analyses because some pairs of Normal Force–Flexural Moment are out the interaction curve of the central column for accelerogram 3 and 4 defined in Chapter 3. This condition must be prevented due to the requirements of the strain energy-based method which assumes that the structure must remain in the elastic range during the seismic event while the dampers dissipate energy. Thus, the columns cannot develop plastic hinges at the ground level once the dissipative devices are implemented. On the other hand, the building with dissipative devices has indexes equal to 1.52 and 1.59 for the retrofitting with Fluid Viscous Dampers and Metallic-Yielding Dampers, respectively, indicating an improvement of the seismic performance compared to the index of the bare building equal to 0.96. In both cases, the columns do not evidence the formation of plastic hinges.

Finally, the vulnerability index indicates the improvement of the seismic performance of the building. The structure without the dampers has an inelastic behavior during the time-history analyses, evidenced in the acceleration-displacement response spectrum verification and in the vulnerability index lower than 1. However, once the dissipative devices are implemented, the structure behaves in the elastic range and the index is higher than 1, without the development of plastic hinges in the columns during the time-history analyses. In addition, the elastic seismic performance during an earthquake is vital because it let the increment the service life of the buildings and reduces the risk to collapse.

The present study emphasizes the advantages of using metallic-yielding dampers and fluid viscous dampers; both are excellent strategies to increase the seismic performance of the building. Hence, it cannot be identified which one has the best seismic performance; it depends on the retrofitting requirements. However, it is recommended to use the fluid viscous dampers on critical structures where the reduction of all internal forces is required due to the uncertainties of the material's resistance properties. Moreover, in modernizing the seismic design demand of a specific building due to the upgrade of the construction codes, both solutions may provide excellent results. Lastly, the drawbacks are related to the economic, technical, and construction aspects. Therefore, future research could investigate the most suitable approach based on those parameters.

# Bibliography

1. P. Negro, G.V., G.E. Maginette, A.V. Pinto., *Test on a Four-Storey Full-Scale R/C Frame Desinged According to Eurocode 8 and 2: Preliminary Report*. 1994: Join Research Center, European Comission.
2. Schiavo, E., *Influence of masonry infills on dynamic behaviour of reinforced concrete framed structures*, in *Scuola di Ingegneria Civile, Ambientale e Territoriale Corso di Laurea Magistrale in Ingegneria Civile - Orientamento Strutture*. 2016, Politecnico Di Milano. p. 286.
3. Domaneschi, M. and L. Martinelli, *Il controllo strutturale delle vibrazioni nell'ingegneria civile*, in *Structural*. 2015.
4. Y. M. Parulekar and G. R. Reddy, *Passive response control systems for seismic response reduction: A state-of-the-art review*. International Journal of Structural Stability and Dynamics, 2008. Vol. 9, No. 1 (2009) 151–177: p. 27.
5. Cimellaro, C.P., *Seismic Protection Systems*, S.o.P. Systems, Editor. 2020: Politecnico di Torino-Safety assessment and retrofitting of existing structures and infrastructures.
6. Michael C. Constantinou, T.T.S., Gary F. Dargush, *Passive Energy Dissipation Systems For Structural Design And Retrofit*. 1998: Research Foundation of the State University of New York and the Multidisciplinary Center for Earthquake Engineering Research.
7. Federal Emergency Management Agency, *FEMA 356, in Prestandard And Commentary For The Seismic Rehabilitation Of Buildings*. 2000.
8. Castaldo, P., *Passive Energy Dissipation Devices*, in *Integrated Seismic Design of Structure and Control Systems*. 2014. p. 21-62.
9. Connor, J. and S. Laflamme, *Structural Motion Engineering*. 2014: Springer Nature.
10. Nishant Kishore Rai, et al., *Seismic Response Control Systems for Structures*. Defence Science Journal, 2009. Vol. 59, No. 3: p. pp. 239-251.
11. Taylor Devices Inc, *Damper Design Manual*, in *General Guidelines for Engineers Including a Brief History*. 2020, TaylorDevicesInc: EEUU. p. 306.
12. Lee D. and Taylor D. P., *Viscous damper development and future trends*. The Structural Design of Tall Buildings, 2001. 10(5): p. 311-320.
13. Michael C. Constantinou, P.T., Wilhelm Hammel, Ani N. Sigaher, *Toggle-Brace-Damper Seismic Energy Dissipation Systems*. Journal Of Structural Engineering, 2001.
14. Ken-Chyuan Tsai, et al., *Design of steel triangular plate energy absorbers for seismic-resistance construction*, in *Earthquake Spectra*. 1993.
15. Aiken, A., *Passive Energy Dissipation - Hardware and Applications*, in *SEAOSC Symposium on passive energy disipation systems for new and existing buildings*. . 1996: Los Angeles.
16. Y. Rochdi , et al., *Parametric Identification of Nonlinear Hysteretic systems*. 17th IFAC World Congress (IFAC'08), 2008.
17. Theodore L. Karavasilis, Sanaya Kerawala, and Emma Hale, *Hysteretic model for steel energy dissipation devices and evaluation of a minimal-damage seismic design approach for steel buildings*. Journal of Constructional Steel Research, 2011.

18. Wen YK, *Method for random vibration of hysteretic systems*. Journal of Engineering Mechanics, 1976. 102: p. 249-263.
19. K.C. Tsai, et al., *Earthquake Spectra*, in *Design of Steel Triangular Plate Energy Absorbers for Seismic-Resistant Construction*. 1993. p. Pag. 24.
20. Chao Zhang, et al., *A methodology for design of metallic dampers in retrofit of earthquake-damaged frame*. Techno-Press Journals, 2015. Vol. 56.
21. Mussa Mahmoudi, Mohammad Ghasem Abdi, and Farid Mahmoudi, *Influence Of The Tadas Dampers On The Ductility Reduction Factor Of Steel Frames*, in *Second European Conference on Earthquake Engineering and Seismology*. 2014: Istanbul.
22. J. B. Mander, M. J. N. Priestley, and R. Park, *Theoretical Stress-Strain Model For Confined Concrete*. Journal of Structural Engineering, 1988. Vol. 114.
23. Computers & Structures, I., *SAP2000 Manual-CSI Analysis Reference Manual*. Vol. 19. 2016.
24. Shaffu, A., *Comparison of analysis techniques for the seismic evaluation of an 88-storey concrete building*, in *Department of Civil Engineering*. 2011, Ryerson University: Digital Commons @ Ryerson.
25. Zongming HUANG, et al., *Effects Of Confined Concrete Models On Simulating Rc Columns Under Low-Cyclic Loading*, in *13th World Conference on Earthquake Engineering*. 2004: Vancouver, B.C., Canada.
26. F. Di Trapani and L. Cavaleri, *Nonlinear Static Aanalysis (Pushover)*. Politecnico di Torino e Università di Palermo.
27. Ministero delle Infrastrutture e dei Trasporti *Norme Tecniche per le Costruzioni*. 2018.
28. Oscar M. Ramirez, et al., *Development and Evaluation of Simplified Procedures for Analysis and Design of Buildings with Passive Energy Dissipation Systems*, in *Technical Report MCEER-00-0010*. 2001, University of Buffalo, State University of New York.